中国科学技术大学

博士学位论文

RHIC 能区重离子对撞中正负电子对和 J/ψ 介子产生的测量

作者姓名： 沈凯峰
学科专业： 粒子物理与原子核物理
导师姓名： 唐泽波 教授 查王妹 副教授 马荣荣 研究员
完成时间： 二〇二四年十月十七日

University of Science and Technology of China

A dissertation for doctor’s degree

Measurements of e^+e^- and J/ψ production in heavy-ion collisions at RHIC

Author: Shen Kaifeng

Speciality: Particle and Nuclear Physics

Supervisors: Prof. Zebo Tang, Prof. Wangmei Zha, Prof. Rongrong Ma

Finished time: October 17, 2024

中国科学技术大学学位论文原创性声明

本人声明所呈交的学位论文，是本人在导师指导下进行研究工作所取得的成果。除已特别加以标注和致谢的地方外，论文中不包含任何他人已经发表或撰写过的研究成果。与我一同工作的同志对本研究所做的贡献均已在论文中作了明确的说明。

作者签名：　　　　　　　　签字日期：

中国科学技术大学学位论文授权使用声明

作为申请学位的条件之一，学位论文著作权拥有者授权中国科学技术大学拥有学位论文的部分使用权，即：学校有权按有关规定向国家有关部门或机构送交论文的复印件和电子版，允许论文被查阅和借阅，可以将学位论文编入《中国学位论文全文数据库》等有关数据库进行检索，可以采用影印、缩印或扫描等复制手段保存、汇编学位论文。本人提交的电子文档的内容和纸质论文的内容相一致。

控阅的学位论文在解密后也遵守此规定。

☑ 公开　□ 控阅（____ 年）

作者签名：　　　　　　　　导师签名：

签字日期：　　　　　　　　签字日期：

摘　要

基于格点量子色动力学（Lattice QCD）的研究阐明一种夸克处于解禁闭状态的全新物质状态——夸克胶子等离子体（Quark Gluon Plasma, QGP）可以在极端相对论重离子对撞中产生。寻找 QGP 形成的信号并深入研究其时空演化和特性，已成为目前高能重离子对撞研究的核心方向。通过重离子对撞产生的 QGP 存续时间极短，对其性质的研究只能通过 QGP 对特定物理过程或粒子产生的影响来间接实现。在众多用于研究 QGP 性质的探针中，重味夸克偶素和双轻子在产生后可以穿越 QGP 并反映 QGP 早期性质，是研究 QGP 的重要探针。对相对论重离子碰撞中重味夸克偶素和双电子产生的实验研究，可以为 QGP 性质的研究提供重要的实验依据，具有重要的物理意义。

重味夸克偶素主要在重离子对撞初期于 QGP 形成之前的部分子硬散射过程中产生。在穿越 QGP 这一热密介质时，解禁闭的夸克和胶子会屏蔽组成重味夸克束缚态的正反重味夸克之间的强相互作用，造成相对论离子对撞中重味夸克偶素产额压低现象，这被认为是 QGP 形成的标志信号。重味夸克偶素还可以通过 QGP 中自由的重味夸克和反夸克的重组合产生，与上述屏蔽效应形成的竞争会给实验上通过重味夸克偶素研究 QGP 的性质造成了很大的困扰。由于两种效应都具有很强的对撞能量依赖，通过研究不同对撞能量下重味夸克偶素的产生，可以帮助人们更好的理解 QGP 的性质。本论文测量了 54.4 GeV 金核-金核对撞中 J/ψ 的产额压低效应，并与 SPS 能区 17.3 GeV 铅核-铅核和 RHIC 能区 200 GeV 金核-金核对撞中的测量结果进行对比。实验结果显示，在 17.3 GeV 到 200 GeV 能量范围内的核核中心碰撞中，J/ψ 产额压低效应没有明显的对撞能量依赖关系，这表明色荷屏蔽效应和重组合效应形成了很好的平衡。我们进一步研究了 J/ψ 产额压低的横动量依赖关系，发现不同对撞能量下该横动量依赖关系有很大的差别。在 54.4 GeV 金核-金核对撞中，其横动量谱的上升趋势比 200 GeV 金核-金核对撞中明显得多。由于重组合产生的 J/ψ 主要集中在低横动量区间，该横动量依赖的差异从实验上证实了 54.4 GeV 能量下重组合效应的贡献明显低于 200 GeV 对撞中的重组合贡献。

J/ψ 介子还可以通过光核相互作用产生，该过程是研究相对论重离子碰撞产生的极强电磁场的主要探针。在相对论重离子对撞的初始阶段，以接近光速运动的带电原子核可以产生 10^{14-16}T 的极强电磁场。极强电磁场下的 QED 可以产生许多新奇的量子反常现象，已成为相对论重离子对撞领域一个研究热点，然而许多研究都集中在寻找 QGP 中极强电磁场相关的信号反而对电磁场本身的研究较少。理论指出该极强电磁场可以等效为一束准实光子，而光子与原子核相互

作用可以产生横动量很低的 J/ψ。因此，实验上可以通过测量光致产生的极低横动量 J/ψ 产额研究极强电磁场的性质。本论文测量了 200 GeV 同质异位素对撞（${}^{96}_{44}\mathrm{Ru}+{}^{96}_{44}\mathrm{Ru}$ 和 ${}^{96}_{40}\mathrm{Zr}+{}^{96}_{40}\mathrm{Zr}$）中极低横动量下 J/$\psi$ 介子的产额。这两种原子核的核子数相同，但电荷数相差 10%，对撞产生的系统除了电磁场强相差约 20% 外其他情况基本相同，是研究相对论重离子对撞产生的电磁场性质的理想实验室。实验结果发现 ${}^{96}_{44}\mathrm{Ru}+{}^{96}_{44}\mathrm{Ru}$ 对撞中 $p_{\mathrm{T}}< 0.2$ GeV/c 的 J/ψ 产额高于 ${}^{96}_{40}\mathrm{Zr}+{}^{96}_{40}\mathrm{Zr}$ 对撞中的产额，两者的比例服从 Z^2 的标度。我们进一步将结果与 200 GeV ${}^{197}_{79}\mathrm{Au}+{}^{197}_{79}\mathrm{Au}$ 和 193 GeV ${}^{238}_{92}\mathrm{U}+{}^{238}_{92}\mathrm{U}$ 对撞中的结果进行比较，发现将产额用 $\frac{1}{Z^2}$ 进行归一之后，其在四种对撞系统中的结果符合得很好。

极强电磁场还可以诱导光子光子相互作用产生正负电子对（双电子），这一产生过程的截面正比于 Z^4，因此对相对论重离子对撞过程初始阶段的电磁场更加敏感。本论文测量了 200 GeV ${}^{96}_{44}\mathrm{Ru}+{}^{96}_{44}\mathrm{Ru}$ 和 ${}^{96}_{40}\mathrm{Zr}+{}^{96}_{40}\mathrm{Zr}$ 对撞中极低横动量下双电子的产额。实验发现 ${}^{96}_{44}\mathrm{Ru}+{}^{96}_{44}\mathrm{Ru}$ 和 ${}^{96}_{40}\mathrm{Zr}+{}^{96}_{40}\mathrm{Zr}$ 对撞中极低横动量下双电子的产额比为 1.44±0.18，与基于量子电动力学的计算结果相符合。本论文还将同质异位素对撞中 60-80% 中心度下极低横动量双电子产额和同中心度下金核-金核和铀核-铀核对撞中的产额进行比较，发现 $\frac{1}{Z^4}$ 归一的双电子的产额随着 Z 的增加而下降，这可能是由于不同对撞系统的碰撞参数差异造成的。该测量结果为研究极强电磁场的空间分布提供了重要的依据。本论文还测量了 60-80% 中心度下同质异位素对撞中极低横动量下双电子的方位角调制，观测到了明显的 $\cos(4\Delta\phi)$ 调制（3.6σ）。该角度调制被认为和真空双折射有关。

关键词：相对论重离子对撞　夸克胶子等离子体　极强电磁场　夸克偶素　双轻子

ABSTRACT

Lattice QCD calculations reveal that a novel state of matter known as the Quark Gluon Plasma (QGP), where quarks and gluons are in a deconfined state, is produced at high temperature or densit, which can be achieved in relativistic heavy-ion collisions. Searching for the evidence of the QGP formation and studying its evolution and properties stand at the forefront of high-energy heavy-ion fields. Given the brief lifetime of the QGP, its properties can only be investigated indirectly, such as by examining the impact of the QGP on specific physical processes or particle production. Among the array of probes employed, heavy-flavor quarkonia and dileptons can offer unique insights into the early-stage dynamics of the collision and QGP's thermal and transport properties.

Quarkonia are primarily produced before the formation of the QGP through the initial hard partonic scatterings. As they travel through the QGP, the deconfined quarks and gluons can dissociate the bound quark and anti-quark state, leading to a suppression of quarkonium yields in heavy-ion collision, which was envisioned as a "smoking gun" signal of the QGP formation. Quarkonia can also be generated through recombination of heavy quarks and anti-quarks in the QGP, acting against the dissociation effect, which poses significant challenges to inferring QGP properties from measurements of quarkonia suppression. As both dissociation and recombination effects are strongly dependent on the collision energy, investigating the suppression of quarkonia at different energies can help disentangle the two effects. In the thesis, the suppression of J/ψ production in 54.4 GeV Au+Au collisions is measured, and compared to those in 17.3 GeV Pb+Pb collisions and 200 GeV Au+Au collisions. The experimental results do not show a significant collision energy dependence of J/ψ suppression in central collisions from 17.3 GeV to 200 GeV within uncertainties, indicating a balanced interplay of dissociation and recombination effects. We also report the transverse momentum dependence of J/ψ suppression in 54.4 GeV Au+Au collisions. The results show that the J/ψ suppression at 54.4 GeV is more pronounced at low p_T region compared to that at 200 GeV, indicating weaker recombination effect at 54.4 GeV.

The J/ψ meson can also be produced through photon-nucleus interactions, which can be used to study the properties of the initial electromagnetic field during relativistic heavy-ion collisions. In such collisions, charged atomic nuclei moving at nearly the speed of light can produce a strong electromagnetic field reaching a magnitude of 10^{14-16} Tesla. Under such strong fields, Quantum Electrodynamics (QED) can manifest many novel quantum anomalous phenomena, making it a hot topic in the field of relativistic heavy-ion collisions. However, while much of the research focus has been on searching for signals related to intense electromagnetic fields trapped in the QGP, direct studys of the strong electromagnetic field are relatively scarce. This electromagnetic field can be equivalently regarded as a flux of quasi-real photons, and the interaction between photons from one of the colliding nuclei with the other nucleus can generate J/ψ mesons at characteristically very low p_{T}. Therefore, measuring the yield of such low p_{T} J/ψ mesons allows us to directly study the properties of the electromagnetic field at initial stages. In the thesis, the yield of J/ψ mesons at very low p_{T} is measured in ${}^{96}_{44}$Ru+${}^{96}_{44}$Ru and ${}^{96}_{40}$Zr+${}^{96}_{40}$Zr at 200 GeV. There are same atomic number while the number of charges are different, which means the electromagnetic field are different between isobaric collisions. The yield ratios between ${}^{96}_{44}$Ru+${}^{96}_{44}$Ru and ${}^{96}_{40}$Zr+${}^{96}_{40}$Zr collisions is higher than unity, consistent with the expected Z^2 scaling. Further comparisons with the published results in 200 GeV ${}^{197}_{79}$Au+${}^{197}_{79}$Au and 193 GeV ${}^{238}_{92}$U+${}^{238}_{92}$U shows good agreement among these four collision systems after normalizing the J/ψ yields by $\frac{1}{Z^2}$.

These equivalent photons can also take part in photon-photon interactions. The cross section for coherent photon-photon interactions to produce e^+e^- pairs is proportional to Z^4, enhancing its sensitive to the electromagnetic field. In this thesis, we report the yields of e^+e^- pairs at very low p_{T} in isobaric collisions. The e^+e^- excess yield beyond the hadronic contribution measured in ${}^{96}_{44}$Ru+${}^{96}_{44}$Ru collisions systematically exceeds that in ${}^{96}_{40}$Zr+${}^{96}_{40}$Zr collisions in all the centralities. The ratio between the two deviates from unity by 2.4 σ, indicating that the initial electromagnetic field in ${}^{96}_{44}$Ru+${}^{96}_{44}$Ru collisions is stronger than that in ${}^{96}_{40}$Zr+${}^{96}_{40}$Zr collisions, which is expected due to the larger charge number of the Ru nucleus. Comparing the measured results in ${}^{96}_{44}$Ru+${}^{96}_{44}$Ru and ${}^{96}_{40}$Zr+${}^{96}_{40}$Zr collisions with the published results in ${}^{197}_{79}$Au+${}^{197}_{79}$Au and ${}^{238}_{92}$U+${}^{238}_{92}$U collisions, a significant system dependence is seen. After scaling the excess e^+e^- yields with $\frac{1}{Z^4}$, there still remains a clear collision system dependence for same centrality, likely due to the impact parameter (b) dependence of photon-photon interactions. The azimuthal anisotropy for e^+e^- at very low p_{T} in 60-80% centrality in ${}^{96}_{44}$Ru+${}^{96}_{44}$Ru and ${}^{96}_{40}$Zr+${}^{96}_{40}$Zr collisions is also measured, and a significant $\cos(4\Delta\phi)$ modulation (3.6σ) is observed, which is believed to be related to the vacuum birefringence. Theoretical calculations based on Equivalent Photon Approximation can well describe the results, confirming that the excess yields are very likely originating from coherent photon-induced interactions.

Key Words: Relativistic Heavy-Ion Collisions, Quark-Gluon Plasma, Ultra-strong Electromagnetic Field, Quarkonia, Dilepton

Contents

List of Figures

List of Tables

Chapter 1 Introduction

1.1 The Particles and Interactions

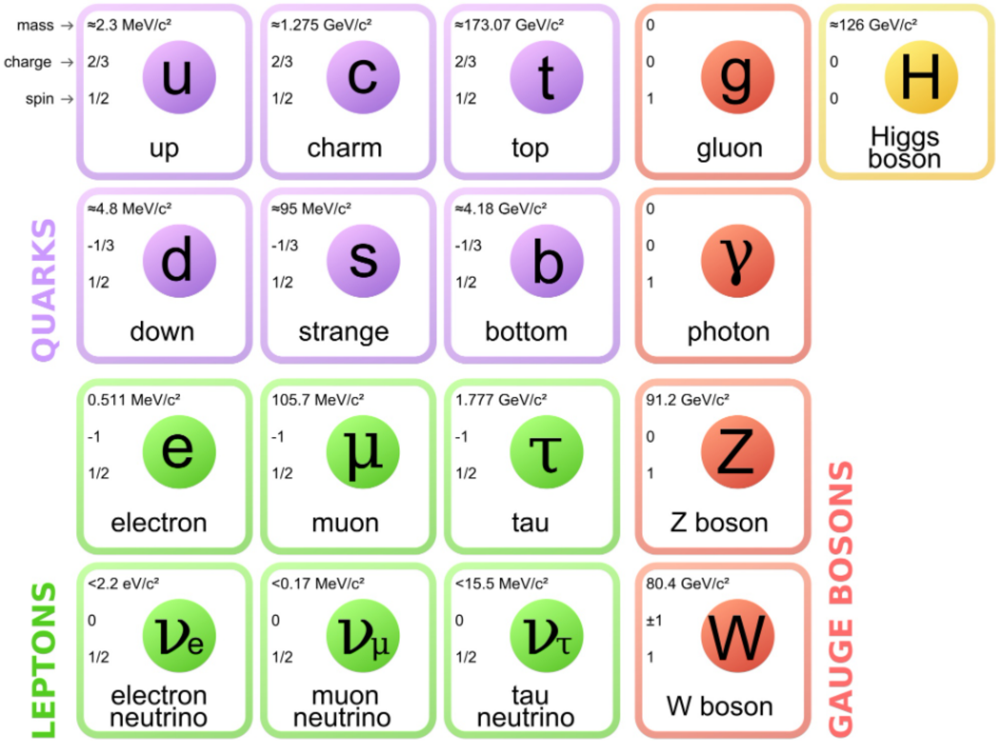

Figure 1.1 The constituents of the Standard Model, including quarks, leptons, vector gauge bosons and higgs. The Figure is from wikipedia [1]

The vast expanse of the known universe is composed of a myriad of fundamental particles, each subject to the governance of fundamental forces including electromagnetic, weak, strong, and gravitational. The interactions among these fundamental particles, with the exception of gravitational interaction, are encompassed by a theory known as the Standard Model, which was formulated in the 1970s. This model elegantly encapsulates the behaviors of seventeen named particles, delineated in Fig. 1.1. Over the course of experimental endeavors, all of these elementary particles have been unearthed, culminating in 2012 when the Higgs boson was discovered by the Large Hadron Collider (LHC). The Standard Model stands as a comprehensive framework, embracing all known subatomic particles and delineating their intricate interactions. It serves as our pinnacle understanding, elucidating the interplay between these particles and three of the fundamental forces. Virtually every experimental observation finds a harmonious explanation within the bounds of the Standard Model, which also boasts precise predictions for a myriad of phenomena. Rooted in the gauge group SU(3)×SU(2)×U(1), the Standard Model remains a cornerstone of modern physics.

The fundamental constituents of matter, as delineated by the Standard Model, are classified into two main categories: quarks and leptons. Each category encompasses six particles, arranged into pairs or “generations”. The first generation comprises the lightest and most stable particles, while the second and third generations consist of heavier and less stable particles. Stable matter in the universe is exclusively composed of particles from the first generation, as any heavier particles undergo rapid decay into more stable forms.

Quarks are categorized into three generations. The first generation consists of the up quark (u) and the down quark (d), followed by the charm quark (c) and strange quark (s) in the second generation, and finally the top quark (t) and bottom (or beauty) quark (b) in the third generation. The u, c, and t carry $+\frac{2}{3}$ electric charge, while the others carry a charge of $-\frac{1}{3}e$. Quarks exhibit three distinct “colors” and combine in a manner that results in colorless objects. Additionally, besides electric and color charge, quarks also possess weak charge, allowing them to engage in strong, electromagnetic, and weak interactions. Although quarks have mass and are susceptible to gravitational interactions, gravitational effects are typically negligible at the microscopic scale.

Leptons follow a similar pattern, organized into three generations: the electron (e^-) and the electron neutrino (υ_e), the muon (μ^-) and the muon neutrino (υ_μ), and the tau (τ^-) and the tau neutrino (υ_τ). While the electron, muon, and tau possess an electric charge and significant mass, neutrinos are electrically neutral and have minimal mass. Charged leptons (e^-, μ^-, and τ^-) possess both electric charge and weak charge, enabling their participation in the electroweak interaction. Meanwhile, the neutrinos (ν_e, ν_μ, and ν_τ) only carry weak charge and participate in weak interactions.

In the universe, interactions among particles and matter are governed by four fundamental forces: the strong force, the weak force, the electromagnetic force, and the gravitational force. These forces operate across varying distances and exhibit differing strengths. While gravity has an infinite range, it is the weakest force. Conversely, the electromagnetic force, also infinite in range, is considerably stronger than gravity. The weak and strong forces, effective only over short distances, dominate interactions at the subatomic level. Despite being weaker than the electromagnetic and strong forces, the strength of the weak force significantly surpasses that of gravity. Each fundamental force corresponds to a specific gauge boson: the strong force utilizes the “gluon” which can be elucidated by QCD, the electromagnetic force, described by the quantum electrodynamics (QED), employs the “photon”, and the weak force relies on the “$W^{\pm}$ and Z bosons”. Above the unification energy, known as the Fermi scale on the order of

246 GeV, the electromagnetic and weak forces could be merge to a single force, called electroweak force.

In addition to quarks, leptons, and gauge vector bosons, the Standard Model also incorporates a scalar boson, referred to as the Higgs boson, to explain the mass of the other elementary particles (except the photon and gluon). A fundamental issue hindering the application of a similar approach to the weak interaction in quantum field theory was the theory's inability to accommodate particle mass. To address this, the Brout-Englert-Higgs (BEH) mechanism was proposed. This mechanism consists of two primary elements: a novel quantum field and a unique technique. The newly introduced field is now referred to as the Higgs field, while the technique is called spontaneous symmetry breaking. The Higgs boson is the particle associated with the Higgs field, and the discovery of this boson can confirm the BEH mechanism and the existence of the Higgs field.

1.2 The Quantum Electrodynamics

Quantum electrodynamics (QED) stands as the definitive relativistic quantum field theory governing electrodynamics. It delineates the intricate dynamics of interaction between light and matter, marking a watershed achievement as the first theory to harmonize quantum mechanics with special relativity in full accord. QED provides a rigorous mathematical framework to encapsulate all phenomena involving the interaction of electrically charged particles through the exchange of photons, serving as the quantum counterpart to classical electromagnetism and offering a comprehensive elucidation of the interplay between matter and light.

From a technical standpoint, QED serves as a highly precise tool for calculating the probability distributions of particle positions and movements, including massless entities such as photons. The theoretical calculations in this thesis regarding the photo-induced production process are based on QED. Next, a brief introduction to the fundamental equations and properties of QED will be provided.

1.2.1 Coupling to Matter

a Lagrangian ($\mathcal{L}$) which couples A_μ to some matter fields, could be writen as:

$$\mathcal{L} = -\frac{1}{4}F_{\mu\upsilon}F^{\mu\upsilon} - j^\mu A_\mu, \tag{1.1}$$

where j^μ is the function stands for the matter fields, either scalars or spinors. The equations of motion are expressed as follow:

$$\begin{aligned} \partial F^{\mu\nu} &= j^\nu, \\ \partial_\mu j^\mu &= 0, \end{aligned} \tag{1.2}$$

which means the j^μ must be a conserved current. While, the Dirac Lagrangian, written as:

$$\mathcal{L} = \bar{\psi}(i\not{\partial} - m)\psi, \tag{1.3}$$

has an internal symmetry $\psi \to e^{-i\alpha}\psi$ and $\bar{\psi} \to e^{+i\alpha}\bar{\psi}$. This leads to the conserved current $j_V^\mu = \bar{\psi}\gamma^\mu\psi$. So we could look at the theory of electromagnetism coupled to fermions, with the Lagrangian:

$$\mathcal{L} = -\frac{1}{4}F_{\mu\nu}F^{\mu\nu} + \bar{\psi}(i\not{\partial} - m)\psi - e\bar{\psi}\gamma^\mu A_\mu\psi, \tag{1.4}$$

where e is the introduced coupling constant. The coupling constant e also represents the electric charge of the ψ particle, thus the total charge Q can be defined as:

$$Q = e\int d^3x\bar{\psi}(\vec{x})\gamma^0\psi(\vec{x}) = e\int \frac{d^3p}{(2\pi)^3}\sum_{s=1}^{2}(b_{\vec{p}}^{s\dagger}b_{\vec{p}}^{s} - c_{\vec{p}}^{s\dagger}c_{\vec{p}}^{s}), \tag{1.5}$$

which is the number of particles minus the number of anti-particles. For QED, the electric charge is usually written in terms of the dimensionless ratio α as:

$$\alpha = \frac{e^2}{4\pi\hbar c} \approx \frac{1}{137}, \tag{1.6}$$

QED has set the standard as the model and template for all subsequent quantum field theories. A prominent example is quantum chromodynamics (QCD),detailed in the next Section, which emerged in the early 1960s and matured into its present form during the 1970s.

1.3 The Quantum Chromodynamics

Quantum chromodynamics, commonly referred to as QCD in high-energy physics, is the quantum field theory that describes the strong interactions. The symmetry group of QCD is known as color SU(3), with eight conserved charges. Strong interactions are understood as the collective consequences arising from the interactions of gluons with both themselves and the quarks described in the Standard Model, organized into three generations. In this thesis, the strong interaction is one of the focuses of the research.

The discovery of the neutron as a constituent of atomic nuclei alongside the proton in 1932 by James Chadwick[2] marked the recognition of strong interactions as a separate force of nature. Neutrons and protons, collectively known as nucleons, exhibit an attractive force at intermediate distances. This force is so potent that it overrides the electric repulsion between protons. A comparison of the relative strengths of the electromagnetic and strong interactions can be inferred from the typical distances between mutually repulsive electrons within an atom, approximately 10^{-10} m, and the typical distances between protons within a nucleus, on the order of 10^{-15} m.

Subsequently, a series of theories emerged aiming to describe strong interactions, culminating in the establishment of QCD. The historical journey began with the Yukawa's theory in 1935[3], proposing that the strong force between nucleons in atomic nuclei is mediated by the exchange of a hypothetical spinless particle, which Yukawa named the pion, with mass between protons and electrons and has been discovered later by experiments. During the 1930s and 1940s, significant strides were made in understanding the force between nucleons through the development of non-relativistic potential models. These models, more flexible than quantum field theories, provided valuable insights into nuclear structure, particularly attractive potentials at large distances combined with repulsive potentials at short distances. Examples include the Paris potential, Bonn potential, and the shell model of the nucleus. However, as relativistic collisions became experimentally feasible, non-relativistic potentials proved inadequate in describing them.

The emergence and development of the non-abelian gauge theories since 1953 represent crucial milestones in theoretical physics. During the summer of 1953, Yang and Mills broadened the framework of gauge theory from abelian groups to non-abelian groups. They chose the SU(2) group to elucidate isospin conservation in interactions governed by strong forces. Other related advancements include the identification of the quantum number known as strangeness, which led to the development of the quark model. In 1964, Gell-Mann[4] and Zweig[5] pointed out that the observed pattern of baryons can be qualitatively explained by assuming that these are composed of three constituent particles while the mesons contain only two of these. Zweig called the constituents “aces” while Gell-Mann uesd the word “quarks”. Then, Bjorken noted that if nucleons consist of point-like constituents, the cross-section of ep scattering should adhere to scaling laws in the deep inelastic region[6]. This inference was finally demonstrated by the scattering experiments carried out by the MIT-SLAC collaboration in 1968-1969[7]. Later, independently, Bogolyubov, Struminsky, and Tavkhelidze, Han and Nambu[8], and Miyamoto pointed out that certain issues encountered in the quark model are resolved if the u, d, and s quarks exist in three states. Gell-Mann introduced the term “color” for this new quantum number. The proposal of color as a global symmetry and the observation of “scaling” in deep-inelastic scattering finally established QCD as the unique explanation for strong interaction.

When the electroweak gauge fields, leptons, and scalars are omitted, the Lagrangian of the Standard Model simplifies to QCD, which can be defined by the follow formula:

$$\begin{aligned}\mathcal{L}_{QCD} = &-\frac{1}{4}F^A_{\mu\upsilon}F^{A\mu\upsilon} + i\bar{q}\gamma^{\mu}(\partial_\mu + ig_s\frac{1}{2}\lambda^A\mathcal{A}^A_\mu)q \\ &- \bar{q}_R\mathcal{M}q_L - \bar{q}_L\mathcal{M}^\dagger\bar{q}_R - \theta\omega,\end{aligned} \tag{1.7}$$

The strong force-carrier, gluons, are described by the gauge field $\mathcal{A}^A_\mu$ in this definition, which belongs to the color group $SU_c(3)$ and the corresponding coupling constant is g_s. The term of field strength tensor, $F^A_{\mu\upsilon}$, is defined by:

$$F^A_{\mu\upsilon} = \partial_\mu\mathcal{A}^A_\upsilon - \partial_\upsilon\mathcal{A}^A_\mu - g_s f_{ABC}\mathcal{A}^B\mathcal{A}^C, \tag{1.8}$$

where the term, f_{ABC}, represents the structure constants of SU(3). The compact notation in the Eq. 1.7 suppresses the labels for flavor, colour and spin: the various quark flavors are represented by Dirac fields, q is from $[\mu, d, s, c, b, t]$, $q_R = \frac{1}{2}(1+\gamma_5)q$ and $q_L = \frac{1}{2}(1-\gamma_5)q$ are the right- and left-handed components, respectively. The field $\mu(x)$ contains 3×4 components. The Gell-Mann matrices λ^A act on the color label and satisfy the commutation relation which is displayed by:

$$[\lambda^A, \lambda^B] = 2if_{ABC}\lambda^C, \tag{1.9}$$

the Dirac matrices γ^μ operate on the spin index while the mass matrix $\mathcal{M}$ takes role in the flavor space. The constant θ is referred to as the vacuum angle and ω represents the winding number density:

$$\omega = \frac{g_s^2}{32\pi^2}F^A_{\mu\upsilon}\tilde{F}^{A\mu\upsilon}, \tag{1.10}$$

where $\tilde{F}^{A\mu\upsilon} = \frac{1}{2}\epsilon^{\mu\upsilon\rho\sigma}F^A_{\rho\sigma}$ is the dual of the field strength.

1.3.1 Asymptotic Freedom and Confinement

Asymptotic freedom stands as a fundamental characteristic of QCD, signifying that the strong interaction between quarks weakens considerably at high energy scales or short distances. Following the proposal of quarks by Gell-Mann and Zweig in the early 1960s, confirmation came from scattering experiments at the Stanford Linear Ac-

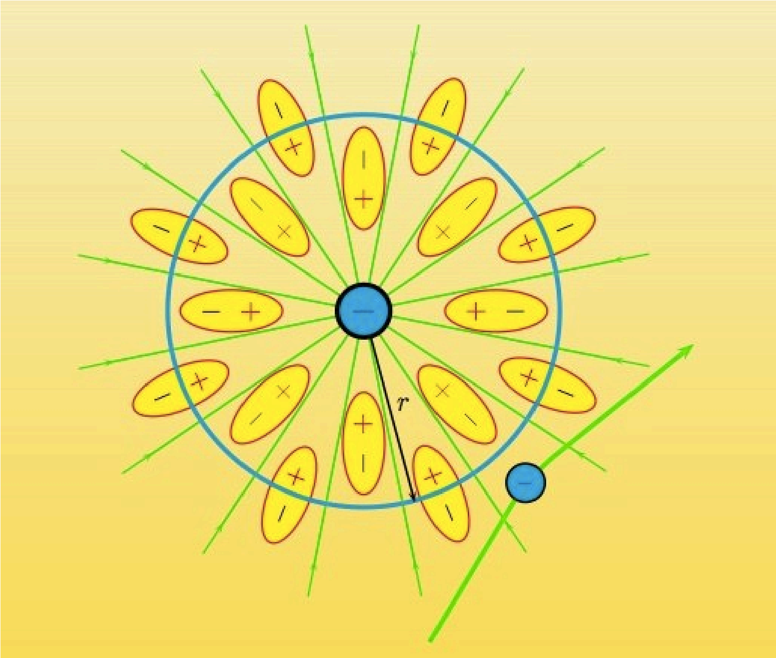

Figure 1.2 The diagrammatic representation of the screening effect of charges in QED[9].

celerator. This shift in understanding, with hadrons no longer considered the smallest building blocks, prompted exploration into the nature of quark interactions within hadrons. It became apparent that quarks hardly interacted when closely situated. The groundbreaking concept of asymptotic freedom in QCD emerged independently in 1973 through the work of David Gross and Frank Wilczek[10], as well as David Politzer[11]. Further validation came from detailed analyses of electron, muon, and neutrino deep inelastic scattering data at the Stanford Linear Accelerator[12]. These studies revealed remarkable consistency between experimental findings and the predictions of asymptotic freedom, particularly at large momentum transfers (Q^2>2 GeV^2). This alignment suggested that quarks inside the hadron behaved as if they were free particles when hit hard.

The change in a physical coupling constant when the scale changes can be qualitatively understood as arising from the interaction of the field with virtual particles carrying the relevant charge. For example the charge screening occurs in the QED, as depicted in Fig. 1.2. Close to a charged object, the vacuum becomes polarized: virtual particles with opposite charges are attracted to the charge, while those with like charges are repelled. This polarization leads to a partial cancellation of the field at finite distances. As one approaches the central charge, the influence of the vacuum diminishes, resulting in an increase in the effective charge.

Similar to the charge screening effect in QED, screening effect also exits in the strong interaction due to color charges. The excited virtual quark and anti-quark pair,

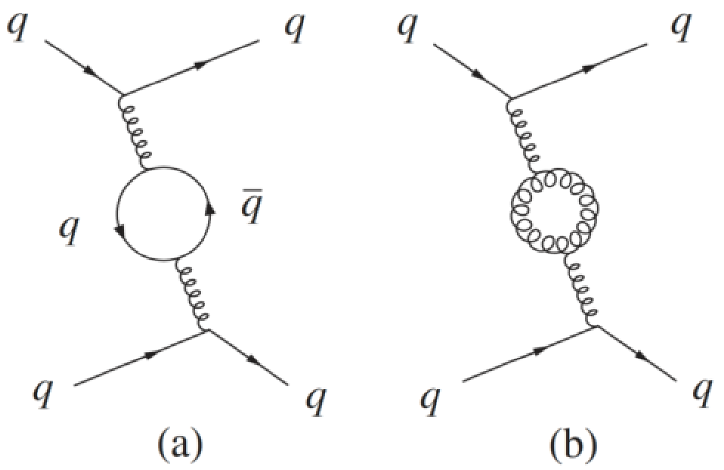

Figure 1.3 The lowest order of screening (a) and anti-screening (b) effects among partons with the color charges.

illustrated in the Feynman diagram in Fig. 1.3 (a), exists in the vacuum. However, QCD introduces an additional complexity: its force-carrying particles, the gluons, can also carry color charge. The overall effect of the polarization of virtual gluons in the vacuum is not to shield the field but to enhance it and alter its color, sometimes referred to as anti-screening effect, as shown in Fig. 1.3 (b). So, as one approaches a quark, the anti-screening effect of the surrounding virtual gluons diminishes, leading to a weakening of the effective charge with decreasing distance, which is the essence of the Asymptotic Freedom.

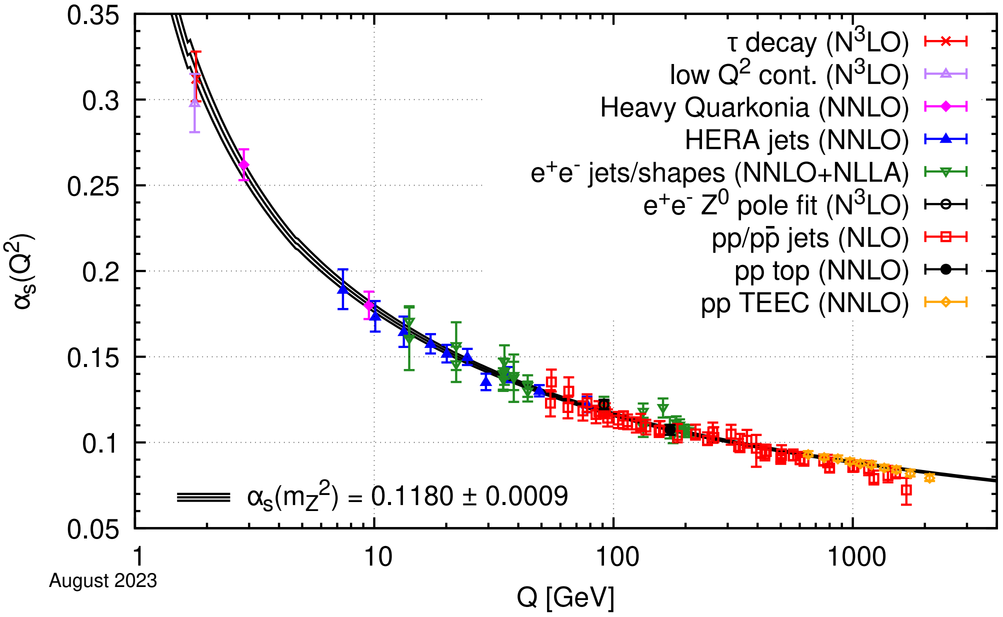

Figure 1.4 The experimentally measured α_s as function of the energy scale Q. The experimental points are consistent with the curve obtained from calculations based on QCD. The NLO is next-to-leading order, NNLO is next-to-next-to-leading order, and NNLO+res is the NNLO matched to a resummed calculation, and N^3LO represents the next-to-NNLO). The picture is taken from[13].

At different renormalization scale μ, the effect value of the QCD coupling constant

α_s changes. The leading order of the perturbative solution is written as:

$$\alpha_s(\mu) \approx \frac{\alpha_s(\mu_0^2)}{1 + b_0\alpha_s(\mu_0^2 ln(\mu^2/\mu_0^2))} = \frac{1}{b_0 ln(\mu^2/\Lambda_{QCD}^2)}, \tag{1.11}$$

where the 1-loop β-function coefficient $b_0 = (11C_A - 2n_f)/12\pi = (33 - 2n_f)/12\pi$, the n_f is the number of "light" quark flavors with mass is lower than μ, the Λ_{QCD} is the non-perturbative constant, which is close to 200 MeV from experiment. When the renormalization scale, μ, is much larger than the Λ_{QCD}, the perturbation approximation is then vaild. Figure 1.4 presents the values of α_s at different energy scales from experimental measurements (markers) and the QCD predictions (curves). As we can see, the QCD predictions show good agreements with the experimental measurements within uncertainties.

Asymptotic Freedom in QCD corresponds to the behavior of the QCD coupling constant α_s at very large momentum transfers ($Q^2 \gg \Lambda^2$QCD), as depicted in Fig. 1.4. At such scales, the interaction between quarks becomes nearly zero as α_s approaches zero. However, when Q^2 decreases, or equivalently, at larger distances, another phenomenon in QCD arises known as color confinement. Color confinement describes the phenomenon wherein color-charged particles like quarks and gluons cannot be individually isolated and observed directly. As shown in Fig. 1.5, when quarks within a hadron attempt to separate, the gluon field arranges into narrow strings of color charge, serving to bind the quarks together effectively. As the distance between quarks increases significantly, the strong interaction intensifies sharply, leading to a rise in the α_s parameter.

Eventually, a new quark-antiquark pair will be created by the gluon field from the vacuum instead of allowing further separation of the quarks. This results in the formation of new hadrons with quarks still confined within them. Additionally, the existence of colorless glueballs composed solely of gluons is consistent with confinement, although their experimental identification poses challenges. In such situations, the prominence of higher-order processes renders perturbative QCD invalid. Hence, researchers resort to methods like Lattice QCD or other non-perturbative approaches to analyze strong interaction phenomena.

1.4 Quark Gluon Plasma and Phase Transition

According to the color confinement in QCD, quarks are confined within hadronic matter, forming the color-neutral quark bound states ($q\bar{q}, qqq$ or $\bar{q}\bar{q}\bar{q}$). However, under extreme conditions such as increasing density, the quarks and gluons can become de-

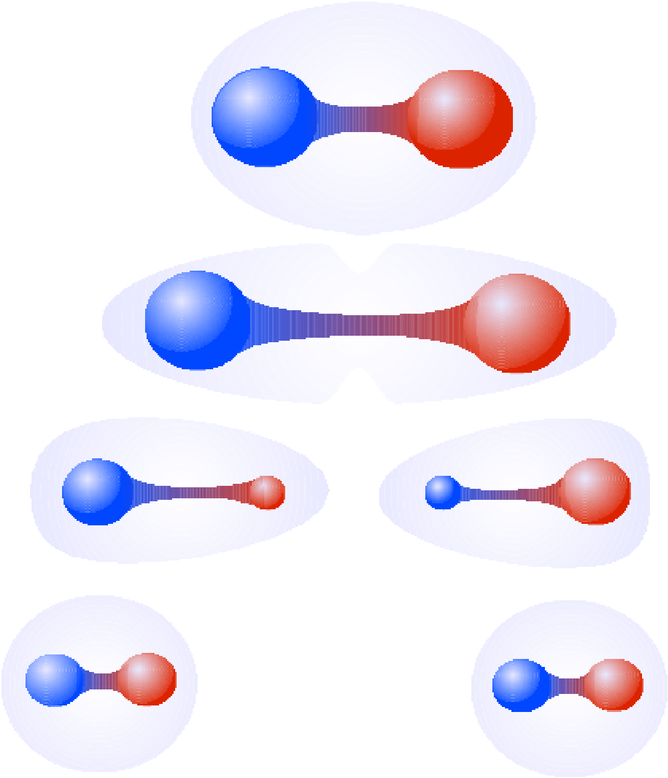

Figure 1.5 The diagrammatic representation of the color confinement in QCD[14].

confined from hadrons. In such scenarios, the hadrons overlap until each quark finds itself surrounded by numerous other quarks. Beyond a certain threshold, it becomes impossible for a quark to discern which other quarks were its counterparts within a specific nucleon in a lower density state. Consequently, the notion of a hadron becomes irrelevant, leading to a transition from nuclear matter to a system composed of unbound quarks as its fundamental constituents. This state of matter is known as Quark-Gluon Plasma (QGP), primarily consisting of free quarks and gluons.

Two primary methods can generate QGP: through "heating" (extremely high temperature) or "compression" (extremely high baryon density). These conditions result in more quarks per hadronic volume than is meaningful for partitioning into color-neutral hadrons. The definition of QGP proposed by the STAR collaboration states that "Quark-Gluon Plasma is defined as a (locally) thermally equilibrated state of matter in which quarks and gluons are deconfined from hadrons, so that they propagate over nuclear, rather than merely nucleonic, volumes[15]". Since the results in this thesis are based on experiments of high-energy heavy-ion collisions, which can also create a "Little Bang", we will focus on discussing the method of extremely high temperature.

Here is a simple example illustrating how hadronic matter transitions to QGP by increasing the temperature. The simplest form of confined matter is an ideal gas of massless pions, whose pressure is given by:

$$P_\pi = \frac{\pi^2}{90} \times 3T^4 \simeq \frac{1}{3}T^4, \tag{1.12}$$

where three possible pion charge states have been considered. In the scenario of deconfined matter, the simplest instance is an ideal quark-gluon plasma, characterized by two massless quark flavors, two quark and two gluon spin orientations (q and $\bar{q}$), as well as three quark and eight gluon color degrees of freedom, the pressure giving as:

$$P_{QGP} = \frac{\pi^2}{90}[2\times 8 + \frac{7}{8}(2\times 2\times 2\times 3)]T^4 - B \simeq 4T^4 - B, \tag{1.13}$$

where B represents the "bag pressure" exerted by the physical vacuum on the colored medium. As nature tends to favor states with the highest pressure (lowest free energy), then the critical temperature (T_c) for a pion gas transition to a QGP can be obtained from:

$$\begin{aligned} P_{QGP} \simeq 4T^4 - B = \frac{1}{3}T^4 \simeq P_\pi \\ T_c \simeq (0.3B)^{1/4}, \end{aligned} \tag{1.14}$$

if we use the $B^{1/4} \simeq 200$ MeV from quarkonium spectroscopy, the T_c is approximately equal to 150 MeV.

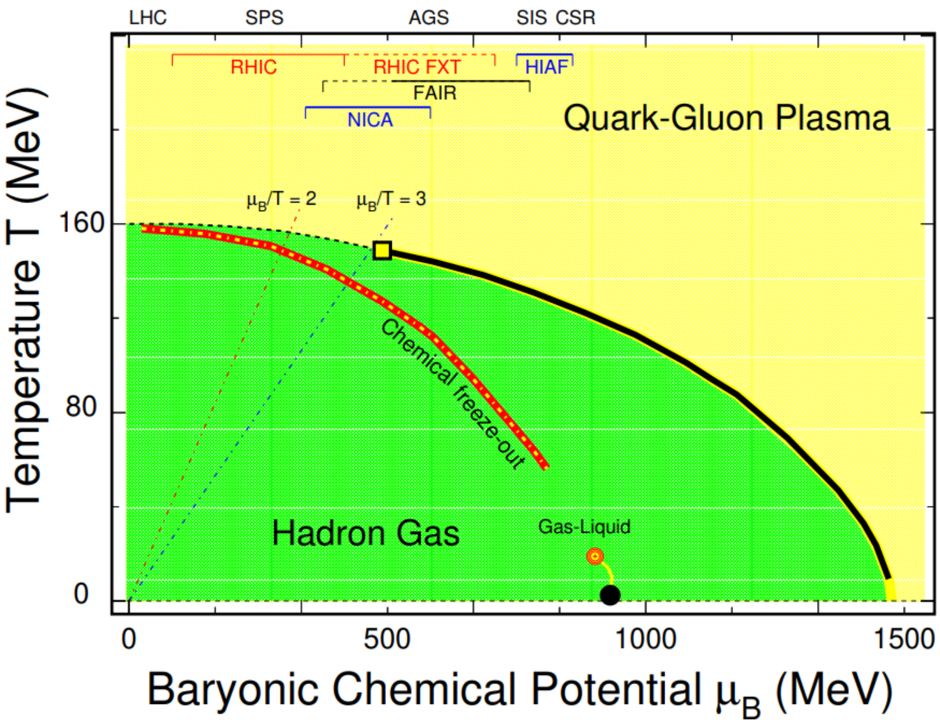

Figure 1.6 The presumed QCD phase diagram depicts temperature (T) plotted against baryonic chemical potential (μ_B)[16].

Figure 1.6 illustrates our current conjectured phase diagram of QCD matter as a function of temperature and baryonic potential μ_B[16]. The phase structure consists of two distinct phases: the de-confined state of quarks and gluons, known as the quark-gluon plasma (QGP), and the confined state comprising a gas of hadrons and resonances (HRG). In the diagram, a solid black line delineates the phase boundary between the hadronic gas phase and the QGP, representing the first-order phase transition line. This line starts at a high baryon chemical potential (μ_B) and low temperature (T) and terminates at the conjectured position of the QCD critical end point, denoted by a square. The exact location of this critical end point remains uncertain both theoretically and experimentally.

As we move towards smaller μ_B, a crossover is marked by a dashed line. The dotted red-yellow line represents the chemical freeze-out derived from fitting particle yields in heavy-ion collisions using a thermal model. Additionally, the yellow line signifies the first-order liquid-gas transition, connecting the second-order critical point (red circle) to the ground state of nuclear matter at $T \sim 0$ and $\mu_B \sim 925$ MeV (black circle)[17]. The regions where previous (the Alternating Gradient Synchrotron(AGS) and the Super Proton Synchrotron(SPS)), current (LHC, RHIC, SPS, and RHIC operating in fixed target mode), and upcoming (the Facility for Antiproton and Ion Research(FAIR), the Nuclotron-based Ion Collider Facility(NICA), and the High Intensity heavy-ion Accelerator Facility(HIAF)) experimental facilities play a crucial role are also highlighted in Fig. 1.6.

Searching for critical end points is one of the most important physics objectives at RHIC. At highest energy of RHIC, the baryonic chemical potential approaches zero in Au+Au collisions. However, at lower collision energies, the initial baryon number of the colliding nuclei increasingly contributes to the formation of QCD matter. Therefore, it becomes feasible to raise μ_B and explore the QCD phase diagram by reducing the collision energy.

STAR has concluded the first phase of the Beam Energy Scan (BES-I) program, and the published results, compared with lattice QCD calculations, disfavor the possible location of the QCD critical point being in the region where $\mu_B/T \leq 2$[18-19], as shown by the dot-dashed line. The second phase of the BES program (BES-II), with much higher collision energies (10-20 times higher), including a fixed target program, was conducted during 2019-2021, and the results are currently undergoing analysis. Figure 1.7 illustrates the BES program at RHIC and future new experiments designed with high rates at energy regions where the baryonic density is high (500 MeV $< \mu_B <$ 800 MeV)[20]. Collider modes are represented by blue symbols (such as ALICE, sPHENIX, RHIC BES-II, and NICA), while those operating in fixed target mode are denoted by red symbols (including STAR fixed target (FXT), FAIR (CBM, SIS), HADES, and HIAF).

Moreover, measurements of experimental observables at various collision energies aid in better comprehending the formation and evolution of the QGP, as its properties, such as temperature, vary across different collision energies. The Beam Energy Scan program at STAR provides an excellent opportunity to study the dependence of the QGP properties on collision energy. In this thesis, the suppression of J/ψ in Au+Au collisions at $\sqrt{s_{\rm NN}}$ = 54.4 GeV is measured and compared to its suppression in various collision systems at different collision energies. This comparison aims to deepen our understanding of the effects of the QGP medium on J/ψ meson production. Relativistic heavy-ion collisions, as the primary approach for studying QGP, also serve as the unique way of simulating cosmic explosions (known as the Big Bang) in laboratory settings. This will be elaborated upon in the next section.

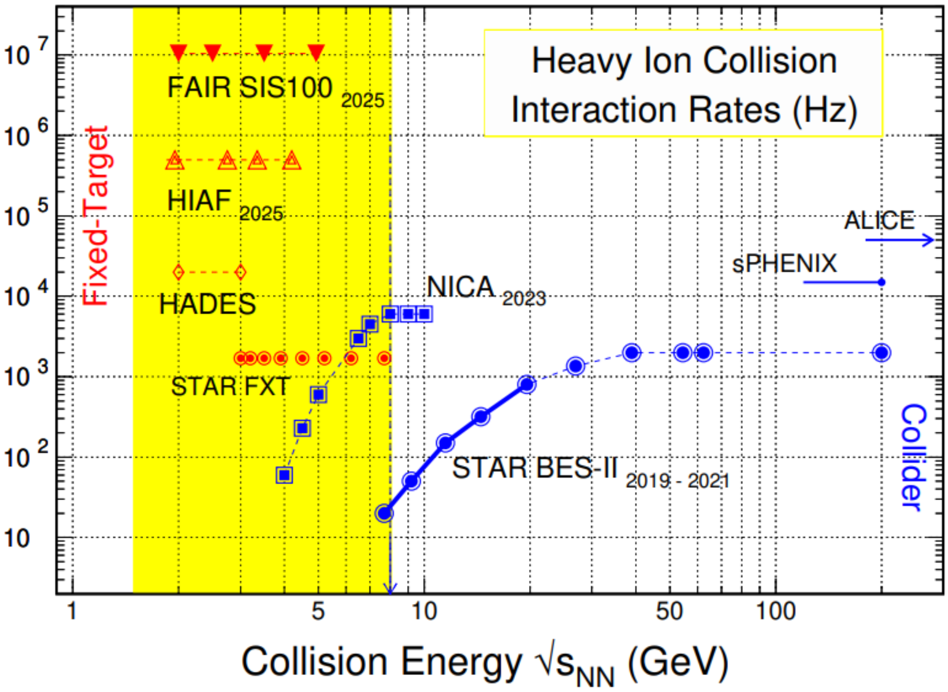

Figure 1.7 Interaction rates (in Hz) for high-energy nuclear collision facilities as function of $\sqrt{s_{\rm NN}}$[20].

1.5 Relativistic Heavy Ion Collisions

Scientific research encompasses two seemingly opposing directions: one delves into the fundamental constituents of matter, advancing towards the micro world, while the other investigates the origin and evolution of the universe, exploring the boundaries of the material world. The science of “small” - elementary particle physics - is deeply intertwined with the science of the “large” - cosmology. This connection is illustrated in Fig. 1.8, showing the temperature history of the universe shortly after the Big Bang.

Approximately 10 μs after the Big Bang, there existed a state of QGP with a temperature exceeding 200 MeV. Today, Colliding two relativistic heavy ions, often referred to as the "Little Bang", provide a remarkable means to recreate this primordial state of matter within laboratory settings, albeit for fleeting moments.

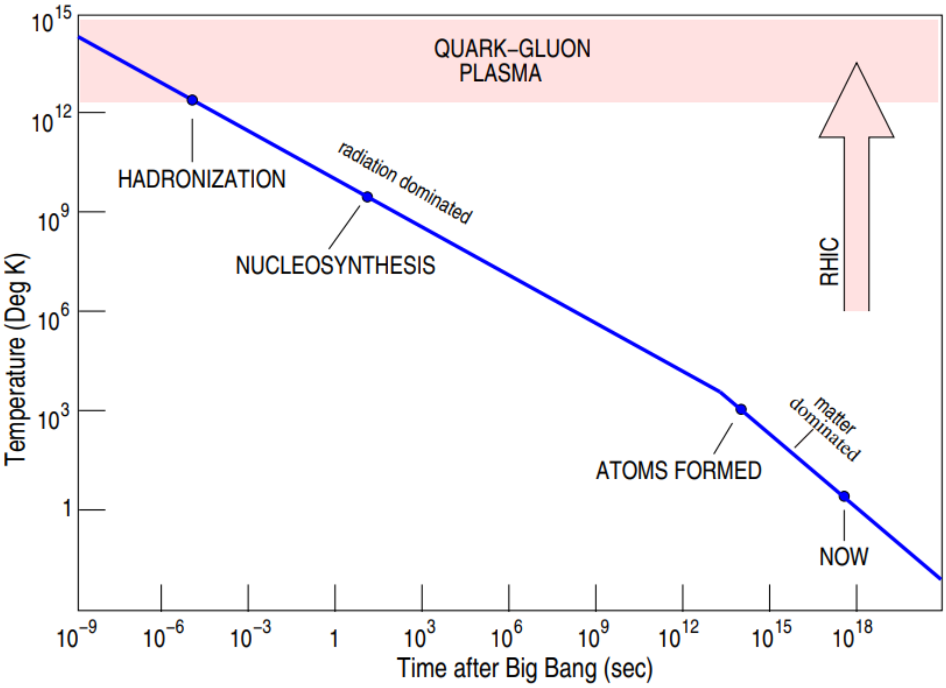

Figure 1.8 The temperature history of the universe. The Big Bang and the Little Bang[21].

The experimental facilities currently available include the Relativistic Heavy-Ion Collider (RHIC) at **BNL** and the Large Hadron Collider (LHC) at **CERN**. Before the construction of RHIC, the Alternating Gradient Synchrotron (AGS) at BNL stood as a leading particle accelerator, holding the title of the world's highest energy accelerator until 1968. Despite 21st-century accelerators now reaching energies in the TeV range, the AGS has played a significant role, earning researchers three Nobel Prizes, including the discovery of the J/ψ meson. Today, it serves as the injector for RHIC. Similarly, at CERN, prior to the operation of the LHC, the Super Proton Synchrotron (SPS) was utilized for accelerating protons, antiprotons, electrons, positrons, and heavy ions. Additionally, upcoming lower-energy facilities include the Facility for Antiproton and Ion Research (FAIR) at **GSI** and the Nuclotron-based Ion Collider Facility (NICA) at **JINR**. Over 30 years of high energy heavy-ion collisions experiments, a series of indirect evidence regarding the existence of QGP in heavy-ion collisions has been found[15,22-26]. However, direct signals of the existence of QGP have still not been measured. The question of whether QGP truly exists remains a significant issue in relativistic heavy-ion collision research. In the following chapters, the formation and evolution of the

QGP created in the relativistic heavy ion collisions, along with relevant experimental observations, will be discussed.

1.5.1 Space-time evolution of Heavy-ion Collision

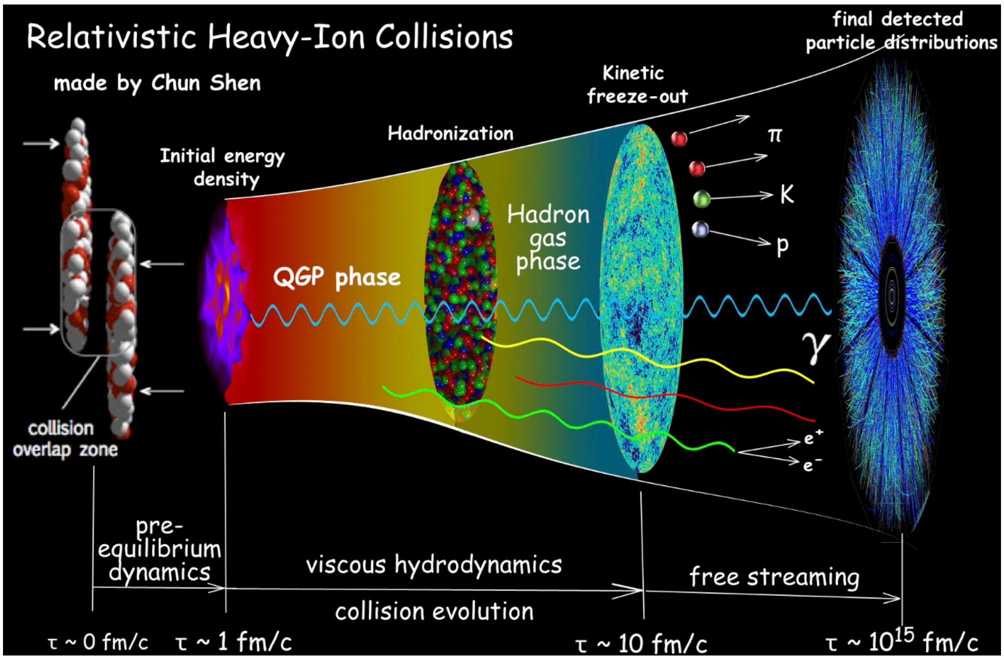

Figure 1.9 The high-energy heavy-ion collisions involve a dynamic space-time evolution, where the QGP is created. The picture is taken from [27].

The Fig. 1.9 illustrates the space-time evolution of a typical nucleus-nucleus collision at near-light speed. In the initial state of the collision, each incoming nucleus appears flattened due to Lorentz contraction, resembling a color-glass condensate (CGC) plate[28]. The collision can be conceptualized as the interaction of two CGC plates. Further discussion on the initial collision geometry and the strong electromagnetic field arising from the charges in the colliding nucleus will be provided in Section 1.6.

When the two colliding nuclei meet in the center-of-mass frame, this moment is defined as $\tau = 0$ fm/c. A significant portion of the incoming kinetic energy is deposited in the collision region, resulting in a highly non-equilibrium state known as the glasma[28]. This state typically lasts for a fraction of a fm/c until partons are liberated from the glasma. After a brief period, collisions among partons lead to a state of near-thermal equilibrium (local thermalization), signifying the formation of the Quark-Gluon Plasma (QGP). This process occurs within a timescale of about 1 fm/c, although it is not fully understood why it transpires so rapidly.

Before hadronization occurs ($\tau < \tau_{\text{had}}$), the state approaches local thermal equilibrium and can be effectively described by relativistic hydrodynamics. The notable suppression of Quarkonia production in high-energy heavy-ion collisions, attributed to the color screening effect, serves as a crucial indicator for QGP formation, although other factors may also influence their yields. Investigating Quarkonia production in nuclear collisions is a primary objective of this thesis, and Section 1.7.3 will delve further into its significance as an important observable.

As the system expands, both temperature and density diminish. When the system's temperature drops below the critical temperature (T_c), the transition from QGP to hadronic matter occurs, a phenomenon termed hadronization. During this process, hadrons undergo elastic collisions, altering their energy and momentum, as well as inelastic collisions, which impact the abundance of individual species. Chemical freezeout occurs when inelastic processes cease, while kinetic freezeout occurs when elastic scatterings come to a halt. Approximately 10-15 fm/c after the collision, hadrons decouple from the system and propagate towards the surrounding detector. At this stage, the relativistic kinetic theory framework proves useful for simulating the late stages of evolution when the system is no longer in local equilibrium.

A "standard model" of ultra-relativistic heavy-ion collisions has been developed: The initial phase is constructed using either the Glauber model[29] or one of the models implementing concepts from CGC [30], with a review paper discussing these approaches[31]. Intermediate evolution from $\sim$ 1 fm/c to $\sim$ 10 fm/c is examined through various versions of the Müller-Israel-Stewart theory [32-33]. This theory incorporates causal relativistic imperfect fluid dynamics, along with a QCD equation of state spanning both the partonic and hadronic phases[34]. For the final evolution of the hadron-rich medium leading to freezeout, the Boltzmann equation in relativistic transport theory is employed[35]. This comprehensive model ultimately yields a plethora of particles, including mesons, baryons, leptons, photons, and light nuclei. These particles have been meticulously measured using various observables in different collision systems, ranging from the Super Proton Synchrotron (SPS) to RHIC to LHC. The objective is to attain a quantitative comprehension of the thermodynamic and transport properties of QGP, encompassing its equation of state and transport coefficients (such as shear and bulk viscosities, diffusivity, conductivity), etc.

1.6 Initial Heavy Ion Collision State

In this section, we delve into the initial stages of high-energy heavy-ion collisions, focusing on the geometric structure of the colliding nuclei and the ultra-strong electromagnetic fields surrounding them. These aspects are particularly pertinent to the research undertaken in this doctoral thesis.

1.6.1 Initial Geometric Structure

In Fig. 1.9, we observe the pancake-shaped nuclei approaching each other at speeds close to that of light prior to collision. However, regardless of the incoming kinetic energy and consequent Lorentz contraction factor, the nucleus is constrained in thickness to about 1 femtometer (fm) due to the presence of so-called “wee partons”[36]. This phenomenon is related to the description of ordinary collisions from a short-range-correlation or parton picture of hadrons, such as the proton.

In a simplistic view, understanding the wave function of a proton in its rest frame would suffice to characterize it under acceleration or at high momentum. By boosting the proton, the spherical volume containing its three quarks would transform into a flattened, pancake-shaped region with a thickness inversely proportional to the proton’s momentum ($p \gg 1$ GeV/c). However, according to the parton picture, this isn’t the complete story. In addition to the original three partons, vacuum fluctuations, like quark-antiquark pairs, also need to be considered. These fluctuations could couple to the boosted proton and are relevant for describing high-energy collisions.

For a relativistic proton with momentum p, we anticipate the original three quarks along with a quantity (approximately of order $log(p)$) of vacuum fluctuations with decreasing momentum. These fluctuations are successively connected to the initial three quark system, with the lowest-momentum fluctuations termed “wee fluctuations” remaining uncontracted. The resting nucleus is typically viewed as a cluster of nucleons, within which exists a group of quarks. If the boost is significant, the pancake’s thickness will be less than 1 fm. Under such conditions, the impact of vacuum fluctuations on the structure of the moving nucleus, akin to that observed for the moving proton, must be reconsidered. As the nucleus is further boosted, the same process observed for a single nucleon repeats itself. The initial vacuum fluctuations attach to vacuum fluctuations of lower rapidity until the last layer of vacuum fluctuations are once again the “wees”. The longitudinal thickness of a vacuum fluctuation with momentum $\sim p$ is inversely proportional to p. Thus, the thickness of a moving nucleus in the longitudinal direction is never less than 1 fm.

The overall shape and longitudinal thickness of colliding nuclei, along with the initial geometry overlap and nucleon momentum, collectively determine the energy density of the collision. Figure 1.10 depicts an illustrative view of a relativistic heavy-ion collision, the distance between the centers of the two nuclei is known as the impact parameter

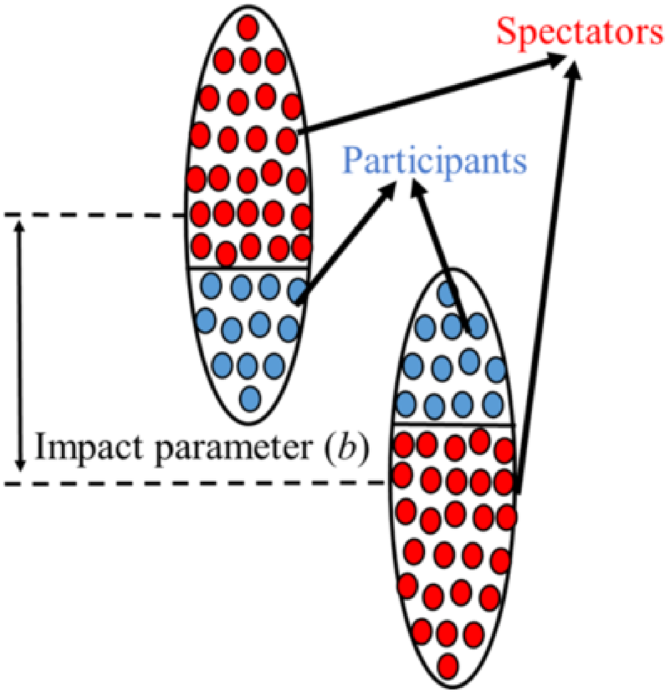

Figure 1.10 The illustrative view of collision geometry for a relativistic heavy-ion collision[37].

b. The nucleons are divided into two groups based on whether their nucleons participate in inelastic scattering with others: Participants (blue markers) and Spectators (red markers).

In studying the suppression of Quarkonia production in heavy-ion collisions, the number of binary nucleon-nucleon collisions (N_{coll}) is commonly used to scale the production yield relative to p+p collisions. The variable N_{part}, defined as the number of nucleons participating in inelastic scattering during the collision, is directly related to the energy deposited in the collisions and is frequently employed to study the dependence of observables on the scale of QGP. However, direct measurement of b, N_{coll}, and N_{part} by detectors is not feasible. Instead, measurable variables in the final state, such as the number of charged particles N_{ch} (as depicted in Fig. 1.11), change with b and have a one-to-one correspondence. In experiments, N_{ch} is typically compared to calculations from the Glauber model[29] to determine the event centrality.

Additionally, N_{coll} and N_{part} can be calculated by the Glauber model at a specific b. Centrality can also be determined by the energy deposition in detectors at zero degree from the beam direction (ZDC), particularly for ultra-peripheral collisions (UPCs, $b > 2R_A$, where R_A is the radius of nuclei). In UPCs, neutrons from the colliding nuclei can be produced by either the QED process of mutual Coulomb excitation or nuclear breakup from hard scattering processes[38]. The patterns of neutron emission are categorized from a higher probability of larger b to a smaller one as follows: $0n0n$ (neither ZDCs at two sides of the detector have detected neutrons); $0nXn$ (one ZDC has detected at least one neutron and the other has none); and $XnXn$ (both ZDCs have detected at least one neutron).

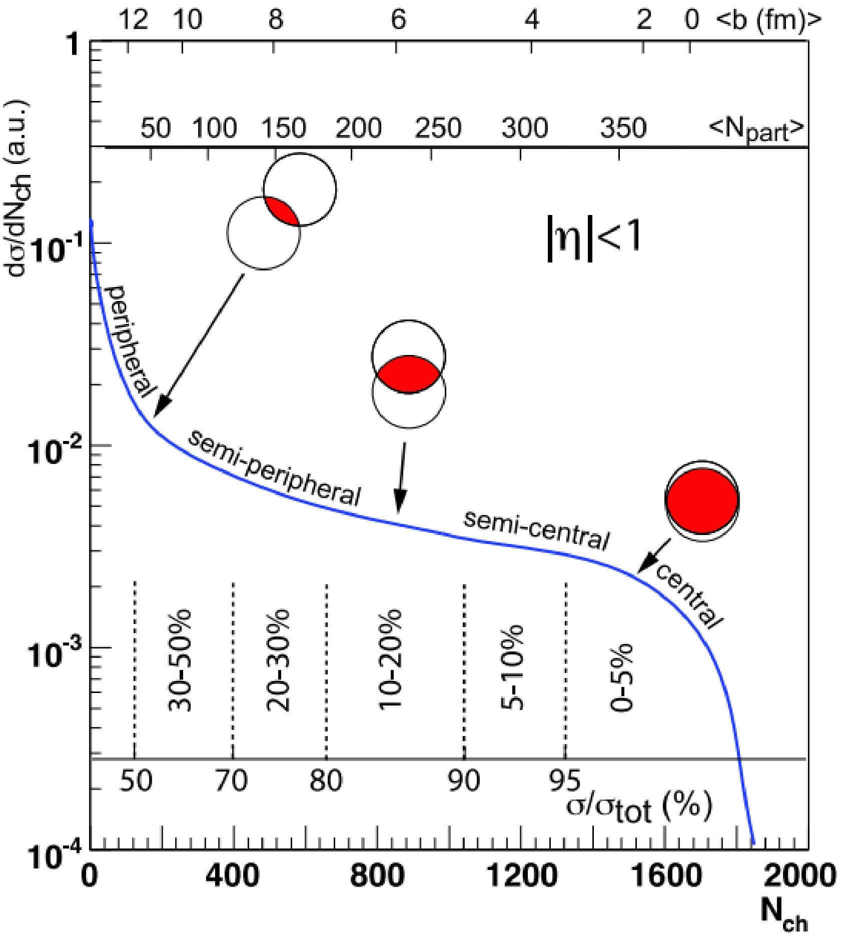

Figure 1.11 The final state observable N_{ch} with Glauber-calculated b and N_{part} are compared. The picture is taken from [29].

1.6.2 Strong Electromagnetic Field

In the initial state of high energy heavy ion collisions, a strong electromagnetic field can be generated by the colliding. Heavy-ion collisions produce magnetic fields because the positively charged nuclei, in motion, create electric currents that induce magnetic fields. Figure 1.12 illustrates a non-central collision, where two nuclei collide with a finite impact parameter (b). The resultant magnetic field at the center of the overlapping region aligns perpendicularly to the reaction plane beacuse the collision geometry exhibits left-right symmetry. Based on some numerical simulation, the strength of the magnetic field in Au+Au collisions at RHIC top energy can reach the order of 10^{14} - 10^{15} T while much larger, $\sim 10^{16}$ T, in Pb+Pb collisions at $\sqrt{s_{\rm NN}}$= 2.76 TeV at LHC[39-48]. This estimation can also be made based on the Biot-Savart law, for example, considering the magnetic field at the center of Au+Au collisions at a fixed impact parameter $b = 10$ fm at $\sqrt{s_{\mathrm{NN}}} = 200$ GeV:

$$-eB_y \sim 2 \times Z_{Au}\gamma \frac{e^2}{4\pi} v_z (\frac{2}{b})^2 \approx 10 m_\pi^2 \approx 10^{19}\text{Gauss}, \tag{1.15}$$

where $\gamma \approx 100$ is the Lorentz factor, the velocity of the nucleus, $v_z = \sqrt{1-(2m_N/\sqrt{s})^2}$, is ≈ 0.99995, and $Z_{Au} = 79$ is the number of charge in gold nucleus. The direction of the magnetic field points towards the negative $\hat{y}$ direction, which results in the negative sign on the left-hand side, as shown in the Fig. 1.12. In the relevant literature, people usually use m_π^2 or MeV^2 as the unit of eB and $m_\pi \approx 140$ MeV is the pion mass. In converting to the Gaussian units, the 1 MeV$^2 = e \cdot 1.6904 \times 10^{14}$ Gauss (if $\hbar = c = 1$).

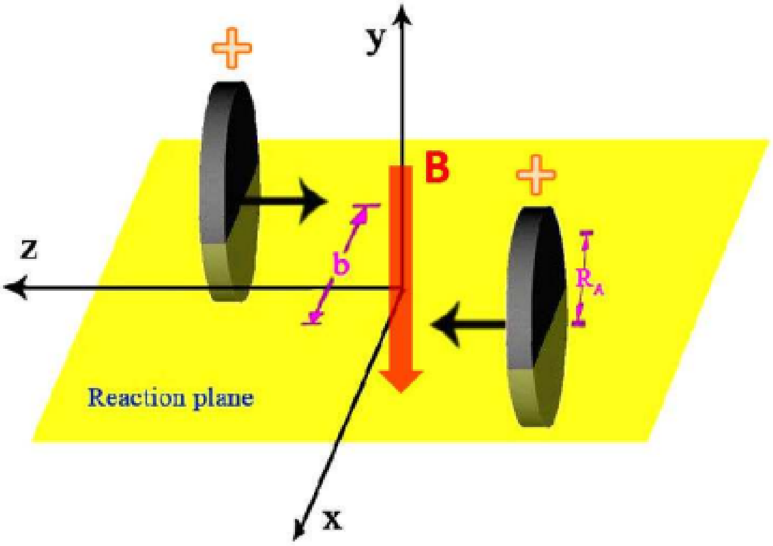

Figure 1.12 The geometric depiction of a non-central relativistic heavy-ion collision. The picture is taken from [49].

The magnetic field generated by colliding nuclei far surpasses even the magnetic fields of neutron stars, whose surface magnetic fields are on the order of 10^{10} - 10^{11} T[50-51], making the magnetic fields produced in high-energy heavy-ion collisions the most powerful observed in the current universe. In the early universe, there was a chance of generating an even stronger magnetic field through the electro-weak transition, as discussed in [52]. For a more accurate calculation of the electromagnetic fields in heavy-ion collisions, the simplified Biot-Savart law should be replaced with the full relativistic Lı̆enard – Wiechert potentials, which account for the retardation effect:

$$\begin{aligned} e\mathbf{E}(t,\mathbf{r}) =& \frac{e^2}{4\pi}\sum_n Z_n \frac{\mathbf{R}_n - R_n v_n}{(R_n - \mathbf{R}_n \cdot v_n)^3}(1 - v_n^2) \\ e\mathbf{B}(t,\mathbf{r}) =& \frac{e^2}{4\pi}\sum_n Z_n \frac{v_n \times \mathbf{R}_n}{(R_n - \mathbf{R}_n \cdot v_n)^3}(1 - v_n^2), \end{aligned} \tag{1.16}$$

where the summation is over all the charged particles, Z_n represents the charge of the nth particle, the relative position of the field point $\mathbf{r}$ in reference to the source point $\mathbf{r}n$ of the nth particle is denoted as $\mathbf{R}n = \mathbf{r} - \mathbf{r}_n$, v_n stands for the velocity of the nth particle at the retarded time $t_n = t - |\mathbf{r} - \mathbf{r}_n|$.

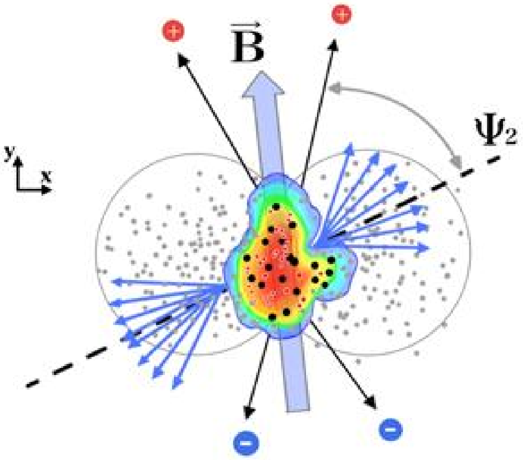

Figure 1.13 A cartoon example of the chiral magneitic effect in heavy-ion collisions. The picture is taken from [53].

Anticipatedly, such an immense magnetic field could significantly influence the dynamics of the quark-gluon matter generated during heavy-ion collisions. One of the most renowned phenomena is the chiral magnetic effect, often abbreviated as CME, which refers to the production of a current in a chirality-imbalanced medium where an strong magnetic field exits[39,54]. In the high energy heavy-ion collisions, the imbalance of left- and right- handed chiral quarks in the QGP will generate an electric current parallel to the magnetic field. This will lead to a separation of charges relative to the reaction plane as shown in the Fig. 1.13. If a definitive detection of the CME were to be confirmed in heavy-ion collisions, it would indicate the presence of CP-violating domains, the restoration of approximate chiral symmetry within the QGP, and the influence of an exceptionally intense magnetic field within the collision region. One of the motivations of this thesis is to deepen our understanding of the current experimental measurements of the CME-sensitive signals in heavy-ion collisions. This will be elaborated upon in Sec. 1.8.1. Additionally, some relatives were also proposed, including the chiral separation effect (CSE) [55-56], chiral electric separation effect (CESE)[57], chiral magnetic waves (CMW)[58], chiral vortical effect (CVE)[59-61], chiral vortional wave[62], chiral heat wave[63], chiral Alfven wave[64], which will not be delved here.

The CME can be succinctly formulated for each specie of massless fermions with charge e as:

$$\begin{aligned}\mathbf{J}_V &= \sigma_{VA}\mathbf{B},\\ \sigma_{VA} &= \frac{e^2}{2\pi^2}\mu_A,\end{aligned} \tag{1.17}$$

where the $\mathbf{J}_V$ is determined by $J_V^\mu = e\langle\bar{\psi}\gamma^\mu\psi\rangle$, μ_A is a parameter that characterizes the chirality imbalance of the medium. In the QGP medium, the current resulting from the CME is calculated by summing up all the contributions from light quarks, so the conductivity σ_{VA} should be $\mathrm{N_C}\mu_A \sum_f q_f^2/(2\pi^2)$, q_f is the charge of quark with flavor f and $\mathrm{N_C}$ is the number of color.

1.6.3 Photon Induced Processes in Heavy-Ion Collisions

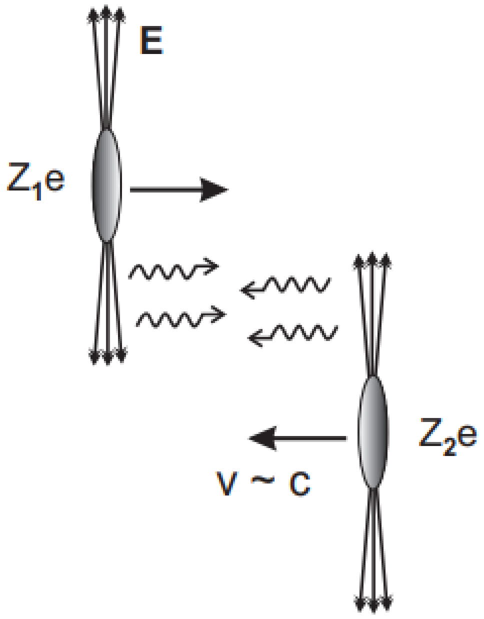

Figure 1.14 A cartoon view of the Lorentz contracted electric field in heavy-ion collisions. The picture is taken from [65].

As mentioned earlier, the colliding nuclei with speeds close to the speed of light, due to the Lorentz contraction effect, will appear pancake-shaped in the longitudinal direction. So, what is the spatial distribution of the ultra-strong electromagnetic field excited by the colliding nuclei? The electric field of colliding nuclei will also point radially outward, as shown in Fig. 1.14, and the magnetic field will circling the electric field. This field at a point located some distance from the nucleus's trajectory exhibits characteristics similar to those of a real photon.

In 1924, a paper titled “On the Theory of Collisions Between Atoms and Elastically Charged Particles” was published by Enrico Fermi in Zeitschrift für Physik[66]. In this paper, Fermi introduced a technique called the equivalent (or virtual) photon method (EPA), wherein he represented the electromagnetic fields of a charged particle as a stream of virtual photons. A decade later, Weizsäcker and Williams expanded upon this method to encompass ultra-relativistic particles, leading to its characterization as the Weizsäcker-Williams method[67].

The flux of equivalent photons emitted by a charged particle can be calculated by performing a Fourier transform of the electromagnetic field produced by the moving charge. Based on the EPA method, the distribution of these photons for heavy-ion collision case can be calculated by:

$$\begin{gathered}\frac{d^3N_\gamma(\omega_\gamma,\vec{x}_\perp)}{d\omega_\gamma d\vec{x}_\perp}=\frac{4Z^2\alpha}{\omega_\gamma}\times\left|\int\frac{d^2k_{\gamma\perp}}{(2\pi)^2}\vec{k}_{\gamma\perp}\frac{F_\gamma(\vec{k}_\gamma)}{\left|\vec{k}_\gamma\right|^2}e^{i\vec{x}_\perp\cdot\vec{k}_{\gamma\perp}}\right|^2\\ \vec{k}_\gamma=(\vec{k}_{\gamma\perp},\frac{\omega_\gamma}{\gamma_c}),\end{gathered}\tag{1.18}$$

where Z signifies the nuclear charge number, α represents the electromagnetic coupling constant, ω_γ is the energy of photon, $F_\gamma(\vec{k}_\gamma)$ is the nuclear electromagnetic form factor and the $\vec{k}_\gamma$ is two-dimensional momentum vectors of the equivalent photons in the transverse momentum space. In the lab frame, the maximum photon energy is:

$$\omega^{max}=\frac{\hbar}{\Delta t}\sim\frac{\gamma\hbar v}{b},\tag{1.19}$$

where the Δt is the interaction time at an nucleus-nucleus collision with impact parameter b, γ is the Lorentz factor of the particle. At RHIC, the center of mass energy of photon-gold interaction could reach about 30 GeV, and photon-photon center of mass energy up to 6 GeV in Au+Au collisions at $\sqrt{s_{\rm NN}}$= 200 GeV[65]. The virtuality of these photons can be estimated by $-q^2 < (\hbar/R_R)^2$, which means these photons are almost real.

According to the Eq 1.18, the photon flux is proportional to Z^2, making relativistic heavy-ion collisions well-suited for studying photon-induced processes. As depicted in Fig. 1.15, a photon from one nuclei can strike the others (panel a), resulting in the production of a vector meson, or photons from each nucleus can collide with each other to generate a lepton pair (panel b). The photonuclear interaction generating vector mesons can be classified into coherent and incoherent processes, distinguished by different interaction mechanisms. In the coherent process, quasi-real photons originating from one nucleus interact with the entirety of the other nucleus, whereas the incoherent process involves interactions with individual nucleons within the traget nucleus. The transverse momentum (p_{T}) of the photo-produced vector meson can be estimated by the size of the interacting target, based on the uncertainty relation. Therefore, the coherent process will cause the vector meson to concentrate in the very low p_{T} region. The coherent photon-photon process, two photons emitted by two colliding nuclei interact to produce dilepton with a very small pair p_{T}, is also referred to as Breit-Wheeler process, which will be further discussed in the Sec 1.8.1.

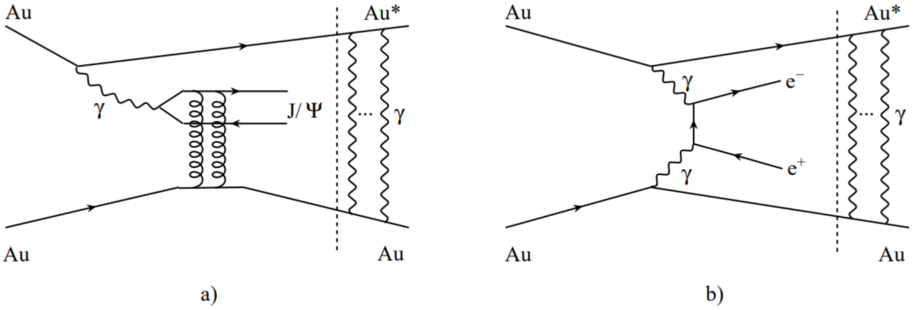

Figure 1.15 Lowest order Feynman diagrams for J/ψ meson (a) and dileptons (b) photoproduction in ultra-peripheral Au+Au collisions are depicted. The picture is taken from [68].

1.7 Quarkonia Measurements in Heavy-Ion Collisions

Quarkonia, bound states of heavy-flavor quarks and their antiquarks, serve as crucial tools in studying Quantum Chromodynamics (QCD) in high-energy hadronic collisions. Understanding quarkonia production in p+p and p+A collisions elucidates their production mechanisms and modifications due to cold nuclear matter. Investigating quarkonium properties in A+A collisions provides insights into the properties of the Quark-Gluon Plasma (QGP).

The J/ψ meson, discovered independently by experiments led by Samuel Ting[69] and Burton Richter[70] in 1974, stands out as one of the most notable quarkonia in particle physics and also a primary probe in this thesis. Excited charmonium states, can cascade down to lower states, contributing to the observed J/ψ meson production alongside directly produced ones. These contributions collectively constitute the “prompt” production. Conversely, “non-prompt” production refers to contributions from the decay of hadrons containing a b quark (B-hadrons) with significantly longer lifetimes.

1.7.1 Quarkonium production from initial hard scattering

In heavy-ion collisions, various mechanisms contribute to the production of heavy-flavor quarkonium. One significant mechanism involves partonic hard scattering processes during the initial stages of the collision. This process encompasses both perturbative and non-perturbative aspects of QCD.

Heavy-quark pairs ($q\bar{q}$) are produced through hard scattering processes which can be calculated perturbatively, necessitating momentum transfers of at least the mass of the heavy quark involved. Subsequently, these $q\bar{q}$ pairs can form quarkonium states. However, the transition from the $q\bar{q}$ pair into the quarkonium bound state is a non-perturbative process.

In theoretical calculation of the quarkonium production, the perturbative part, the $q\bar{q}$ pair production process involving large momentum transfer, can be separated with the non-perturbative process of forming a bound state within small momentum scales. This separation is known as the “factorization”, is a common approach used in various models. There are several models for quarkonium production with differences primarily lying in the treatment of the non-perturbative part, like the Colour-Evaporation Model (CEM)[71-72], the Colour-Singlet Model (CSM)[73-75], and the Color-Octet Mechanism (COM)[76]. These models offer different perspectives on quarkonium production, with varying emphases on perturbative and non-perturbative aspects of the process. Each model has its strengths and limitations, and their predictions can be compared with experimental data to test their validity and refine our understanding of quarkonium production in high-energy collisions.

1.7.2 Cold Nuclear Matter Effects

Cold Nuclear Matter (CNM) effects refer to the modifications of quarkonium production due to the presence of the nuclei in the initial state, without the formation of a Quark-Gluon Plasma (QGP). These effects are typically studied in collisions involving a projectile proton or deuteron (or nucleus) colliding with a target nucleus, denoted as p+A or d+A collisions, respectively.

Indeed, the modification of parton distribution functions (PDFs) in colliding nuclei compared to those in free nucleons is a significant Cold Nuclear Matter (CNM) effect in the initial state of heavy-ion collisions. As shown in the Fig. refnPDF, the ratio of the valence quark, sea quark, and gluon in the moving Pb (nPDF) to that in a free nucleon (PDF) as a function of momentum fraction x at $Q^2 = 1.69\ GeV^2$ provides crucial information about the nuclear medium’s influence on parton distributions. Schematically, we

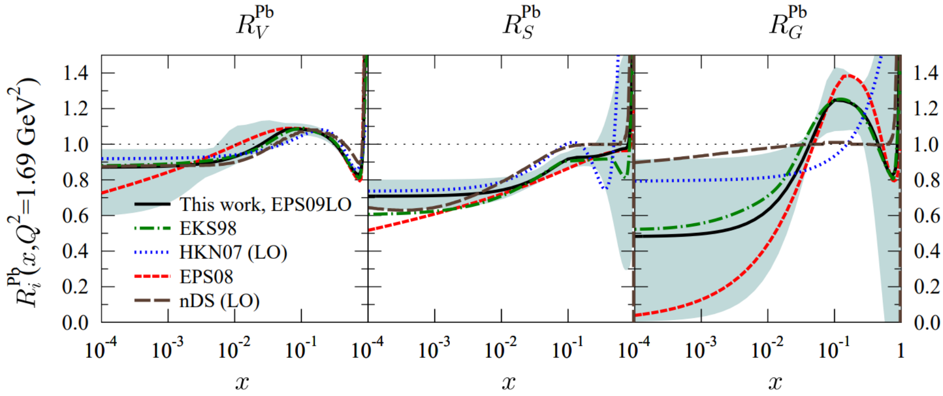

Figure 1.16 Comparision of the average valence and sea quark, and gluon modifications at Q^2 = 1.69 GeV^2 for Pb nucleus from LO global DGLAP analyses EKS98[77], EKPS[78], nDS[79], HKN07[80] and EPS09LO[81].

can identify three distinct regimes for the ratio of nPDF to PDF: at x smaller than ~ 0.01, the nPDF is suppressed (shadowing); at intermediate x from ~ 0.01 to ~ 0.1, there is an possible enhancement (anti-shadowing); at x larger than ~ 0.1, deviations from unity in the nPDF/PDF ratio are observed, indicating the EMC (European Muon Collaboration) effect. In addition to the modification of PDFs, partons in colliding nuclei can experience multiple scattering interactions within the nuclear environment before and/or after hard scattering processes. These interactions lead to energy loss mechanisms such as radiative or collisional processes, resulting in parton energy loss and transverse momentum broadening. This broadening effect is known as the Cronin effect and is observed as an enhancement of the transverse momentum distributions at intermediate p_{T} region (~few GeV/c) of produced particles in nuclear collisions compared to proton-proton collisions. The Cronin effect arises from the increased number of scattering centers in the nuclear medium, leading to additional transverse momentum kicks for partons before they undergo hard scatterings.

In additional to the CNM effects associated with partons inside the colliding nuclei, $q\bar{q}$ bound states may also undergo absorption as they traverse through the nucleus, a phenomenon commonly referred to as “nuclear absorption”. The breakup cross section, denoted as σ_{abs}, serves as a crucial parameter for assessing this effect. Studies have demonstrated that the breakup cross section of J/ψ mesons depends on the center-of-mass energy $\sqrt{s_{NN}}$ and is largely independent of the chosen nuclear Parton Distribution Function (nPDF) parametrization[82]. Anticipations suggest that at energies reached by the Large Hadron Collider (LHC), nuclear absorption effects are expected to diminish significantly, given that the formation time of quarkonium greatly exceeds the size of nuclei across all rapidity values.

In a study by McGlinchey et al.[83], it was observed that the suppression of J/ψ mesons, when scaled by the crossing time (τ_{cross}), appears to be independent of the center-of-mass energy when the crossing time exceeds approximately $\sim$ 0.05 fm/c. The crossing time is defined as:

$$\tau_{cross} = \frac{L}{\beta_z \gamma}, \tag{1.20}$$

where the L is the longitudinal path of the $q\bar{q}$ pair through the nucleus, β_z and $\gamma = \sqrt{1-\beta_z^2}$ are the velocity and Lorentz factor of the J/ψ mesons in the direction of the beam, both provided in the rest frame of the nucleus. Additionally, J/ψ mesons can be dissociated by "comovers", which pertain to partons or hadrons generated in the collision in close proximity to the J/ψ meson. These comovers may interact further with the J/ψ meson, leading to its dissociation.

Studying CNM effects in p+A or d+A collisions provides valuable insights into the nuclear structure and dynamics, and it serves as a baseline for understanding the modifications of quarkonium yield in relativistic heavy-ion collisions, where both CNM effects and QGP effects may contribute to the observed phenomena. Comparing quarkonium production in p+A or d+A collisions with that in A+A collisions allows researchers to disentangle the contributions of CNM effects and QGP effects, advancing our understanding of the properties of the produced quark-gluon matter.

1.7.3 Quarkonium in medium

In a hot and deconfined environment, such as the QGP, the production of quarkonium is expected to be significantly suppressed compared to its scaled yield in p+p collisions according to the N_{coll}, assuming the overall charm cross-section remains unchanged. This suppression in QGP is believed due to the color screening of the force that binds the $c\bar{c}$ or $b\bar{b}$ state, which has been proposed by T. Matsui and H. Satz in 1986[84], known as color screening effect.

To further understand the color screening effect, particularly the suppression of J/ψ mesons in the QGP, several questions need to be addressed. Firstly, can J/ψ mesons escape from the production region before the QGP forms? The typical time (τ_0) for QGP formation after the collision is expected to be on the order of one femtosecond (fm/c). While the time for $c\bar{c}$ pair production is much smaller than τ_0, the transition from $c\bar{c}$ pair to a J/ψ meson will require a time of order τ_0. Additionally, anything produced in the interaction region must travel at least a distance of about $A^{1/3}$ fm before it can exit. Therefore, J/ψ mesons produced by the initial hard scattering have the possibility to traverse the QGP.

Next, at what temperature could J/ψ mesons no longer maintain their bound state? Inside the QGP, the color-screened Coulombic potential can be calculated as:

$$V(r) = -\frac{\alpha_{eff}}{r}\exp[-\frac{r}{\lambda_D}], \tag{1.21}$$

where λ_D is the Debye screening radius, and r is the distance between interacting partons in a bound state. If the Debye radius, which is inversely proportional to the medium temperature, becomes smaller than the radius of the $q\bar{q}$ bound state, then the confining force between the $q\bar{q}$ pair can no longer hold the bound state and dissociation occurs. According to the calculation[85], the dissociation temperature (T_D/T_c) for J/ψ is about 2.0. Thus, the J/ψ could be dissociated in the QGP at certain collision energy. Therefore, the dissociation points of the various quarkonium states offer a means to gauge the temperature of the medium. As the temperature increases, the different charmonium states are anticipated to ”melt” sequentially based on their binding strength: the most loosely bound state disappears first, followed by subsequent states, with the ground state being the last to dissolve. As one can see in Fig. 1.17, this sequential suppression is illustrated schematically by the various charmonium states.

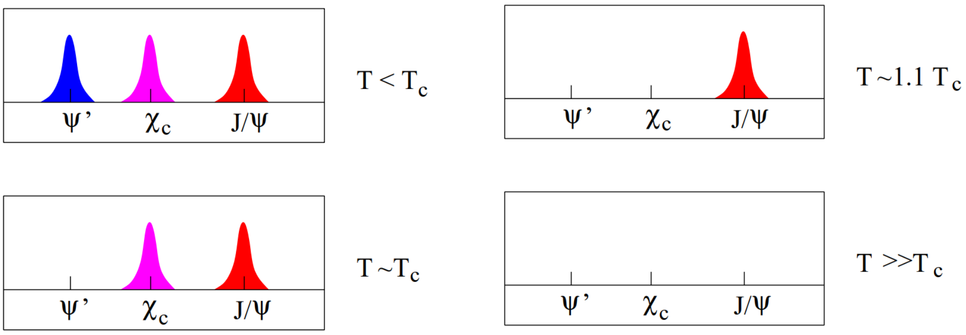

Figure 1.17 Charmonium spectra at different temperatures. The picture is taken from[85].

However, the reality is far more complex than this; the color screening effect is not the sole influence on heavy quarkonium in hot and dense matter, such as the dynamical screening effect[86-88] and regeneration effect[89-90]. The dynamical screening effect refers to the dissociation of quarkonium in a medium due to collisions with its constituents. This dissociation process occurs primarily through the gluon absorption process $g + Q\bar{Q} \rightarrow Q + \bar{Q}$ at the leading order in the coupling constant, where ($Q\bar{Q}$) denotes a quarkonium state. Additionally, at the next-leading order, inelastic scattering between $Q\bar{Q}$ and medium constituents, $l(\bar{l}, g) + Q\bar{Q} \rightarrow l(\bar{l}, g) + Q + \bar{Q}$ where l represents a light quark, also contributes to the dissociation.

As mentioned above, the heavy quark and anti-quark within a quarkonium bound state are no longer constrained by a confining force and tend to diffuse away from each other during the lifetime of the Quark-Gluon Plasma (QGP). As the system cools and the deconfined phase dissipates, these heavy quarks are likely to combine with the much more abundant light quarks to form final hadronic states. However, new quarkonium states may also form from combinations of heavy quarks and anti-quarks. This process, known as the regeneration effect, involves the recombination of unbound quark and anti-quark pairs within the medium[91].

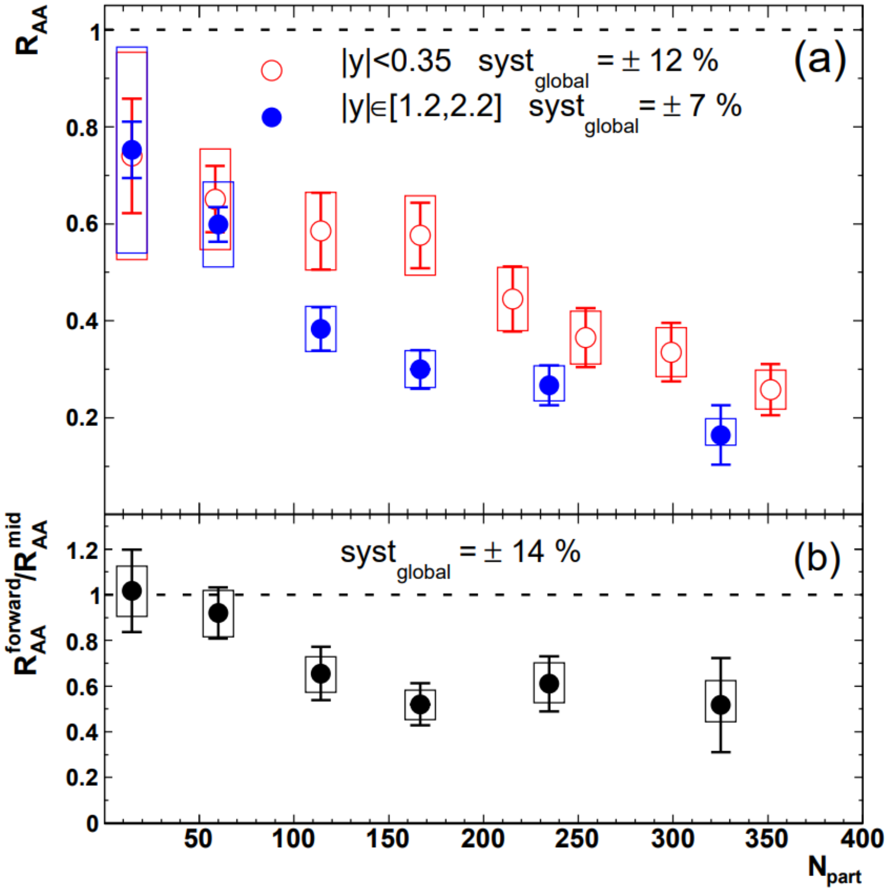

Figure 1.18 (a) J/ψ R_{AA} as function of N_{part} for Au+Au collisions. Mid (forward) rapidity data are shown with open (filled) circles. (b) Ratio of forward/mid rapidity J/ψ R_{AA} as function of N_{part}.

Experimental measurements of the J/ψ suppression in heavy-ion collisions have been conducted for over thirty years, initially at the SPS ($\sqrt{s_{\text{NN}}}$= 17.3 GeV) and subsequently at RHIC from $\sqrt{s_{\text{NN}}}$= 39 to $\sqrt{s_{\text{NN}}}$= 200 GeV, as well as at much higher energies of $\sqrt{s_{\text{NN}}}$= 2.76 and 5.02 TeV at the LHC. The measured suppression of the J/ψ at SPS [92-94] is comparable to that at RHIC energy[95-96] at mid-rapidity, despite the considerable difference in center-of-mass energies by a factor of ten. This observation suggests the existence of additional effects that set in already at RHIC energies and may offset some of the quarkonium suppression due to screening in the QGP. Furthermore, as depicted in Fig. 1.18, a lesser suppression at mid-rapidity compared to forward rapidity has been observed, despite the higher energy density at mid-rapidity[95]. Among these effects, J/ψ production from recombination in the medium[97-98] could account for the similar suppression at SPS and RHIC energies[99]. However, the contribution from recombination is expected to exhibit minimal dependence on rapidity[100-101]. Thus, the observed rapidity dependence of J/ψ suppression could also be elucidated by cold nuclear matter effects[102].

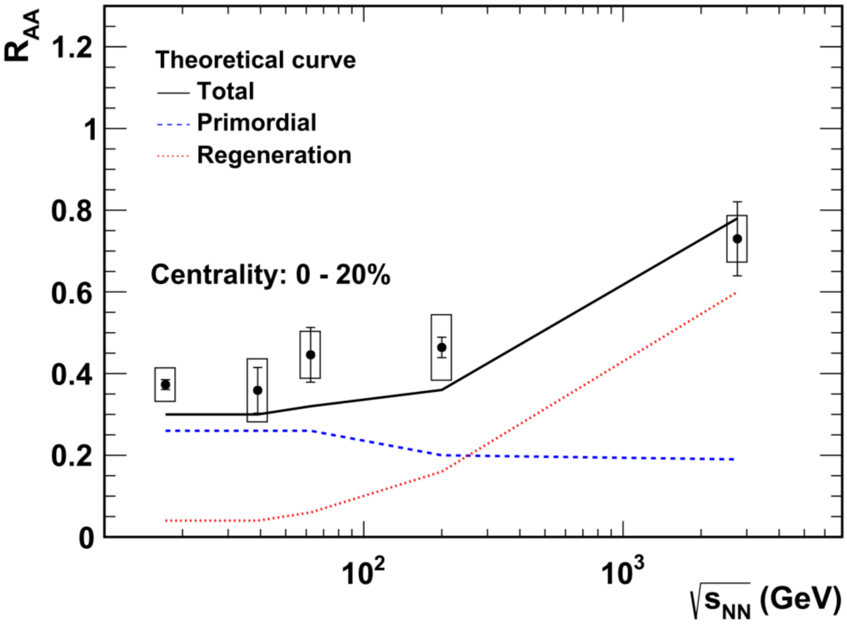

Figure 1.19 The R_{AA} of J/ψ as a function of collision energy in central collisions[103-107], in comparison with transport model calculations from the TAMU group[99]. The transport model calculations are shown as dashed line for the total J/ψ R_{AA}, dash-dot-tripled line for the suppressed primordial production and long dash line for the regeneration.

Figure 1.19 illustrates the nuclear modification factor R_{AA} results as a function of collision energy for 0-20% centrality. The calculations[99], depicted by the solid line, encompass two components: the direct suppression from color screening and CNM effects, represented by the blue line; and the regeneration contribution, depicted by the red line. The suppression solely due to CNM effects in central Au+Au collisions at $\sqrt{s_{\mathrm{NN}}}$= 200 GeV is estimated to be approximately 0.6 according to calculations[99]. Hence, the measured suppression at the same energy encompasses contributions from the hot medium effect. Furthermore, the regeneration effect could elucidate why the measured R_{AA} at the LHC is even larger than that at RHIC. Within the uncertainties, no significant energy dependence of R_{AA} for 0-20% centrality is observed up to 200 GeV.

There are several theoretical models which employ different dynamic processes, such as J/ψ mesons considered to be dissociated and regenerated continuously during the medium evolution[99,108-110] or be completely melted above the dissociation temperature and then regenerated at the chemical freeze-out[89,111], and can quantitatively describe the experimental measurements. However, the uncertainties on theoretical calculations are still large because the underlying mechanisms responsible for the hot medium and CNM effects are not well understood, and the model parameters, such as the dissociation temperatures of quarkonium states, the temperature profile of the medium, the heavy quark production cross section and their dynamic evolution in the medium, are badly constrained. All these aspects strongly depend on the collision energy, and thus a fine collision energy dependence of quarkonium suppression in relativistic heavy-ion collisions can provide stringent constraints on theoretical calculations, which are essential for inferring the properties of the QGP from quarkonium measurements.

The RHIC beam energy scan program, mainly designed for the exploration of the QCD phase structure and searching for the critical end point, enables a collision energy scan of J/ψ production between the SPS energy and the top RHIC energy. In 2017, the STAR collaboration recorded a significantly larger sample of Au+Au collisions at $\sqrt{s_{\mathrm{NN}}} = 54.4$ GeV compared to those at 39 and 62.4 GeV. Measurements of the J/ψ production at a new energy with improved precision will shed additional light on both the cold and hot medium effects on the J/ψ production in heavy-ion collisions.

1.7.4 J/ψ Production from Photon-Nucleus Interaction

As depicted in the panel (a) of Fig. 1.15, the production of J/ψ can occur in photon-nucleus interactions via Pomeron exchange under the influence of strong electromagnetic fields generated by the colliding nuclei. In the coherent process, where the incoming quasi-real photon interacts with the entire target nucleus, the final products typically consist of two intact nuclei and a J/ψ meson with very low transverse momentum ($p_{\mathrm{T}} <$ 0.1 GeV/c), making it sensitive to the nuclear gluon distribution at low Bjorken x[112]. In order to keep coherent condition, this process are conventionally expected to be only detectable when there are no accompanying hadronic interactions, in the so-called ultraperipheral collisions (UPC) where the impact parameter b exceeds twice the nuclear radius (R_A). The first measurement of photon-nucleus production of charmonium in UPC of relativistic heavy ion was performed by the PHENIX Collaboration in Au+Au collisions at $\sqrt{s_{\mathrm{NN}}}$= 200 GeV[68]. This measurement corresponded to $W_{\gamma Au} \approx 24$ GeV ($x \approx 1.5\times10^{-2}$). Although this measurement has a large uncertainty, it was very important as a proof of principle.

However, a question arises: Can the coherent photon-nucleus interaction also occur in the heavy-ion collision where the nuclei collide and break up? In 2017, a significant excess of J/ψ production at very low p_{T} has been first observed by the ALICE Collabo-

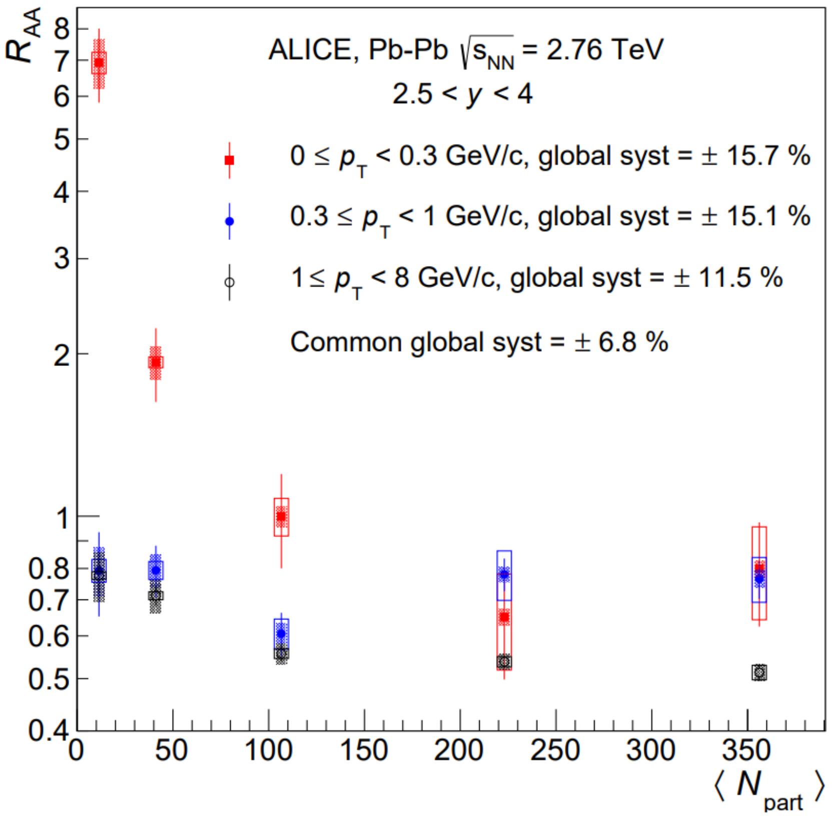

Figure 1.20 The J/ψ R_{AA} as a function of $\langle N_{part} \rangle$ for 3 p_T ranges in Pb+Pb collisions at $\sqrt{s_{NN}}$= 2.76 TeV.

rations in peripheral hadronic heavy-ion collisions[113], as shown in the Fig. 1.20.

The J/ψ R_{AA} in Fig. 1.20 at the p_T from 0 to 0.3 GeV/c shows a strong excess in the most peripheral Pb+Pb collisions, which can not be explained by any transport models[114-115]. Then, the similar excesses were observed at RHIC in the peripheral Au+Au at $\sqrt{s_{NN}}$= 200 GeV and U+U collisions at $\sqrt{s_{NN}}$= 193 GeV by the STAR collaboration, shown in the Fig. 1.21.

Explaining this excess with existing theoretical models, which solely incorporate hadronic processes, would pose a significant challenge. While the coherent photoproduced J/ψ could be formed in the initial state of the heavy-ion collisions, and then contribute to the final J/ψ yield at very low $p_T$region. If we assume that the coherent photoproduction is responsible for the excess of J/ψ yield at very low $p_T$region, then the excess in U+U collisions is expected to larger than that in Au+Au collisions at similar collision energies due to more number of charges in U than that in Au. While due to the uncertainties, the observed difference is only $\sim 2.0\sigma$, which is shown in the Fig. 1.22. The isobaric collisions, $^{96}_{44}$Ru+$^{96}_{44}$Ru and $^{96}_{40}$Zr+$^{96}_{40}$Zr, taken in 2018 at $\sqrt{s_{NN}}$= 200 GeV, will provide a ideal chance to further understanding this excess.

Different lines in the Fig. 1.22 stands for the model calculation[116] for Au+Au

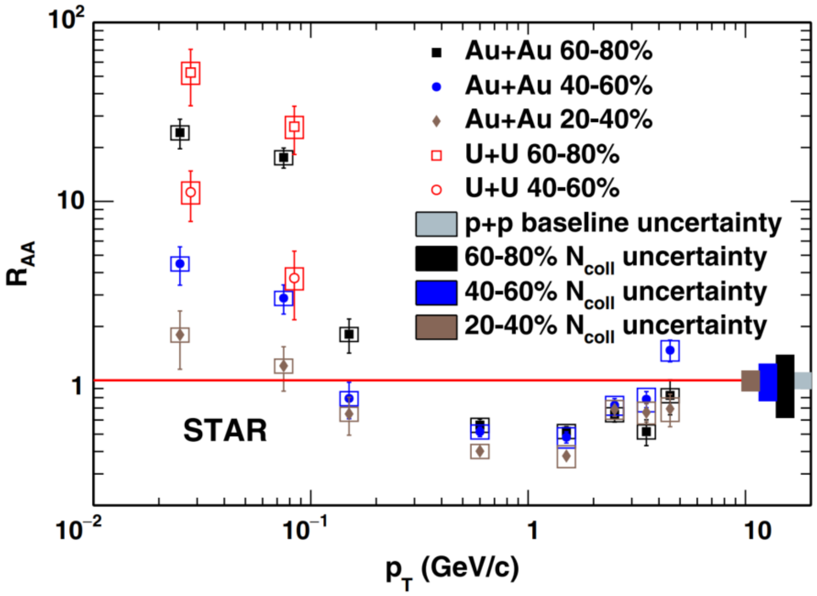

Figure 1.21 The J/ψ R_{AA} as a function of p_{T} in different centrality bins in Au+Au collisions at $\sqrt{s_{\mathrm{NN}}}$= 200 GeV and U+U collisions at $\sqrt{s_{\mathrm{NN}}}$= 193 GeV.

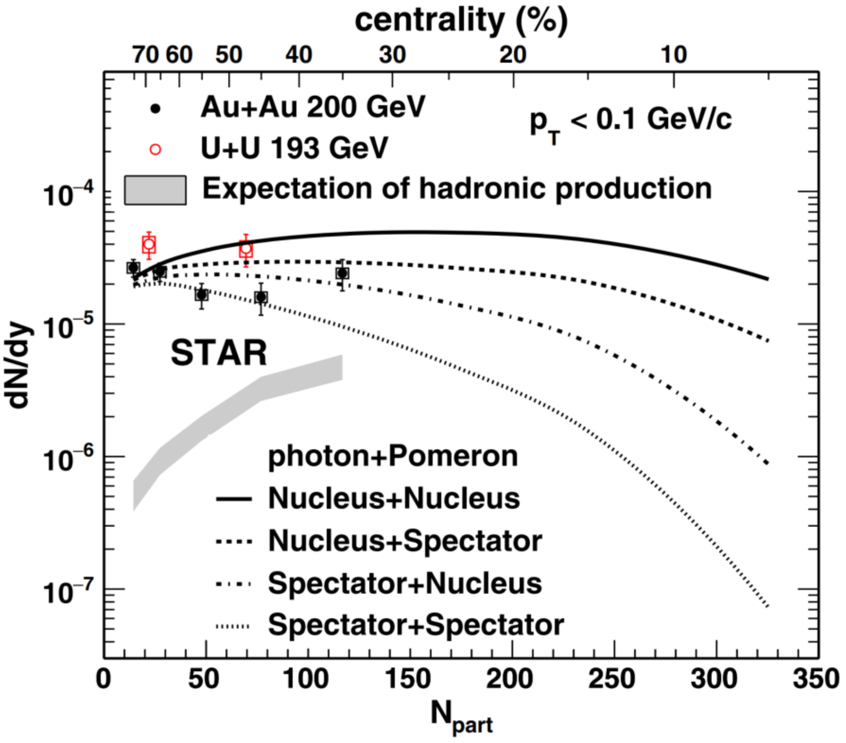

Figure 1.22 The p_{T}integrated J/ψ yield (p_{T}<0.1GeV/c) as a function of N_{part} in 30-80% centrality in Au+Au collisions and 40-80% centrality in U+U collisions, after estimated hadronic contribution subtraction.

collisions with the coherent photon-nucleus assumption. For the theoretical calculation, photon and Pomeron emitters can be either the entire nucleus or just the spectator, resulting in four possible configurations: (1) nucleus for photon emitters + nucleus for Pomeron emitters, (2) nucleus for photon emitters + spectator for Pomeron emitters, (3) spectator for photon emitters + nucleus for Pomeron emitters, and (4) spectator for photon emitters + spectator for Pomeron emitters. All four configurations are consistenct with the measurements in 60– 80% centrality class, while the results in semi-central collisions appear to favor the nucleus for photon emitters + spectator for Pomeron emitters or spectator for photon emitters + nucleus for Pomeron emitters scenarios. The (1) scenario significantly overestimates the results in the more central collisions, which means there may exist a partial disruption of the coherent production by the intense hadronic interactions in this centrality.

In this thesis, the measurements of very low p_{T} J/ψ production in ${}^{96}_{44}$Ru+${}^{96}_{44}$Ru and ${}^{96}_{40}$Zr+${}^{96}_{40}$Zr provide a direct investigation into the initial electromagnetic dependence of this photon-nucleus process in high-energy hadronic heavy-ion collisions, given that the flux of quasi-real photons is $\propto Z^2$. From this perspective, the photon-photon process is more conducive to studying the dependence of the initial electromagnetic field generated by the colliding nuclei, as discussed in the following Section 1.8.1. Additionally, since the coherent photon-nucleus process is sensitive to the nuclear gluon distribution due to its involvement with Pomeron exchange, the measurements of very low p_{T} J/ψ production in Ru+Ru and Zr+Zr collisions will also contribute to our understanding of the gluon distribution in different nuclei when compared to published results from Au+Au, U+U, and Pb+Pb collisions.

1.8 Photon-Photon in Heavy-Ion Collisions

1.8.1 Very-Low p_{T} Dilepton Production

Besides the photon-nucleus process, the quasi-real photons generated by the relativistic contraction and large number of charges in the colliding nuclei, could also participate in the photon-photon interactions, for example the so-called Breit-Wheeler process ($\gamma + \gamma \rightarrow l^+ + l^-$), as depicted in Fig. 1.15. in 1934, Breit and Wheeler proposed this process, suggesting that the collision of two photons could produce a dilepton pair[117]. This phenomenon, wherein light is transformed into matter, directly embodies Einstein's mass-energy equation $E = mc^2$, illustrating the interconversion of energy and mass. These photon interactions have been extensively investigated in UPCs[38,68,118-119]. The

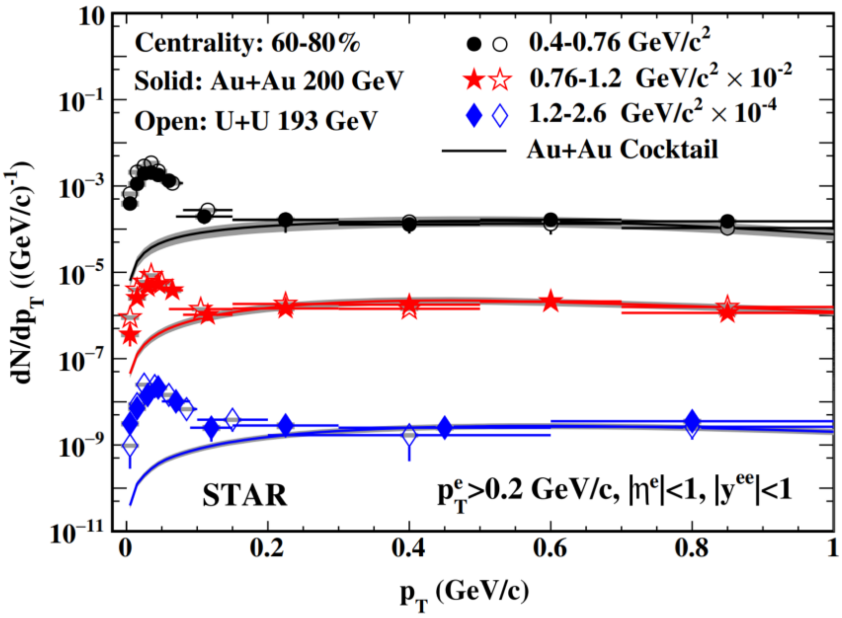

Figure 1.23 The e^+e^- pair distributions as a function of $p_T$for three mass regions in 60-80% 200 GeV Au+Au and 193 GeV U+U collisions. The hadronic cocktail is displayed as the solid lines.

STAR collaboration first measured a significant excess yield of e^+e^- pair production at very low $p_T$in 200 GeV Au+Au collisions as well as 193 GeV U+U collisions, as depicted in Fig. 1.23. As one can see, the excess yields of e^+e^- pair are concentrated below p_T≈0.15 GeV/*c*, while the hadronic cocktail (solid lines) describes the data well for p_T> 0.15 GeV/*c* in all three pair mass regions.

The invariant mass distributions for excess e^+e^- pairs at very low p_T (< 0.15 GeV/*c*) are shown in the panel (a) and (b) of Fig. 1.24 for 60-80% and 40-60% centralities, and the hadronic contribututions were subtracted statistically. The e^+e^- excess yield are obtained by integrating the very low-p_T invariant mass distributions over the three aforementioned mass regions, as shown in the panel (c) of Fig. 1.24. Various model calculations are compared to the measured excess yield in Au+Au collisions[116,120-121]. The calculated results from[120], which consider the charge distribution in the colliding nucleus to estimate the photon flux, describe the 60-80% centrality data quite well. However, calculations from the STARlight MC generator[121], which considers the nucleus as a pointlike charge when evaluating the photon flux and ignores e^+e^- production within the geometrical radius of the nucleus, underestimate the data, as illustrated in Fig. 1.24. Comparisons with model calculations strongly suggest that the observed excess for p_T < 0.15 GeV/*c* is attributed to photon-photon production.

In this thesis, the measurements of very low p_T e^+e^- pair production in $^{96}_{44}$Ru+$^{96}_{44}$Ru and $^{96}_{40}$Zr+$^{96}_{40}$Zr collisions offer a unique opportunity to examine the dependence of

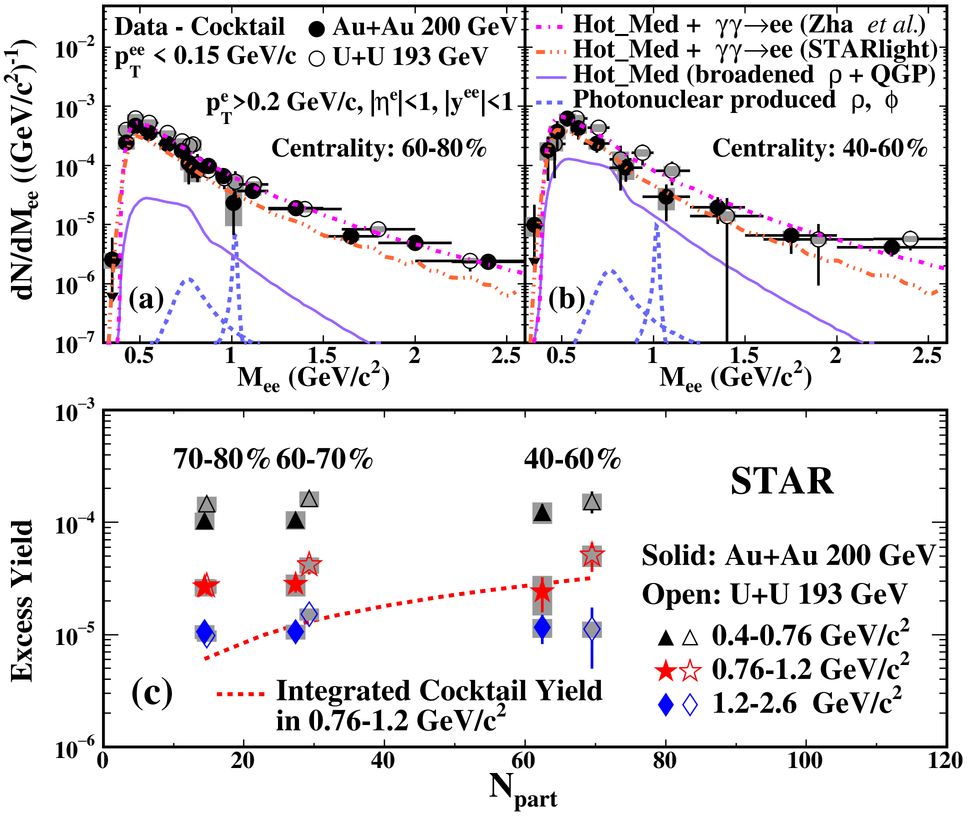

Figure 1.24 After hadronic contribution subtraction, the mass spectra of e^+e^- excess yield at low-p_T region within the STAR acceptance in (a) 60-80% and (b) 40-60% for Au+Au at $\sqrt{s_\mathrm{NN}}$ = 200 GeV and U+U at $\sqrt{s_\mathrm{NN}}$ = 193 GeV collisions. (c) The centrality dependence of excess yields is shown in three different mass regions for both collision systems. Additionally, the hadronic cocktail yields in different centralities in the mass region of 0.76-1.2 GeV/c^2 is displayed for both collisions to facilitate comparison.

photon-photon interactions on the initial electromagnetic field. The rationale behind this lies in the fact that the yields of e^+e^- pairs from photon-photon interaction are proportional to Z^4, while the contributions from hadronic processes are similar within the same centrality class due to the identical atomic number (both collision systems have a Z value of 96). Furthermore, the difference of the strong magnetic field between Ru+Ru and Zr+Zr collisions is crucial for searching the signals related to Chiral Magnetic Effect (CME) in isobaric collisions. Therefore, studying the initial electromagnetic field through photon-photon interaction is imperative for gaining further insights into the observed CME-sensitive signals in isobaric collisions.

1.8.2 Vacuum Birefringence

The vacuum is not simply empty vacuum when there is a existence of a background field, it can be polarized due to the interaction between the field and short-lived particles which are continuously and nearly instantaneously created and annihilated. In the 1930s, the work of Euler, Heisenberg, and Schwinger showed that the presence of a background field will polarizes the vacuum[122-124]. If the field is Strong enough, for example the existence of electric or magnetic field is comparable to the critical field $E_{cr} = m^2c^3/e\hbar = 1.3 \times 10^{16}$V/cm or $B_{cr} = m^2c^3/e\hbar = 4.4 \times 10^{13}$G, the electron-positron pairs can be efficiently produced, known as Schwinger effect.

Subsequently, Toll conducted groundbreaking research aimed at comprehending vacuum polarization in the strong-field regime of QED[125]. The core concept highlighted in his research is that the vacuum exhibits characteristics of a polarizable and magnetizable medium. This behavior can lead to birefringence, also known as double refraction, of light when it traverses a space region under the influence of an external magnetic field. This is known as vacuum magnetic birefringence (VMB), a phenomenon in which the QED vacuum gains unique refractive indices which depends on the relative angle between the photon polarization and the magnetic field direction.

As we mention in Sec. 1.6.1, the colliding nuclei with appear pancake-shaped in the longitudinal direction, due to the Lorentz contraction effect. Also, the electric field outside the colliding nuclei can be treated as a linearly polarized photon flux. The photon-photon processes can be described as a scenario where a linearly polarized photon originating from one nucleus traverses through the electromagnetic field generated by the other nucleus, known as vacuum birefrigence. This process could cause the angular modulation of the produced dileptons. The angular modulation of e^+e^- pair at very low p_{T} in 60-80% and ultra-peripheral 200 GeV Au+Au collisions has been observed by STAR collaboration, as shown in Fig. 1.25. As one can see, a clear $\cos(4\Delta\phi)$ modulation are observed, and theoretical calculation[126] based on QED can describe the measurements very well. In this thesis, the measurements of e^+e^- angular modulation in Ru+Ru and Zr+Zr collisions, will allow us to explore any collision system dependence of this phenomenon.

1.9 Motivation of this Thesis

The suppression of J/ψ mesons, considered a “smoking gun” of Quark-Gluon Plasma (QGP) formation in heavy-ion collisions, has been extensively studied over nearly three decades across various collision systems. These investigations have significantly enriched our comprehension of QGP properties. It’s now acknowledged that J/ψ suppression is influenced by several factors. Dissociation in the medium involves color screening and dynamic screening effects. Additionally, the regeneration effect,

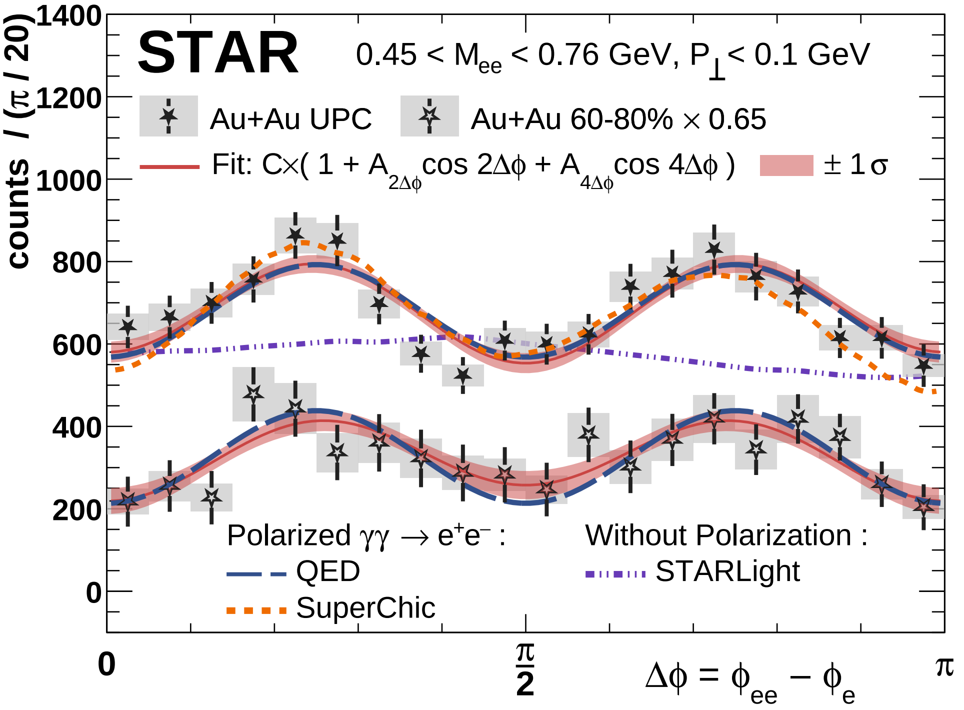

Figure 1.25 The angular modulation in 60-80% and ultra-peripheral 200 GeV Au+Au collisions for M_{ee} > 0.45 GeV.

which entails the recombination of unbound c and $\bar{c}$ quarks in the deconfined medium, contributes to J/ψ production. Alongside these medium effects, Cold Nuclear Matter (CNM) effects alter J/ψ production due to nuclear presence. Different theoretical models have been proposed based on various assumptions and considerations regarding these effects. However, due to imperfect understanding of QGP properties and CNM effects, uncertainties in theoretical calculations remain significant. In this thesis, we measure inclusive J/ψ production at a novel collision energy (54.4 GeV) in Au+Au collisions. We calculate the centrality and p_{T} dependence of the nuclear modification factor R_{AA} for inclusive J/ψ mesons. These results are compared with previous results from different collision systems, aiming to explore the energy dependence of J/ψ suppression.

In addition to J/ψ mesons originating from initial partonic hard scattering, they can also be generated by the photon-nucleus interaction in relativistic heavy-ion collisions. Conventionally thought to occur primarily in Ultra-Peripheral Collisions (UPC), the coherent photon-nucleus process was first observed by the ALICE collaboration in Pb+Pb collisions at 2.76 TeV in 2017. In this process, a quasi-real photon emitted by one nucleus interacts with another nucleus via Pomeron exchange, leading to the production of vector mesons at very low p_{T}, such as the J/ψ meson. The Pomeron exchange, involving two gluons, makes this process sensitive to the gluon distribution of the colliding nuclei. The flux of quasi-real photons is proportional to Z^2. In 2018, the STAR collaboration collected a substantial sample ($\sim$ 4 billion events) of $^{96}_{44}$Ru+$^{96}_{44}$Ru and $^{96}_{40}$Zr+$^{96}_{40}$Zr collisions, providing an excellent opportunity to investigate the dependence of photon-nucleus processes on the initial electromagnetic field, as well as the gluon distribution in the colliding nuclei. Furthermore, the production of very low p_{T} $e^{+}e^{-}$ pairs in heavy-ion collisions from photon-photon interactions, initially observed by the STAR collaboration, is anticipated to be even more sensitive to the initial electromagnetic field. This is because the cross section of $\gamma + \gamma \rightarrow e^{+} + e^{-}$ is proportional to Z^{4}. In this thesis, the production of very low p_{T} $e^{+}e^{-}$ pairs and J/ψ mesons is measured in Ru+Ru and Zr+Zr collisions, and compared with published results from Au+Au and U+U collisions. The possible collision system dependence of photon-induced interaction are studied. The angular modulation measurements in Ru+Ru and Zr+Zr collisions can be used to further explore the collisions system dependence of the vacuum birefringence phenomenon in heavy-ion collisions. Through comparisons between experimental measurements and theoretical models based on the equivalent photon method (EPA), we have deepened our theoretical understanding of photon-induced interactions.

In the upcoming chapters, we will meticulously introduce the analysis methods concerning the production of $e^{+}e^{-}$ pairs and J/ψ mesons. Since the techniques for J/ψ production are highly analogous, whether it's measuring its photon-nucleus production at very low p_{T} in 200 GeV Ru+Ru and Zr+Zr collisions or assessing its suppression in 54.4 GeV Au+Au collisions, we will initially present the analysis setup for J/ψ mesons production in Ru+Ru and Zr+Zr collisions, alongside $e^{+}e^{-}$ pairs measurements in these same collision systems, in a cohesive manner in Chapter 3. Subsequently, Chapter 4 will offer a succinct overview of the analysis setup for J/ψ suppression in 54.4 GeV Au+Au collisions, with a primary focus on the distinctions in measuring J/ψ production between 200 GeV Ru+Ru and Zr+Zr collisions versus 54.4 GeV Au+Au collisions. Following this, we will delve into a discussion on the results obtained in this thesis, along with exploring future prospects.

Chapter 2 Experimental Setup

2.1 Relativistic Heavy Ion Collider

The Relativistic Heavy Ion Collider (RHIC), as depicted in the Fig. 2.1, is the US Department of Energy's forefront research facility for nuclear physics at Brookhaven National Laboratory (BNL) in New York. It is also one of the two operating heavy ion colliders in the world[127]. The RHIC facility could accelerate the Au ions up to 100 GeV/nucleon and protons to 255 GeV. The primary research target of RHIC is to investigate the formation and properties of the QGP, a hot and dense QCD matter.

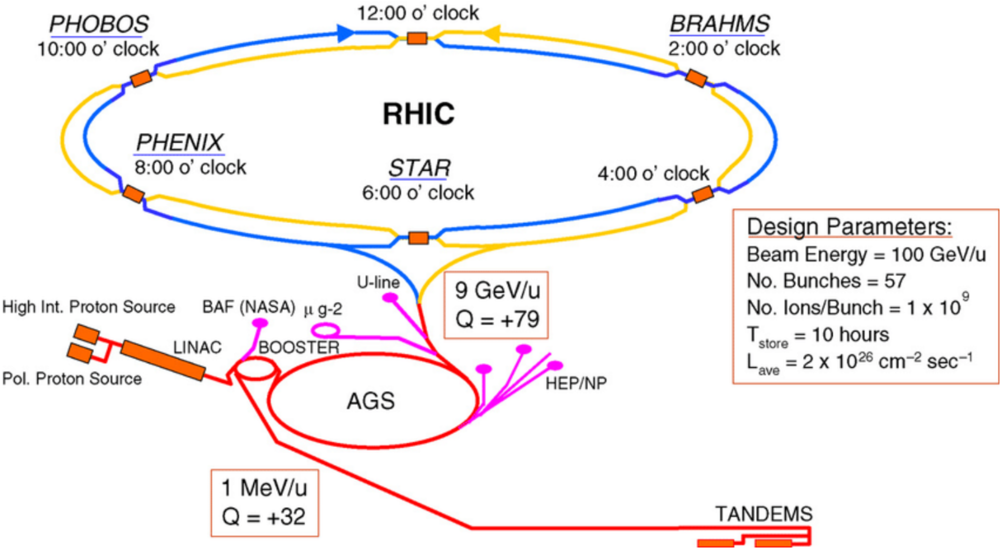

Figure 2.1 RHIC accelerator complex.

Figure 2.1 shows a sketch of the accelerator complex, which includes ion and proton sources, linear accelerator (LINAC), Booster Synchrotron (BS), Alternating Gradient Synchrotron (AGS), RHIC, and transition lines. RHIC is a two-ring superconducting hadron collider with 3.8 km in circumference. The two rings, "Blue Ring" for the beam traveling clockwise and "Yellow Ring" for counter-clockwise, are designed to intersect at six locations. For the Au ion beam, the pulsed sputter ion source at the Tandem Van de Graaff (100μA, 700μs) first provides negatively charged gold ions ($Q = -1$). By the second stage of the Tandem, electrons are further stripped with a foil at the Tandem's high voltage terminal and the ions are accelerated to the energy of 1 MeV/nucleon. After undergoing additional stripping at the Tandem exit and charge selection via bending magnets, gold ions with a charge state of $Q = +32$ are transported to the BS, where they are subsequently accelerated to 96 MeV/nucleon. The ions are stripped again when exiting from the Booster with the chagre state of +77 to be injected to the AGS in 24 bunches. In the AGS, the gold ion beams are accelerated to the RHIC injection energy of 10.8 GeV/nucleon. After reaching that energy, the ion beams are debunched and then re-bunched to 4 bunches which will be ejected one bunch at a time and transferred to RHIC at the injection front porch prior to the acceleration. After exiting from the AGS, the gold ions are fully stripped to the charge state of +79. For the proton beam, a slightly differnt acceleration procedure is used. The polarized protons are injected from the existing LINAC to the BS with a energy of 200 MeV, and then to the AGS and RHIC ring finally. Since year 2021, RHIC has successfully collided various collision systems at different energies, and will continue to deliver p+p, p+Au and Au+Au collision at top energy, a summarized Table2.1 can be found below.

Year	Collision species	Total events
2023	Au+Au @ 200 GeV	6.74 B
	Au+Au (500A) @ 200 GeV	66.77 M
	Au+Au (half field) @ 200 GeV	256.87 M
	Au+Au (zero field) @ 200 GeV	223.68 M
2022	p+p @ 500 GeV	11.3 B
2021	Au(Fixed) @ 100(lab)/13.7(cms) GeV	69.76 M
	Au(Fixed) @ 70(lab)/11.5(cms) GeV	75.81 M
	Au(Fixed) @ 44.5(lab)/9.2(cms) GeV	69.72 M
	Au(Fixed) @ 26.5(lab)/7.2(cms) GeV	126.98 M
	Au(Fixed) @ 3.85(lab)/3.0(cms) GeV	2.45 B
	Au+Au @ 17.3 GeV	890.94 M
	Au+Au @ 7.7 GeV	959.48 M
	d+Au @ 200 GeV	356.2 M
	O+O @ 200 GeV	577.34 M
	O+O(pre-scaled) @ 200 GeV	788.07 M
	O+O(full field minbias) @ 200 GeV	208.08 M

Table 2.1 Summary of collision systems at RHIC, from year 2021 to the near future 2025.

BNL has been selected by US DOE as the host lab for the future Electron-Ion Collider (EIC) in the United States in 2030s, and therefor RHIC will be upgraded to eRHIC[128] by adding a high current, multi-pass Energy Recovery Linac (ERL) and electron recirculation rings to the existing RHIC facility. This will enable eRHIC to deliver a polarized electron beams with energies up to 15.9 GeV, which can collide with hadrons like polarized protons with the top energy of 250 GeV or fully stripped Uranium ions with energies up to 100 GeV/nucleon. The EIC is aimed to produce snapshots of those hadrons' internal structures, like a CT scanner for atoms.

2.2 The Solenoidal Tracker At RHIC

The layout of detectors encircling the RHIC ring is also depicted in Fig. 2.1, at 6 o'clock is STAR, at 8 o'clock is PHENIX, at 10 o'clock is PHOBOS, and at 12 o'clock is BRAHMS.. The PHENIX (2000~2016), PHOBOS (2000~2005) and BRAHMS (2000~2006) experiments have decommissioned after finishing their physics researches, while the STAR detector is still operating and is expected to shutdown after data taking in 2025 together with RHIC. A new detector, called sPHENIX, has been constructed at the old PHENIX hall, and started to take data in 2023.

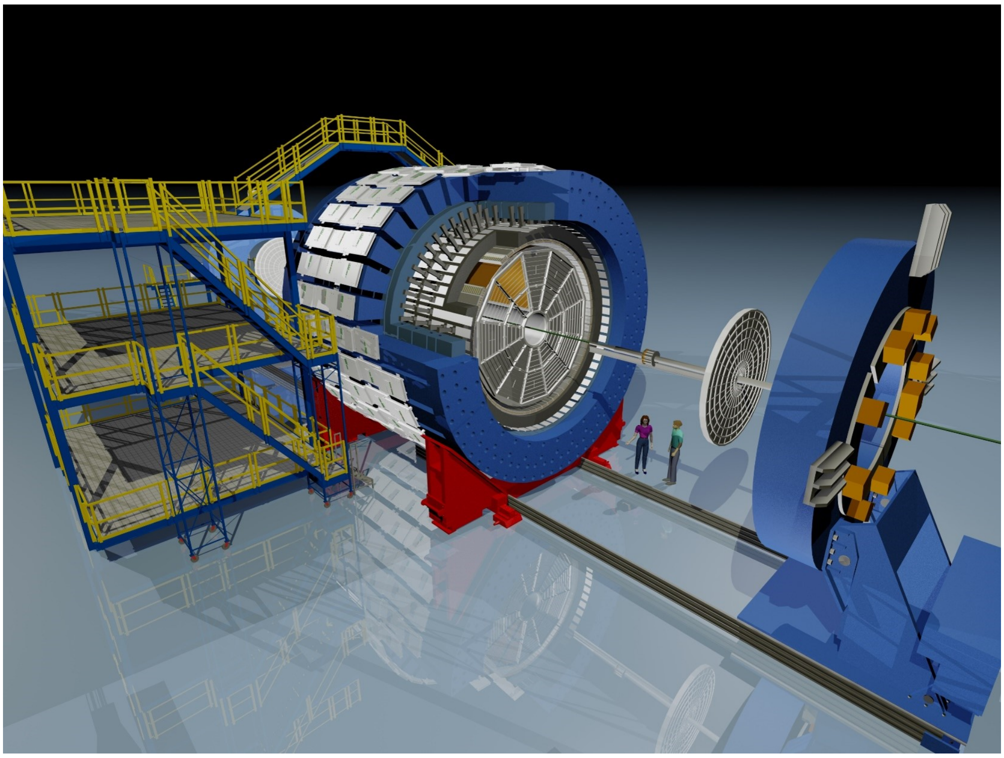

Figure 2.2 The illustrated depiction of the STAR detector.

The STAR experiment, short for the Solenoidal Tracker at RHIC, was designed for studying the properties of the QGP in the high multiplicity environment of heavy-ion collisions, as shown in the Fig. 2.2. The STAR detector has full azimuthal coverage at mid-rapidity, which makes STAR well suited for event-by-event characterization. The direction of the magnetic field, generated by a solenoidal magnet, is along the beam pipe with the maximum magnitude being $|B| = 0.5$ T. All sub-detectors in the barrel region, with the exception of the Muon Telescope Detector (MTD), are encompassed within the magnetic field. STAR can be operated in full field, reverse full field, half field and zero field configurations.

The main tracking system at STAR is the large cylindrical Time Projection Chamber (TPC)[129], which is 4.2 meters long along the beam axis (serves as the z axis). Located at radial distances of 50 and 200 cm, respectively, away from the beam line, are the inner and outer field cages of the TPC. The center of the TPC is also the original point of the lab coordinates, and the x direction points towards to the south and the y

direction is away from the ground. The TPC provides pseudo-rapidity (η) range from -1.8 to 1.8 and full azimuthal angle range (ϕ). Beside tracking, the TPC can also enables particle identification based on measurements of ionization energy loss (dE/dx). Outside the TPC is the Time-of-Flight (TOF) detector which has same azimuthal coverage as the TPC but smaller η coverage from -0.9 to 0.9. Particularly, TOF can separate slow hadrons from fast electrons by measuring particles' arrival time at TOF. The Barrel ElectroMagnetic Calorimeter (BEMC)[130], outsider of TOF with a acceptance of $0 < \phi < 2\pi$ and $|\eta| < 1$, is used to trigger on and measure the deposited energy and position information of the high transverse momentum (p_T) electrons and photons. The energy and position information can be used to improve the electron purity at high p_T. What's more, for the vertex reconstruction in high luminosity $p+p$ collisions, the BEMC and Endcap Electromagnetic Calorimeters (EEMC) together with TOF, are used to mitigate pile-up effects since they are all fast detectors, and thus resilient to pile-up. The MTD[131], located at the outermost of STAR and covering about 45% in azimuth from -0.5 to 0.5 in η, is used to trigger on di-muon event and distinguish muons from hadrons based on time and position measurements. The magnet in front of the MTD serves as a hadron absorber as most of the hadrons are stopped by the coils and steel while muons can pass through.

In the forward and backward region, there are three fast trigger detectors which are located on both west and east side of the TPC, the Beam Beam Counter[132], the Vertex Position Detector (VPD)[133], and the Zero Degree Calorimeter (ZDC)[134]. The BBC, shown in Fig. 2.3 and located at 3.75 meters from the center of the TPC, consists of two sets of scintillator annuli installed around the beam pipe on the pole tips of the magnet. The each side of the BBC has two annuli, the inner hexagonal tile annulus covering $|\eta|$ range from 3.3 to 5.0 and the outer annulus that overlaps slightly with the inner one. There are two rings of scintillator tiles in both inner and outer annuli. The inner ring comprises six tiles, whereas the outer ring consists of twelve tiles. The BBC based minimum-bias trigger, using only the inner annuli, requires a coincidence signal in east and west sides and corresponds to a $p + p$ cross section of about 26 mb[132].

The VPD shown in the Fig. 2.4 is another trigger detector used at STAR. Additionally, it furnishes position information regarding the collision vertex along the beam line and the "start time" of the collision for other timing sub-detectors, such as the TOF and MTD. The VPD is made of two identical assemblies, with 19 channels in each assembly in order to provide good trigger efficiency for $p + p$ and Au+Au collisions at lower energies with low multiplicities of very forward particle production. The location of the

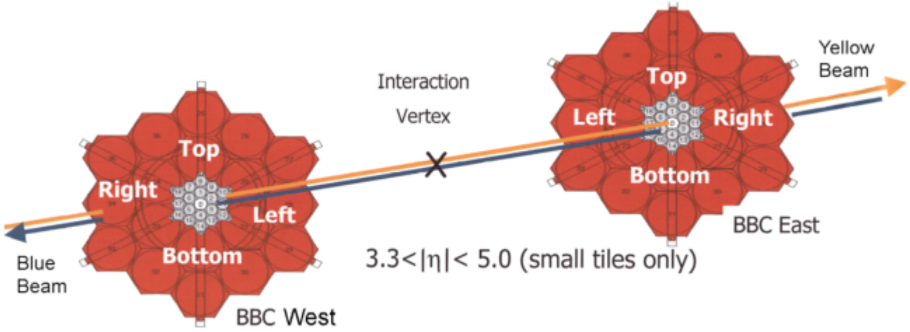

Figure 2.3 The arrangement of innner and outer tile annuli in the BBC.

VPD is a distance of 5.7 meters away from the center of the STAR along the beam line, and the η coverage is from 4.24 to 5.1.

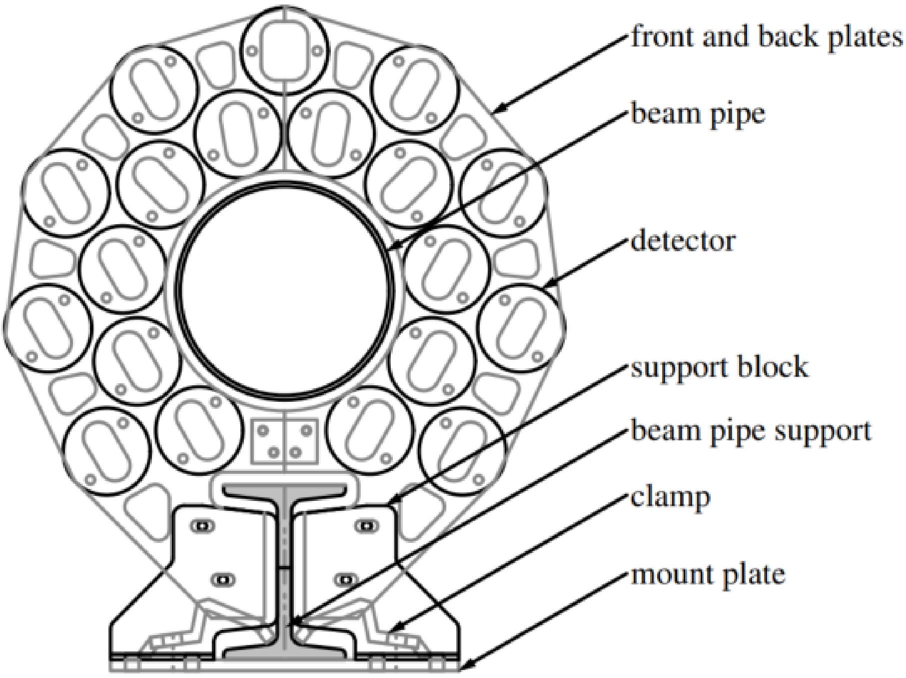

Figure 2.4 The schematic front view of a VPD assembly

As shown in the Fig. 2.5, the two assemblies of the ZDC, designed to detect emitted neutrons from colliding beam, are located 18 meters away from the center of STAR. The coincidence of the signals from the two ZDC assemblies could be used to select hadronic heavy-ion collisions, which makes ZDC a trigger detector and a luminosity monitor. Also, the neutron emission is correlated with the impact parameter of the collision, so the information from the ZDC could be used to estimate the collision centrality.

The STAR experiment proposed a second phase of the BES (BES-II) at RHIC, aiming to search for the critical point and first-order phase transition with much better precision and more focused energy regions based on the results from BES-I. To

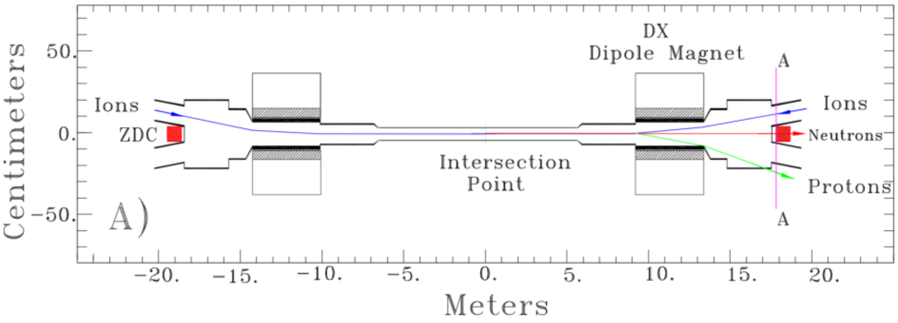

Figure 2.5 The top view of the ZDC location along the beam line.

facilitate achieving these physics goals, STAR installed three upgrades to improve the detector acceptance and particle identification abilities, including the inner TPC upgrade (iTPC)[135], the Event Plane Detector (EPD)[136], and the end-cap Time-of-Flight (eTOF)[137]. The data-taking of BES-II has been completed during 2019 - 2021.

After the BES-II program, STAR proposed upgrades in the forward region as shown in the Fig. 2.6, including a Forward Tracking System (FTS) that consists of three layers of Silicon mini-strip detectors (FST) and four small-Strip Thin-Gap Chamber (sTGC) as well as a Forward Calorimeter System (FCS) that is made up of a sampling electromagnetic calorimeter (ECal) and a hadronic calorimeter (HCal) of sandwiched iron and scintillator plates. Both FTS and FCS share the same η range from 2.5 to 4, and are located on the west side of the TPC. The three silicon disks reside at 152, 165 and 179 cm from the center of the TPC, and each disk has 12 wedges covering the full 2π range in azimuth and 2.5 to 4 in pseudo-rapidity. The four sTGC disks are 307, 325 , 343 and 361 cm away from the TPC center, and each disk consists of four pentagon modules. The spatial resolution of the sTGC is better than 200 μm and the working gas is a mixture of n-pentane (45%) and CO_2 (55%). The FCS is located 7 m away from the center of the TPC, and there are a total of 1496 channels for ECal and 520 channels for HCal. The FTS can measure charged particles of $0.2 < p_T < 2$ GeV/c with a momentum resolution of 20-30% in Au+Au collisions. The designed energy resolution for ECal and HCal are $10\%{\sim}20\%/\sqrt{E}$ and $\sim 60\%/\sqrt{E}$, respectively. The forward upgrades will enable STAR to study the internal structures of proton and nucleus at high and low x regions. Furthermore, these upgrades will allow the investigations of the initial stages of Au+Au collisions, the measurements of flow harmonics and their correlations at forward rapidity and longitudinal de-correlation. They can also extend the $W_{\gamma Au}$ range of measurement in Ultra-Peripheral Collisions (UPC).

For the results presented in this thesis, the TPC, TOF and BEMC are the most rele-

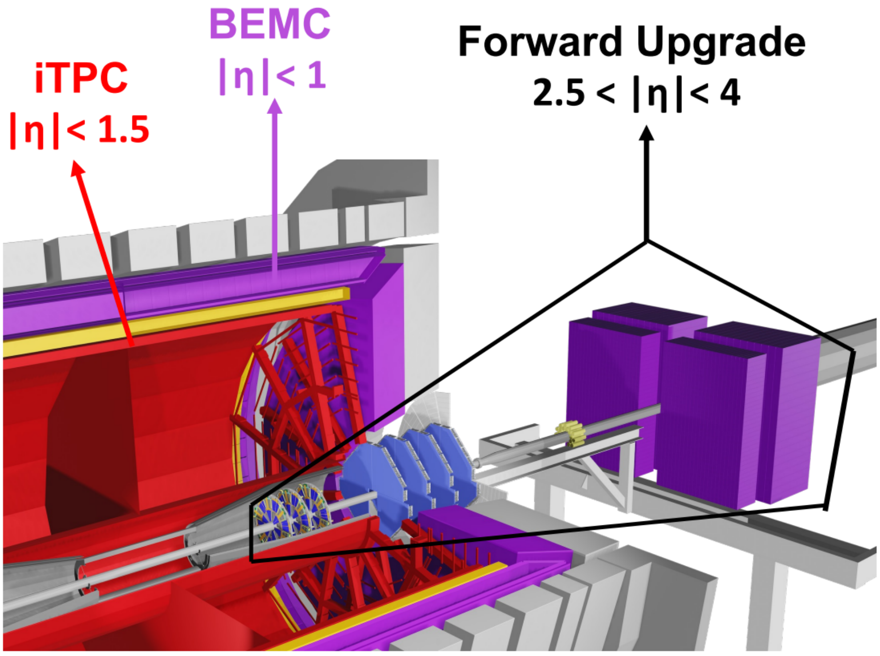

Figure 2.6 An overview of the STAR forward upgrades.

vant sub-detectors, therefore we will introduce them in details in the following sections.

2.2.1 Time Projection Chamber

The TPC serving as the primary tracking device at STAR, has the ability to measure the event multiplicity even for most central Au+Au collisions at top RHIC energy. The TPC measures 4 m in diameter by 4.2 m long. Charged particles with momenta from 0.1 to 30 GeV/c can be reconstructed, while the particle identification can be carried out by the TPC up to 1 GeV/c.

The STAR TPC is shown schematically in Fig. 2.7. A large solenoidal magnet that operates at 0.5 T surrounds the TPC, and inside the TPC is a volume of the P10 gas (90%Ar+10%CH_4) in a well defined, uniform, electric field ($\approx$ 135 V/cm). When charged particles from nuclear collisions pass trough the gas volume, released secondary electrons from the pathlengths of the charged particles will drift to the readout end-caps at both ends of the chamber due to the existence of the electric field, and then the paths of the primary ionizing particles can be reconstructed with high precision based on these secondary electrons. The position precision of the reconstructed tracks can achieve sub-millimeter level and the secondary electrons can drift up to 2.1 meters in the TPC, so the uniformity of the electric field is of paramount importance. The electric field within the TPC is determined by several components: a thin conductive Central Membrane (CM) located with -28kV, concentric field-cage cylinders, and the readout end-caps at ground

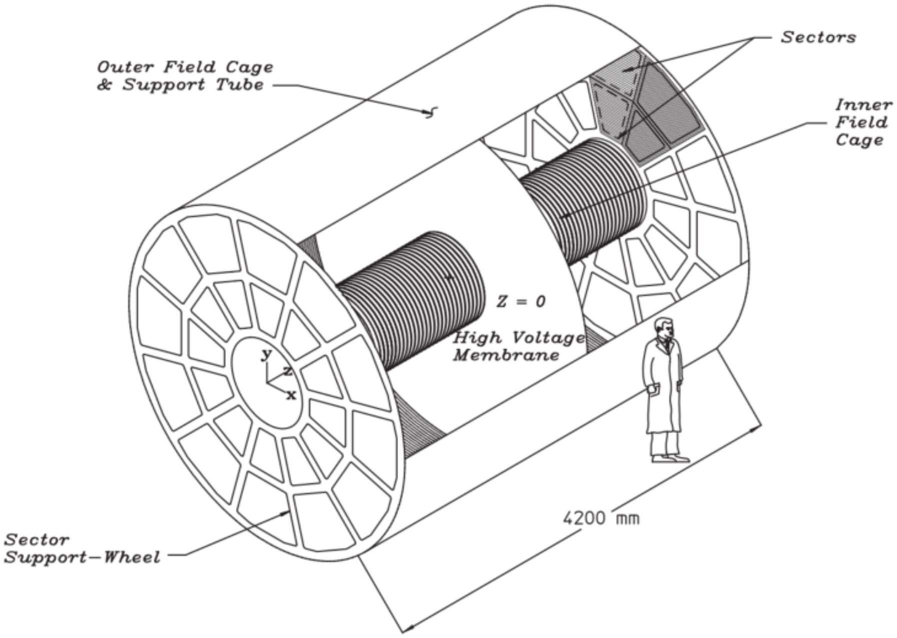

Figure 2.7 An overview of the STAR TPC.

potential. The transverse and longitudinal diffusions are about σ_T = 3.3 mm (230 μm per $\sqrt{\text{cm}}$) and σ_L = 5.2 mm (360 μm per $\sqrt{\text{cm}}$) after drift paths up to 2.1 meters.

The STAR TPC's readout system employs Multi-Wire Proportional Chambers (MWPC) featuring readout pads.The MWPC comprises a pad plane along with three wire planes including a gating grid, a ground plane, and anode wires, which are illustrated in Fig. 2.8. In the high fields surrounding the 20 μm anode wires, the drifting electrons undergo an avalanche, leading to an amplification of 1000 to 3000. A temporary image charge is created by the positive ions generated from the avalanche, which will disappear when the ions move away from the anode wire. The end-cap readout planes consist of the MWPC chambers with readout pads, and the planes are mounted on aluminum support wheels with 12 sectors around the circle. Figure. 2.9 illustrates how each sector is divided into an outer and inner sub-sector. The total number of pads in the readout system is 136608. There is a continuous pad coverage to optimize the energy loss measurement and tracking resolution in the outer sub-sector, while the inner sub-sector, subject to the maximum track density, is adjusted to ensure enough two-hit resolution.

For the track reconstruction, first, the clusters are found separately in the x-y plane (r-ϕ plane) and in the z direction. The recorded charges in a single pad row with adjacent pads are used to determine the x and y coordinates of a cluster. The z position is calculated by considering the measured drift time from the ionization point to the anodes and the average drift velocity of the released secondary electrons, which is ap-

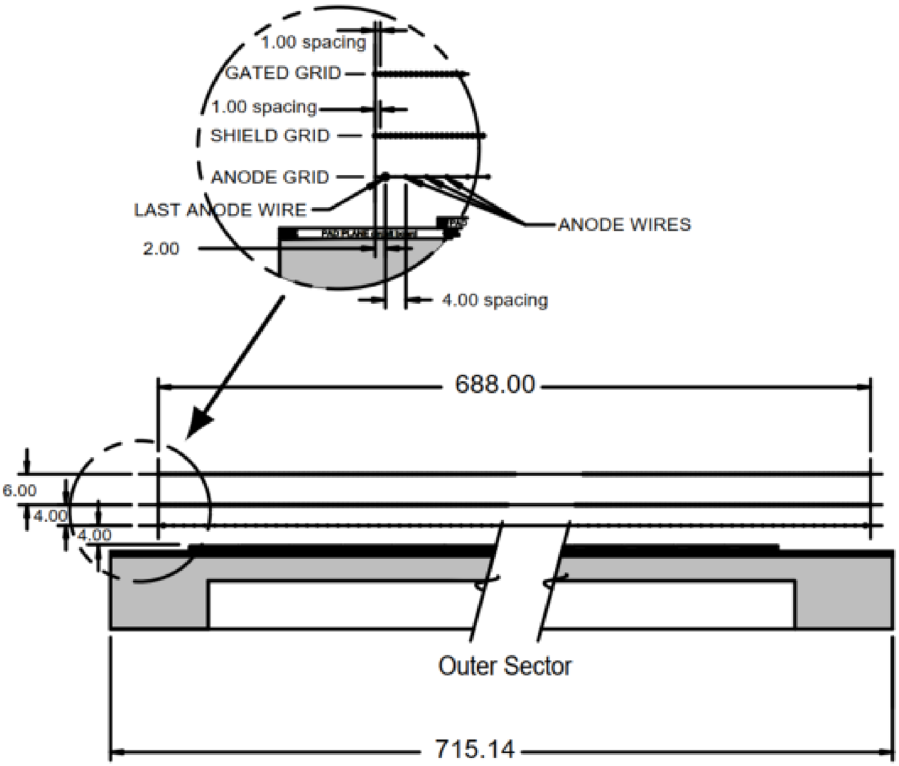

Figure 2.8 A cutaway of an outer sub-sector pad plane.

proximately ~5.45 cm/μs. Then, individual clusters (hits) found in the TPC are used to reconstruct the charged particle tracks with a Kalman filter routine. These tracks are called global tracks. In order to improve the momentum resolution, the global track, with a Distance of Closest Approach (DCA) to the primary vertex less than 3 cm, is refit including the primary vertex position during the reconstruction, and the resulting track is called a primary track. The detailed procedure for primary vertex reconstruction can be found in Section 3.2. The primary track's momentum resolution, $\sigma(p_{\mathrm{T}})/p_{\mathrm{T}}$, could reach 1% + 0.5%×p_{T} in $p+p$ collisions.

Besides the track reconstruction, the TPC could also be used to identify particle species through the energy loss (dE/dx) measurement. The Bichsel function is usually used to describe mean dE/dx of a certain particle species, and different particle species at the same momentum may exhibit varying values of dE/dx. The resolution of the dE/dx measurement in nuclear collisions is about 8%, which enables π/K identification up to about 0.7 GeV/c while (π,K)/p separation can reach about 1.1 GeV/c, as shown in Fig. 2.10.

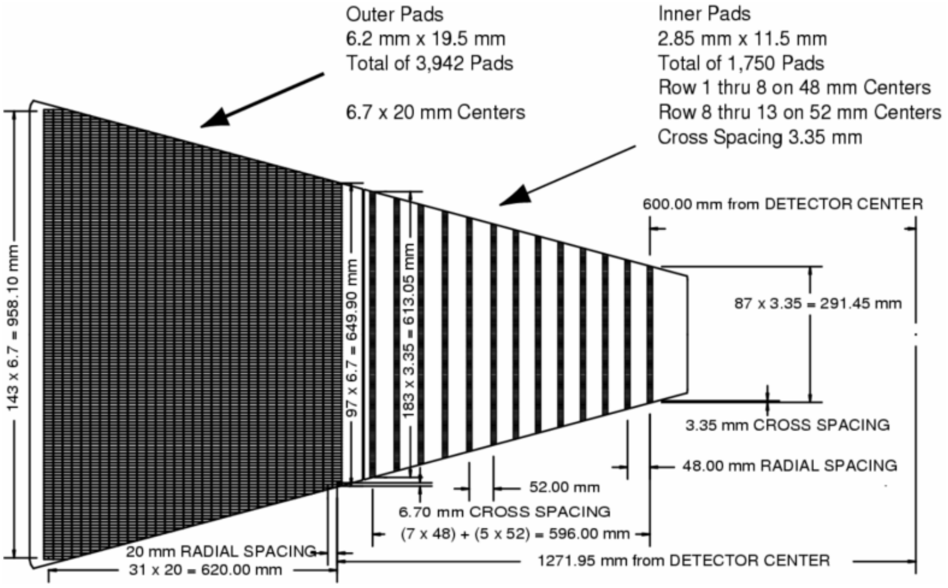

Figure 2.9 One full sector of the anode pad plane is depicted.

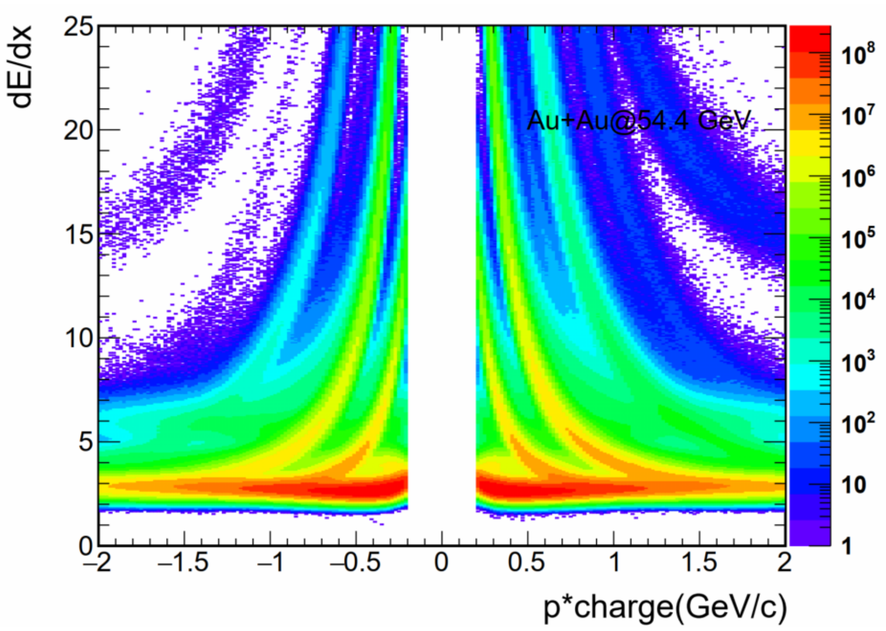

Figure 2.10 TPC dE/dx versus momentum in 54.4 GeV Au+Au collisions.

2.2.2 The Time Of Flight Detector

The barrel Time-of-Flight (TOF) detector which employs the Multi-gap Resistive Plate Chamber (MRPC) technology[138], was fully installed at STAR in 2010, with the design goal of extending STAR's particle identification capability to higher p_T by measuring the arrival time of charged particles. TOF consists of 120 trays with 60 trays on each side with respect to $\eta = 0$. Each tray has 32 modules of the MRPC, which is shown in Fig. 2.11, and each module has 6 single-end readout pads (called "cell").

The TOF system also includes the VPD, in addition to the barrel TOF. As mentioned in the previous section, the VPD provides the “start” time (t_0) of the collision. “stop” time (t_1) is measured by the barrel TOF. The VPD achieves a measured time resolution of approximately 30 ps, while the barrel TOF achieves a time resolution of less than 80 ps, in heavy-ion collisions. After obtaining the time of flight from TOF and path length information from TPC, the inverse velocity of charged particles ($1/\beta$) can be calcualated as:

$$\frac{1}{\beta} = c\frac{\Delta t}{L} = \frac{\sqrt{p^2 + m^2c^2}}{p}, \tag{2.1}$$

where the $\Delta t = t_1 - t_0$.

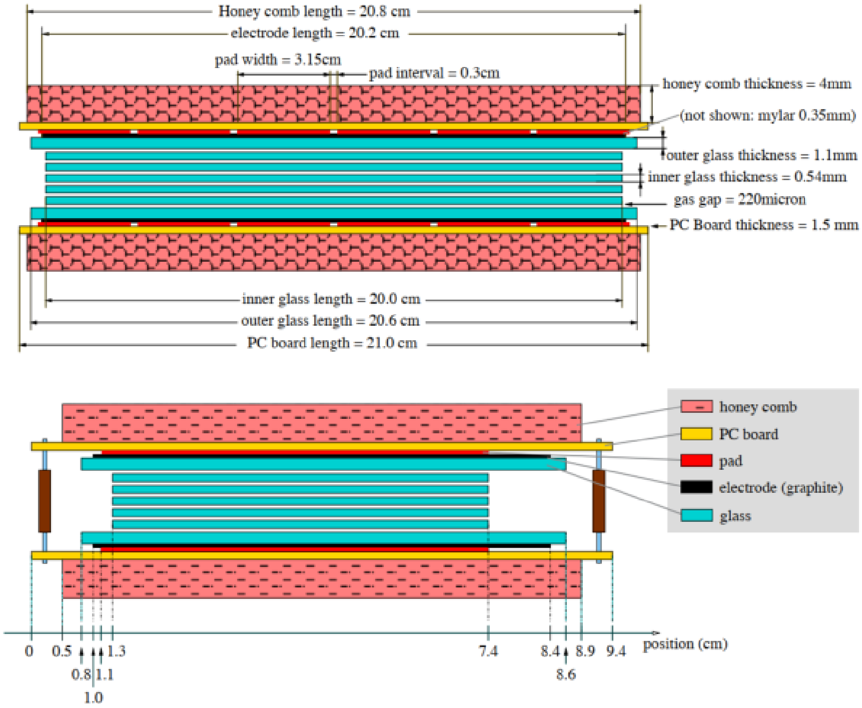

Figure 2.11 The configuration of a single MRPC module, depicted in both long (upper) and short (lower) side views.

In Fig. 2.12, charged particles’ $1/\beta$ distribution, as measured by the TOF system in Au+Au collisions at $\sqrt{s_{\rm NN}}$ = 54.4 GeV/c, is shown. As one can see, the momentum range of π and K is extended from 0.7 to 1.6 GeV/c, and from 1.1 GeV/c to 3 GeV/c for proton identification. For electron identification, TOF is crucial for rejecting hadrons at low momentum range , where the dE/dx band for electrons crosses with hadrons, while for high momentum electron identification, the BEMC is more efficient than the TOF, which will be introduced in the next section.

2.2.3 The Barrel Electromagnetic Calorimeter

In this section, the details concerning the design, fabrication and performance of the STAR BEMC is described. The BEMC is designed to trigger on and study rare,

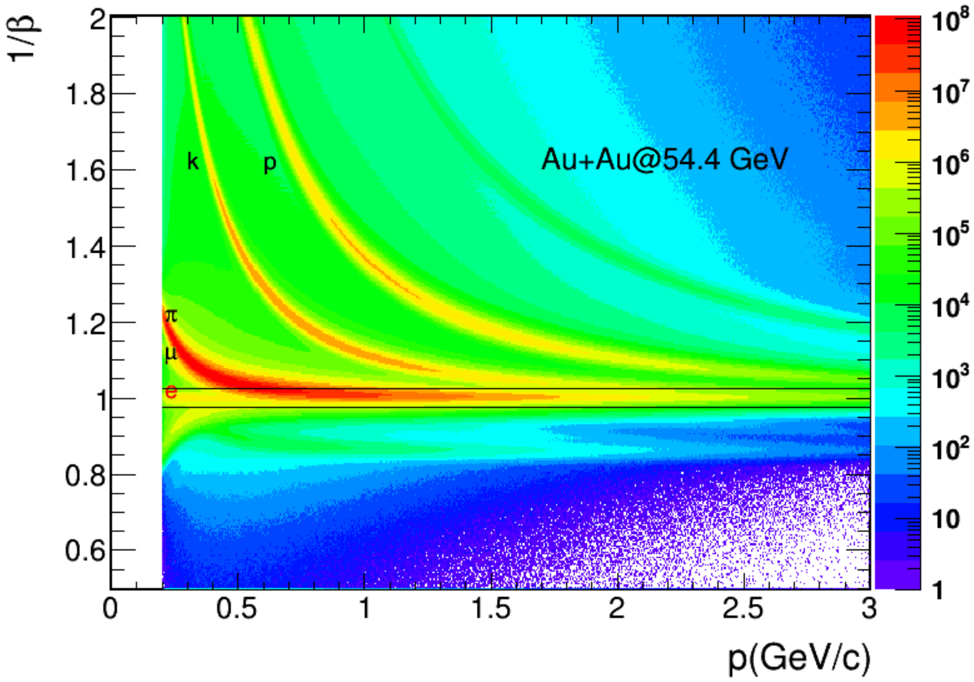

Figure 2.12 The momentum dependence of $1/\beta$ distribution in 54.4 GeV Au+Au collisions.

high p_T object, including jets, heavy quarks, and so on in p+p and heavy-ion collisions including UPCs. A sampling calorimeter using lead and plastic scintillator was selected in order to achieve these physics goals, including adequately containing 60 GeV electromagnetic showers, and to satisfy all the mechanical constraints of the STAR experiment. The BEMC has a total depth of about 20 radiation lengths at $\eta = 0$. All of the scintillation light is transported to outside of the magnet steel in order to have enough space to accommodate the photomultiplier tubes (PMT), bases, high-voltage system and front-end electronics. This design reduces the PMT system cost and complexity since the PMT is operated in a near zero magnetic field environment. For the high-resolution measurement of electromagnetic showers, a shower maximum detector (two layers of gaseous wire pad chambers) is inserted inside the BEMC lead/scintillator stack. Finally, an independent preshower readout is installed for each BEMC tower. It can measure the longitudinal shower development after only 1 to $1.5X_0$, which significantly improves the separation power between π^0 and γ and between electrons and hadrons. For example, the electron will exhibit a substantially higher ionization dE/dx than hadrons even before the ionization of electromagnetic showers. On the top of this, about 63% of electrons shower before reaching preshower and about 84% around the middle of the preshower detector, which is much higher than the corresponding interaction probabilities for hadrons (3% and 6%, respectively).

Installed within the aluminum coil of the STAR solenoid, the BEMC covers $|\eta| \leq$

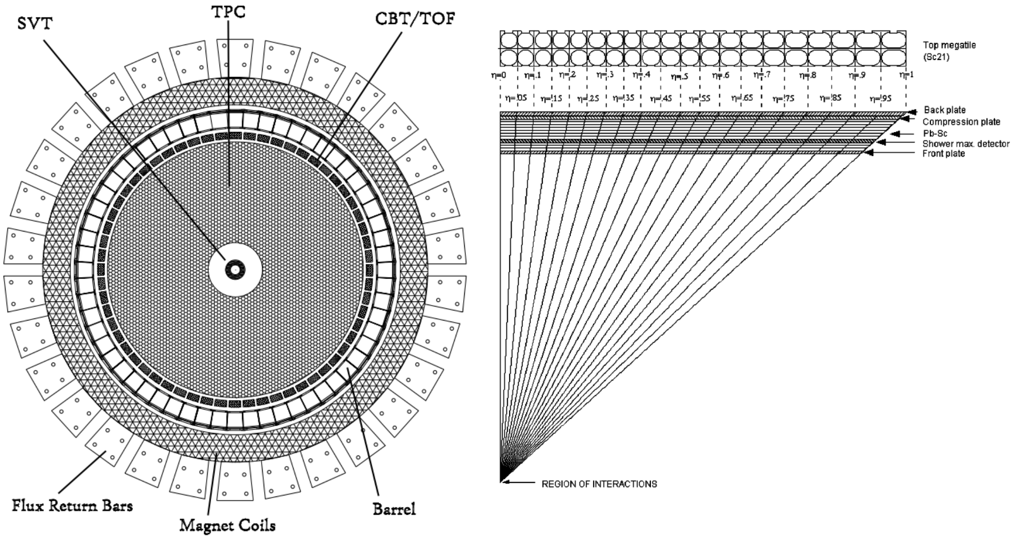

Figure 2.13 ***Left panel*: Cross-sectional view of the STAR detector showing the location of the BEMC, which is labelled as "Barrel". *Right panel*: The projective nature of the towers are displayed by a side view of a calorimeter module.**

1 and the full azimuthal angle, aligning with the TPC acceptance. The left panel of Fig. 2.13 shows the position of BEMC, labelled as "Barrel", inside the STAR detector schematically. The front face of the BEMC is about 220 cm away from the center radially. The BEMC comprises 120 calorimeter modules, each spanning 0.1 rad in $\Delta\phi$ and 1.0 unit in $\Delta\eta$. They are arranged in a grid of 60 in ϕ and 2 in η. Each module measures approximately 26 cm wide and 293 cm long, with an active depth of 23.5 cm, in addition to 6.6 cm of structural plates (of which approximately 1.9 cm is situated in front of the detector). A module is divide into 40 towers with 2 in ϕ and 20 along the beam direction, and each tower occupies approximately 0.05 in $\Delta\phi$ and 0.05 in $\Delta\eta$. Thus, the full BEMC is physically constiuted by 4800 towers, each pointing back to the center of the STAR detector, as shown in the right panel of Fig. 2.13.

The mounting system and the compression components of a tower is shown in Fig. 2.14. There are 21 active scintillating layers, with 19 of them being 5 mm thick, and 2 associated with the preshower detector are 6 mm thick. All the scintillator layers alternate with 20 layers of thick lead absorber plates. The energy resolution of the BEMC is $\approx 1.5\% \oplus 14\%/\sqrt{E}$ GeV. Electrons deposit close to 95% of their energies through electromagnetic showers while hadrons deposit a much smaller fraction. Such a difference can be utilized to identify electrons from hadrons.

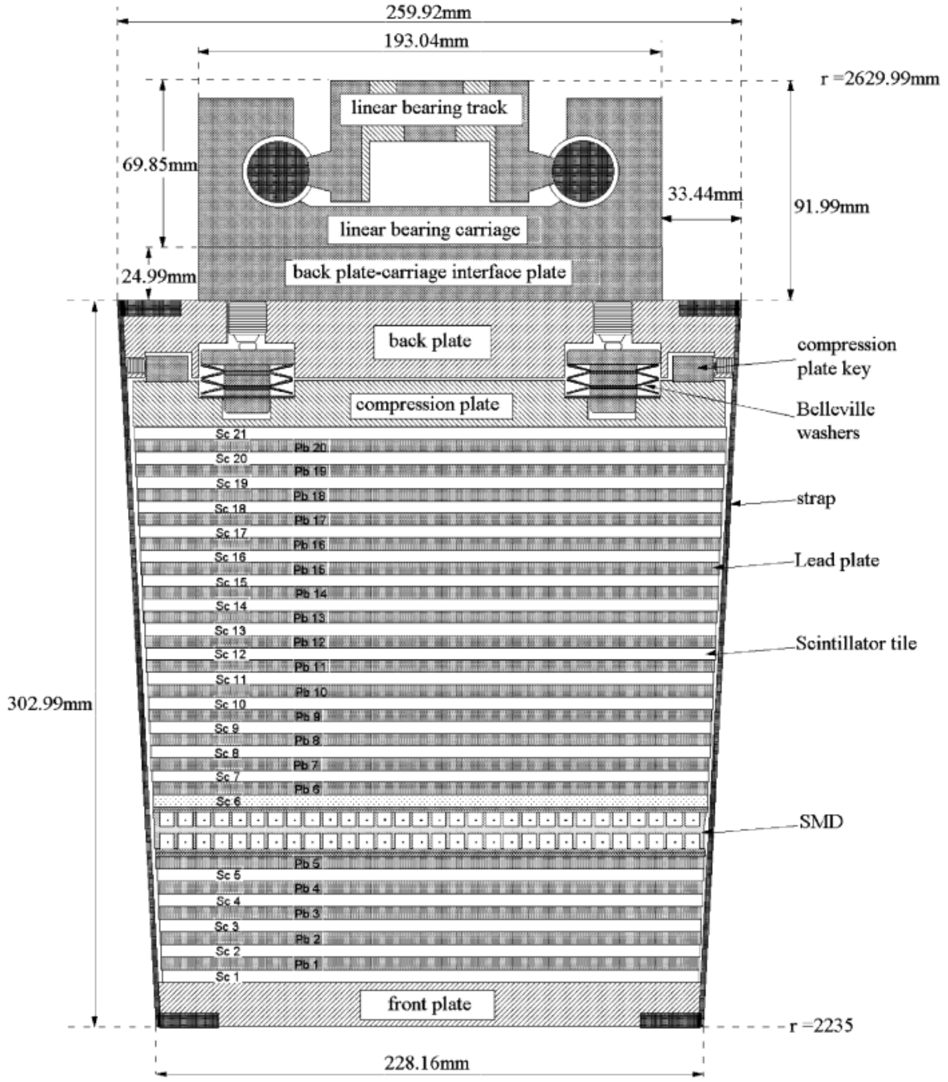

Figure 2.14 The mechanical assembly of a BEMC module is displayed, including the compression components and the rail mounting system.

Chapter 3 Measurements e^+e^- pair and J/ψ meson production in $^{96}_{44}$Ru+$^{96}_{44}$Ru and $^{96}_{40}$Zr+$^{96}_{40}$Zr collisions at $\sqrt{s_{\rm NN}}$= 200 GeV

Understanding the formation and properties of the novel QCD matter, the quark-gluon plasma (QGP), is a main science goal for RHIC[15,24-26]. Dileptons, pairs of oppositely charged leptons, can be produced during the entire evolution of the QGP and don't take part in the strong interactions. Therefore, they are considered one of the ideal probes to study the QGP. Measurements of dilepton invariant mass spectra have been carried out at the Super Proton Synchrotron (SPS)[139-144] and RHIC[145-148], which show a signficant enhancement with respect to known hadronic sources in the mass region below ~0.7 GeV/c^2. This excess can be explained by the in-medium broadening of the ρ meson spectral function[149-151]. In addition to dileptions, the J/ψ meson ($c\bar{c}$) suppression in heavy-ion collisions due to the color screening effect inside the hot and dense medium was proposed as a "smoking gun" for the QGP formation[84]. The J/ψ suppression has been measured in different collision systems and energies over the past 20 years, and these measurements indicate that the observed J/ψ suppression is an interplay of different effects, not only the color screening effect, but also dynamical dissociation, the regeneration effect[152] and Cold Nuclear Matter (CNM) effect[153].

Strong electromagnetic fields, generated by highly-charged nuclei traveling at relativistic speed in high-energy heavy-ion collisions, can be approximated as a large flux of high-energy quasi-real photons[65,154]. Dileptons and vector mesons, for example the e^+e^- pair and J/ψ meson, can also be produced through interactions involving these photons, such as the photon-photon process ($\gamma + \gamma \rightarrow e^+ + e^-$) and photon-nucleus process via Pomeron exchange ($\gamma + A \rightarrow J/\psi + A$) respectively. Among these photons interactions, the coherent interaction will lead to a distinctive configuration that the final products consist of two intact nuclei and only an e^+e^- pair or a J/ψ meson with very low $p_{\rm T}$ (usually $p_{\rm T}$ < 0.1 GeV/c) and nothing else. The characteristics of very low $p_{\rm T}$ products can be used to select coherent photon-photon and photon-nucleus production experimentally. Conventionally, these interactions are only studied in UPCs where there are no hadronic interactions. So, could the coherent photon-photon or photon-nucleus processes also occur in collisions where the colliding nuclei break up? The answer is yes. Significant excesses of J/ψ and e^+e^- pair production in peripheral high-energy heavy-ion collisions at very low p_{T} have been observed by the ALICE[113] and STAR[155-156] collaborations. These excesses can not be explained by any medium effects on the hadronic production, while model calculations based on photon-induced interactions could describe the observed excesses quite nicely.[116,120-121,157-160].

What can we do to further our understanding of photo-induced processes in peripheral high-energy heavy-ion collisions? In 2018, STAR recorded high-quality, large-statistics datasets of $^{96}_{44}$Ru+$^{96}_{44}$Ru and $^{96}_{40}$Zr+$^{96}_{40}$Zr collisions. The colliding nuclei share the same atomic number (A) of 96, but differ in the charge number (Z) by 10%. Since the flux of quasi-real photons is expected to be proportional to Z^2 of the colliding nuclei, the cross section of $\gamma + \gamma \rightarrow e^+ + e^-$ process is proportional to Z^4 while $\gamma + A \rightarrow J/\psi + A$ cross section is proportional to Z^2. Consequently, the isobaric Ru+Ru and Zr+Zr collisions provide a unique opportunity to study the electromagnetic field dependence of photon-induced production. Furthermore, comparing these results to those from $^{197}_{79}$Au+$^{197}_{79}$Au and $^{238}_{92}$U+$^{238}_{92}$U collisions allows for further studies of electromagnetic filed dependence as well as an additional exploration of nucleus structure dependence. It is worth mentioning that the isobar dataset primarily aims at searching for signals related to the Chiral Magnetic Effect (CME), since the effect from large background in hadronic heavy ion collisions could be significantly reduced[161]. By measuring photo-induced processes, we could test the difference of the initial electromagnetic field between Ru+Ru and Zr+Zr collisions, which provides important input to CME search efforts in these collisions.

3.1 Data Set and Event Selection

In this analysis, the data set was collected in 2018 for 200 GeV Ru+Ru and Zr+Zr collisions by the STAR experiment. The minimum-bias (MB) trigger was employed for data taking, which is defined as a coincidence between the two VPDs. The trigger IDs used in this analysis are 600001, 600011, 600021 and 600031, which are summarized in Table 3.1 together with offline production tag, production library as well as the number of triggered events. The total number of MB events recorded is around 6.27 billion, and about 5.16 billion events were reconstructed for further analysis.

data set	trigger id	production tag	library	number of event
production_isobar_2018	600001	P20ic	SL20c	39.58 M
	600011			476.2 M
	600021			105.87 B
	600031			5.61 B

Table 3.1 Summary of trigger ids, offline production libraries and recorded number of minimum-bias events.

3.2 Vertex Selection and Track Quality Cuts

Dielectron pair and J/ψ meson production from photon-photon and photon-nucleus interactions, the main interest of this work, are originated from the interaction point, also referred to as the event vertex or event primary vertex, since those photon-induced processes occur instantaneously when the two colliding nuclei move close to each other. Thus, primary tracks produced at the primary vertex are used in this analysis.

Efficient and precise event vertex finding plays a vital role for almost all the analyses carried out at STAR, including the ones presented in this work. Due to much longer readout time of the TPC compared to the time span between consecutive collision events, the recorded event which is initiated by a collision that fires the trigger, is likely to contain tracks from other beam crossings or additional collisions in the same beam crossing when the instantaneous luminosity is high. This is usually referred to as the pile-up effects, which can interfere with finding the correct collision vertex using reconstructed tracks. Such effects can be mitigated by using tracks matched to fast detectors, such as the TOF detector, BEMC and EEMC, when reconstructing the event vertex. There are two main vertex-finding algorithms used by the STAR experiment: the Minuit based vertex finder (**MinuitVF**) and the Pile-Up Proof Vertexer (**PPV**)[162]. The **MinuitVF** is primarily utilized for heavy-ion collisions characterized by high track multiplicity and low pile-up effects, while the **PPV** is commonly used in low multiplicity p+p events with a high pile-up rate. The **MinuitVF** method find the three-dimensional location of the vertex where the Distance of Closest Approach (DCA) for all associated tracks is at the minimum, while the **PPV** uses a one-dimensional truncated log-likelihood method to determine the most probable z location of the vertex and the x and y positions are determined from beam line[163]. For both **MinuitVF** and **PPV**, the vertex seeding procedure is based on finding clusters of tracks along the z-axis. The main difference between two methods is that there is additional re-weighting used in **PPV**, such as the uncertainty of the track's projection at the point of closest approach to the beam line and the extrapolation of the track to either an EMC or TOF cell with a signal above a certain threshold. The primary vertex used in this analysis is reconstructed with the **MinuitVF** method using the global tracks, and primary tracks are found by combining primary vertex with global tracks in the fitting to improve the momentum resolution.

The z position of the primary vertex determined with the MinuitVF method is denoted as V_z(TPC). In this analysis, to ensure good TPC acceptance, the vertex position should fall within -35 cm to 25 cm relative to the TPC center along the z direction. The V_z(TPC) distributions in isobaric Ru+Ru collisions at $\sqrt{s_{\rm NN}}$= 200 GeV are displayed in Fig. 3.1. The black solid line stands for the distribution of V_z(TPC) for MB-triggered events before vertex selection cuts while the red dash lines are the vertex selection cuts. The difference between V_z(TPC) and V_z(VPD) should be within 3 cm to reject the event with wrong reconstructed TPC or VPD vertex due to pile-up effects. The left panel of Fig. 3.2 shows the two-dimensional distribution of V_z(TPC) versus V_z(VPD), while the right panel of Fig. 3.2 is the distribution of the distance between V_z(TPC) and V_z(VPD). The horizontal and vertical bands in the right panel of Fig. 3.2 are events with wrongly-reconstructed vertices, which need to removed from further analysis. Furthermore, to reject events originating from the beam striking the beam pipe, the radial distance (V_r) of the primary vertex is required to be less than 2 cm with respect to the beam pipe center. As shown in Fig. 3.3, the survived events are concentrated around (0,0). The vertex selection cuts are summaried in Table 3.2 and the total number of events used in this analysis after vertex selection is around 1.8 billion for each collision system.

Event selection criteria
-35 cm < V_z(TPC) < 25 cm
$\lvert V_z(\mathrm{TPC}) - V_z(\mathrm{VPD})\rvert$ < 3 cm
V_r(TPC) < 2 cm

Table 3.2 Summary of event selection cuts.

3.3 Centrality Definition

The centrality definition in nucleus nucleus collisions used by the STAR collaboration is based on the offline charged-track multiplicity ($N_{\rm tracks}^{\rm offline}$) measured by the TPC within $|\eta| < 0.5$. The reconstructed tracks used for centrality classification must have a DCA to the primary vertex less than 3 cm and at least 10 TPC hit points for reconstruction (nHitsFit $\geq$ 10). The TPC tracking efficiency affects the number of reconstructed tracks offline, and it is dictated by the TPC occupancy which is related to the instantaneous luminosity monitored by the ZDC coincidence rate. So, the $\langle N_{\rm tracks}^{\rm offline}\rangle$ is found to decrease linearly with increasing ZDC coincidence rate, and the parameterization of this dependence is used to correct $N_{\rm tracks}^{\rm offline}$ for luminosity effect. In addition, the $N_{\rm tracks}^{\rm offline}$

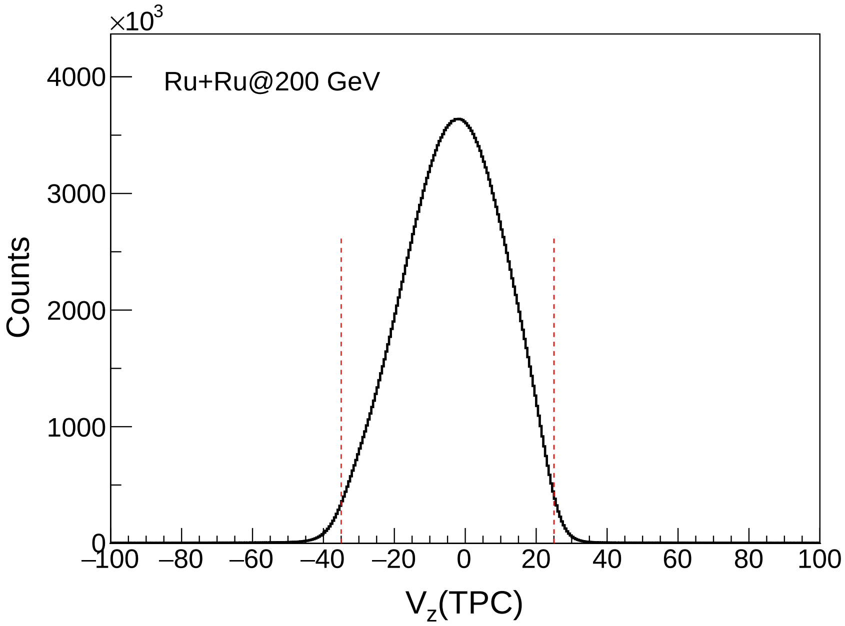

Figure 3.1 Distribution of V_z(TPC) for primary vertex, the vertex selection cuts are shown as the red dash lines.

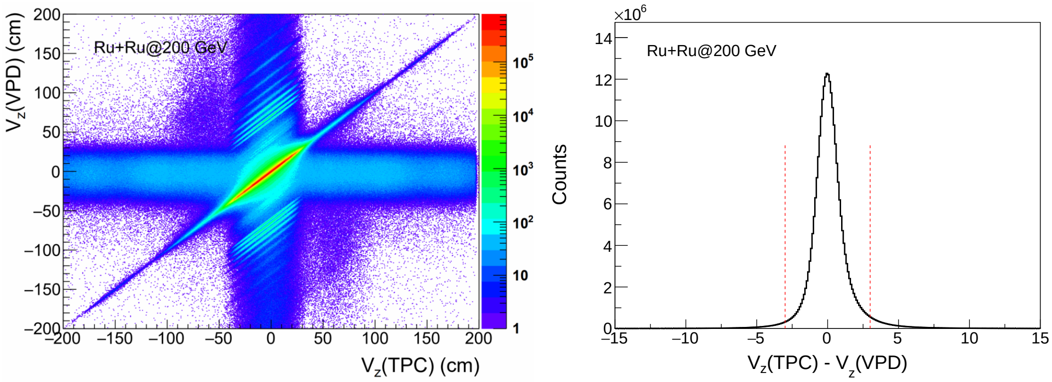

Figure 3.2 *Left panel*: Two-dimensional distribution of V_z(TPC) versus V_z(VPD) before applying vertex cuts. *Right panel*: Distance between V_z(TPC) and V_z(VPD) before applying vertex selection cuts.

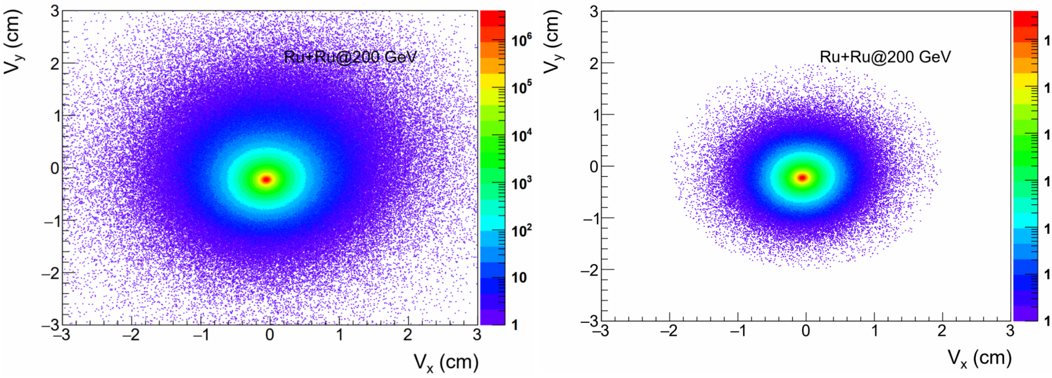

Figure 3.3 Two-dimensional distributions of V_x(TPC) versus V_y(TPC) before (*left panel*) and after (*right panel*) vertex cuts in MB-triggered isobar collisions at $\sqrt{s_{\rm NN}}$= 200 GeV.

is also affected by the TPC acceptance which is variational as a function of V_z(TPC). The correction factor is obtained by normalizing the $N^{\rm offline}_{\rm tracks}$ distribution, $P(N^{\rm offline}_{\rm tracks})$, in different V_z(TPC) bins with a step of 2 cm to a certain reference V_z(TPC) range. After the correction of luminosity and V_z(TPC) dependence, the $N^{\rm offline}_{\rm tracks}$ distributions at different ZDC coincidence rates and V_z(TPC) ranges become very similar. Then the corrected $N^{\rm offline}_{\rm tracks}$ distribution is fitted with the distribution P($N^{\rm MC}_{\rm tracks}$) from MC Glauber model simulations[29,164]. Usually, a discrepancy between $N^{\rm offline}_{\rm tracks}$ and $N^{\rm MC}_{\rm tracks}$ can be observed at low event multiplicity due to trigger inefficiency in peripheral collisions. This discrepancy can be corrected for by ratio of $N^{\rm MC}_{\rm tracks}$ / $N^{\rm offline}_{\rm tracks}$ as weights in analyzing data.

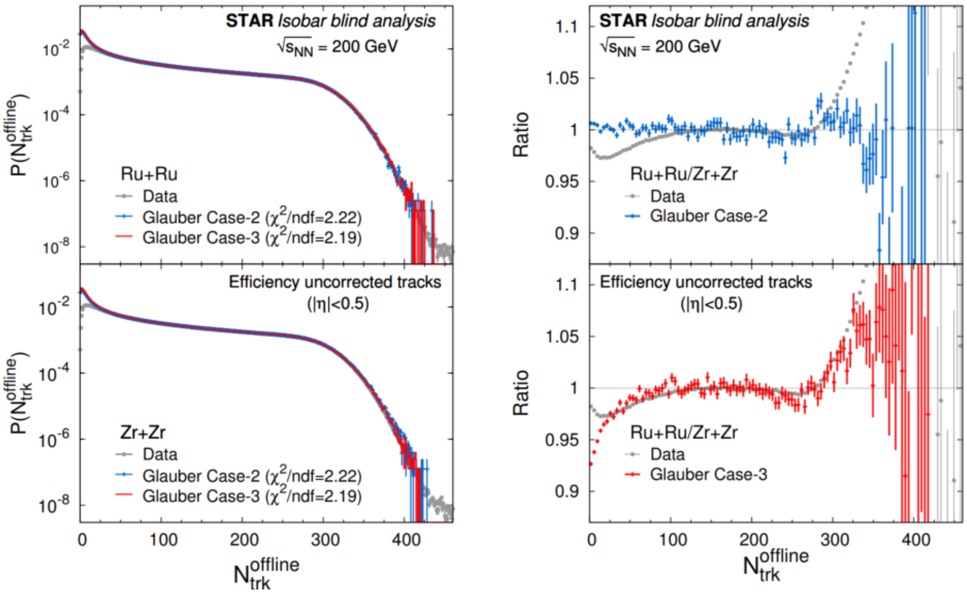

Figure 3.4 Distributions of the number of charged tracks ($N^{\rm offline}_{\rm tracks}$) from the TPC in Ru+Ru (upper left panel) and Zr+Zr (lower left panel) collisions. The luminosity and vertex position V_z(TPC) dependence have been corrected for Glauber model distributions using two sets of WS parameters , as listed in Table 3.3, are used to fit the experimental distributions. Ratios of the $N^{\rm offline}_{\rm tracks}$ distribution in Ru+Ru collisions over that in Zr+Zr collisions, using the experimental data and those from Glauber model fits, are shown in the upper right and lower right panels.

Distributions of charged-track multiplicity, $P(N^{\rm offline}_{\rm tracks})$, are shown in Fig. 3.4 for Ru+Ru and Zr+Zr collisions. In MC Glauber Model simulations[29,164], the nuclear thickness function and the inelastic nucleon-nucleon cross section ($\sigma^{inel}_{\rm NN}$ = 42 mb for $\sqrt{s}$ = 200 GeV[165]) are needed as inputs.

The nuclear thickness function is obtained by sampling nucleons in the colliding nuclei based on the nuclear density distribution described by the Woods-Saxon (WS) distribution. One challenge is that the nuclear density distributions of $^{96}_{44}$Ru and $^{96}_{40}$Zr nuclei are not measured accurately[166-168]. So, three sets of WS parameters are investigated in defining the centrality for isobaric collisions [166,169]. The WS distribution can be defined as:

$$\rho(r,\theta) = \frac{\rho_0}{1+\exp[\frac{r-R(1+\beta_2 Y_2^0)}{a}]}, \tag{3.1}$$

where R is the radius parameter, a is the diffuseness parameter, β_2 quatifies the quadruple deformation, $Y_2^0(\theta) = \frac{1}{4}\sqrt{\frac{5}{\pi}}(3cos^2\theta - 1)$, and ρ_0 is the normalization factor. The three tested sets of parameters for R, a, and β_2, are summarized in Table 3.3.

	Case-1			Case-2			Case-3		
Nucleus	R (fm)	a (fm)	β_2	R (fm)	a (fm)	β_2	R (fm)	a (fm)	β_2
$^{96}_{44}$Ru	5.085	0.46	0.158	5.085	0.46	0.053	5.067	0.500	0
$^{96}_{40}$Zr	5.02	0.46	0.08	5.02	0.46	0.217	4.965	0.556	0

Table 3.3 Woods-Saxon parameters used in MC Glauber model simulations for the centrality determination.

Since the Ru nucleus contains more protons than Zr nucleus, Ru has a larger charge radius, which is reflected in Case-1 and Case-2. The two cases differ in the deformation parameter β_2. The third set of parameters (Case-3) are obtained from recent calculations based on energy density functional theory (DFT)[169-170] and assume that both nuclei are spherical without any deformation. In the Case-3, distributions of protons and neutrons are calculated separately and the overall size of Ru is found to be smaller than Zr because of a significantly thicker neutron skin in the Zr nuclei. The first set of parameters (Case-1) is rejected since it yields the largest χ^2/ndf values. Although the Case-2 and Case-3 sets have similar χ^2/ndf values when fitting P($N_{\rm tracks}^{\rm offline}$) distributions in data with Glauber model., the Case-3 set is chosen for the centrality definition because the Case-3 could reproduce the ratio of the $N_{\rm tracks}^{\rm offline}$ distributions between the two collision systems at large multiplicity values (Fig. 3.4, right panel), despite there is room for future improvement. The centrality definition and the corresponding $\langle N_{\rm tracks}^{\rm offline}\rangle$, $\langle N_{\rm part}\rangle$ and $\langle N_{\rm coll}\rangle$ for 200 GeV Ru+Ru and Zr+Zr collisions are listed respectively in Table 3.4 and Table 3.5.

Centrality (%)	Ru+Ru				
	Centrality (%)	$N_{\rm tracks}^{\rm offline}$	$\langle N_{\rm tracks}^{\rm offline}\rangle$	$\langle N_{\rm part}\rangle$	$\langle N_{\rm coll}\rangle$
0-5	0-5.01	258.-500.	289.32	166.8±0.1	389±10
5-10	5.01-9.94	216.-258.	236.30	147.5±1.0	323±5
10-20	9.94-19.96	151.-216.	181.76	116.5±0.8	232±3
20-30	19.96-30.08	103.-151.	125.84	83.3±0.5	146±2
30-40	30.08-39.89	69.-103.	85.22	58.8±0.3	89.4±0.9
40-50	39.89-49.86	44.-69.	55.91	40.0±0.1	53.0±0.5
50-60	49.86-60.29	26.-44.	34.58	25.8±0.1	29.4±0.2
60-70	60.29-70.04	15.-26.	20.34	15.83±0.03	15.6±0.1
70-80	70.04-79.93	8.-15.	11.47	9.34±0.02	8.03±0.04

Table 3.4 Centrality definition by $N_{\rm tracks}^{\rm offline}$ (efficiency-uncorrected charged-track multiplicity in the TPC within $|\eta| < 0.5$) in Ru+Ru collisions. The first column is the centrality range labels , while the second column denotes the actual centrality ranges which are slightly different from the first column because of integer edge cuts used for centrality determination.

Centrality (%)	Zr+Zr				
	Centrality (%)	$N_{\mathrm{tracks}}^{\mathrm{offline}}$	$\langle N_{\mathrm{tracks}}^{\mathrm{offline}} \rangle$	$\langle N_{\mathrm{part}} \rangle$	$\langle N_{\mathrm{coll}} \rangle$
0-5	0-5.00	256.-500.	287.36	165.9±0.1	386±10
5-10	5.00-9.99	213.-256.	233.79	146.5±1.0	317±5
10-20	9.99-20.08	147.-213.	178.19	115.0±0.8	225±3
20-30	20.08-29.95	100.-147.	122.35	81.8±0.4	139±2
30-40	29.95-40.16	65.-100.	81.62	56.7±0.3	83.3±0.8
40-50	40.16-50.07	41.-65.	52.41	38.0±0.1	48.0±0.4
50-60	50.07-59.72	25.-41.	32.66	24.6±0.1	26.9±0.2
60-70	59.72-70.00	14.-25.	19.34	15.10±0.03	14.3±0.1
70-80	70.00-80.88	7.-14.	10.48	8.58±0.02	7.12±0.04

Table 3.5 Centrality definition by $N_{\mathrm{tracks}}^{\mathrm{offline}}$ (efficiency-uncorrected charged-track multiplicity in the TPC within $|\eta| < 0.5$) in Zr+Zr collisions. The first column is the centrality range labels , while the second column denotes the actual centrality ranges which are slightly different from the first column because of integer edge cuts used for centrality determination.

3.4 Electron Identification

To select high-quality primary tracks, the following selection criteria are applied: the track's transverse momentum (p_T) should be larger than 0.2 GeV/c to ensure the track can pass through the TPC; the pseudorapidity of the selected tracks is required to be less than 1 to stay within the TOF acceptance; the number of TPC hit points (nHitsFit) used for track reconstructed larger than 20, out of a maximum of 45, to high enough momentum resolution, and the ratio of nHitsFit over the number of maximum possible TPC hit points along the track trajectory (nHitsPoss) is required to be larger than 0.52 in order to reject track splitting; to ensure good dE/dx resolution, the number of points for $\langle dE/dx \rangle$ calculation (nHitsDedx) should be more than 15; last but not the least, the DCA between the primary track and the primary vertex is less than 1 cm to suppress tracks from secondary decays. The track selection criteria is summarized in the Table 3.6.

Primary track selection criteria
$p_T > 0.2$ GeV/c
$\lvert\eta\rvert < 1$
nHitsFit > 20
nHitsDedx > 15
nHitsFit/nHitsPoss > 0.52
DCA < 1 cm

Table 3.6 Summary of primary track quality cuts.

In order to measure the yields of e^+e^- pair and J/ψ meson (through the dielectron decay channel) production from photon-induced interactions in Ru+Ru and Zr+Zr collisions at mid-rapidity ($|y|<1$), it is crucial to separate electron (denoting both electron and positron if not specified) candidates from all other particles. The sub-detectors used to identify electrons are the TPC through the ionization energy loss (dE/dx) and the TOF flight time measurements. For electrons from J/ψ meson decays, their p_{T} are around 1.5 GeV/c, and therefore information from BEMC can also be used for identifying electrons.

3.4.1 Particle identification with the TPC

In addition to measuring charged-particles' momenta, the TPC can also be utilized for particle identification (PID) through measurement of ionization energy loss per unit length (dE/dx). The dE/dx distribution for charged particles as a function of momentum (p) is shown in Fig. 3.5. Different particle species with the same momentum have different dE/dx values. To perform PID, dE/dx is first normalized by the expected ionization energy loss for electrons predicted by the Bichsel function ($(dE/dx)_{\mathrm{theory}}$)[171], and then scaled by the dE/dx resolution ($R_{dE/dx}$) to obtain the possibility of a track being an electron, known as the $n\sigma_e$. The variable $n\sigma_{\mathrm{e}}$ is defined as:

$$n\sigma_{\mathrm{e}} = \frac{\ln(dE/dx)_{\mathrm{measured}} - \ln(dE/dx)^{\mathrm{e}}_{\mathrm{theory}}}{R_{dE/dx}}, \tag{3.2}$$

The $n\sigma_{\mathrm{e}}$ distribution for electrons is expected to follow a Gaussian distribution with a mean of 0 and width of 1. Thus the $n\sigma_e$ (based on dE/dx) variable can be used for electron identification.

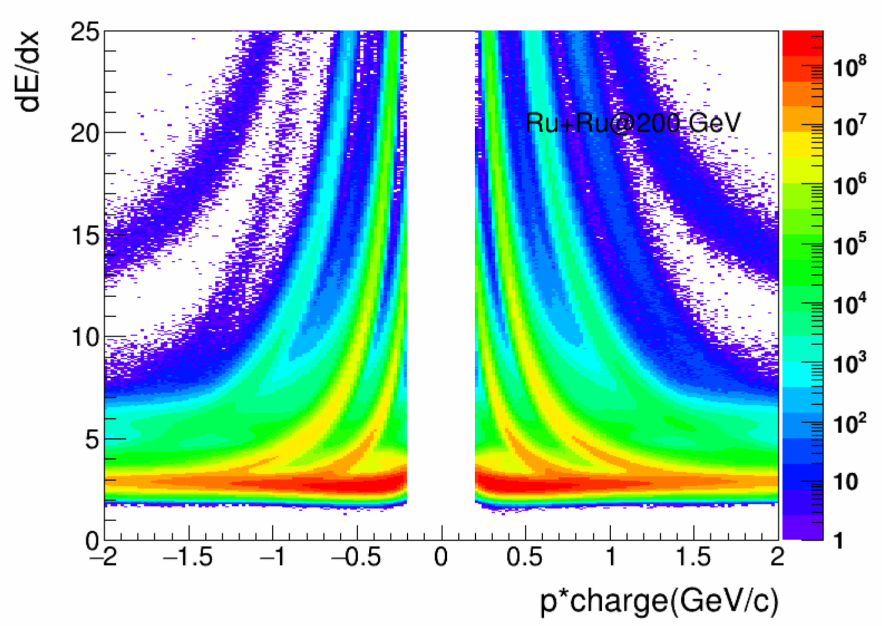

Figure 3.5 The dE/dx of charged particles in Ru+Ru collisions at $\sqrt{s_{\mathrm{NN}}}$ = 200 GeV.

Figure3.6 shows the $n\sigma_e$ distribution as a function of η for a pure electron sample in 0-10% central Ru+Ru collisions at $\sqrt{s_{\mathrm{NN}}}$= 200 GeV/c. The procedure to obtain the pure electron sample will be introduced in Sec. 3.4.5. The black points are the mean value in each η bin, which shows a strong η dependence caused by imperfect calibration.

The solid line is the fitting result of the black points with the formula:

$$f(\eta) = p_0 - ln(e^{-\eta} + e^{\eta}) \times p_1, \tag{3.3}$$

where the p_0 and p_1 are free parameters.

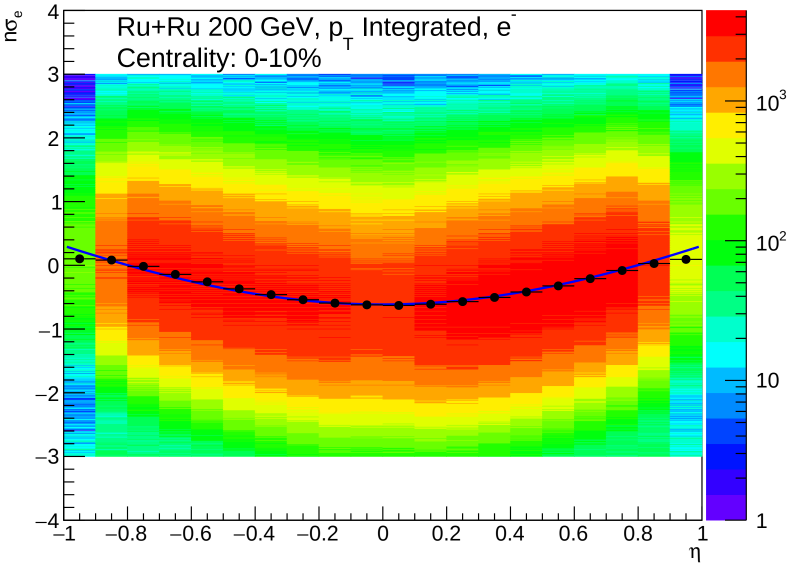

Figure 3.6 $n\sigma_e$ **distribution as a function of** η **for a pure electron sample in 0-10% central in Ru+Ru collisions at** $\sqrt{s_{\rm NN}}$**= 200 GeV.**

This strong η dependence of $n\sigma_e$ distribution affects the raw signal extraction and detector efficiency correction in this analysis. In order to simplify the $n\sigma_e$ and avoid additional complications when estimating the $n\sigma_e$ cut efficiency, we correct for this η dependence before determining the electron identification cuts. We also checked if the $n\sigma_e$ distribution depends on track's p_T and ϕ, as shown in the left and right panels of Fig. 3.7. As one can see, the ϕ distribution shows some dip structure while the $p_{\rm T}$ dependence shows a flatter trend. Since a track's $p_{\rm T}$ η and ϕ are independent variables and the η dependence is the strongest, we identify the η dependence as the leading-order effect and the structures of the ϕ dependence as the second-order effect in the correction scheme. The correction factor is calculated as:

$$\Delta_{n\sigma_e} = \langle n\sigma_e(\eta)\rangle + \langle n\sigma_e(\phi)\rangle - \Big\langle \langle n\sigma_e(\phi)\rangle \Big\rangle, \tag{3.4}$$

where $\langle n\sigma_e(\eta)\rangle$ is the mean value of $n\sigma_e$ in each η bin obtained from the fitting (Fig. 3.6), $\langle n\sigma_e(\phi)\rangle$ is the mean value of $n\sigma_e$ in each ϕ bin read off from the black points in the right panel of Fig3.7, and $\Big\langle \langle n\sigma_e(\phi)\rangle \Big\rangle$ is the mean of the black points in the right panel of Fig. 3.7.

The corrected mean $n\sigma_e$ distribution in different centrality bins are shown in

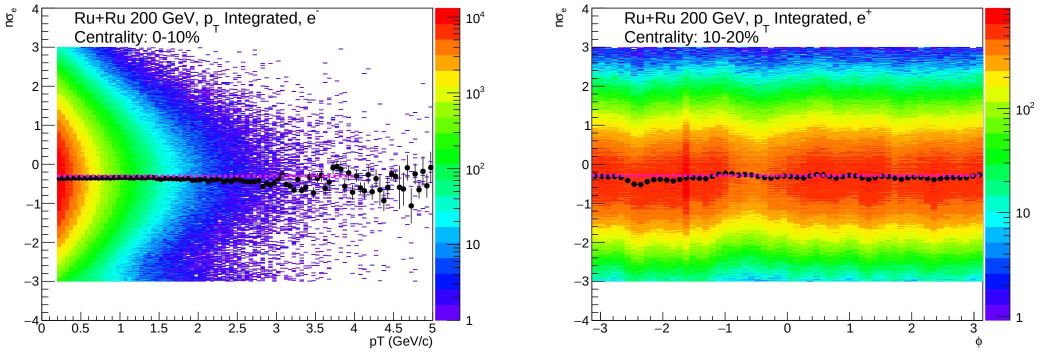

Figure 3.7 $n\sigma_e$ **distribution as function of** p_{T} **(left) and** ϕ **(right) for a pure electron sample in 0-10% central Ru+Ru collisions at** $\sqrt{s_{\mathrm{NN}}}$**= 200 GeV.**

Fig. 3.8. The left panel is the $n\sigma_e$ distribution as a function of track's η in Ru+Ru and Zr+Zr. The solid points are the mean values of $n\sigma_e$ in Ru+Ru collisions before correction, while the open markers are the same but for Zr+Zr collisions after correction. As one can see, after the $n\sigma_e$ correction, the strong η dependence is eliminated and the mean values of $n\sigma_e$ in different η ranges are all close to zero, which makes it easier to apply $n\sigma_e$ cut and estimate the $n\sigma_e$ cut efficiency. The right panel of Fig. 3.8 shows the ϕ dependence of the $n\sigma_e$ distribution in different centrality bins. Similar as shown in the left panel, after correction, not only the mean values in different ϕ bins are shifted to zero, but also dip structure is gone.

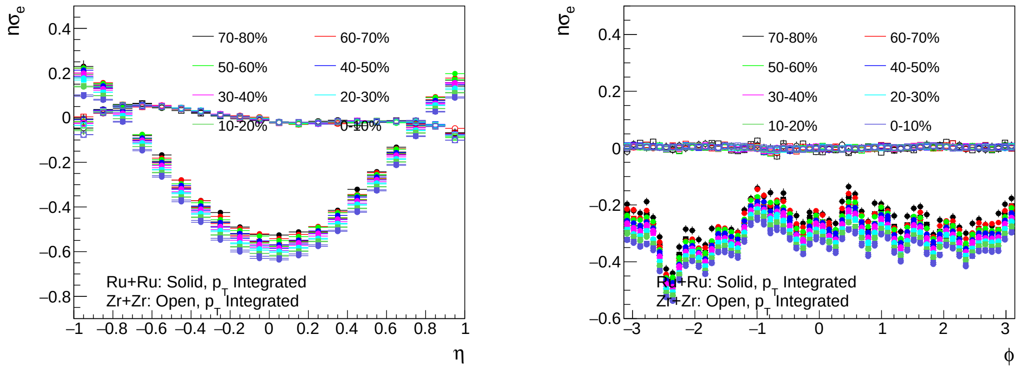

Figure 3.8 $n\sigma_e$ **as a function of electron's** η **(left panel) and** ϕ **(right panel) in different centrality classes of isobaric collisions at** $\sqrt{s_{\mathrm{NN}}}$**= 200 GeV before (solid symbols) and after (open symbols) the** $n\sigma_e$ **correction.**

After applying the correction, the $n\sigma_e$ distributions of pure electron and hadron samples are obtained to check the PID capability with dE/dx does not deteriorate. The pure π, K and p samples are selected by combining tight m^2 and loose $n\sigma_{\pi/K/p}$ cuts. The m^2 can be calculated as:

$$m^2 = \frac{p^2(1-\beta^2)}{\beta^2} = p^2(\frac{c^2\Delta t^2}{L^2} - 1), \tag{3.5}$$

A pure sample of "merged π", caused by two tracks of the same charge and similar momenta get reconstructed into one track, is selected by the same m^2 cut as for selecting the pure π sample but with a $n\sigma_\pi > 6$ cut since the ionization energy loss of a "merged π" is expected to two times that of a regular. The $n\sigma_e$ mean values for pure hadron and electron samples as a function of p_{T} after the correction are displayed in Fig. 3.9. As expected, the $n\sigma_e$ distribution of the pure electron sample (blue marker) shows a flat trend around zero. Still, the electron $n\sigma_e$ distribution shows a clear distinction to other hadrons, which is the basis for identifying electrons with the TPC.

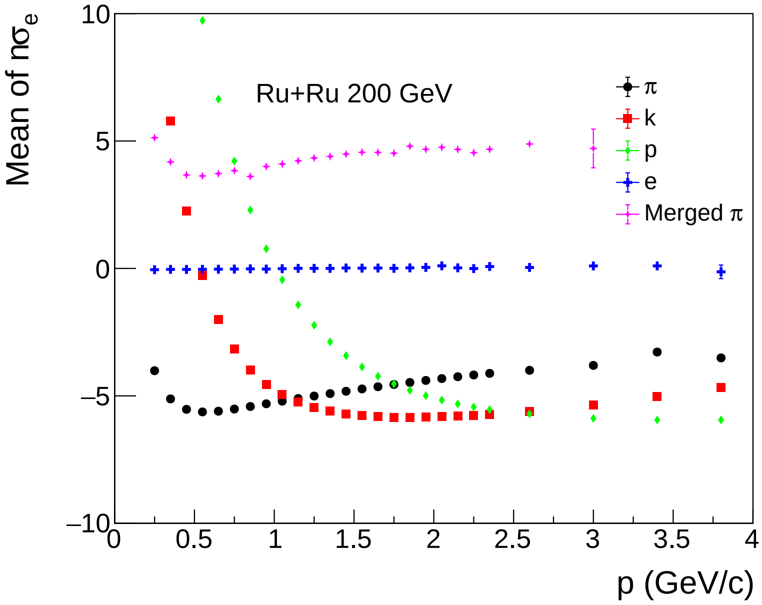

Figure 3.9 Mean $n\sigma_e$ values as a function of p_{T} for different particle species in isobaric collisions at $\sqrt{s_{\mathrm{NN}}}$= 200 GeV.

However, in some specific momentum regions, the dE/dx values are very similar for different particles, these overlap regions can be clearly seen in Fig. 3.9, such as the dE/dx for electrons and kaons around $p \approx 0.5$ GeV/c, for electrons and protons around $p \approx 1$ GeV/c. Furthermore, the dE/dx values are close to each other at $p > 1.3$ GeV/c for all charged particles. So the TOF (low momentum) and BEMC (high momentum) are used to improve the electron identification in different momentum regions.

3.4.2 Particle identification with the TOF

Given its very small mass (0.511 MeV/c^2), an electron is expected to have a velocity around 1 ($1/\beta \approx 1$), while heavier hadrons (like π, K and p) will spend more time to reach the TOF at a given momentum. Therefore, the velocity of charged particle with different mass measured by the TOF can be used to select electrons from heavier hadrons, especially in the low momentum regions. As shown in Fig. 3.10, $1/\beta$ can be used to identify electrons from heavier hadrons in the low momentum region up to 1.5

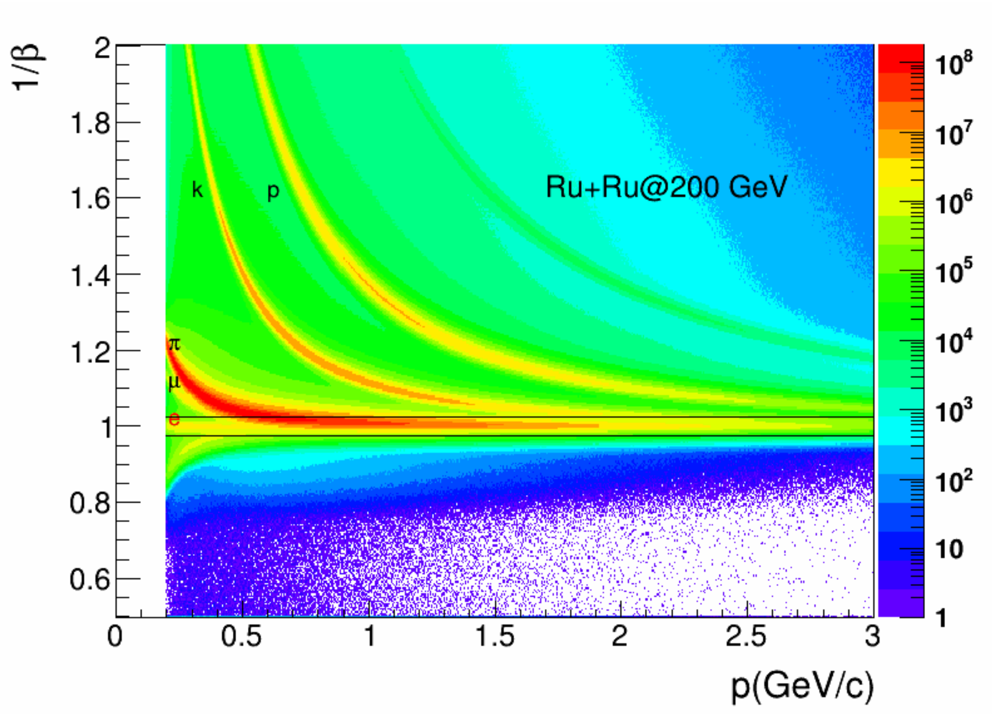

Figure 3.10 The momentum dependence of $1/\beta$ for charged particles. Black soild lines indicate the default $1/\beta$ cut ($|1/\beta - 1| < 0.025$) for selecting electrons.

GeV/c, even though it could not completely eliminate pions due to their low masses and limited TOF resolution. In the higher momentum region, velocities of all particles approaches the speed of light (c) and hadrons can no longer be discriminated from electrons, for which the BEMC, based on the measurements of deposited energies by incident particles, can be used to suppress hadron contamination. Figure 3.11 shows $n\sigma_e$ as a function of momentum before (left panel) and after (right panel) the $1/\beta$ cut. As one can seen, the $1/\beta$ cut can reject most of heavier hadrons (like π, k and p) and the remaining π can be removed with the $n\sigma_e$ cut.

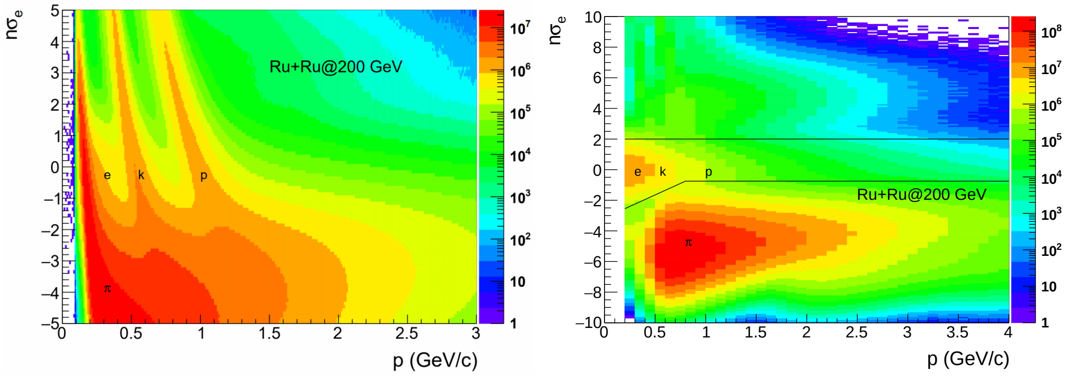

Figure 3.11 Momentum dependence of $n\sigma_e$ distribution before (*Left panel*) and after (*Right panel*) $1/\beta$ cut in MB triggered isobaric collisions at $\sqrt{s_{\mathrm{NN}}}$ = 200 GeV. The solid black lines in the right panel indicate the $n\sigma_e$ cuts.

3.4.3 Particle identification with the BEMC

As mentioned before, the BEMC can be used to discriminate between electrons and hadrons in the high p_T region ($p_T > 1$ GeV/c). The BEMC-related PID cuts are only used for J/ψ reconstruction since the daughter electrons have p_{T} around 1.5 GeV/c most of the time, while for low-mass $e^{+}e^{-}$ pairs from photon-photon interactions, BEMC is not useful for identifying such electrons. The deposited energy in the BEMC by an electron is approximately equal to its momentum while for a hadron it is considerably smaller. So the deposited energy to momentum ratio (E/p) is used for electron identification. However, the BEMC cluster energy (E) of an incident electron may be effected by other particles, especially in high-multiplicity central heavy-ion collisions, since the BEMC cluster is reconstructed by grouping adjacent towers which can be hit by multiple particles including an electron. To mitigate such effects, the highest tower energy in a BEMC cluster (E_0) is used instead of E. The E_0/p distributions for electrons and hadrons (mainly π) in different p_T regions can be found in Fig. 3.12. The black lines are for pions selected by a tight m^2 cuts, the red open rectangles represent electrons from photon conversion and π^0 Dalitz decay selected with the invariant mass method (see in Sec. 3.4.5). As shown in the figure, the separation between electrons and pions increases with increasing p_T, and the E_0/p cut, indicated by vertical dashed lines in the figure, could keep most of electrons while significantly reducing hadron contamination.

The distance distributions between track projection and the matched BEMC cluster in η and ϕ planes are displayed in Fig. 3.13 for electron and hadron samples within $2 < p_T < 3$ range GeV/c. Hadrons (black lines) show similar distributions as the electron sample (red markers) in both η and ϕ plane. Therefore, these information is not used for electron identification. The absence of the Barrel Shower Maximum Detector (BSMD), which is positioned at approximately 5.6 radiation lengths deep within the Barrel Electromagnetic Calorimeter (BEMC), results in the loss of high spatial resolution capability. The BSMD is usually turned off in heavy-ion collisions during the data-taking because of its much slow readout compared to that of TPC.

3.4.4 Electron identification cuts

Table 3.7 summarizes detectors used for electron identification in different p_{T} ranges and corresponding cuts for reconstructing J/ψ from photon-nucleus processes in isobaric collisions. For tracks with $p_{\mathrm{T}} \leq 1$ GeV/c, a momentum dependent $n\sigma_{\mathrm{e}}$ cut, in combination with the $|1/\beta - 1| < 0.025$ requirement, is used. For $p_{\mathrm{T}} > 1$ GeV/c, different combinations of PID cuts are used, depending on the availability of TOF and

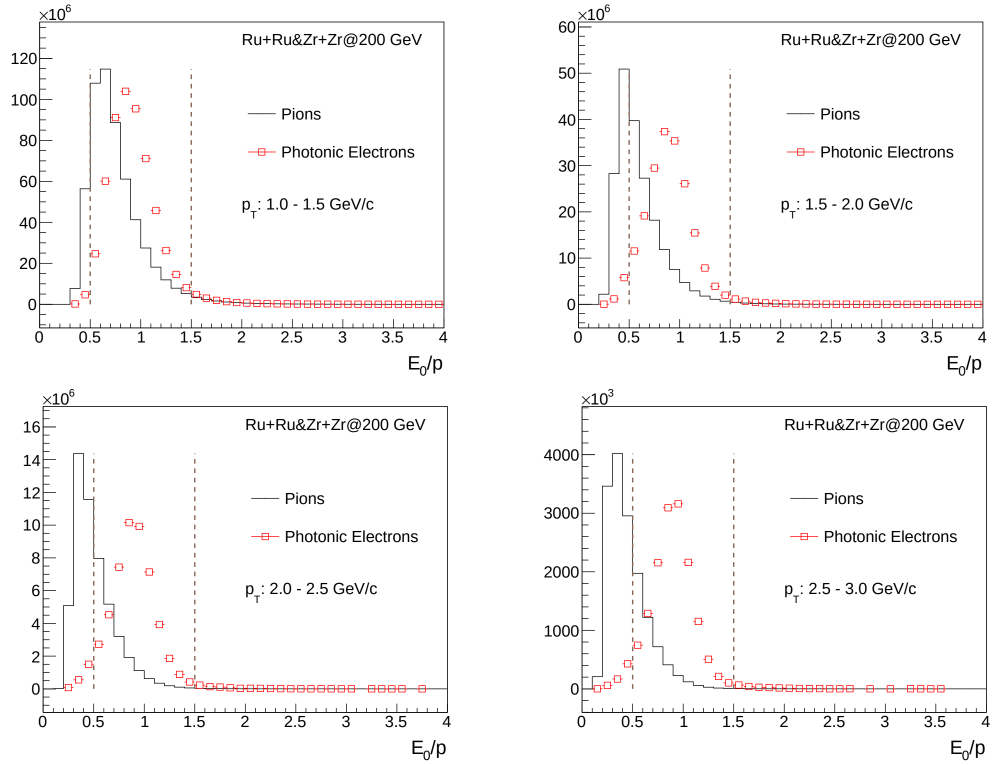

Figure 3.12 **E_0/p distributions of electron samples and hadrons (mainly π) in different p_T regions. The black line stands for hadrons, the red open rectangles are electron samples from photon conversions and π^0 Dalitz decays. The vertical brown dash lines indicate E_0/p cuts from 0.5 to 1.5.**

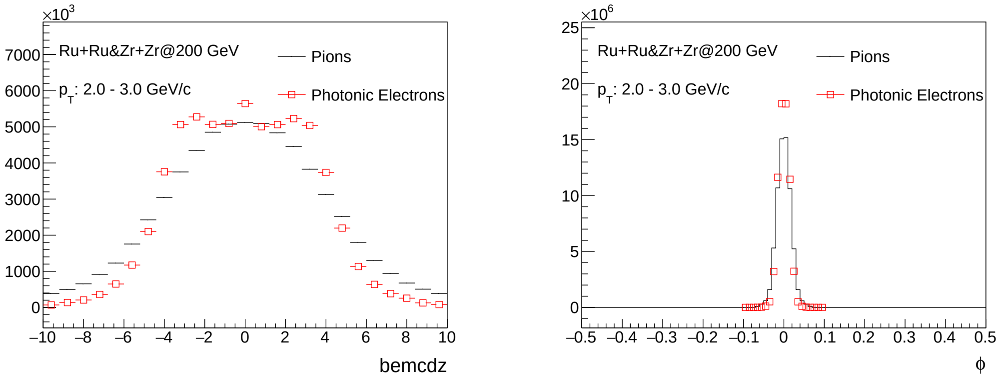

Figure 3.13 **The distance distributions between track projection and matched BEMC cluster in η (*left panel*) and ϕ (*right panel*) planes in the p_T range from 2 to 3 GeV/c.**

Track $p_{\rm T}$	Detectors used	Electron PID cuts
$p_{\rm T} \leq 1.0$ GeV/c	TPC, TOF	$\lvert 1/\beta - 1\rvert < 0.025$; for $p > (\leq)0.8$ GeV/c: $-0.75\ (3 \times p - 3.15) < n\sigma_e < 2$
$p_{\rm T} > 1.0$ GeV/c	TPC, TOF and not matched to BEMC	$\lvert 1/\beta - 1\rvert < 0.025$; $-0.75 < n\sigma_e < 2$
	TPC, BEMC and not matched to TOF	$-1 < n\sigma_e < 2$; $0.5 < E_0/p < 1.5$
	TPC, TOF and BEMC	$\lvert 1/\beta - 1\rvert < 0.025$; $-1.5 < n\sigma_e < 2$; $0.5 < E_0/p < 1.5$

Table 3.7 List of electron PID cuts for J/ψ alaysis in isobaric collisions at $\sqrt{s_{\rm NN}}$ = 200 GeV.

BEMC information, in order to maximize the hadron rejection power while maintaining a high PID efficiency. In the case when only the TOF information is available, PID cuts of $|1/\beta - 1| < 0.025$ and $-0.75 < n\sigma_{\rm e} < 2$ are used. If a track leaves a signal in the BEMC but not in the TOF, the BEMC cut of $0.5 < E_0/p < 1.5$ is utilized in conjuncture with the TPC cut of $-1 < n\sigma_{\rm e} < 2$. A third scenario is that the PID information from TPC, TOF and BEMC can all be used, and the corresponding electron selection cuts are: $|1/\beta - 1| < 0.025$, $-1.5 < n\sigma_{\rm e} < 2$ and $0.5 < E_0/p < 1.5$. It is worth noting that the $n\sigma_{\rm e}$ cut is asymmetric with a tighter lower boundary on the negative side. This is because charged pions are the most abundant hadron species that contaminates the electron sample and their $\langle n\sigma_{\rm e}\rangle$ values are smaller than that of electrons. The lower boundary of the $n\sigma_{\rm e}$ cut also changes with $p_{\rm T}$, while the upper boundary is kept at 2.

For reconstructing e^+e^- pairs from photon-photon interaction in isobaric collisions, only TPC and TOF related PID cuts are used, which are summarized in Table3.8. As mentioned before in Sec 3.4.2, the BEMC information, most relevant for electron identification above 1 GeV/c, is not used for this part of the analysis.

Track's p_T	Detectors	Electron PID cuts
$p_T > 0.2$ GeV/c	TPC, TOF	$\lvert 1/\beta - 1\rvert < 0.025$; for $p > (\leq)0.8$ GeV/c: $-0.75\ (3 \times p - 3.15) < n\sigma_e < 2$

Table 3.8 List of electron PID cuts for e^+e^- pair reconstruction in isobaric collisions at $\sqrt{s_{\rm NN}}$ = 200 GeV.

3.4.5 Method to obtain a pure electron sample

An electron sample with high purity (usually more than 99%) is usually needed for optimizing electron identification and estimating various efficiencies for electrons in a data-driven manner. However, such a high purity can not be achieved with only TPC, TOF and BEMC PID cuts. Alternatively, one can exploit the physics property of two specfic processes, the photon conversion and the π^0 Dalitz decay, *i.e.*, resulting electron pairs have near zero invariant mass, which can be used to obtain an almost pure electron sample. Since primary tracks, forced to originate from the primary vertex, are used in the main analysis, they are also used for obtaining the pure electron sample based on the invariant mass method. However, the photon conversion point typically doesn't coincide with the primary vertex. This discrepancy introduces an artificial angular separation between the electron and positron, consequently yielding a non-zero invariant mass measurement. The magnitude of the opening angle hinges on the separation between the photon conversion point and the primary vertex. Thus, distinct conversion points will yield varying invariant masses for e^+e^- pairs. Usually, a $M_{ee} < 0.015\ GeV/c^2$ is used to select electrons from the photon conversion and π^0 Daliz decay. However the background will increase when the collision centrality becomes central, thus the M_{ee} cut should be tighter in order to keep the signal-to-background ratio high enough. The invariant mass distributions of electron pairs in four different centrality classes in isobaric collisions at $\sqrt{s_{\rm NN}}$= 200 GeV are displayed in Figure 3.14. The black points are unlike-sign pairs while the red points stand for like-sign for background estimation. The signal can be obtained by subtracting like-sign pairs from unlike-sign pairs. The first peak in the unlike-sign distribution is electrons from the π^0 Daliz decay while the second peak is from the photon conversion, and two processes can be easily singled out by a M_{ee} cut. For each centrality class, the pink dash line stands for the M_{ee} cut used, a looser cut is used in peripheral centrality classes, and the signal-to-background ratio (as listed in each sub-figure) is all above 100, high enough for obtaining an electron sample with larger than 99% purity.

3.5 e^+e^- pair and J/ψ meson yield extraction

As previously carried out in Au+Au collisions at STAR[155-156], e^+e^- pair and J/$\psi \rightarrow e^+e^-$ (5.94±0.06%) decay are reconstructed using electron candidates identified by the cuts described in Sec. 3.4.4. The rapidity of e^+e^- pair and J/ψ candidates are constrained to be within $|y| < 1.0$. In order to select e^+e- pair and J/ψ from coherent processes, the candidates are required to have very low $p_{\rm T}$ ($p_{\rm T} \leq 0.15$ GeV/c) to suppress contributions from hadronic sources. Although the hadronic contamination is very small in such low $p_{\rm T}$ region, the knowing hadronic contribution will still be estimated and subtracted from the measurement (detials in Sec. 3.7). A mixed-event technique (detailed in Sec. 3.5.2) is used to estimate the combinatorial background, which gets subtracted from the unlike-sign electron pair distribution (detailed in Sec. 3.5.1). The J/ψ sig-

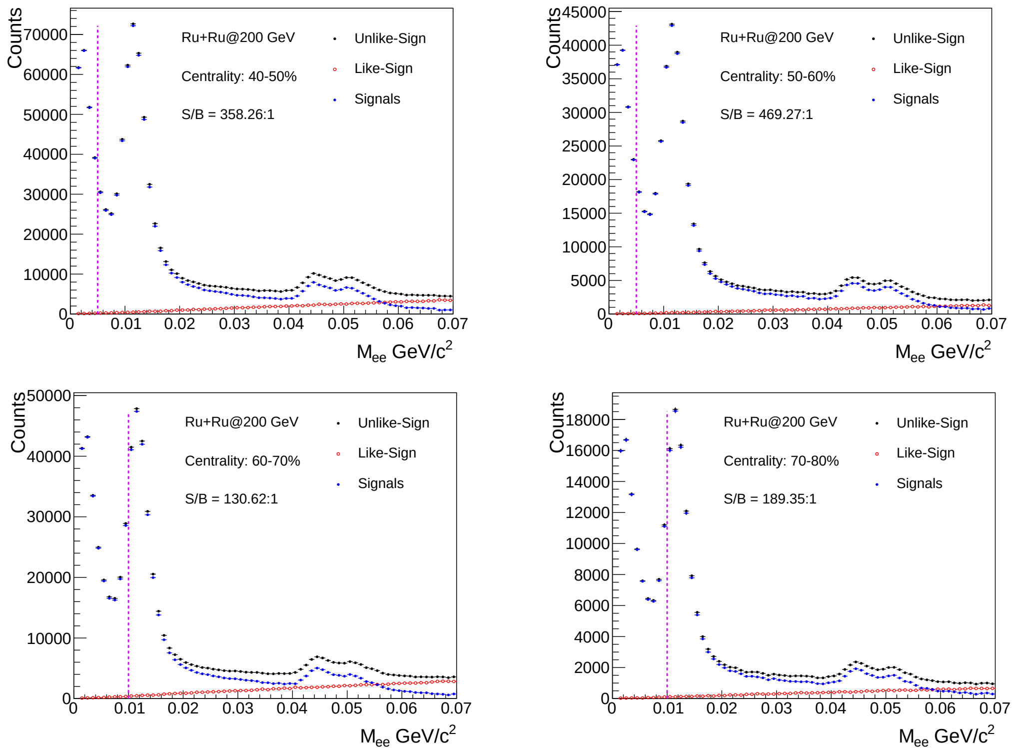

Figure 3.14 Electron pair invariant mass distributions in different centrality classes of isobaric collisions.

nal shape from detector simulations with additional momentum smearing to match data (detailed in Sec 3.5.4) is used to obtain the J/ψ yield through a fitting procedure.

3.5.1 Pair reconstruction in same event

The unlike-sign pairs originating from the same event (N_{+-}), inclusive of both signal and background elements, are reconstructed by merging all candidate electrons and positrons, also known as the foreground. The J/ψ signal is mainly included in the invariant mass range from 2.9 to 3.2 GeV/c^2 of the unlike-sign pair distribution, while the e^+e- signal has a continuous invariant mass distribution, mainly in the mass range of 0.4 to 2.6 GeV/c^2. The lower limit is due to the p_{T} cut on primary tracks, and the upper limit is selected to avoid interference with the J/ψ signal region. There are other physical processes that will contribute to the invariant mass range interested in this analysis (0.4 - 2.6 and 2.9 - 3.2 GeV/c^2) in the unlike-sign pairs, like radiative decay, QGP thermal radiation, vector mesons in-medium decay, heavy flavor semi-leptonic decay and Drell-Yan production, which should be estimated and subtracted from final yield, called hadronic cocktail. Within the mass range of interest, background sources also consist of both combinatorial and correlated backgrounds. The former arises from pairing of electrons and positrons which are not derived from the same decay process, whereas the correlated background is the pairs from Dalitz decay (e.g. $\pi^0 \to \gamma + e^+ + e^- \to e^+ + e^- + e^+ + e^-$). The like-sign technique, which pairs electrons of the same charge within a same event (N_{++} and N_{--}), is employed to address both combinatorial and correlated background contributions. The geometric mean, $2\sqrt{N_{++} \cdot N_{--}}$, can describe the background well in the unlike-sign pairs distributions for the e^+ and e^- are produced in statistically independent pairs. Thus the combinatorial background and correlated background, $N_{++\&--}$, can be defined as:

$$N_{++\&--}(M_{ee}) = 2\sqrt{N_{++}(M_{ee}) \cdot N_{--}(M_{ee})}, \tag{3.6}$$

The statistical uncertainty in the like-sign pairs distribution will contributes to the uncertainty in the e^+e^- pair and J/ψ signal when the like-sign pairs removed as the background, and to minimize this, a mixed-event background calculation was used in this analysis for J/ψ signal extraction, while for e^+e^- pair extraction, the the like-sign pairs distribution from same event is still used due to the lack of the correlated background in mixed event.

3.5.2 Mixed-event technique

In order to improve the statistical precision in estimating the combinatorial background, the mixed-event technique, which pairs electrons and positrons from different events with similar characteristics, is used. The dataset is partitioned into various event pools based on the following global properties: the direction of field, the position of collision vertex along the beam direction, and the event centrality. The collision vertex position and centrality are used to ensure that events in the same event pool have similar detector acceptance and reconstruction efficiency. The vertex z position, from -35 to 25 cm, is divided into 20 equidistant bins, while the event centrality is divided into 16 bins of equal intervals within 0-80%. Each event pool holds 100 events at maximum, and one event in the event pool is randomly updated when the poll is full. Since mixed events can be reconstructed with arbitrary statistics, a normalization factor is needed for utilizing the mixed events as an estimate of the combinatorial background, which is obtained by taking the ratio in like-sign distributions between same-event and mixed-event. Of course, the normalization factor should be established within a kinematic region where the correlated background in the same-event like-sign distribution is minimal, since mixed events do not include this kind of background. In this analysis, the kinematic region is chosen to be from 2.6 to 3.6 GeV/c^2 in M_{ee} for all p_{T} bins. Then the normalized combinatorial background (B_{+-}^{comb}) can be calculated as the following[172] can be:

$$\begin{aligned}
A_+ &= \frac{\int_{N.R.} N_{++}(M,p_T)dMdp_T}{\int_{N.R.} B_{++}(M,p_T)dMdp_T} \\
A_- &= \frac{\int_{N.R.} N_{--}(M,p_T)dMdp_T}{\int_{N.R.} B_{--}(M,p_T)dMdp_T} \\
B_{++}^{norm} &= \int_0^\infty A_+ B_{++}(M,p_T)dMdp_T \\
B_{--}^{norm} &= \int_0^\infty A_- B_{--}(M,p_T)dMdp_T \\
B_{+-}^{comb} &= \frac{2\sqrt{B_{++}^{norm} B_{--}^{norm}}}{\int_0^\infty B_{+-}(M,p_T)dMdp_T} B_{+-}(M,p_T)
\end{aligned} \tag{3.7}$$

where $N.R.$ signifies the normalization region, $A_{+/-}$ represents the normalization factor based on like-sign distributions, $B_{++/--}^{norm}$ stands for the normalized mixed-event like-sign distribution and B_{+-}^{comb} represents the normalized mixed-event unlike-sign distribution. The statistical uncertainty of B_{+-}^{comb} is negligible and thus the significance of the J/ψ signal can be defined as $S/\sqrt{S+B}$, where the S is $N_{+-} - B_{+-}^{comb}$ and the B is B_{+-}^{comb} plus the residual background estimated by the fitting (detailed in Sec 3.5.3).

3.5.3 Signal extraction

The e^+e^- pair invariant mass spectrum for $|y_{ee}| < 1$ in 70-80% Ru+Ru collisions is shown in Fig. 3.15 for pair $p_{\mathrm{T}} < 0.1$ GeV/c. The like-sign distribution, shown as the black open circles, is employed as an estimate for both the combinatorial and correlated background. The raw invariant mass distribution of e^+e^- pairs rapidly decreases with increasing mass, while the peak of the J/ψ can also be observed. The raw e^+e^- pair signal is obtained by subtracting the like-sign distribution from unlike-sign distribution. As one can see, the signal of background ratio is about 0.25 and the e^+e^- signal significance reaches 11.5 in the 70-80% Ru+Ru collisions at $\sqrt{s_{\mathrm{NN}}}$= 200 GeV/c, within the invariant mass region of 0.4 to 2.6 GeV/c^2 and $p_{\mathrm{T}}^{ee} < 0.1$ GeV/c. Similar invariant mass spectra of e^+e^- in 60-70% and 40-60% Ru+Ru collisions are displayed in the left and right panels of Fig. 3.16, the S/B ratios decreases towards central collisions while the significance is similar.

Figure. 3.17 shows the results in Zr+Zr collisions within same centrality classes and kinematic regions. The trends of S/B ratios and significance are similar to that of Ru+Ru collisions.

The electron pair invariant mass distribution, used for extracting J/ψ yield, is shown

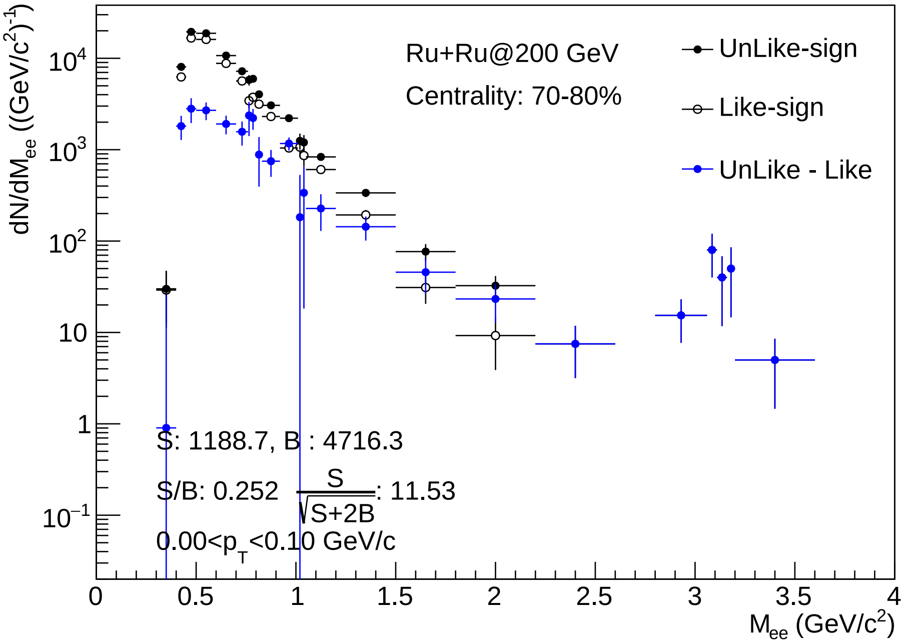

Figure 3.15 e^+e^- **pair invariant mass distribution for pair** p_{T} **smaller than 0.1 GeV/**c **in 70-80‰ Ru+Ru collisions at** $\sqrt{s_{\mathrm{NN}}}$**= 200 GeV. The black solid circles represent the unlike-sign distribution, while the like-sign distribution are shown by the black open circles, and the blue solid circles stand for the raw signal of** e^+e^- **pairs by subtracting like-sign distribution from unlike-sign.**

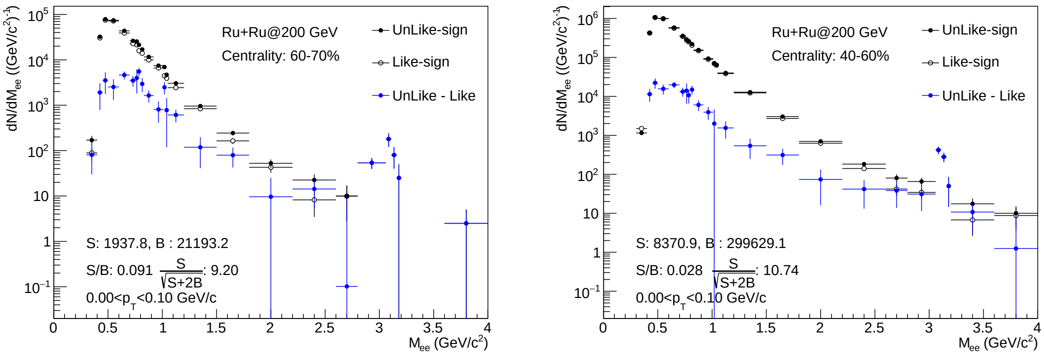

Figure 3.16 e^+e^- **pair invariant mass distribution for pair** p_{T} **smaller than 0.1 GeV/**c **in 60-70‰ (left panel) and 40-60‰ (right panel) Ru+Ru collisions at** $\sqrt{s_{\mathrm{NN}}}$**= 200 GeV. The black solid circles represent the unlike-sign distribution, while the like-sign distribution are shown by the black open circles, and the blue solid circles stand for the raw signal of** e^+e^- **pairs by subtracting like-sign distribution from unlike-sign.**

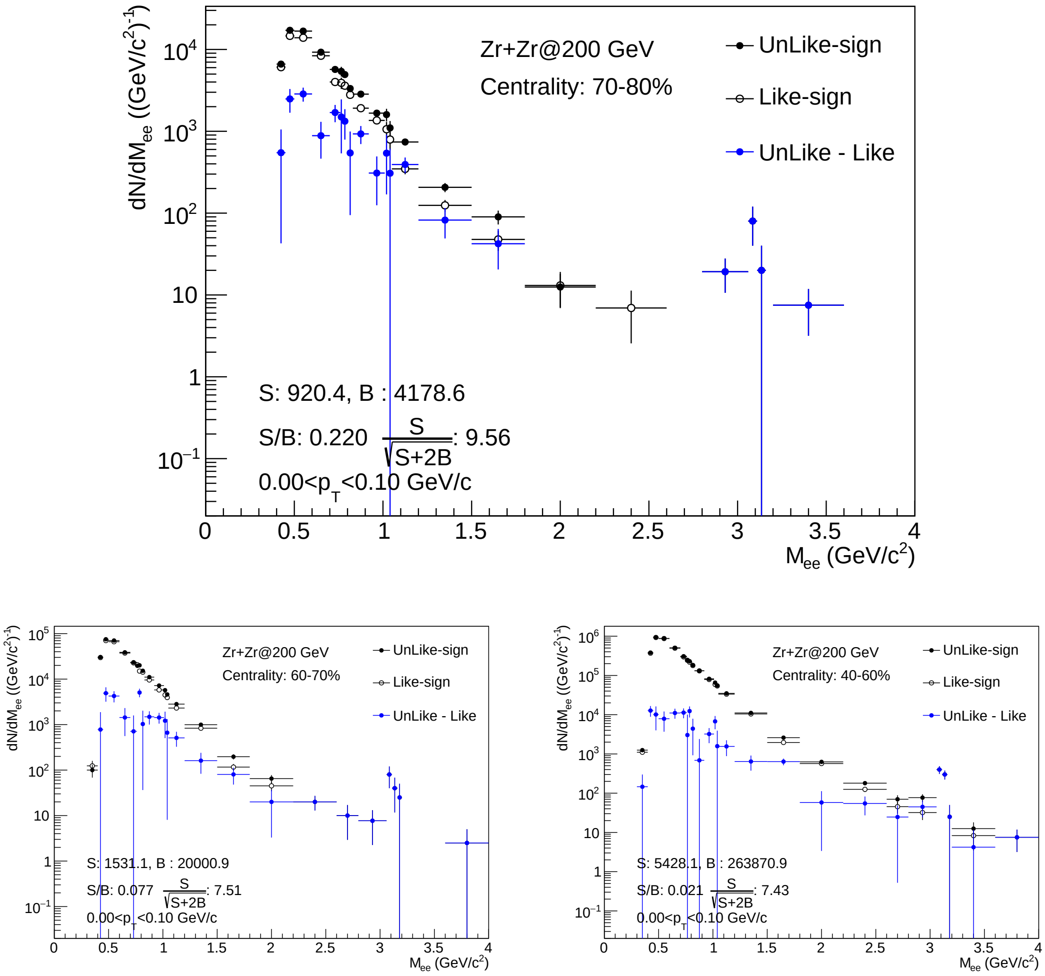

Figure 3.17 $e^{+}e^{-}$ **pair invariant mass distribution for pair** p_{T} **smaller than 0.1 GeV/**c **in Zr+Zr collisions at** $\sqrt{s_{\mathrm{NN}}}$**= 200 GeV. The black solid circles represent the unlike-sign distribution, while the like-sign distribution are shown by the black open circles, and the blue solid circles stand for the raw signal of** $e^{+}e^{-}$ **pairs by subtracting like-sign distribution from unlike-sign.**

in Fig. 3.18 in 40-80% Ru+Ru collisions at $\sqrt{s_{\mathrm{NN}}}$= 200 GeV at pair p_{T} smaller than 0.2 GeV/c. Here, the raw signal of J/ψ is more pronounced compared to that in the $e^{+}e^{-}$ analysis, primarily because in the J/ψ analysis, PID is optimized using BEMC for the high mass region. The total J/ψ counts are obtained in the invariant mass region from 2.9 to 3.2 GeV/c^{2} by the bin-counting method as the following:

$$N_{J/\psi} = N_{unlike-sign,same-event} - N_{unlike-sign,mixed-event} - N_{residual}, \tag{3.8}$$

The unlike-sign distributions is fitted with three components using the binned Maximum Likelihood (ML) method:

- The J/ψ signal template with a Crystal-Ball function from detector simulation, as detailed in Sec 3.5.4
- The combinatorial background (brown histogram in Fig. 3.18) from mixed event,

as described in the previous section.

- A first-order polynomial function used to account for the residual background, mainly from $c\bar{c}$ pair decay and the Drell-Yan process.

The black solid squares in Fig. 3.18 are the e^+e^- pair invariant mass distribution after the combinatorial background substraction, and the fitted results of the J/ψ shape and residual background are shown as the black solid line and pink dashed line, respectively. The overall fit result is shown as the red solid curve in Fig. 3.18.

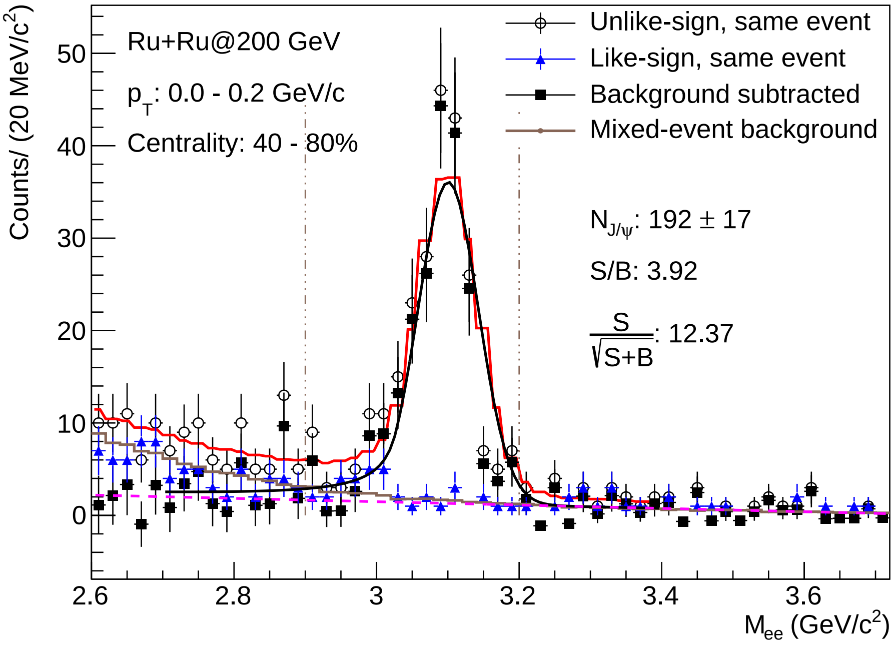

Figure 3.18 The e^+e^- pair invariant mass distribution at pair $p_{\rm T}$ smaller than 0.2 GeV/c in 40-80% Ru+Ru collisions at $\sqrt{s_{\rm NN}}$= 200 GeV. The black open circles represent the same-event unlike-sign distribution, the brown solid line stands for the mixed-event and the black solid squares represent the raw signal of J/ψ by subtracting combinatorial background.

Within the invariant mass region of 2.9 to 3.2 GeV/c^2, the S/B ratio is about 3.9 and the J/ψ signal significance is about 12.4 in the 40-80% centrality Ru+Ru collisions at $\sqrt{s_{\rm NN}}$= 200 GeV/c. Since the J/ψ from coherent photon-nucleus processes are dominated in very low $p_{\rm T}$ region, we use a pair $p_{\rm T}$ cut to select the raw J/ψ signal interested in this analysis. This pair $p_{\rm T}$ cut is related to the nuclear radius according to the uncertainty relation, smaller nuclear radius will lead to larger pair $p_{\rm T}$ distributions, that's why the pair $p_{\rm T}$ cut utilized in Ru+Ru and Zr+Zr collisions is larger than that employed in Au+Au collisions at same collision energy ($p_{\rm T}$ < 0.1 GeV/c). The similar J/ψ raw signal spectrum at pair $p_{\rm T}$ smaller than 0.2 GeV/c in 40-80% Zr+Zr collisions at $\sqrt{s_{\rm NN}}$= 200 GeV is shown in Fig. 3.19.

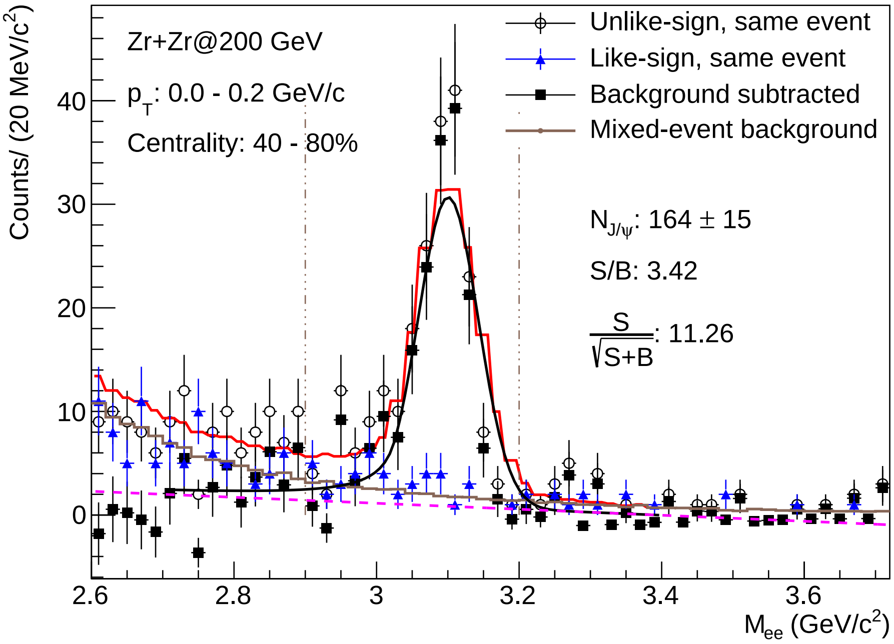

Figure 3.19 The e^+e^- pair invariant mass distribution at pair p_{T} smaller than 0.2 GeV/c in 40-80% Zr+Zr collisions at $\sqrt{s_{\mathrm{NN}}}$= 200 GeV. The black open circles represent the same-event unlike-sign distribution, the brown solid line stands for the mixed-event and the black solid squares represent the raw signal of J/ψ by subtracting combinatorial background.

3.5.4 Momentum smearing in simulation

As aforementioned, when fitting the invariant mass distribution to estimate the residual background contribution, the J/ψ signal template is parametrized using a Crystal-Ball function. Its parameters are extracted from a Toy Monte Carlo (ToyMC) simulation with the momentum resolution of tracks from embedding (the details of embedding in Sec 3.6.1). However, the primary track momentum resolution extracted from embedding is observed to be better than that in the real data, probably because of the exclusion of primary vertex resolution. Therefore, additional momentum smearing is needed to match embedding with real data. To obtain this additional smearing, the J/ψ width as a function of p_{T} is compared between data and embedding. First, we extract the primary track p_T resolution as a function of p_T from embedding for different centrality bins, which is shown in Fig. 3.20. The momentum resolution deteriorates rapidly as the track p_{T} increases, and it can be parameterized with an empirical function:

$$\sigma(p_T) = \sqrt{a^2 p_T^2 + b^2}, \tag{3.9}$$

Since the first term dominates the resolution in Eq. 3.9, the additional momentum smearing is done by varying parameter a, and for each varied parameter, we denote it

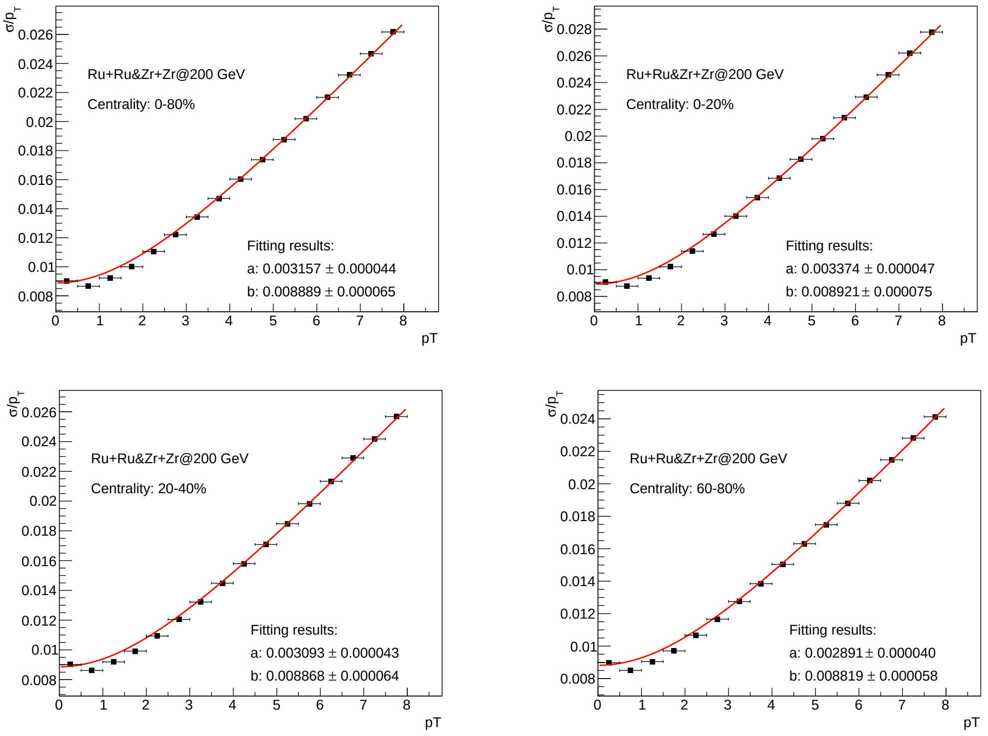

Figure 3.20 The primary track resolution as a function of $p_{\rm T}$ in various centrality bins from dielectron embedding in Ru+Ru collisions. The red line represents fitted result to the $p_{\rm T}$ dependence.

as a'. The smeared $p_{\rm T}$ for each a' is calculated as:

$$p_{T,smear} = p_{T,true} - p_{T,true} \times \frac{\Delta p_T}{p_{T,true}} \times \frac{\sqrt{(a')^2 p_{T,true}^2 + b^2}}{\sigma(p_{T,true})}, \tag{3.10}$$

where $p_{T,true}$ is the true $p_{\rm T}$ for a MC track, $p_{T,reco}$ is the reconstructed $p_{\rm T}$ of the corresponding MC track, and the Δp_T is $p_{T,true} - p_{T,reco}$. We then scan the parameter a' from 0 to 0.02 in the ToyMC and extract the resulting J/ψ signal width as a function of p_T, compare it to the J/ψ signal width from real data and calculate the χ^2 between the two distributions. The resulting χ^2 as a function of a' in 0-80% centrality can be found in Fig. 3.21. A 4th-order polynomial function is fit to the distribution of χ^2 vs. a', as shown in Fig. 3.21, in order to obtain the a' value with minimum χ^2, which is around 0.0056 for the 0-80% centrality bin. The best value a' in 0-80% is used to all the other centrality class due to no significant centrality dependence of the estimated best value.

3.6 Efficiency Correction

To obtain the invariant mass spectrum of e^+e^- pair within the STAR acceptance ($p_T^e > 0.2$ GeV/c, $|\eta_e| < 1$ and $|y_{ee}| < 1$), the raw mass spectrum, as obtained in Sec. 3.5.3, should be corrected for efficiency loss. The e^+e^- pair efficiency is calculated by

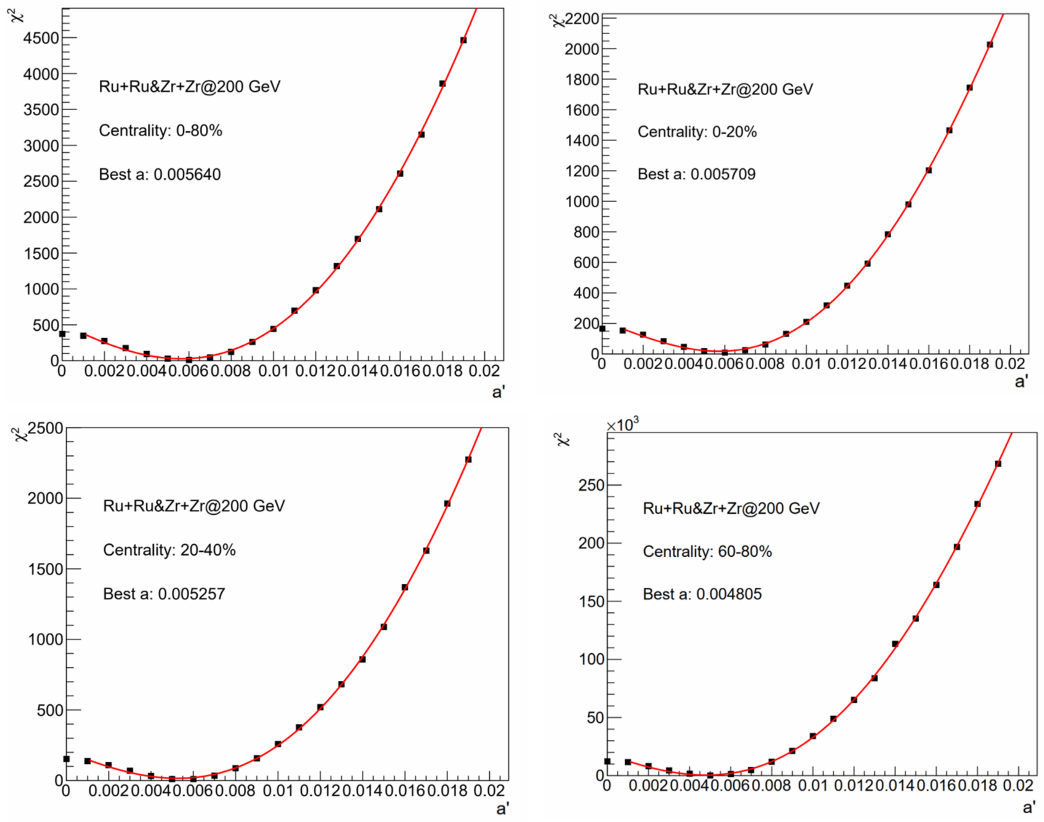

Figure 3.21 The χ^2 between the J/ψ width vs. p_{T} distribution from ToyMC and real data as a function of the smearing factor in 0-80% Ru+Ru collisions.

folding single electron track efficiencies, including the TPC tracking efficiency, the TOF matching efficiency and electron identification efficiency. The single electron efficiency can be written as:

$$\epsilon_e = \epsilon_{\mathrm{TPC}} \times \epsilon_{\mathrm{TOF}} \times \epsilon_{\mathrm{eID}}(\beta, n\sigma_e), \tag{3.11}$$

Silimar, to obtain the invariant yield for the J/ψ meson, the raw counts need to be corrected for efficiency and acceptance loss. The J/ψ meson (ϵ_{pair}) reconstruction efficiency is evaluated by folding the single track efficiency (ϵ_e), similar as for the e^+e^- analysis. For daughter electrons from J/ψ meson decays, the single track efficiency is the same as Eq. 3.15 for p_{T} smaller than 1 GeV/c. For the case of p_{T} larger than 1 GeV/c, the combined single track efficiency can be defined as:

$$\begin{aligned}\epsilon_e =& \epsilon_{\mathrm{TPC}} \times \epsilon_{\mathrm{TOF}} \times (1-\epsilon_{\mathrm{BEMC}}) \times \epsilon_{\mathrm{eID}}(\beta, n\sigma_e) + \\ & \epsilon_{\mathrm{TPC}} \times (1-\epsilon_{\mathrm{TOF}}) \times \epsilon_{\mathrm{BEMC}} \times \epsilon_{\mathrm{eID}}(E_0/p, n\sigma_e) + \\ & \epsilon_{\mathrm{TPC}} \times \epsilon_{\mathrm{TOF}} \times \epsilon_{\mathrm{BEMC}} \times \epsilon_{\mathrm{eID}}(\beta, E_0/p, n\sigma_e),\end{aligned} \tag{3.12}$$

where:

- ϵ_{TPC}: TPC tracking efficiency

- ϵ_{TOF}: TOF matching efficiency
- ϵ_{BEMC}: BEMC matching efficiency
- ϵ_{eID}: electron PID efficiency

3.6.1 Tracking reconstruction efficiency

The tracking reconstruction efficiency is evaluated via the standard STAR embedding technique, which is done by mixing Monte Carlo signals with real data to simulate realistic running conditions. The MC tracks, sampled from specified kinematic ranges, start from event vertex in real data, and their energy losses in the TPC are simulated with GEANT and the TPC respose simulator[173], during which MC TPC electronic signals are generated. These MC signals are then mixed with those from real data to reconstruct TPC clusters, hits, as well as tracks. For this analysis, embedded particles are electrons and positrons with a flat $p_{\rm T}$ distribution from 0 - 10 GeV/c, a flat η distribution from -1.2 to 1.2 and a flat ϕ distribution within 0 to 2π. To prevent any influence on the tracking reconstruction efficiency, the quantity of embedded Monte Carlo (MC) tracks is restricted to 5% of the particle multiplicity observed in the actual event.

The tracking reconstruction efficiency is established by the ratio of the number of reconstructed Monte Carlo (MC) tracks ($N_{\rm Rec}$) that meet the track quality criteria to the number of embedded MC tracks ($N_{\rm Mc}$), as shown in the following equation:

$$\epsilon_{TPC} = \frac{N_{Rec}(|\eta| < 1, nHitsFit > 20, nHitsDedx > 15, DCA < 1, nHitsRatio > 0.52)}{N_{MC}(|\eta| < 1)}, \quad (3.13)$$

We do not expect any difference in the TPC tracking efficiency between Ru+Ru and Zr+Zr collisions, since they have similar multiplicities and the two data sets were taken under almost identical conditions. Nevertheless, this is checked by taking a ratio of the TPC tracking efficiency between Ru+Ru and Zr+Zr collisions, shown in Fig. 3.22. As we can see, ratio is consistent with unity within statistical errors, and therefore, a single TPC tracking efficiency is used for both collision systems. The TPC tracking efficiencies as a function of $p_{\rm T}$ in different centrality classes of isobar collisions are shown in Fig. 3.23, while the 3-D ($p_{\rm T}\,\eta, \phi$) dependence of the TPC tracking efficiency is used in the final correction.

3.6.2 TOF matching efficiency

The TOF matching efficiency is evaluated via a data-driven method by using a pure electron samples from photon conversion and π^0 Daliz decay (see Sec. 3.4.5 for details). It is estimated by the number of electron which are matched to TOF and has a

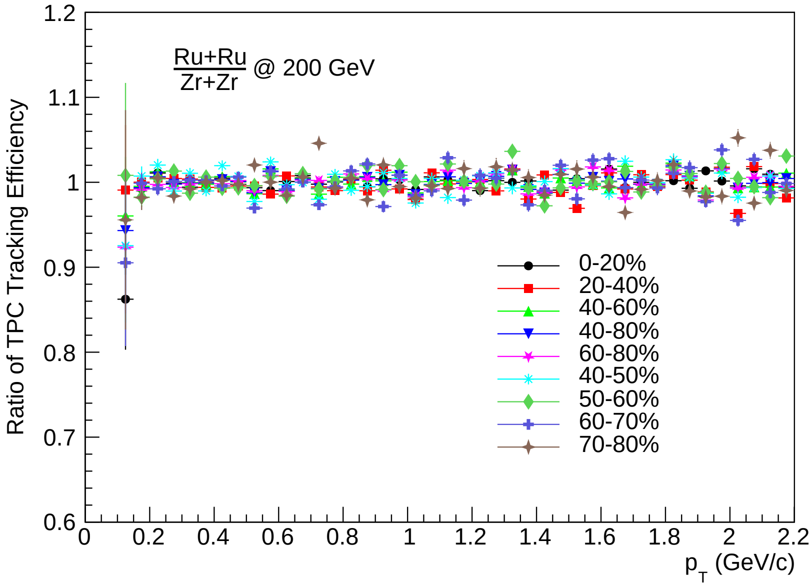

Figure 3.22 **Ratios of the TPC tracking efficiency between Ru+Ru and Zr+Zr collisions as a function of p_T in different centrality bins.**

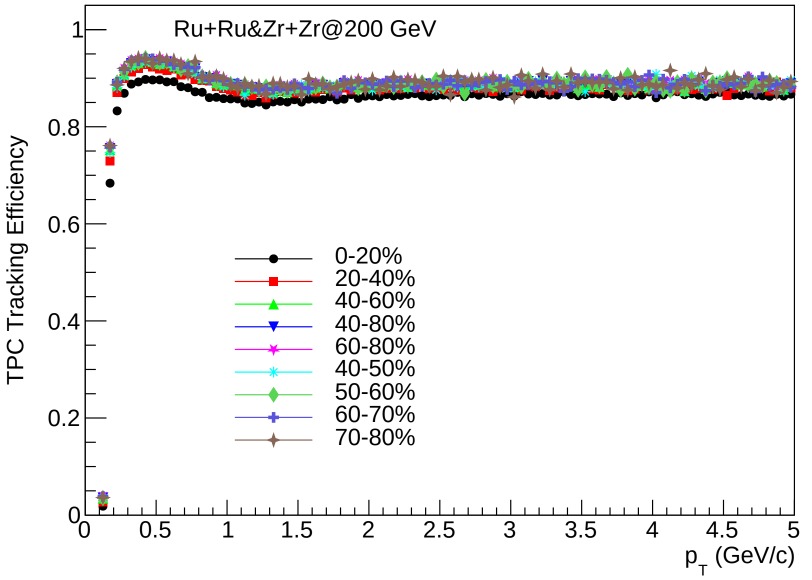

Figure 3.23 **The TPC tracking efficiency in isobaric collisions as a function of p_T in different centrality bins.**

valid TOF measurements ($N_{matched,\beta>0}$) over the total number of photonic electrons in the TPC (N_{TPC}). Here the electron tracks should pass the track quality cuts. To generate 3-D (p_{T} η, ϕ) TOF matching efficiency, a pure pion sample, selected by a tight $n\sigma_\pi$ cut ($|n\sigma_\pi|$ < 0.6), is used [155], due to the limited statistics of the pure electron sample. To correct for the difference in the TOF matching efficiency between electrons and pions, the ratio of the p_{T} dependence of TOF matching efficiency from electron samples to that from pion samples is used to correct for the pion TOF matching efficiency in each η and ϕ bin. The p_{T} dependence of the TOF match efficiency for electrons and poins, as well as their corresponding in 70-80% centrality bin are shown in the left and right panels of Fig. 3.24.

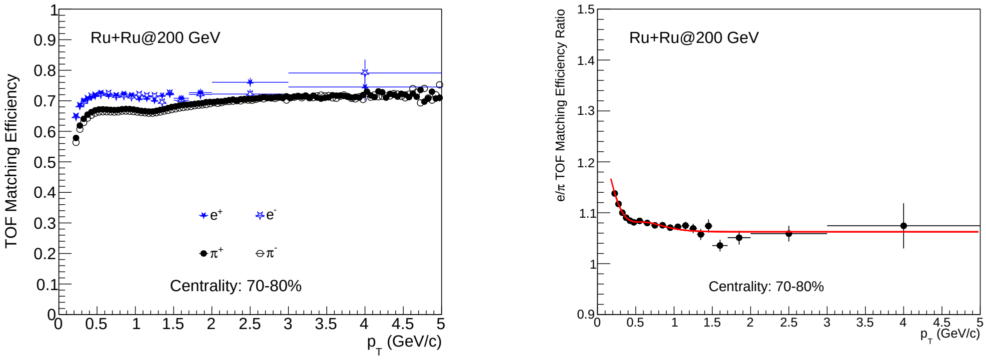

Figure 3.24 The TOF matching efficiency distribution of pure electron and pion samples in 70-80% Ru+Ru collisions (*left panel*) and the corresponding TOF matching efficiency ratio of electron over pion (*right panel*).

3.6.3 BEMC matching and PID efficiencies

The BEMC matching and PID efficiencies are evaluated from the electron embedding sample mentioned above. Tracks reconstructed from Monte Carlo electrons are matched to the BEMC to determine efficiency. For the BEMC matching efficiency, it is calculated as:

$$\epsilon_{BEMC} = \frac{N_{Rec}(E_0 > 0.1, |\eta| < 1, nHitsFit > 20, nHitsDedx > 15, Dca < 1, nHitsRatio > 0.52)}{N_{Rec}(|\eta| < 1, nHitsFit > 20, nHitsDedx > 15, Dca < 1, nHitsRatio > 0.52))}, \qquad (3.14)$$

When the E_0/p is used as one of the electron identification cuts, the PID cut efficiency is combined with the BEMC matching efficiency, which is evaluated as:

$$\epsilon_{BEMC\&PID} = \frac{N_{Rec}(E_0 > 0.1, 0.5 < E_0/p < 1.5, |\eta| < 1, nHitsFit > 20, nHitsDedx > 15, Dca < 1, nHitsRatio > 0.52)}{N_{Rec}(|\eta| < 1, nHitsFit > 20, nHitsDedx > 15, Dca < 1, nHitsRatio > 0.52))}, \qquad (3.15)$$

Figure 3.25 shows the BEMC matching efficiency for electrons as a function of p_{T} in different centrality classes of isobar collisions.

As one can see, there is no obvious centrality dependence in the BEMC matching

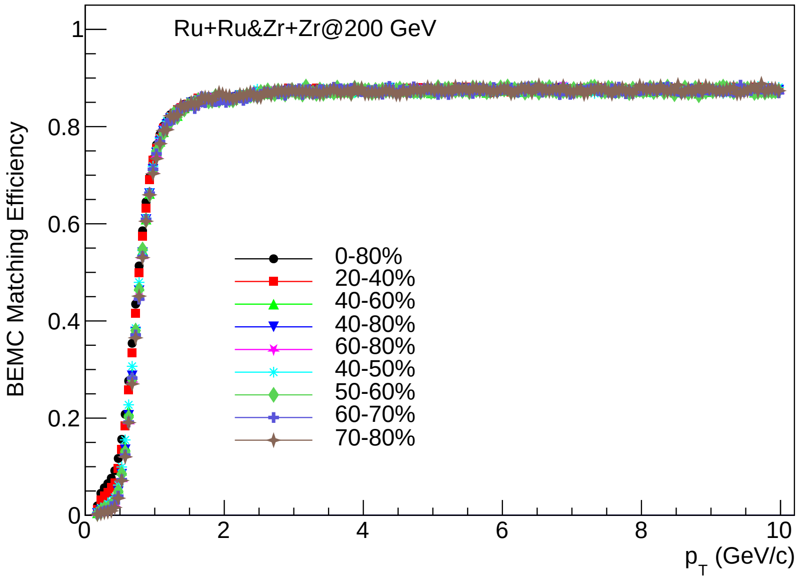

Figure 3.25 The BEMC matching efficiency as a function of $p_{\rm T}$ in isobaric collisions at $\sqrt{s_{\rm NN}}$= 200 GeV/c for different centrality classes.

efficiency. Since the BEMC coverage is similar as the TPC and TOF, the 3-D (p_T, η, ϕ) BEMC matching efficiency is used for final efficiency correction. Figure 3.26 shows the BEMC matching combining E_0/p cuts efficiency for electrons as a function of $p_{\rm T}$ in different centrality classes of isobar collisions.

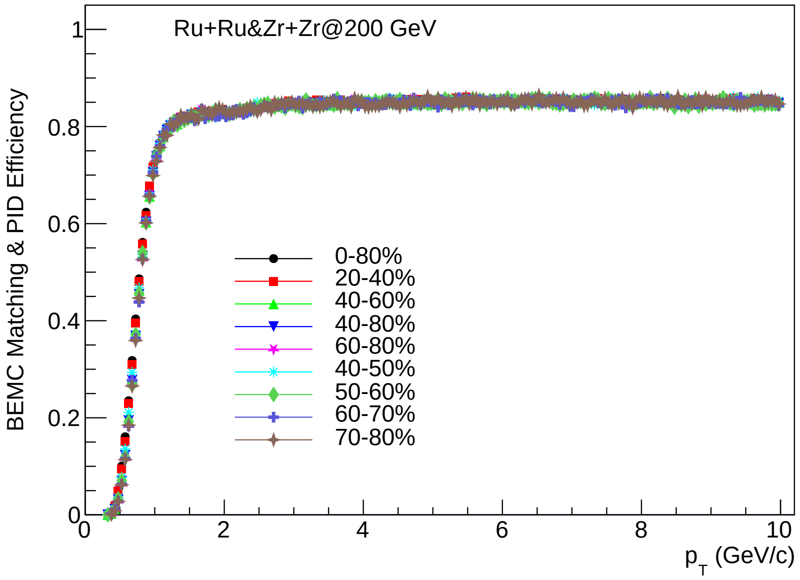

Figure 3.26 The BEMC matching plus PID cut efficiency as a function of $p_{\rm T}$ in isobaric collisions at $\sqrt{s_{\rm NN}}$= 200 GeV/c for different centrality classes.

3.6.4 β and nσ_e cut efficiencies

The electron identification cut efficiency (ϵ_{eID}) includes three components: the TOF velocity ($1/\beta$) cut efficiency, the E_0/p cut efficiency (only for J/ψ signal reconstruction) and the dE/dx ($n\sigma_e$) cut efficiency. The E_0/p cut efficiency has been estimated together with the BEMC matching efficiency, as discussed in previous section. The pure electron sample from data is used to evaluate the $1/\beta$ and $n\sigma_e$ cut efficiencies, separately, because the $n\sigma_e$ distribution from embedding cannot reproduce that in data, as illustrated in Fig. 3.27.

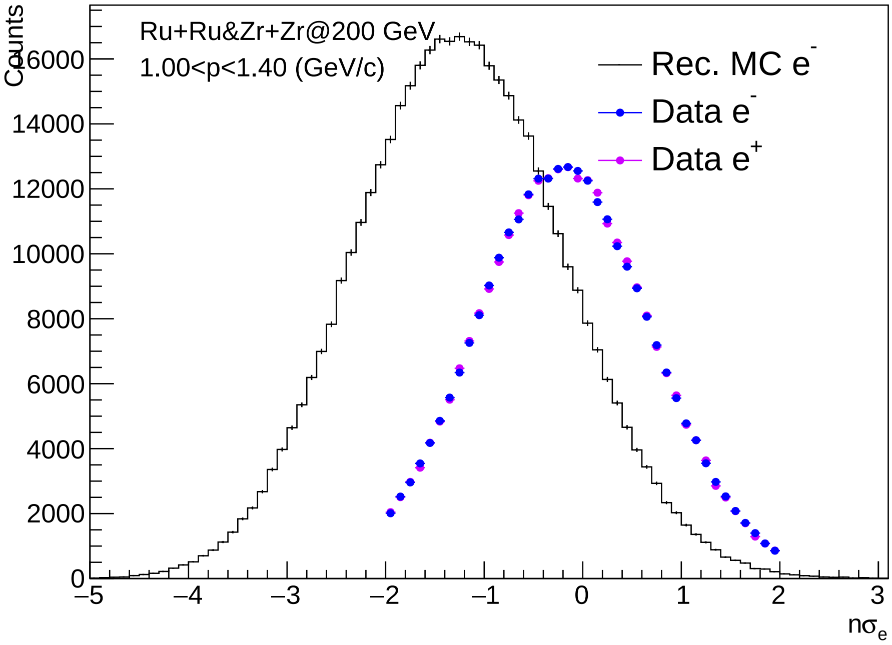

Figure 3.27 The $n\sigma_e$ distribution for electrons within 1-1.4 GeV/c from data and embedding.

The distribution of $1/\beta$ versus momentum is shown in the left panel of Fig. 3.28, where the red dashed lines stand for the $1/\beta$ cuts used in this analysis. Its efficiency is calculated using two methods: the Gaussian fit and bin counting. The default $1/\beta$ cut efficiency is calculated via the counting method, shown in the right panel of Fig. 3.28, while the difference between this two methods is treated as the systematic uncertainty.

The $n\sigma_e$ cut efficiency is derived from fitting the $n\sigma_e$ distribution in each momentum bin with a Gaussian distribution, and shown in Fig. 3.29 for three different sets of cut values, corresponding to different combinations of detectors used for PID. The left panel of Fig. 3.29 shows the $n\sigma_e$ cut efficiency for tracks with $p_{\rm T}$ smaller than 1 GeV/c and those matched only to TOF (for p_T > 1 GeV/c), the middle panel is for tracks only matched BEMC (for $p_{\rm T}$ > 1 GeV/c) and the right panel is for tracks matched to both TOF and BEMC (for $p_{\rm T}$ > 1 GeV/c). For the analysis of e^+e^- pair production, no

BEMC-related PID cuts are used, and only the $n\sigma_e$ cut efficiency shown in the left panel of Fig. 3.29 is used.

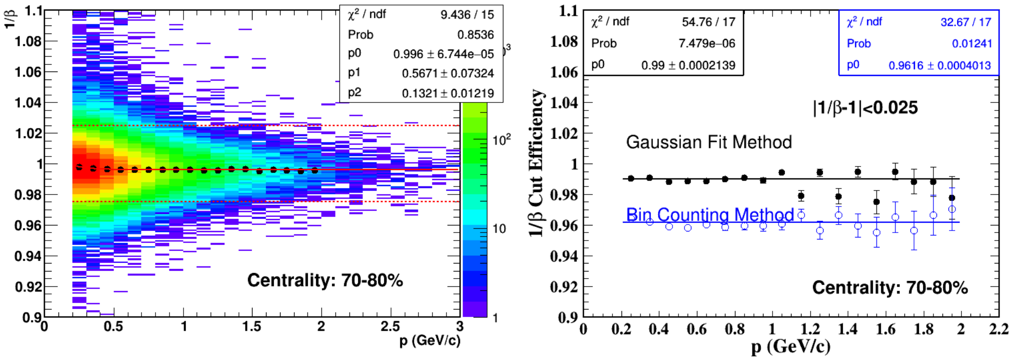

Figure 3.28 The p dependence of electron $1/\beta$ in 70-80% isobaric collisions (*left panel*) and the corresponding $1/\beta$ cut efficiency (*right panel*).

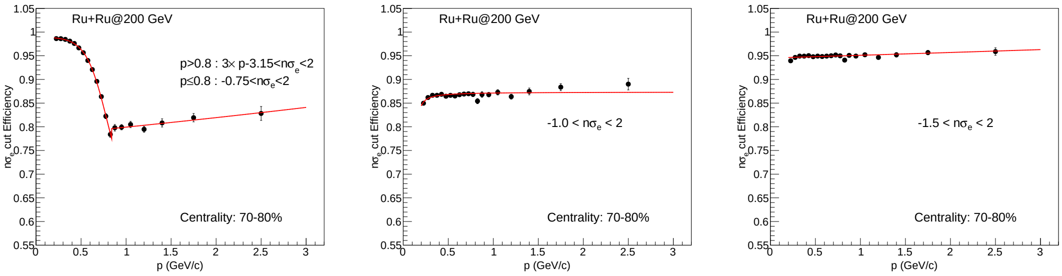

Figure 3.29 The p dependence of the $n\sigma_e$ cut efficiency for different cut values.

3.6.5 Total Detection Efficiency

After the single electron efficiencies are obtained, the e^+e^- pair efficiency is evaluated within the STAR acceptance ($p_T^e > 0.2$ GeV/c, $|\eta_e| < 1$ and $|y_{ee}| < 1$) based on a virtual photon simulation. In such a simulation, a flat distribution of virtual photons in $p_{\rm T}^{ee}$ and M_{ee} decay into electron and positron pairs isotropically. The single track efficiencies, including 3-D TPC tracking and TOF matching efficiencies in ($p_{\rm T}\, \eta, \phi$) and 1-D electron identification efficiency in p, are folded to obtain the 2-D e^+e^- pair efficiency in $p_{\rm T}^{ee}$ and M_{ee}. Figure 3.30 shows the e^+e^- pair efficiency projected to M_{ee} from the virtual photon simulation in different centralities of isobaric collisions at $\sqrt{s_{\rm NN}}$ = 200 GeV.

The total J/ψ reconstruction efficiency is determined by folding the efficiencies of the electron daughters using the J/ψ decay kinematics. A ToyMC model simulation, taking realistic J/ψ kinematic distributions and single electron efficiencies as inputs, is used to calculate the total J/ψ efficiency. The J/ψ $p_{\rm T}$ distribution follows a Tsallis function fit to the RHIC data at 200 GeV in Au+Au collisions. Flats distributions in rapidity (y) from -1 to 1 and in ϕ from -π to π are used. In the decay process, the J/ψ

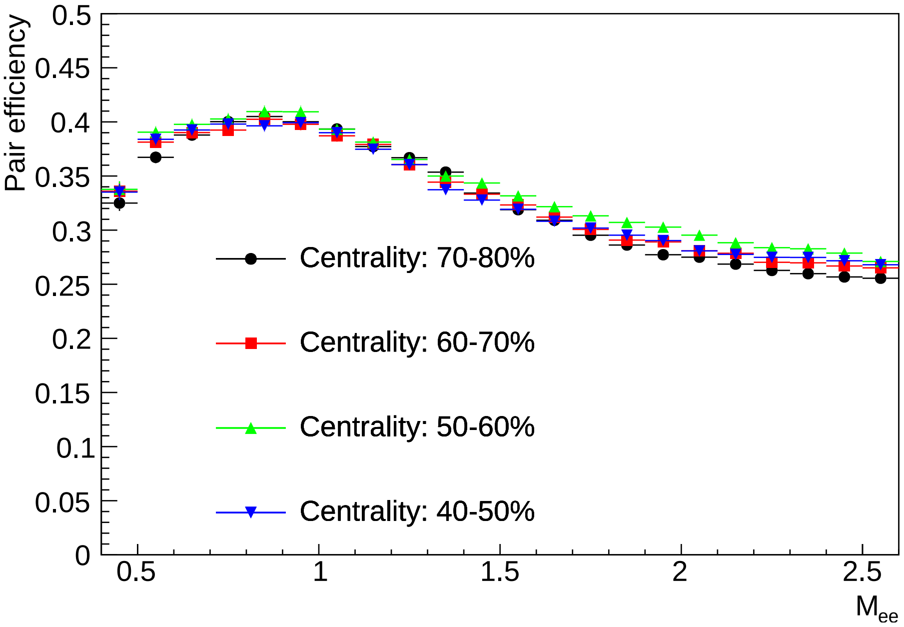

Figure 3.30 The projected 1-D e^+e^- pair efficiency as a function of M_{ee} in different centralities of isobaric collisions at $\sqrt{s_{\mathrm{NN}}}$= 200 GeV/c.

at very low p_T (< 0.2 GeV/c) is set to be fully transversely polarized due to that the coherent produced J/ψ inherits the polarization of colliding photons (fully transverse), while the J/ψ at higher p_{T} are set to be unpolarized. The p_{T} and centrality dependence of the total J/ψ reconstruction efficiency in isobaric collisions at $\sqrt{s_{\mathrm{NN}}}$= 200 GeV/c are shown in Fig. 3.31. There is no clear centrality dependence, and the efficiency decreases as the pair mass increases.

3.7 Hadronic Cocktail for e^+e^- pairs

In addition to e^+e^- pairs from photon-induced interactions, they can also be produced through hadronic decays, known as the hadronic cocktail, whose contribution should be evaluated and subtracted from the corrected inclusive e^+e^- pair mass spectrum. MC simulations are used to estimate the contributions from the following processes:

1) Two-body decays:

- $\omega \rightarrow e^+e^-$
- $\phi \rightarrow e^+e^-$
- $J/\psi \rightarrow e^+e^-$
- $\psi' \rightarrow e^+e^-$

2) Dalitz decays:

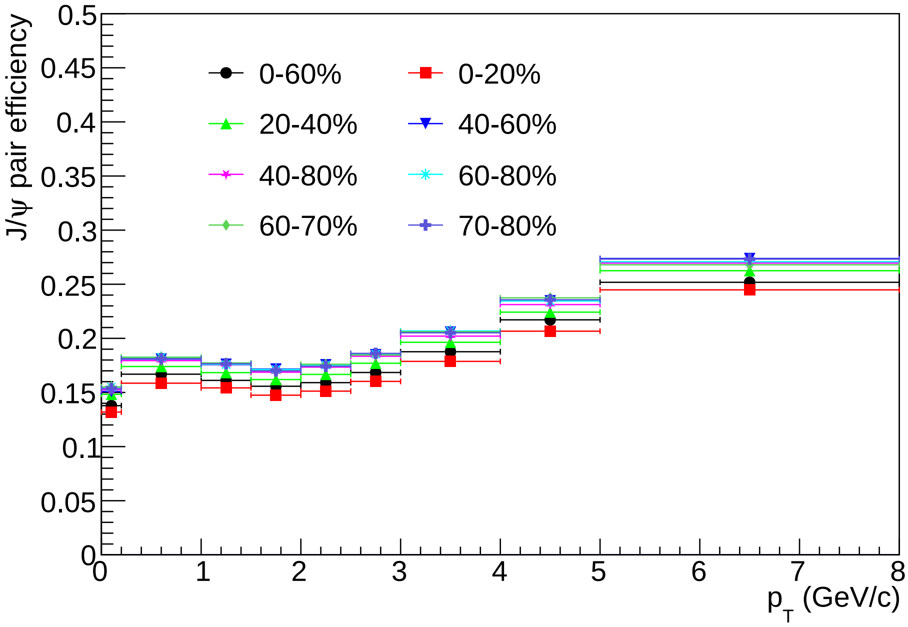

Figure 3.31 The 1-D J/ψ reconstruction efficiency as a function of $p_{\rm T}$ for different centralities of isobaric collisions at $\sqrt{s_{\rm NN}}$= 200 GeV/c.

- $\pi^0 \to e^+e^-\gamma$
- $\eta \to e^+e^-\gamma$
- $\eta' \to e^+e^-\gamma$
- $\omega \to e^+e^-\pi^0$
- $\phi \to e^+e^-\eta$

3) Heavy-flavor decays:

- $c\bar{c}$ $(or\ b\bar{b}) \to e^+e^- + X$

4) Drell-Yan process

The ρ^0 meson, whose spectral function is broadened by the QGP medium, is not considered in the cocktail simulation in this analysis.

Due to the lack of measurements for the hadron yield in isobaric collisions at $\sqrt{s_{\rm NN}}$= 200 GeV, their spectra[147] in Au+Au collisions at the same energy, shown in Fig. 3.32, are used for the cocktail simulation. The measured spectra of various light hadrons, including π, K, η meons, shown as markers in Fig. 3.32, are simultaneously fitted with a core-corona-based Tsallis Blast-Wave (TBW) model[174-175]. The reason why the J/ψ meson is excluded from simultaneously fit is that the J/ψ is not considered as a component of the bulk medium which can be described by the core-corona-based TBW. The $p_{\rm T}$ spectra for unmeasured mesons, like the low $p_{\rm T}$ η, η' and ω , are predicted based on the TBW parameters from fitting light hadron spectra, and shown as solid lines in Fig. 3.32. The rapidity and azimuthal distributions of all input hadrons are assumed

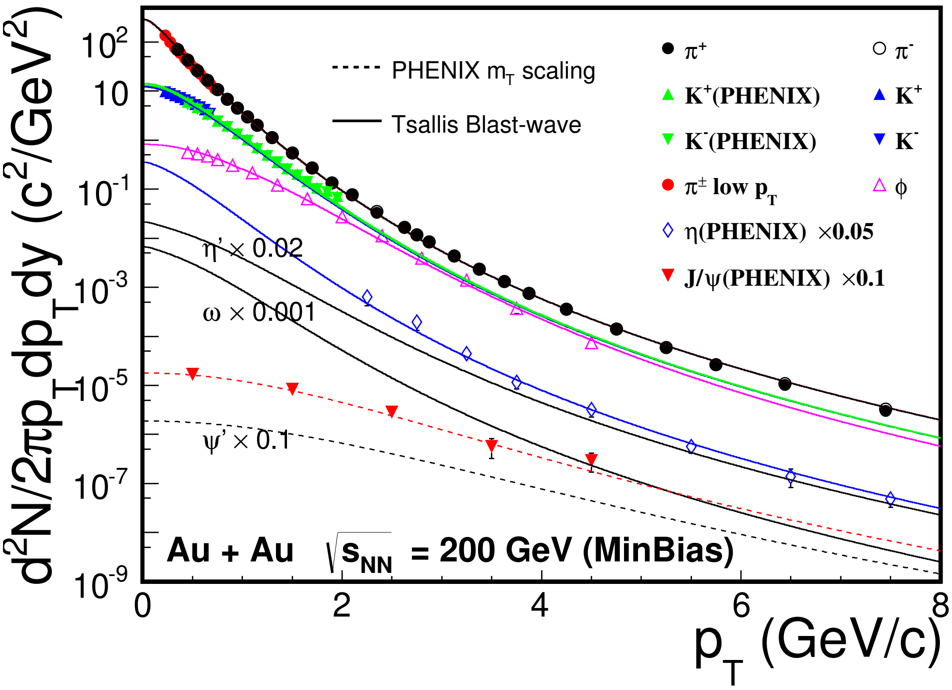

Figure 3.32 Invariant yields of various hadrons in MB Au+Au collisions at $\sqrt{s_{\rm NN}}$= 200 GeV. The simultaneous TBW fit to the measured yields of π, K and ϕ mesons and the predicted yields for η, η' and ω based on the fitted TBW parameters are shown as the solid lines. The dashed lines stand for a TBW fit to the measured J/ψ yield and the predicited yield for the ψ' meson.

to be flat.

In addition to the $p_{\rm T}$ spectrum shapes, the total yields (dN/dy) or cross sections (σ) of input hadrons are also needed. These yields or cross sections in Au+Au collisions at $\sqrt{s_{\rm NN}}$= 200 GeV, along with their uncertainties and corresponding decay branching ratios, can be found in Table III of Ref.[147]. Their yields in isobaric collisions are derived from those in Au+Au collisions based on the N_{part}-scaling. For ω, ϕ, η, and η' in a certain centrality class of the isobaric collisions, the following procedure is followed: i) choose a centrality interval in Au+Au collisions which has the closest N_{part} to that in desired centrality class in isobaric collisions; ii) calculate the hadron yield in Au+Au collisions in chose centrality interval as $\frac{dN}{dy}(hadrons, 0-80\%) \times \frac{dN/dy(\pi^0, Cent)}{dN/dy(\pi^0,\ 0-80\%)}$; iii) scale the hadron yield in the chosen Au+Au centrality interval with the N_{part} ratio between Au+Au and isobar collisions. For the π^0 meson, the yields have already been measured in different centrailty bins of Au+Au collisions, and therefore can be directly scaled by the N_{part} ratio between Au+Au and Isobar collisions. The J/ψ and ψ' mesons, as the bound state of heavy flavor quark(c), are mainly produced during the initial hard scattering which have different production mechanism compared to the light flavor mesons. So, the yields of J/ψ and ψ' meson are from the direct measurement in isobaric collisions.

The daughter electrons' kinematics ($p_{\rm T}$, η and ϕ) are mainly determined by the decay mode when the kinematics and species of the parent hadron fixed. There are two different decay mode for the simulated cocktail processes, the two-body decay and Dalitz decay.

The contributions of heavy flavor decays and the Drell-Yan process are simulated by the PYTHIA (version 6.419) event generator[176]. Their contributions in a certain centrality class of isobaric collisions are obtained by simulating these processed in p+p collisions at $\sqrt{s}$ = 200 GeV and then scaling them by the N_{coll} value of the corresponding centrality class. The parameters used for PYTHIA simulations are the following:

- $c\bar{c} \to e^+e^-$: MSEL = 4 (c trigger), PARP(91) = 1 ($\langle k_T \rangle$ = 1.0 GeV/c), PARP(67) = 1.0 (parton shower level)
- $b\bar{b} \to e^+e^-$: MSEL = 5 (b trigger), PARP(91) = 1.5 ($\langle k_T \rangle$ = 1.5 GeV/c)
- Drell-Yan: MSEL = 11 (Z_0 or γ^* trigger), PARP(91) = 1.5 ($\langle k_T \rangle$ = 1.5 GeV/c)

For $c\bar{c}$ production, the PYTHIA parameters are tuned to match the measured charmed-meson spectrum and charm-quark production cross section p+p collisions at STAR[177-178]. For the Drell-Yan process and $b\bar{b} \to e^+e^-$, the same PYTHIA parameters are used except for the trigger setting. The input cross sections for the $b\bar{b}$ pair and Drell-Yan production are $\sigma^{b\bar{b}}_{pp}$ = 3.7 μb and $\sigma^{b\bar{b}}_{\rm DY}$ = 42 nb, respectively.

The cocktail simulation is done in the same STAR acceptance ($p^e_{\rm T}$ > 0.2 GeV/c, $|\eta_e| < 1$ and $|y_{ee}| < 1$) as the e^+e^- measurement with the same momentum resolution, as evaluated in the Sec. 3.5.4.

Since the $\langle N_{part} \rangle$ and $\langle N_{coll} \rangle$ values for the same centrality in Ru+Ru and Zr+Zr collisions are slightly different, the cocktail simulation is carried out for the two collision systems separately. The interested signal of e^+e^- pairs are from coherent photon-photon interactions, the pair $p_{\rm T}$ is dominated by the very low $p_{\rm T}$ region (< 0.15 GeV/c), so, the cocktail simulation for this $p_{\rm T}$ region is obtained and shown in Fig. 3.33.

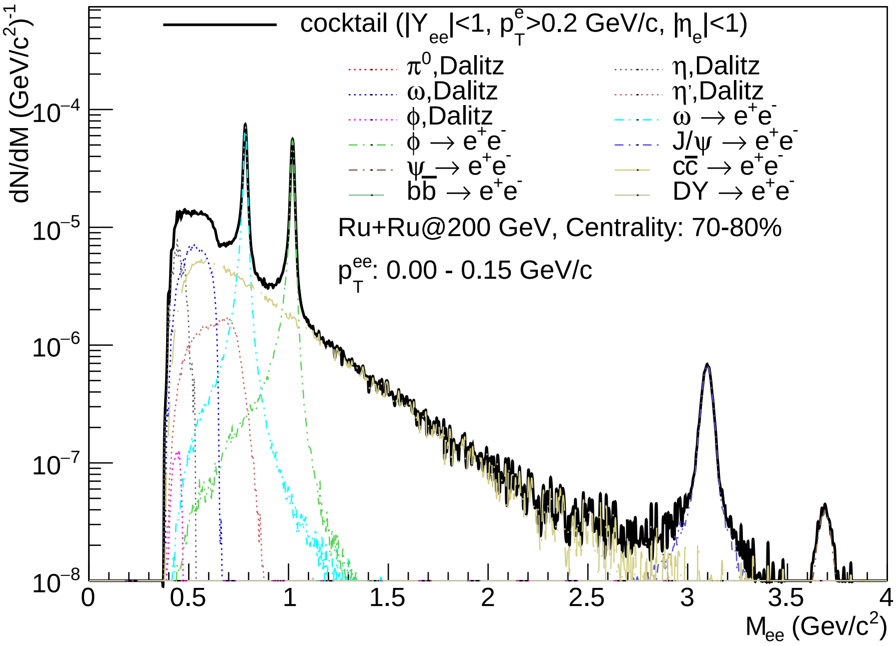

Figure 3.33 The cocktail simulation within the STAR acceptance (solid line) in Ru+Ru collisions at $\sqrt{s_{\rm NN}}$= 200 GeV for $p_{\rm T}$ < 0.15 GeV/c. The different styles of dashed lines are for different processes.

3.8 Systematic Uncertainties

The systematic uncertainties in this work are calculated by comparing the default results with the results obtained from varied cuts as the following::

$$
\begin{aligned}
\sigma^{i}_{sys} &= \frac{\text{Results}_{\text{varied cut i}} - \text{Results}_{\text{default}}}{\text{Results}_{\text{default}}} \\
\sigma^{tot}_{sys} &= \sqrt{\sum_{i=1}^{k}(\sigma^{i}_{sys})^2}
\end{aligned}
\tag{3.16}
$$

where the σ^{i}_{sys} is the systematic uncertainty from varying cut i, and different sources are added quadratically to obtain the total systematic uncertainty, σ^{tot}_{sys}.

Due to the differences in the analysis procedures for the measurements of e^+e^- pair and J/ψ production, the systematic uncertainties of the two analyses are evaluated separately.

3.8.1 Systematic uncertainties for e^+e^- pair production

For the meaurements of the e^+e^- pair production, the final results include the invariant mass and $p_{\rm T}$ spectra, the excess yield of e^+e^- pair production and the excess yield ratio between Ru+Ru and Zr+Zr collisions, which will be presented in details in Sec. 5.1. The systematic uncertainties are estimated by varying the tracking quality cuts and electron identification cuts.

The track quality cuts are varied as the following:

- The DCA cut is changed from the default value of 1.0 cm (DCA < 1.0 cm) to 0.8 cm and 1.5 cm
- The nHitsDedx and nHitsFit (default: nHitsDedx < 15 and nHitsFit < 20) cuts are changed to nHitsDedx < 10 and nHitsFit < 15

The track quality cuts are changed simultaneously in real data and embedding to estimate the associated uncertainties. The differences between default e^+e^- pair invariant mass spectrum and those obtained with varied cuts in 70-80% Ru+Ru collisions are shown in Fig. 3.34. From left to the right panel, they correspond to varied track quality cuts of tighter dca cut, looser dca cut and looser nHitsFit/nHitsDedx cut. Since no significant dependence on the invariant mass is observed, the differences are fit with a constant, which is taken as the systematic uncertainty from the certain cut variation. The fit results are also listed in the figure. Similar results for e^+e^- pair p_{T}spectrum, excess e^+e^- yield and excess yield ratio between Ru+Ru and Zr+Zr collisions are shown in Fig. 3.35,3.36,3.37,3.38.

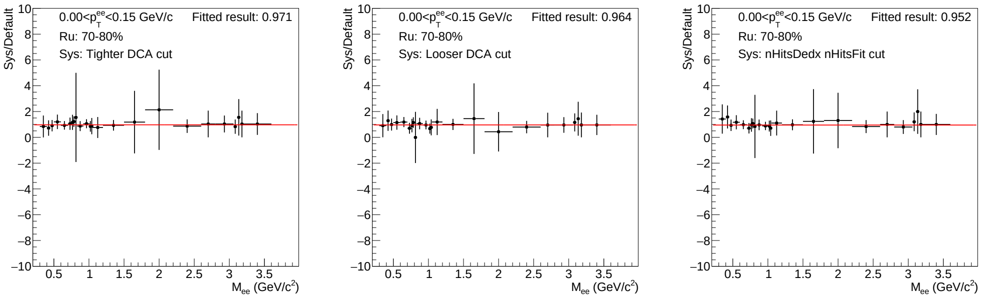

Figure 3.34 Invariant mass dependence of the differences between default and varied results due to changes in track quality cuts in 70-80% Ru+Ru collisions. The red lines are the fit results to the differences using a constant function.

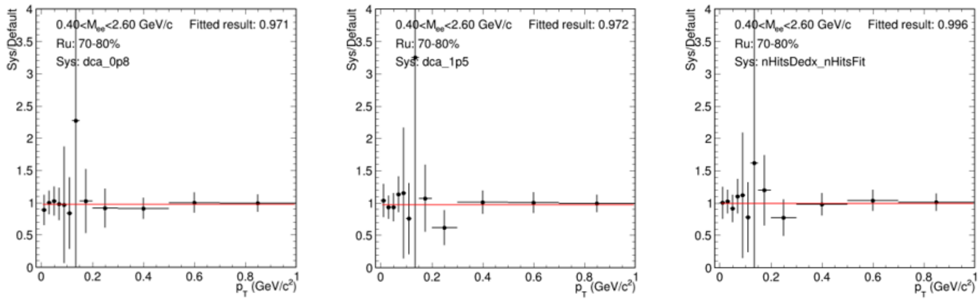

Figure 3.35 Pair p_{T} dependence of the differences between default and varied results due to changes in track quality cuts in 70-80% Ru+Ru collisions. The red lines are the fit results to the differences using a constant function.

The uncertainties of electron PID for e^+e^- pair production measurement are evalu-

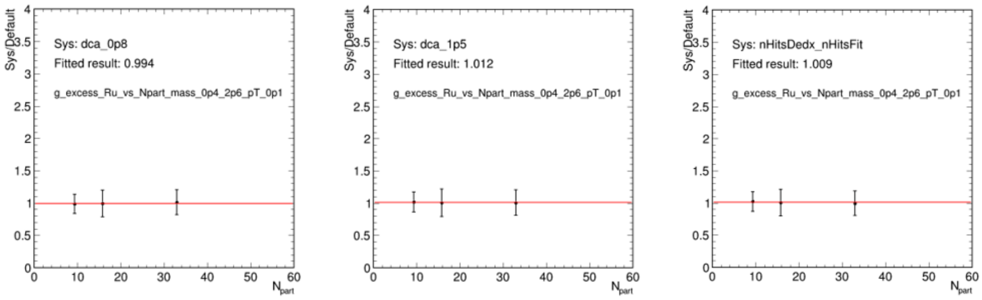

Figure 3.36 $\langle N_{part} \rangle$ **dependence of the differences between default e^+e^- pair excess yield and varied results due to changes in track quality cuts in 70-80% Ru+Ru collisions. The red lines are the fit results to the differences using a constant function.**

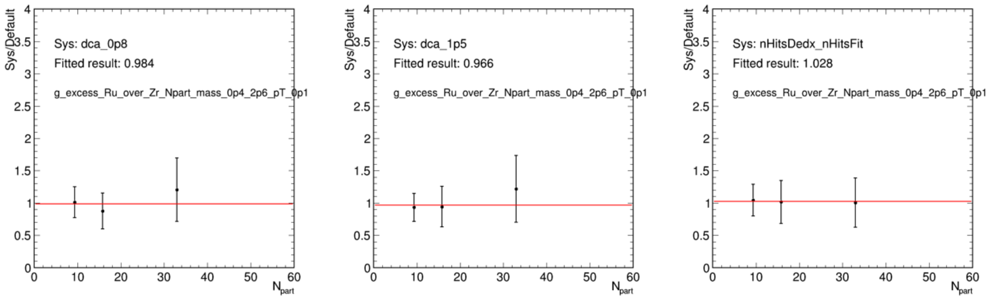

Figure 3.37 $\langle N_{part} \rangle$ **dependence of the differences between default e^+e^- pair excess yield ratio and varied results due to changes in track quality cuts in 70-80% Ru+Ru collisions. The red lines are the fit results to the differences using a constant function.**

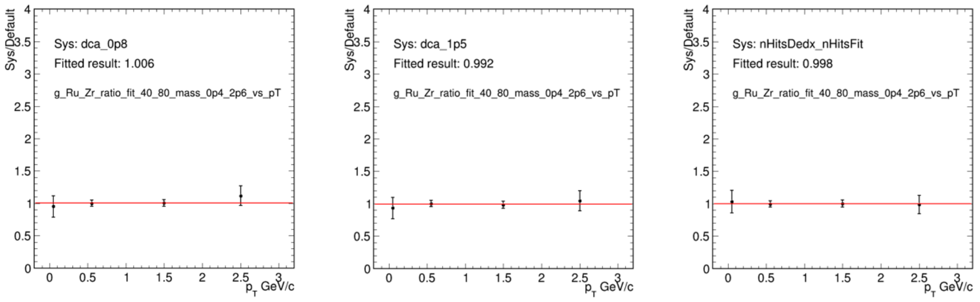

Figure 3.38 Pair p_{T} dependence of the differences between default e^+e^- pair excess yield ratio and varied results due to changes in track quality cuts in 70-80% Ru+Ru collisions. The red lines are the fit results to the differences using a constant function.

ated by varying $n\sigma_e$ and $1/\beta$ cuts, as the electron candidates sample selected based only on the TPC and TOF information. The specific cut variations are listed below:

- The boundaries of the nσ_e cut is reduced by 0.1.
- The boundaries of the nσ_e cut is increased by 0.1.
- The boundaries of the $1/\beta$ cut is increased by 0.005.

The electron identification cuts are also changed simultaneously in real data and efficiency correction to estimate the associated uncertainties. Figure 3.39 shows the corresponding differences of the e^+e^- pair mass spectra with respect to those using varied electron identification cuts in 70-80% Ru+Ru collisions. As is the case for the tracking quality cut uncertainty, the difference are fitted by a constant function, which are shown as the red lines. Similar results for e^+e^- pair $p_{\rm T}$ spectrum, excess e^+e^- yield and excess yield ratio between Ru+Ru and Zr+Zr collisions are shown in the Figure3.40,3.41,3.42,3.43.

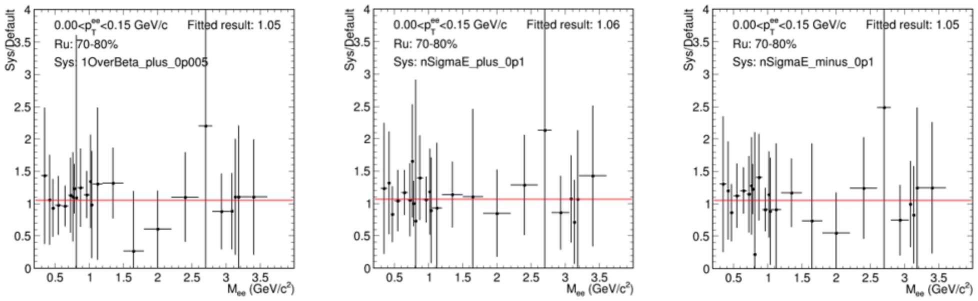

Figure 3.39 The invariant mass dependence of the differences between default e^+e^- pair production and varied results in 70-80% Ru+Ru collisions. The red lines are the fit results using a constant function.

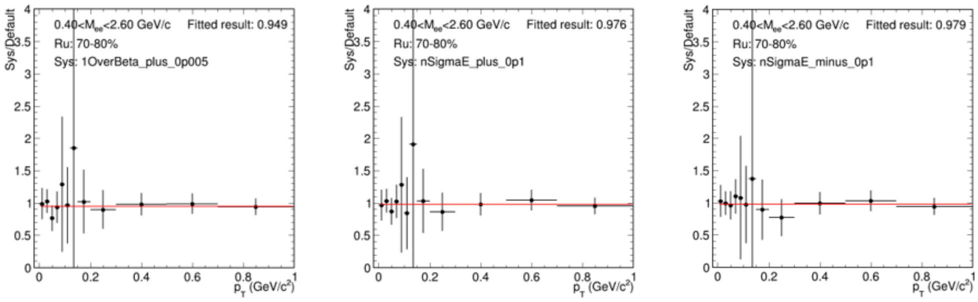

Figure 3.40 The pair $p_{\rm T}$ dependence of the differences between default e^+e^- pair production and varied results in 70-80% Ru+Ru collisions. The red lines are the fit results using a constant function.

The systematic uncertainties for measurements in Zr+Zr collisions are estimated using the same method as in Ru+Ru collisions, and the results are summarized in Table 3.10, Table 3.11, Table 3.12 for both systems.

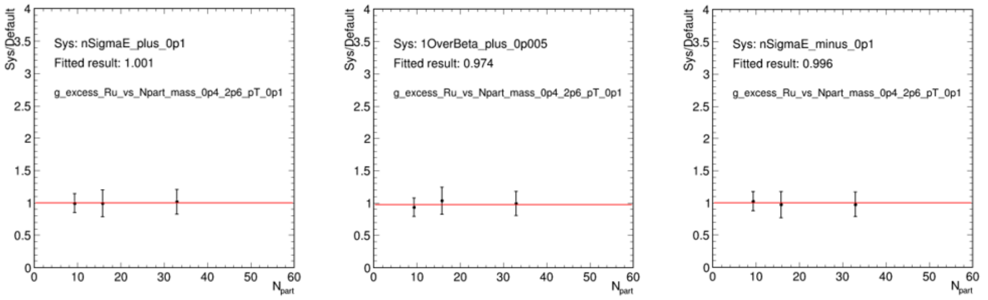

Figure 3.41 The $\langle N_{part} \rangle$ dependence of the differences between default e^+e^- pair excess yield and varied results in 70-80% Ru+Ru collisions. The red lines are the fit results using a constant function.

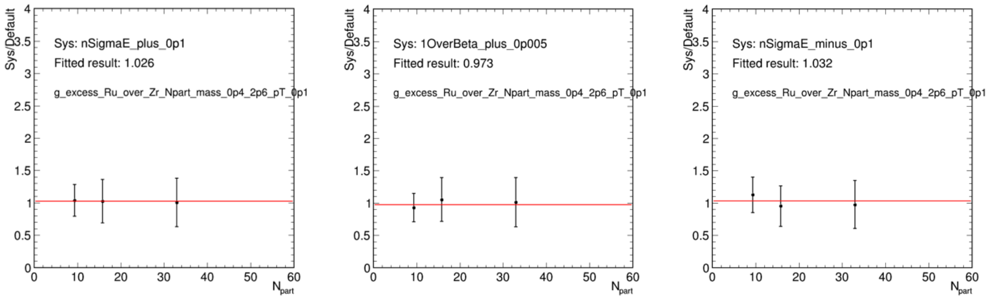

Figure 3.42 The $\langle N_{part} \rangle$ dependence of the differences between default e^+e^- pair excess yield ratio and varied results in 70-80% Ru+Ru collisions. The red lines are the fit results using a constant function.

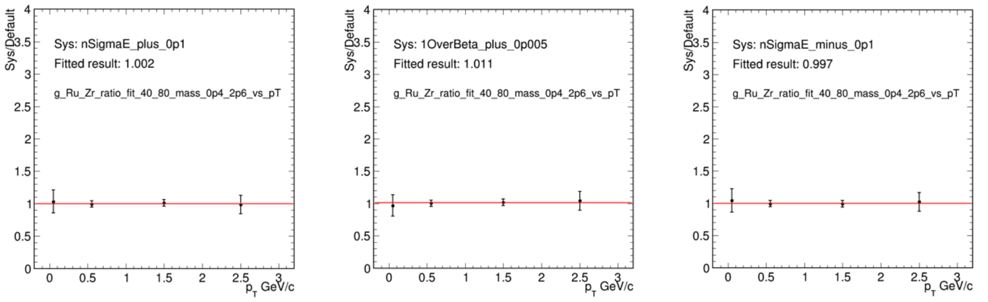

Figure 3.43 The pair $p_{\rm T}$ dependence of the differences between default e^+e^- pair excess yield ratio and varied results in 70-80% Ru+Ru collisions. The red lines are the fit results using a constant function.

Ru/ Zr (%)	70 - 80 %	60 - 70 %	40 - 60 %
Dca	3.6/12.1	8.4/2.6	7.8/4.3
nHitsDedx/nHitsFit	4.8/3.5	2.5/7.2	0.2/0.2
nσ_e	6.0/10.0	4.0/6.0	6.0/8.0
1/β	5.0/1.5	1.0/7.0	3.0/5.0
Total	9.8/16.0	9.7/12	10.3/10.4

Table 3.9 The systematic uncertainties for the e^+e^- pair mass spectra in Ru+Ru and Zr+Zr collisions respectively, the number on the left side (black) is results in Ru+Ru collisions and the right (red) one is from Zr+Zr collisions.

Ru/ Zr (%)	70 - 80 %	60 - 70 %	40 - 60 %
Dca	2.9/2.2	1.3/3.5	0.4/0.6
nHitsDedx/nHitsFit	0.4/1.0	1.9/0.8	0.3/0.2
nσ_e	2.4/1.4	0.6/1.9	0.4/0.5
$1/\beta$	0.5/3.3	0.5/0.9	0.4/0.4
Total	3.8/4.3	2.4/4.2	0.8/0.9

Table 3.10 The systematic uncertainties for the e^+e^- pair $p_{\rm T}$ spectra in Ru+Ru and Zr+Zr collisions respectively, the number on the left side (black) is results in Ru+Ru collisions and the right (red) one is from Zr+Zr collisions.

Ru/ Zr (%)	Excess Yield (vs $\langle N_{part}\rangle$)
Dca	1.2/3.0
nHitsDedx/nHitsFit	0.9/1.7
nσ_e	0.4/4.6
$1/\beta$	2.6/0.3
Total	3.0/5.8

Table 3.11 The systematic uncertainties for the e^+e^- pair excess yield as function of $\langle N_{part}\rangle$ distribution in Ru+Ru and Zr+Zr collisions respectively, the number on the left side (black) is results in Ru+Ru collisions and the right (red) one is from Zr+Zr collisions.

	Excess Yield ratio (vs $\langle N_{part}\rangle$)	Excess Yield ratio (vs $p_{\rm T}$)
Dca	3.4	0.8
nHitsDedx/nHitsFit	2.8	0.2
nσ_e	3.2	0.3
$1/\beta$	2.7	1.1
Total	6.1	1.4

Table 3.12 The systematic uncertainties for the e^+e^- pair excess yield ratio as function of $\langle N_{part}\rangle$ and pair $p_{\rm T}$ distribution in Ru+Ru and Zr+Zr collisions respectively, the black one is results in Ru+Ru collisions and the red one is from Zr+Zr collisions.

3.8.2 Systematic uncertainties for J/ψ production

For the measurement of J/ψ production at very low $p_{\rm T}$ in isobaric collisions, the systematic uncertainties are estimated for the following sources: signal extraction, TPC tracking efficiency, TOF and BEMC matching efficiencies as well as the electron identification efficiency. The total systematic uncertainties are determined by summing the individual sources in quadrature, are 7.4%, 9.0%, and 12.5% in 20-40%, 40-60%, and 60-80% centrality respectively.

The J/ψ raw signal extraction procedure is described in Sec. 3.5.3 and the associated systematic uncertainty is evaluated by applying the following variations:

- The invariant mass range used to obtain the normalization factor for mixed events is varied from [2.6, 3.6] GeV/c^2 to [2.5, 3.7] GeV/c^2 and [2.7, 3.5] GeV/c^2.
- The bin width of the invariant mass distribution is changed from 20 MeV/c^2 to 50 MeV/c^2.
- The fitting range for extracting residual background contribution is changed from [2.6, 3.4] GeV/c^2 to [2.7, 3.3] GeV/c^2 and [2.5, 3.5] GeV/c^2.

- The fit function for the residual background is changed from a linear function to a constant function.
- The raw counts are obtained from fitting instead of the default bin-counting method.

After changing the signal extraction procedure, the raw J/ψ yields are obtained and compared to the default one as a function of $p_{\rm T}$ bins in different centrality classes. Ratios of varied results to the default one are displayed in the Figure 3.44. The red lines in Fig. 3.44 stand for the fit results via a constant of the maximum ratio which is shown as the black dash lines in each $p_{\rm T}$ bins, due to quite weak dependence of $p_{\rm T}$. The maximum deviation is taken as the uncertainty for each $p_{\rm T}$ while the fitting result in each centrality is taken as the uncertainty for this centrality class.

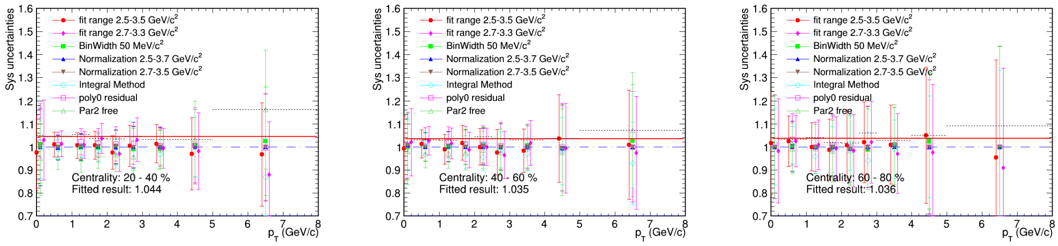

Figure 3.44 **Ratio of the raw J/ψ counts as function of $p_{\rm T}$ between different variations and the default case. From left to right are results in 20-40%, 40-60%, and 60-80% centrality classes, respectively.**

The systematic uncertainties for the TPC tracking efficiency are estimated by varing the track quality cuts, the same method as used for the e^+e^- pair production measurement. The changes in the corrected J/ψ yields are shown in Fig. 3.45 by taking into account both the variantions in the raw J/ψ counts and the corresponding TPC tracking efficiency. The black dash lines are the maximum deviations in each $p_{\rm T}$ bin and the red solid lines are the fitted results to the maximum deviation by a constant line, since its $p_{\rm T}$ dependence is quite weak. The fitted result in each centrality class is taken as the uncertainty.

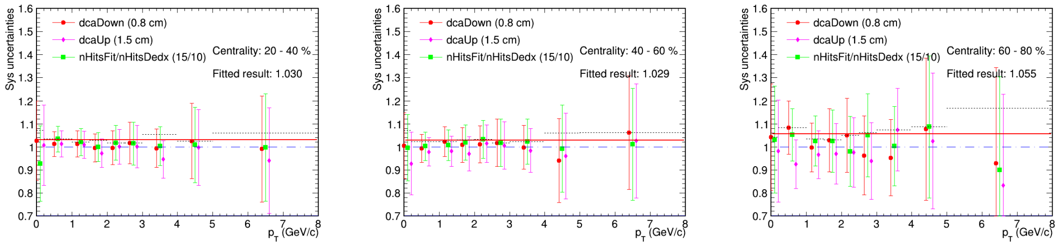

Figure 3.45 **The ratio of the corrected J/ψ counts as function of p_T between different variations and the default case in different centrality bins. From left to right are results in 20-40%, 40-60%, and 60-80% respectively.**

The third systematic source for the J/ψ analysis is related to the electron identification, including those originating from the $n\sigma_e$, the E_0/p and $1/\beta$ cuts. These are estimated using the same procedure as for the e^+e^- pair production analysis. The $n\sigma_e$ cut is varied from the default one to those increased or decreased by 0.1 for both lower and upper bounds. The E_0/p cut is changed from the default cut of (0.5,1.5) to (0.4,1.6) and (0.6,1.4). The uncertainty of $1/\beta$ has been discussed in the Sec. 3.6.4. The variations of corrected J/ψ counts using different $n\sigma_e$ and E_0/p cuts, compared to the default one, are shown in Fig. 3.46 in each p_T bin for different centrality classes. Similarly, the fitted results to maximum deviations are used as the uncertainties.

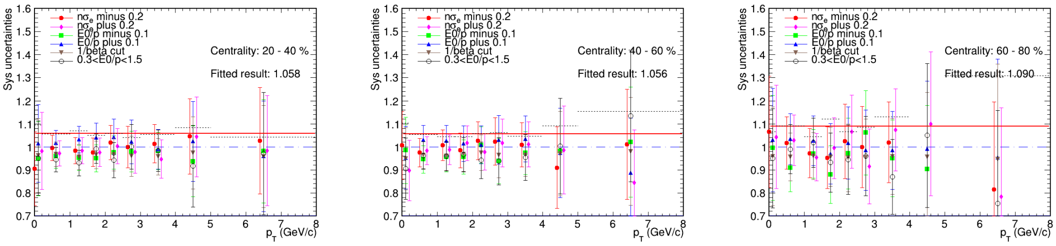

Figure 3.46 The ratio of the corrected J/ψ counts as function of p_T between different variations and the default case in different centrality bins. From left to right are results in 20-40%, 40-60%, and 60-80% respectively.

The BEMC matching efficiency and the TOF matching efficiency are not completely independent, however the acceptances of TOF and BEMC are largely overlapping which largely reduces the correlation between BEMC and TOF matching efficiency. Such a correlation is considered as one of systematic uncertainty sources. Its magnitude is estimated as the difference in the BEMC matching efficiency with or without matching to TOF. The systematic uncertainties for the measurement of J/ψ production at very low $p_{\rm T}$ in isobaric collisions are summarised in the Table 3.13.

Systematic(%)	20 - 40 %	40 - 60 %	60 - 80 %
Signal Extraction	4.4	3.5	3.6
TPC tracking	3.0	2.9	5.5
PID	4.7	5.1	8.4
TOF&BEMC Geometry	2.2	5.9	6.5
Total	7.4	9.0	12.5
0-0.2 GeV/c	8.1	8.9	10.3
0.2-1.0 GeV/c	6.4	8.0	9.7
1.0-1.5 GeV/c	7.4	7.8	9.9
1.5-2.0 GeV/c	6.4	8.0	9.1
2.0-2.5 GeV/c	5.8	8.2	8.9
2.5-3.0 GeV/c	6.4	8.3	11.1
3.0-4.0 GeV/c	6.0	7.7	9.4
4.0-5.0 GeV/c	6.6	8.7	10.9
5.0-8.0 GeV/c	9.7	13.0	15.1

Table 3.13 Total and individual systematic uncertainties for the J/ψ production at very low $p_{\rm T}$ in isobaric collisions.

Chapter 4 J/ψ Yield in Au+Au Collisions at $\sqrt{s_{\rm NN}}$= 54.4 GeV/c

Among various probes utilized for studying QGP properties, quarkonia play a unique role. These are bound states of heavy quarks and their anti-quarks, with masses significantly larger than the QCD scale. Quarkonia production yields are subject to modifications in the presence of the QGP. Effects of the hot medium on quarkonia encompass dissociation due to static color screening of the potential between the heavy quark pair[179], dynamical color screening or collisional dissociation caused by interactions with medium constituents[86-88], and regeneration from deconfined heavy quarks and anti-quarks[89-90]. Additionally, due to the presence of nuclei in the collisions, there are unavoidable modifications from Cold Nuclear Matter (CNM) effects. These arise from changes in parton distribution functions in nuclei compared to those in free nucleons, energy loss in the colliding nuclei, the Cronin effect, nuclear absorption, and other final state effects such as dissociation by co-movers[180-184].

The J/ψ meson, the most abundantly produced quarkonium state accessible experimentally, has been studied extensively over the past nearly thirty years[185-189]. Inclusive J/ψ yield includes three main sources: J/ψ mesons produced directly during the initial partonic scatterings, those from decays of excited charmonium states, such as χ_c and ψ(2S), as well as those from decays of long-lived b-hadrons (called non-prompt J/ψ). Measurements of J/ψ production yields at mid-rapidity have been achieved in Pb+Pb collisions at center-of-mass energy per nucleon-nucleon collision ($\sqrt{s_{\rm NN}}$) of 17.3 GeV at SPS[103-104], 2.76 and 5.02 TeV at the LHC[105,190], as well as in Au+Au collisions at $\sqrt{s_{\rm NN}}$ = 39, 62.4 and 200 GeV at RHIC[96,106-107,191-192]. Significant suppression is observed at SPS and RHIC compared to the scaled J/ψ yields in p+p collisions of the same energy, and the level of the suppression is found to be similar although the temperature and energy density of the produced medium are significantly different due to an order of magnitude difference in $\sqrt{s_{\rm NN}}$. The similarity of the suppression is interpreted as the interplay of the energy dependent dissociation in the QGP, CNM effects, and the regeneration contribution. The importance of the regeneration contribution is corroborated by the observation of decreasing J/ψ suppression from the top RHIC energy to LHC energies[105,193-194].

In this chapter, we explore the transverse momentum ($p_{\rm T}$) and centrality dependence of the nuclear modification factor for inclusive J/ψ at mid-rapidity ($|y| < 1$) using a significantly larger sample of Au+Au collisions at $\sqrt{s_{\mathrm{NN}}}$ = 54.4 GeV. Additionally, we present the average transverse momentum as a function of collision centrality. To gain further insights into the collision energy dependence of inclusive J/ψ production, we compare the new measurements with published data and theoretical calculations.

4.1 Analysis setup

4.1.1 Data set information

The dataset was collected during the RHIC year run 2017 in Au+Au collisions at $\sqrt{s_{\mathrm{NN}}}$ = 54.4 GeV by STAR. The MB trigger was employed for event selection, defined as a coincidence between the two vertex position detectors (VPD) or a coincidence between the two zero-degree calorimeters (ZDC). The trigger IDs used in this analysis are 580001, 580011, and 580021, as summarized in Table 4.1, along with the offline production tag, production library, and the number of triggered events. The total number of minimum-bias events utilized in this analysis is approximately 1.3 billion.

data set	trigger id	production tag	library	number of event
AuAu54_production_2017	580001	P18ic	SL20c	201 M
	580011			1.04 M
	580021			1.13 B

Table 4.1 Summary of trigger ids, offline production libraries and recorded number of minimum-bias events

The event-level and track quality cuts employed in this analysis are similar to those used in the isobaric analysis, as introduced in Section 3.2, summarized in Table 4.2 and Table 4.3 , respectively.

Figure 4.1 depicts the distribution of primary vertex positions along the beam line, reconstructed from offline tracks. The black solid line represents the distribution before event-level cuts, while the red dashed line indicates the same distribution after applying event-level cuts. In this analysis, the offline primary vertex is required to be within 60 cm of the TPC center along the z direction (along the beam) to ensure reasonable TPC acceptance. The consistency check between V_z(TPC) and V_z(VPD) is displayed in the left and right panels of Figure 4.2.

Event Selection Criteria
$\left\lvert V_z(TPC)\right\rvert$ < 60 cm
$\left\lvert V_z(TPC) - V_z(VPD)\right\rvert$ < 3 cm
$\left\lvert V_r(TPC)\right\rvert$ < 2 cm

Table 4.2 Summary of event selection cuts.

In Au+Au collisions at $\sqrt{s_{\mathrm{NN}}}$ = 54.4 GeV, the centrality is determined based on the uncorrected charged particle density (dN_{ch}/dy), similar method which has been in-

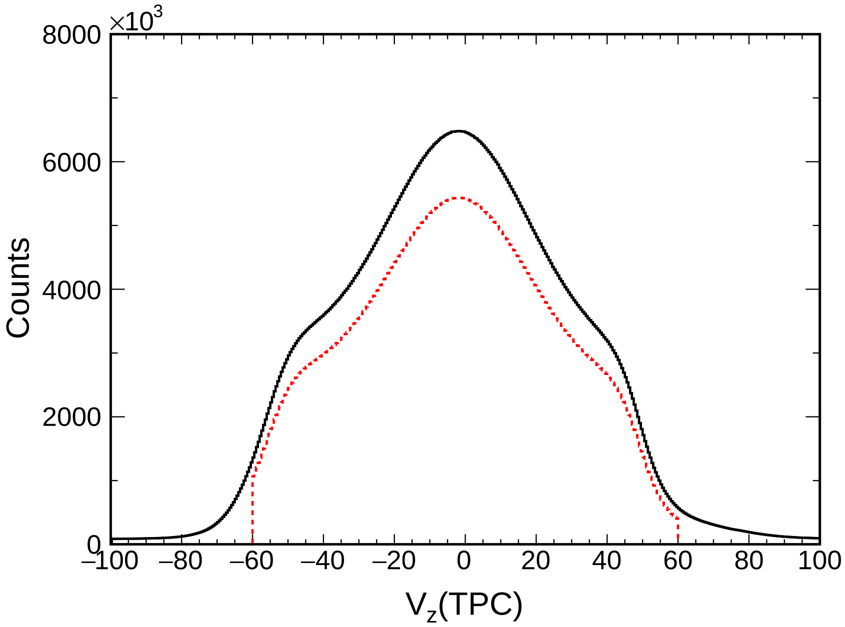

Figure 4.1 **Distribution of V_z(TPC) for primary vertex before (black) and after (red) vertex selection cuts.**

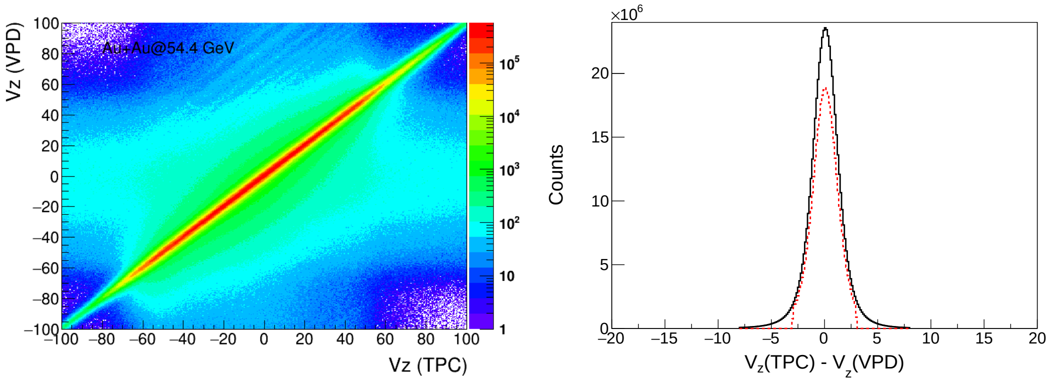

Figure 4.2 ***Left panel*: Two-dimensional distribution of V_z(TPC) versus V_z(VPD) before applying vertex cuts. *Right panel*: Distance between V_z(TPC) and V_z(VPD) before (black) and after (red) event level cuts.**

Primary Track Selection Criteria
$p_T > 0.2$ GeV/c
$\lvert\eta\rvert < 1$
nHitsFit > 20
nHitsDedx > 15
nHitsFit/nHitsPoss > 0.52
Dca < 1 cm

Table 4.3 **Summary of primary track quality cuts.**

troduced in Sec.3.3. dN_{ch}/dy is obtained by counting the number of charged tracks within $|\eta| < 0.5$ and corrected for vertex position and luminosity to account for acceptance and efficiency changes. Subsequently, dN_{ch}/dy is compared to a Monte Carlo Glauber calculation to determine the centrality bins, the equivalent number of binary collisions (N_{coll}), and the number of participants (N_{part}).

4.2 Electron Identification

The reconstruction of J/ψ candidates is performed via the $J/\psi \rightarrow e^{+}e^{-}$ decay channel, consistent with the method employed for studying very low p_{T} J/ψ production in isobaric collisions. After applying track quality cuts, primary tracks undergo electron identification criteria to determine their classification as electron candidates. The main detectors used for electron identification in this analysis are the TPC, TOF, and BEMC. Here, the term "electron" encompasses both electrons and positrons. The measured charged particle ionization energy loss per unit length (dE/dx) and velocity (β) are depicted in the left and right panels of Fig. 4.3. Concerning the BEMC information, as discussed in Sec. 3.4.3, only the highest tower energy from the associated BEMC cluster (E_0) is utilized in the electron identification method for the same reason. The distribution of E_0/p for electron samples and hadrons (mainly π) is illustrated with different markers, categorized by different track p_{T} ranges in Fig. 4.4.

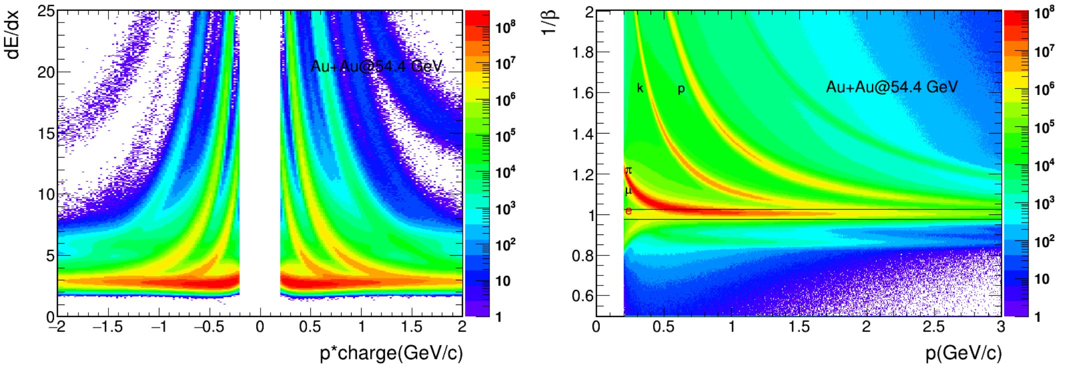

Figure 4.3 ***Left panel*: Energy loss per unit length, dE/dx, of charged particles in Au+Au collisions at 54.4 GeV. *Right panel*: The momentum dependence of $1/\beta$ for charged particles. Black soild lines indicate the default $1/\beta$ cuts ($|1/\beta - 1| < 0.025$) for selection electrons.**

Table 4.4 provides the combinations of detectors and corresponding cut values utilized for electron identification across different p_{T} ranges, mirroring those employed in the analysis of very low p_{T} J/ψ in isobaric collisions. This consistency stems from the highly similar detector configurations and the use of the same probe (J/ψ). Despite variations in the production mechanisms of the J/ψ mesons of interest, the reconstruction process within the detector remains similar.

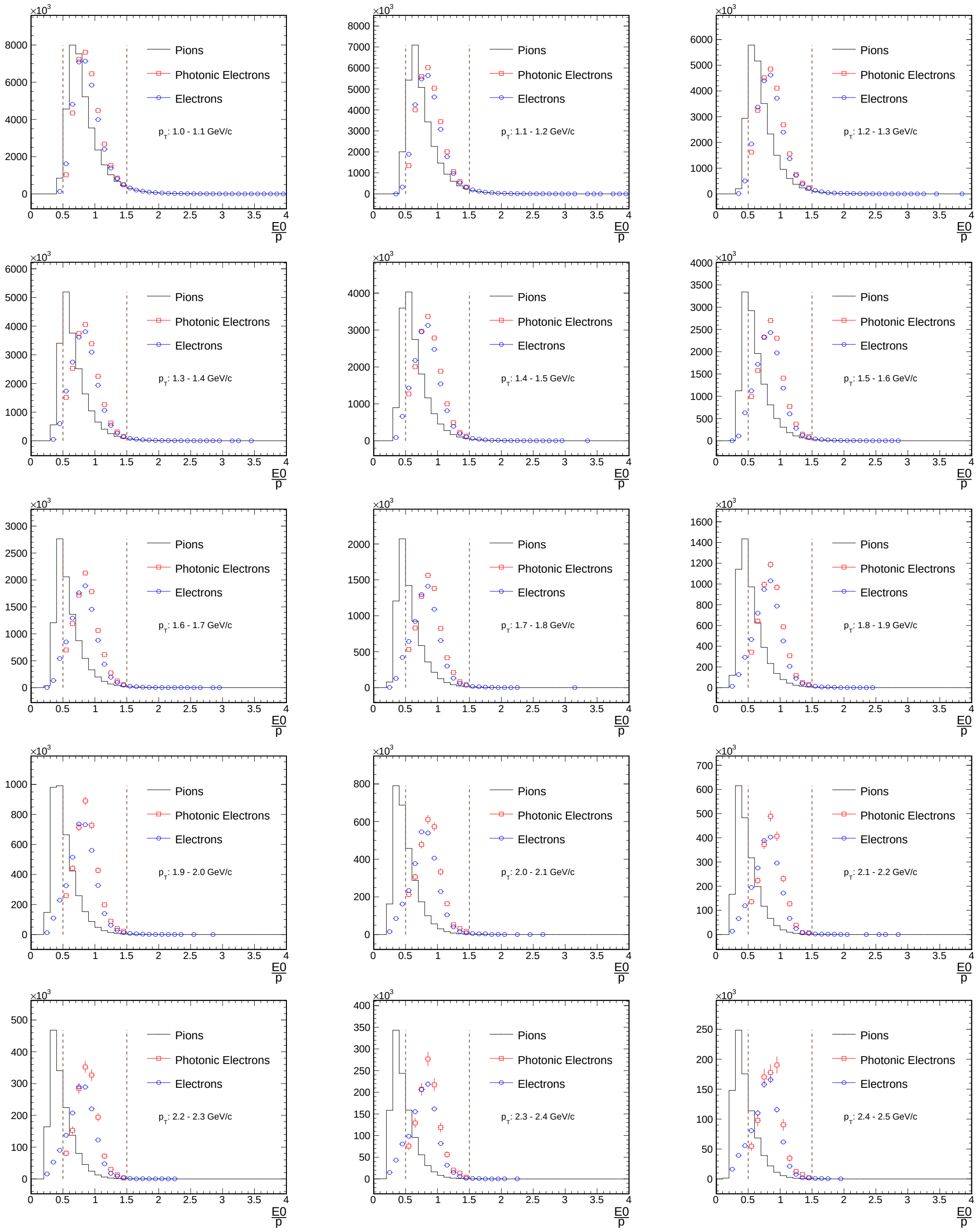

Figure 4.4 E_0/p distributions of electron samples and hadrons (mainly π) in different p_T regions. The black line stands for hadrons, the red open rectangles are electron samples from photon conversions and π^0 Dalitz decays while the blue open circles are electron samples identified by the $1/\beta$ and $n\sigma_e$ cuts. The brown dash lines indicate E_0/p cuts from 0.5 to 1.5.

4.3 Signal extraction

The J/ψ reconstruction in Au+Au collisions at STAR is conducted via the dielectron decay channel, $J/\psi \to e^+e^-$ (5.94±0.06%). Candidates must have rapidity falling within $|y| < 1.0$, and a pair p_T greater than 0.2 GeV/c to mitigate contributions from co-

Track p_{T}	Detectors used	Electron PID cuts
$p_{\mathrm{T}} \leq 1.0$ GeV/c	TPC, TOF	$\lvert 1/\beta - 1 \rvert < 0.025$; for $p > 0.8$ GeV/c: $-0.75 < n\sigma_e < 2$, for $p \leq 0.8$ GeV/c: $3 \times p - 3.15 < n\sigma_e < 2$;
$p_{\mathrm{T}} > 1.0$ GeV/c	TPC, TOF and not matched to BEMC	$\lvert 1/\beta - 1 \rvert < 0.025$; $-0.75 < n\sigma_e < 2$
	TPC, BEMC and not matched to TOF	$-1 < n\sigma_e < 2$; $0.5 < E_0/p < 1.5$
	TPC, TOF and BEMC	$\lvert 1/\beta - 1 \rvert < 0.025$; $-1.5 < n\sigma_e < 2$; $0.5 < E_0/p < 1.5$

Table 4.4 List of electron PID cuts in different p_{T} intervals.

herent photonuclear interactions. The mixed-event technique (detailed in Sec. 3.5.2) is employed to estimate combinatorial backgrounds, which are subtracted from unlike-sign same-event distributions. Signal shapes are derived from embedded data with additional momentum smearing (based on the method described in Sec. 3.5.4).

For J/ψ raw count extraction, a methodology similar to that in isobaric collisions is employed, with the primary distinction being the target pair p_{T} range. In this analysis, J/ψ signals primarily originate from initial hard scattering during high-energy nucleus-nucleus collisions, while photon-nucleus processes predominate in the very low p_{T} range, constituting one of the background sources in this analysis and can be reduced by applying a pair p_{T} cut (> 0.2 GeV/c). The detailed signal extraction method is not reintroduced, but the raw signal distribution is depicted in Fig. 4.5 for minimum-bias triggered data in 0-60% central collisions.

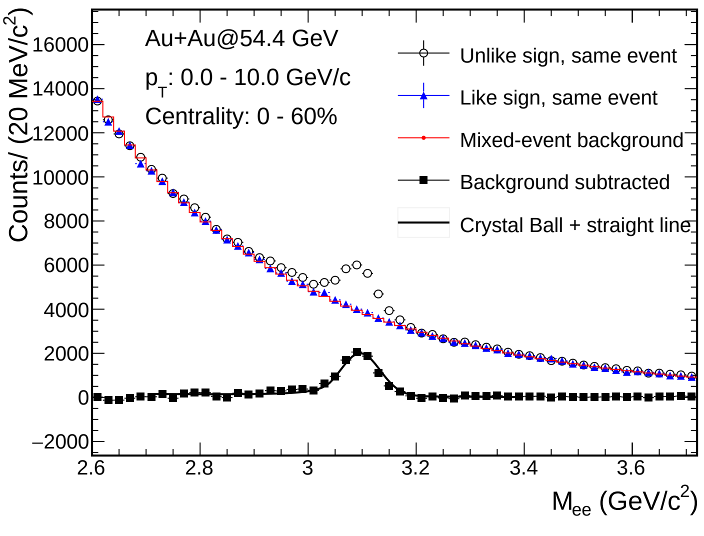

Figure 4.5 The invariant mass distribution of e^+e^- pair for the Au+Au collision in 0-60% at $\sqrt{s_{\mathrm{NN}}}$= 54.4 GeV.

The black solid squares in Fig. 4.5 represent the e^+e^- pair invariant mass distributions after subtracting the combinatorial background from same-event unlike-sign distributions. The fitted results with components of the J/ψ signal and residual background are depicted by the black solid lines. Total J/ψ counts are obtained in the invariant mass region from 2.9 to 3.2 GeV/c^2 using the bin-counting method, as follows:

$$N_{J/\psi} = N_{unlike-sign,same-event} - N_{unlike-sign,mixed-event} - N_{residual}, \tag{4.1}$$

The signal-to-background ratio is approximately 0.14, with a significance of about 35, observed in 0-60% central Au+Au collisions at $\sqrt{s_{\mathrm{NN}}}$= 54.4 GeV/c. The e^+e^- invariant mass distributions for different pair p_T bins in the 0-60% centrality range are presented in Fig. 4.6, with the J/ψ signal extracted using the same method. Similar e^+e^- pair invariant mass distributions are depicted in Figs. 4.7, 4.8, 4.9, corresponding to 0-20%, 20-40%, and 40-60% centrality bins, respectively.

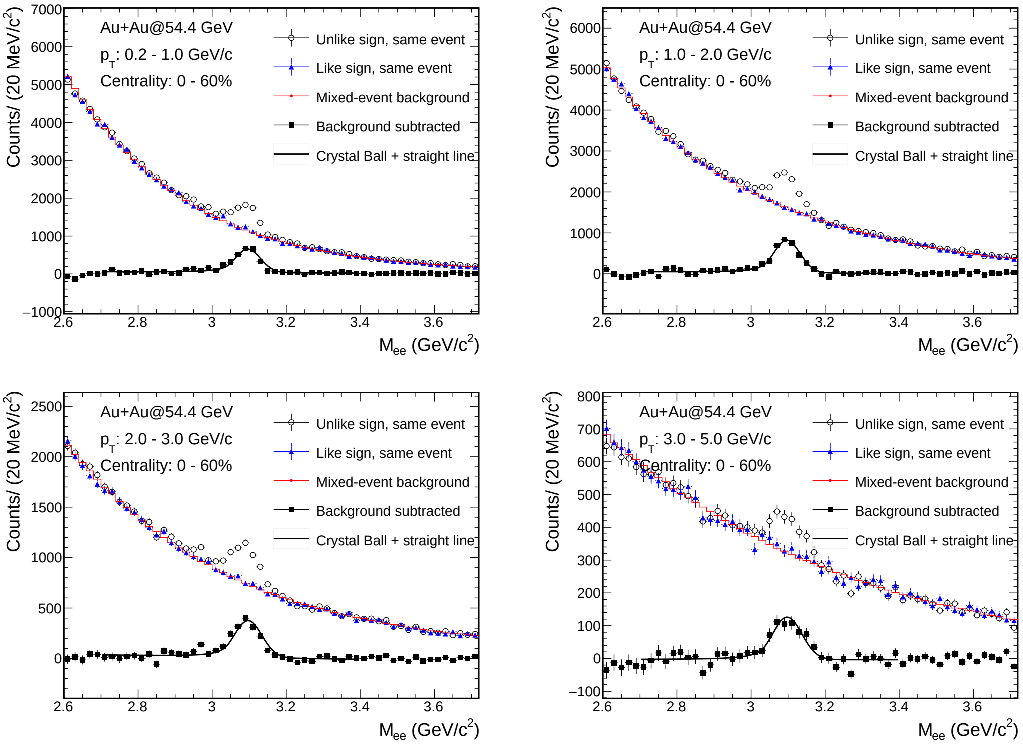

Figure 4.6 The e^+e^- pair invariant mass distribution for different p_T bins in 0-60% centrality at $\sqrt{s_{\mathrm{NN}}}$= 54.4 GeV/c.

4.4 Efficiency and Acceptance

To obtain the invariant yield of J/ψ meson, the raw counts should be corrected for efficiency and acceptance losses. The pair efficiency of J/ψ meson (ϵ_{pair}) is evaluated

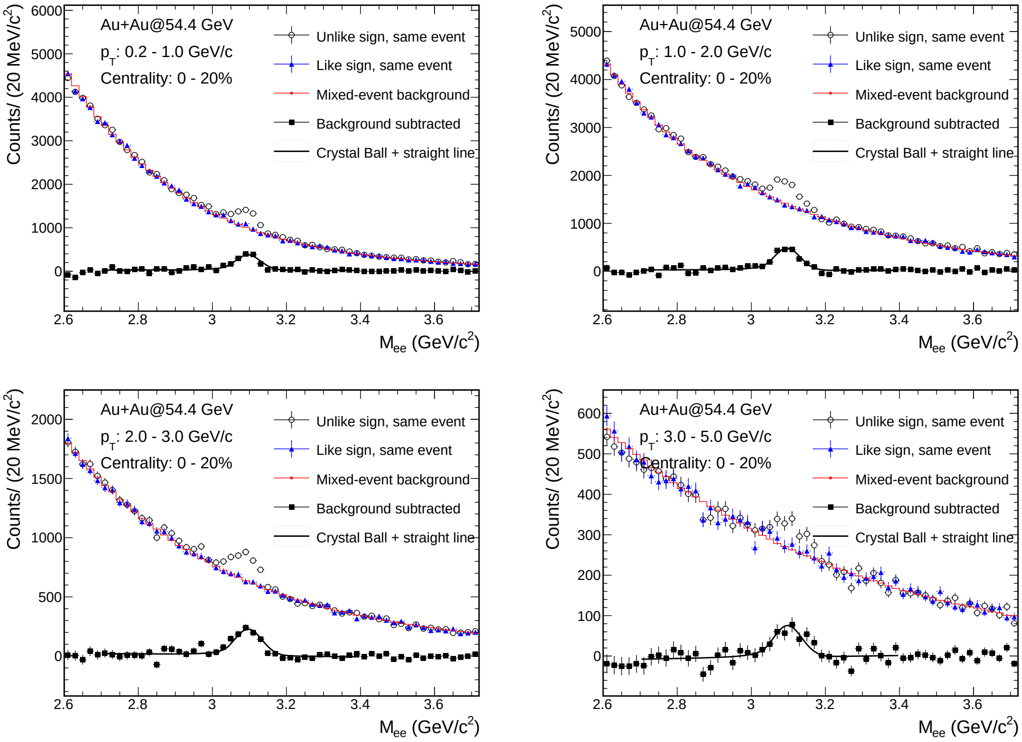

Figure 4.7 The e^+e^- pair invariant mass distribution for different p_T bins in 0-20% centrality at $\sqrt{s_{\mathrm{NN}}}$= 54.4 GeV/c.

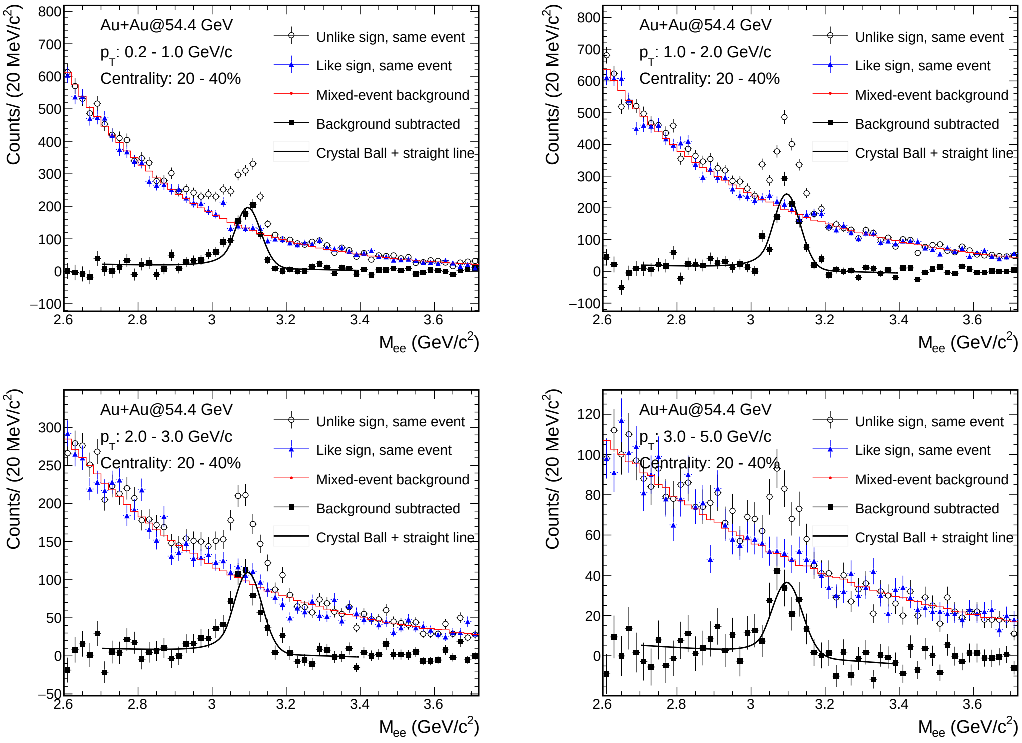

Figure 4.8 The e^+e^- pair invariant mass distribution for different p_T bins in 20-40% centrality at $\sqrt{s_{\mathrm{NN}}}$= 54.4 GeV/c.

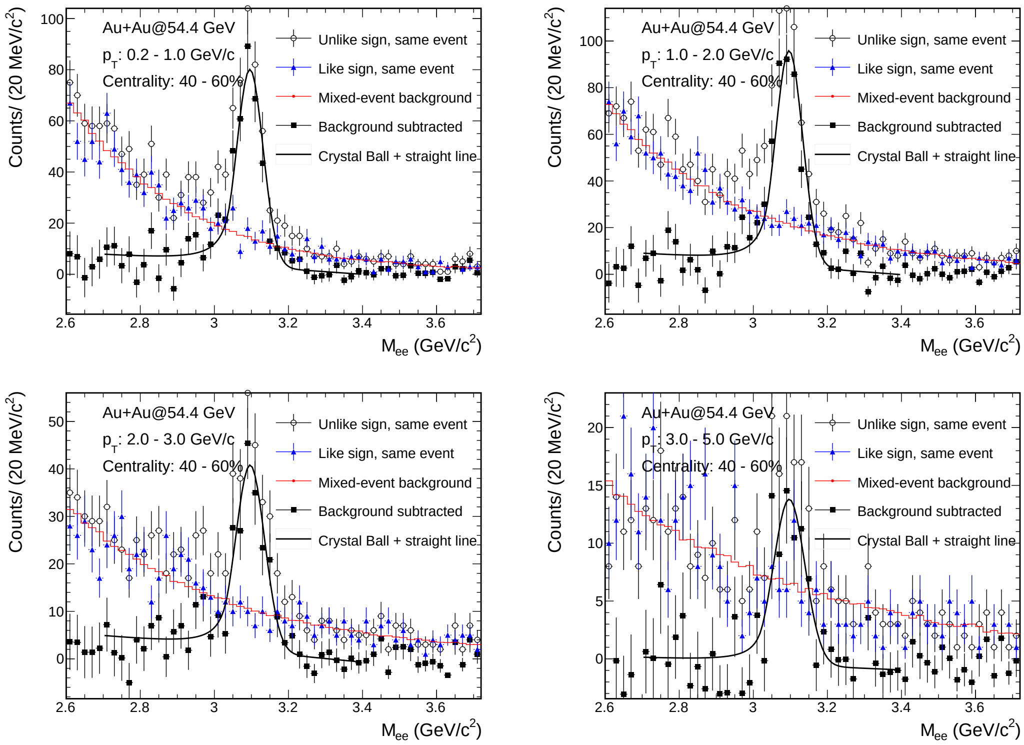

Figure 4.9 The $e^{+}e^{-}$ pair invariant mass distribution for different p_T bins in 40-60% centrality at $\sqrt{s_{\mathrm{NN}}}$= 54.4 GeV/c.

by folding the single track efficiency (ϵ_e). When the p_T of single track is smaller than 1 GeV/c, the single track efficiency can be defined as:

$$\epsilon_e = \epsilon_{TPC} \times \epsilon_{TOF} \times \epsilon_{eID}(\beta, n\sigma_e) \tag{4.2}$$

when the p_T of single track is larger than 1 GeV/c, according to the default electron identification method, the single track efficiency can be defined as:

$$\begin{aligned} \epsilon_e =& \epsilon_{TPC} \times \epsilon_{TOF} \times (1 - \epsilon_{BEMC}) \times \epsilon_{eID}(\beta, n\sigma_e) + \\ & \epsilon_{TPC} \times (1 - \epsilon_{TOF}) \times \epsilon_{BEMC} \times \epsilon_{eID}(E_0/p, n\sigma_e) + \\ & \epsilon_{TPC} \times \epsilon_{TOF} \times \epsilon_{BEMC} \times \epsilon_{eID}(\beta, E_0/p, n\sigma_e), \end{aligned} \tag{4.3}$$

where:

- ϵ_{TPC}: TPC tracking efficiency
- ϵ_{TOF}: TOF matching efficiency
- ϵ_{BEMC}: BEMC matching efficiency
- ϵ_{eID}: electron PID efficiency

Since the methodology to obtain the efficiency of different sub-detectors is similar to that in isobaric collisions, as outlined in Sec. 3.6, it will not be reintroduced here. Following the determination of single electron efficiency, the total J/ψ pair efficiency is then determined by combining the efficiencies of the decay electrons using the kinematics of J/ψ decays. A ToyMC model, employing almost identical methods to those used in the Au+Au analysis at $\sqrt{s_{\mathrm{NN}}}$ = 200 GeV, is employed to calculate the total J/ψ pair efficiency. The p_T and centrality dependence of the total J/ψ pair efficiency and acceptance correction factor in Au+Au collisions at $\sqrt{s_{\mathrm{NN}}}$= 54.4 GeV/c are illustrated in Fig. 4.10.

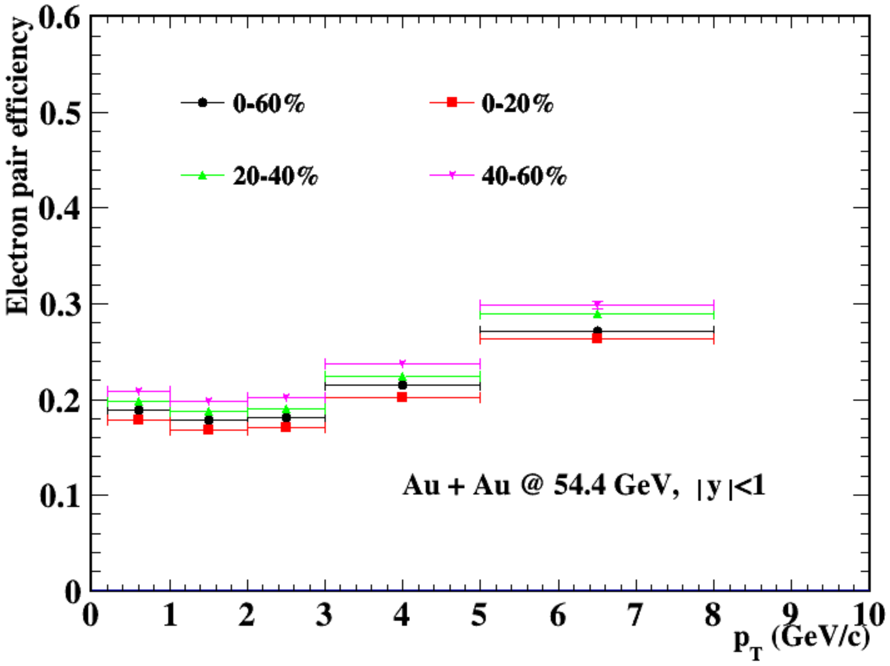

Figure 4.10 The J/ψ total pair efficiency as a function of p_T in Au+Au collisions at $\sqrt{s_{\mathrm{NN}}}$= 54.4 GeV/c in different centrality classes.

4.5 Systematic Uncertainties

The systematic uncertainties stemming from various aspects of this analysis are discussed in this section, primarily including signal extraction, TPC tracking efficiency from embedding technique, TOF and BEMC matching efficiency, and electron identification method. The total systematic uncertainties, obtained by summing the individual sources in quadrature, are 10%, 11%, 10%, and 10% in the 0-60%, 0-20%, 20-40%, and 40-60% centrality classes, respectively.

4.5.1 Uncertainties on Signal extraction

Many aspects of the signal extraction procedure are varied to evaluate the uncertainty:

- The invariant mass range used to obtain the normalization factor for mixed-event technique. The default region is from 2.6 to 3.6 GeV/c^2, and changed from 2.4(2.7) to 3.8(3.5) GeV/c^2.

- The default bin widths of the invariant mass distributions are chosen to be 20 MeV/c^2, and changed to be 50 MeV/c^2.
- The raw counts are obtained from bin-counting method, and changed to fit method.
- The fitting range for signal extraction is changed from (2.7, 3.4) to (2.6, 3.5)
- The additional smearing parameter is varied by ± 0.0005.

All variations are displayed in the Figure 4.11.

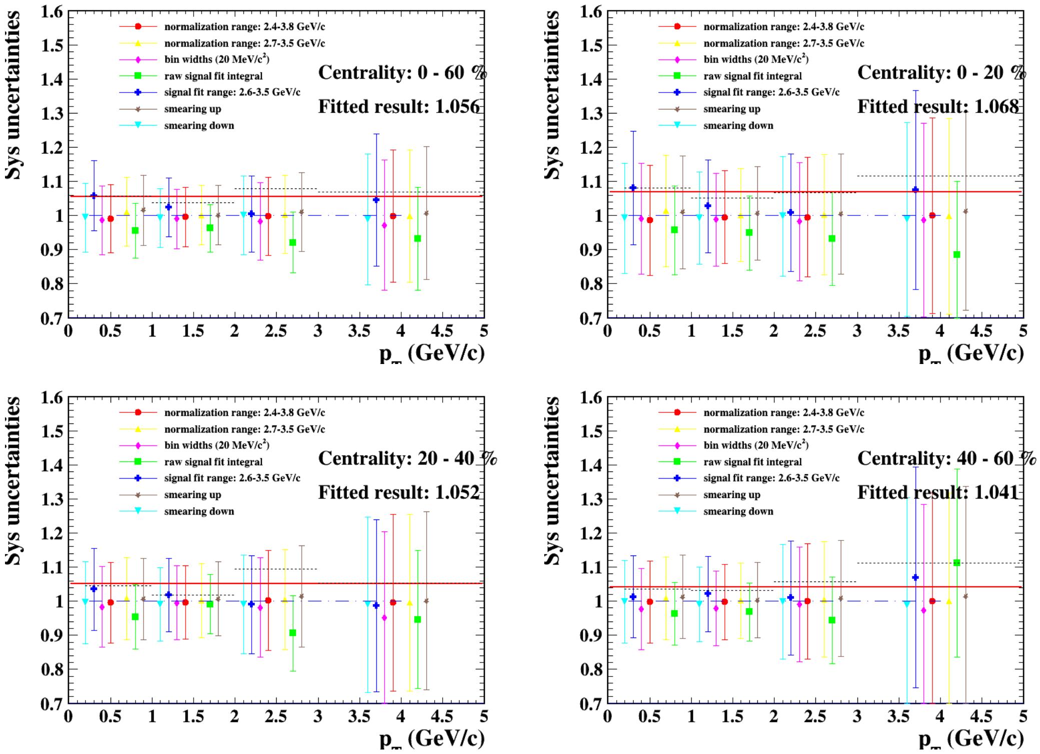

Figure 4.11 The ratio of the raw J/ψ counts as function of p_{T} between different variations and the default case in different centrality bins.

The red lines stand for the fit results via a constant of the maximum ratio, which is shown as the black dash lines, in each p_{T} bins. The centrality dependence of these variations are shown in the Figure 4.12 for integrated ranges of $p_{\mathrm{T}} > 0.2$ GeV/c. The maximum deviation is taken as the uncertainty for each p_{T} and centrality bins.

4.5.2 Uncertainties on TPC tracking

The track quality cuts are changed simultaneously in real data and embedding to estimate the associated uncertainties. The variations are listed here:

- The default dca cut is change from 1 cm to 0.8 and 1.5 cm.

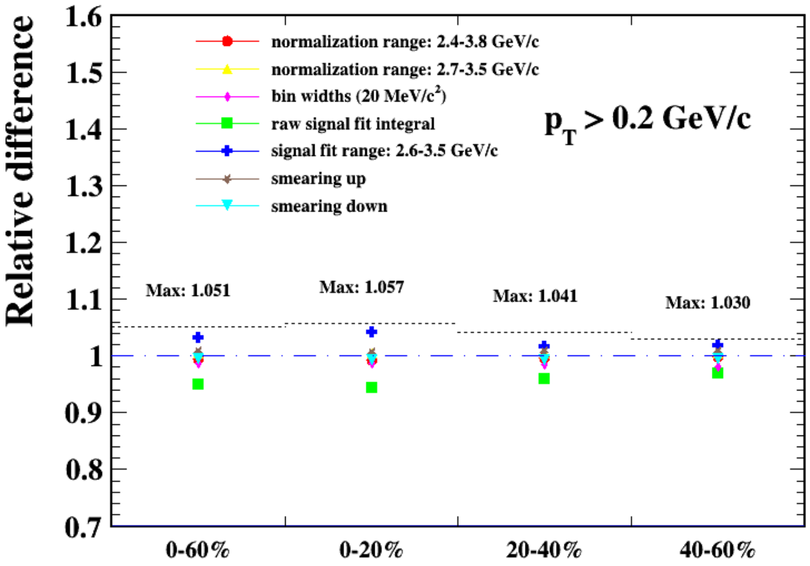

Figure 4.12 The ratio of the raw J/ψ counts as function of centrality bin between different variations and the default case.

- The default nHitsFit and nHitsDedx is change from 20,15 to 15,10, respectively. The changes in the corrected J/ψ yield are shown in the Figure 4.13 by taking into account both the variantions in the raw J/ψ counts and the corresponding TPC tracking efficiency. The black dash lines are the maximum deviations in each $p_{\rm T}$ bin and the red solid lines are the fitted results of the maximum deviations by a constant line since there is not much $p_{\rm T}$ dependence seen in the figure. Thus, the fitted results in each centrality bins are used as the uncertainty.

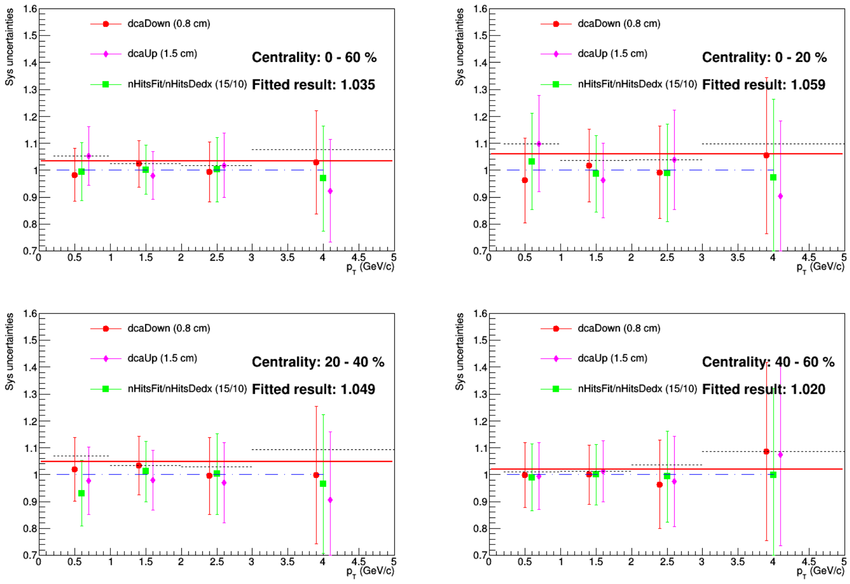

Figure 4.13 The ratio of the corrected J/ψ counts as function of $p_{\rm T}$ between different variations and the default case in different centrality bins.

4.5.3 Uncertainties on TOF and BEMC matching

The systematic uncertainties of the TOF matching is evaluated by comparing the corresponding efficiency differences between different pure electron samples (using different invariant mass cuts to select the pure electron samples). The uncertainty of the BEMC matching is primarily from the disagreement between simulation and data (using pure electron samples), which can be shown in the Figure 4.14 for different centrality bins. The variations of corrected J/ψ counts using different TOF and BEMC match efficiency, compared to the default one, are shown in the Figure 4.15 in each p_{T} bin for different centrality bins. The BEMC information is only utilized for track p_{T} greater than 1 GeV/c. Additionally, the momenta (p) of electrons originating from J/ψ meson decays predominantly lie around 1.5 GeV/c, where the matching efficiency of the BEMC from embedding aligns closely with that from data. As a result, the systematic uncertainties associated with the BEMC matching efficiency are considered negligible. Similarly, the fitted results of mamximum deviations in each centrality bins are used as the uncertainty.

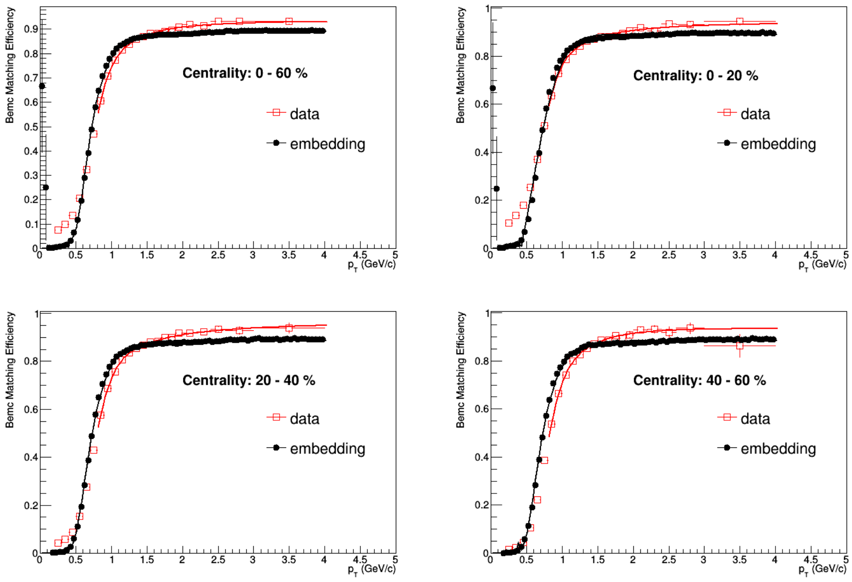

Figure 4.14 The BEMC matching efficiency from simulation and data in Au+Au collisions at $\sqrt{s_{\mathrm{NN}}}$= 54.4 GeV.

4.5.4 Uncertainties on Electron Identification

The uncertainties of electron PID include the uncertainties on $n\sigma_e$ cut, the E_0/p cut and $1/\beta$ cut. These are estimated using the same procedure as for the TPC tracking efficiency, which is described in Sec. 4.5.2. The $n\sigma_e$ cut is changed from the default one to that the interval width of $n\sigma_e$ cut increases 0.2 or decrease 0.2. The E_0/p cut

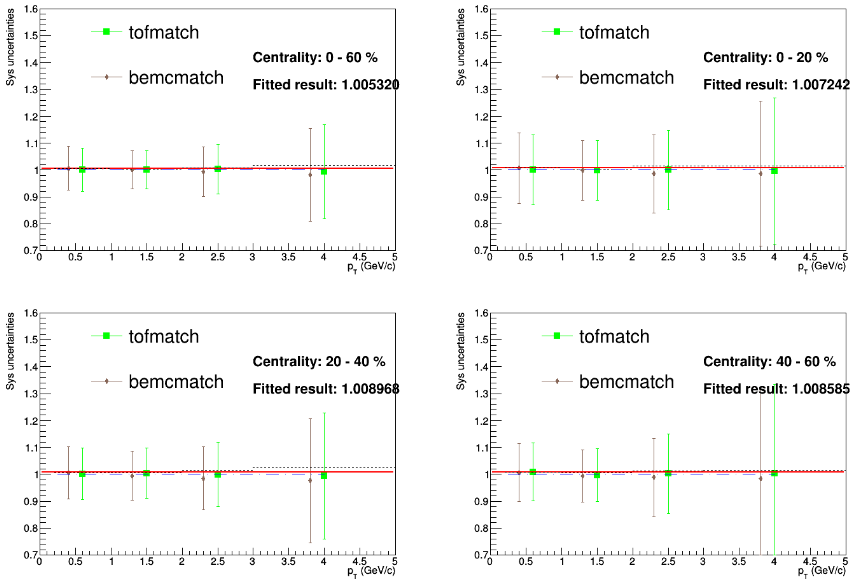

Figure 4.15 The ratio of the corrected J/ψ counts as function of p_{T} between different variations and the default case in different centrality bins.

is changed from default cut (0.5,1.5) to (0.4,1.6) or (0.6,1.4). The uncertainty of $1/\beta$ cut has been discussed in the Sec. 3.6.4. The variations of corrected J/ψ counts using different $n\sigma_e$ and E_0/p cuts, compared to the default one, are shown in the Figure 4.16 in each p_{T} bin for different centrality bins. Similarly, the fitted results of maximum deviations in each centrality bins are used as the uncertainty. The centrality dependence of these variations are shown in the Figure 4.17 for integrated ranges of $p_{\mathrm{T}} > 0.2$ GeV/c.

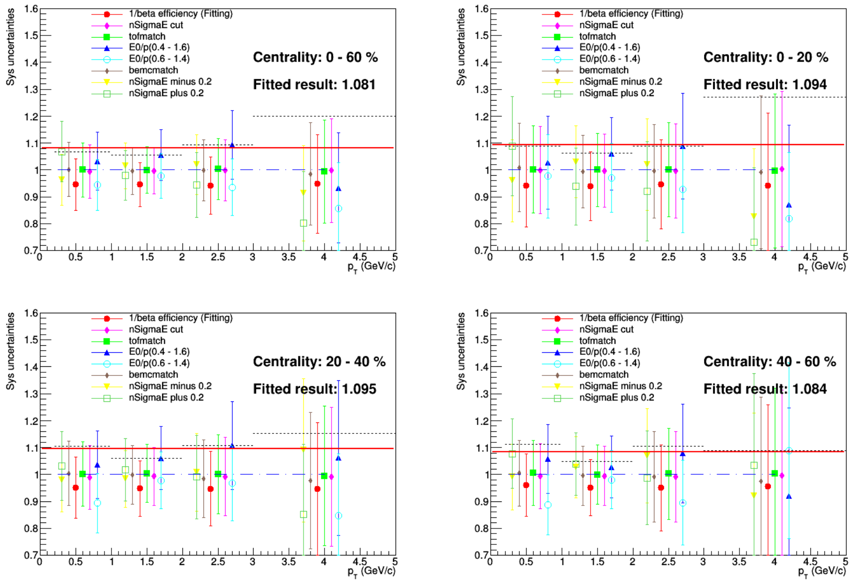

Figure 4.16 The ratio of the corrected J/ψ counts as function of p_{T} between different variations and the default case in different centrality bins.

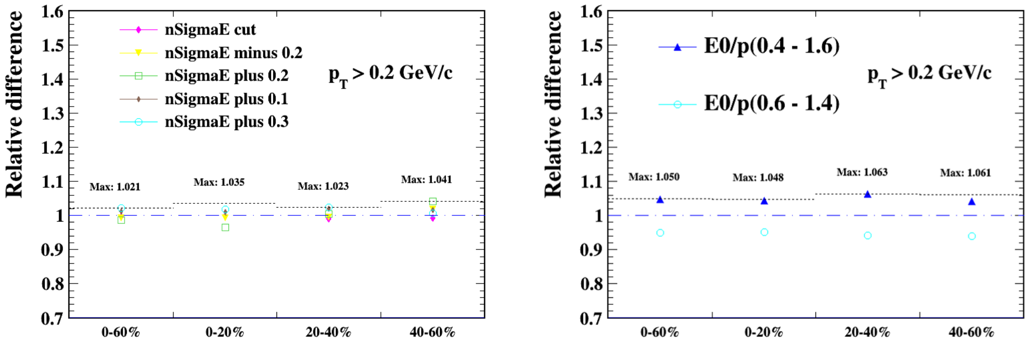

Figure 4.17 The centrality dependence of $n\Sigma_e$ cut uncertainty in different centrality Au+Au collisions (*Left panel*) and the similar results of E_0/p cut (*Right panel*).

4.5.5 The Summarized Uncertainties

The systematic uncertainties for the measurement of inclusive J/ψ production in Au+Au collisions at $\sqrt{s_{\mathrm{NN}}}$ = 54.4 GeV/c are summarised in the Table 4.5.

Sources	0-60%	0-20%	20-40%	40-60%
Signal extraction	5.1%	5.7%	4.1%	3.0%
TPC tracking	10.6%	10.6%	10.6%	10.6%
TOF matching	0.2%	0.1%	0.3%	0.3%
BEMC matching	0.4%	0.7%	0.7%	0.6%
$1/\beta$ cut	5.5%	5.9%	5.2%	4.6%
$n\sigma_{\mathrm{e}}$ cut	2.1%	3.5%	2.3%	4.1%
E_0/p cut	5.0%	4.8%	6.3%	6.1%
Total	14%	15%	14%	14%

Table 4.5 Individual and total systematic uncertainties for J/ψ with p_{T} > 0.2 GeV/c in different centrality classes.

Chapter 5 Results and Discussions

5.1 e^+e^- pair Coherent photon-photon production in isobaric collisions

In the upper panel of Fig. 5.1, the e^+e^- invariant mass distributions corrected for detector inefficiency in Ru+Ru and Zr+Zr collisions are shown as solid and open circles respectively in 70-80% centrality for pair p_T < 0.15 GeV/c within STAR acceptance (p_T^e > 0.2 GeV/c, $|\eta^e| < 1$, and $|y^{ee}| < 1$). Compared to the hadronic cocktail, there is a significant enhancement observed in the yield of e^+e^- pairs, which is believed to originate from the photon-induced production. The corresponding enhancement factors are defined as ratios of data over hadronic cocktail in the same mass regions, which are displayed in the bottom panel of Fig. 5.1. The enhancement factors reach local minima around M_ϕ before rising towards larger mass, similar to the trends seen in Au+Au and U+U collisions[155].

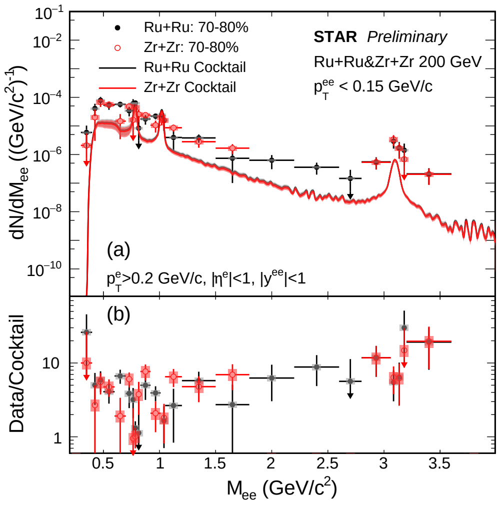

Figure 5.1 (a) The e^+e^- invariant mass spectra within the STAR acceptance from Ru+Ru and Zr+Zr collisions for pair p_T^{ee} < 0.15 GeV/c in 70-80% centrality. The hadronic cocktails are shown as solid lines of different colors, with shaded bans representing the systematic uncertainties. (b) The corresponding ratios of data over cocktail.

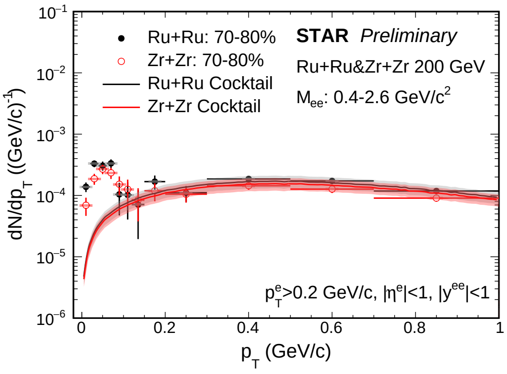

Figure 5.2 The e^+e^- pair p_T distribution within the STAR acceptance in 0.4-2.6 GeV/c^2 mass region in 70-80% centrality, compared to cocktails. The statistical uncertainties are depicted by the vertical bars, and the systematic uncertainties are displayed as shaded bands.

The p_T distributions of e^+e^- pairs in the mass region from 0.4-2.6 GeV/c^2 are shown in Figure. 5.2 for 70-80% isobaric collisions. While for p_T^{ee} > 0.15 GeV/c, data are consistent with hadronic cocktails, significant excesses above hadronic cocktails are seen at p_T^{ee} < 0.15 GeV/c.

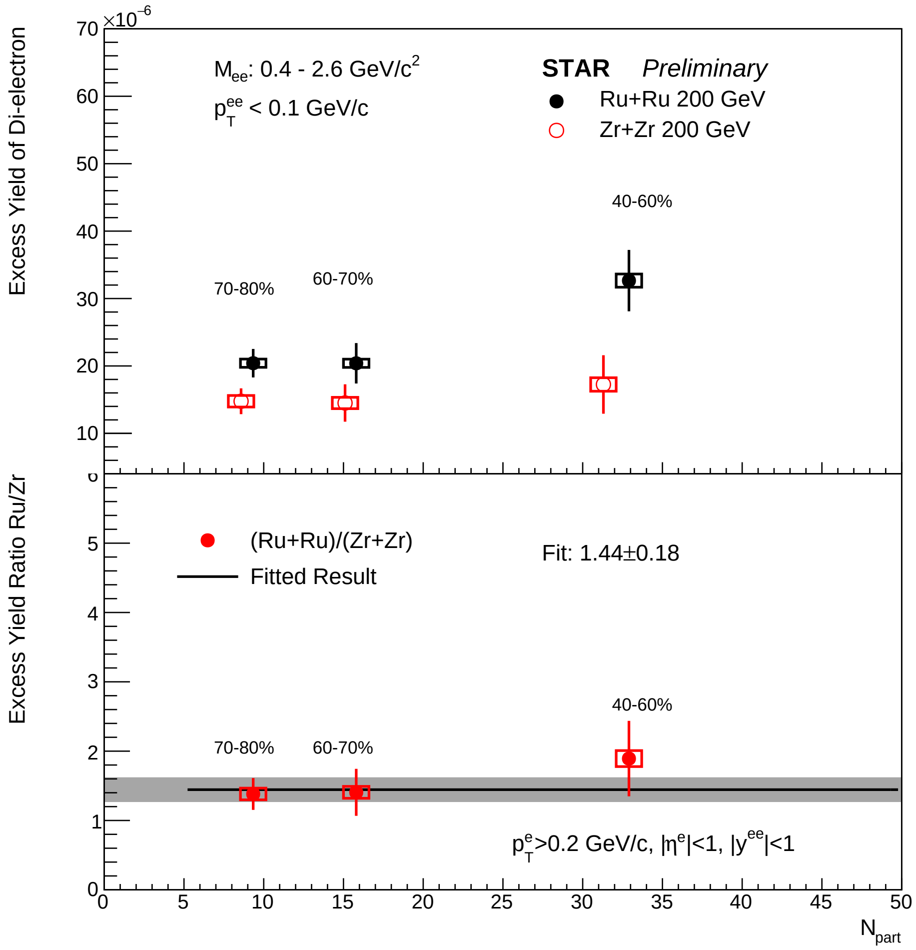

Figure 5.3 ***Upper panel*: The excess yields as a function of N_{part} with p_T^{ee} < 0.1 GeV/c in the invariant mass region from 0.4 to 2.6 GeV/c^2 in Ru+Ru and Zr+Zr collisions within the STAR acceptance. *Bottom panel*: The centrality dependence of the ratios of integrated low-p_T excesses between Ru+Ru and Zr+Zr collisions. The solid line is the fitted result to data points by a constant function.**

After the hadronic cocktail subtraction, the very low-p_{T} e^+e^- excess yields as a function of average number of participating nucleons $\langle N_{\text{part}}\rangle$ are shown in the upper panel of Fig. 5.3. The black solid circles are the excess yield of e^+e^- pair at very low p_{T} from Ru+Ru collisions, while the red open circles are same results from Zr+Zr collisions. The integrated excesses yields in Ru+Ru collisions are systematically higher than those in Zr+Zr collisions, which is expected by the coherent photon-photon interaction, because of larger Z in Ru than that in Zr. The bottom panel of Fig. 5.3 is the centrality dependence of excess yield ratios between Ru+Ru and Zr+Zr collisions, and a constant function is utilized to fit the ratios. The fitted result is 1.44±0.18, about 2.4σ higher than unity, which hints that the initial electromagnetic field in Ru+Ru collisions is indeed stronger than that in Zr+Zr collisions.

Figure 5.4 shows the p_{T} dependence of the e^+e^- yield ratios in the pair mass range from 0.4 to 2.6 GeV/c^2 between Ru+Ru and Zr+Zr collisions in the 40-80% centrality.

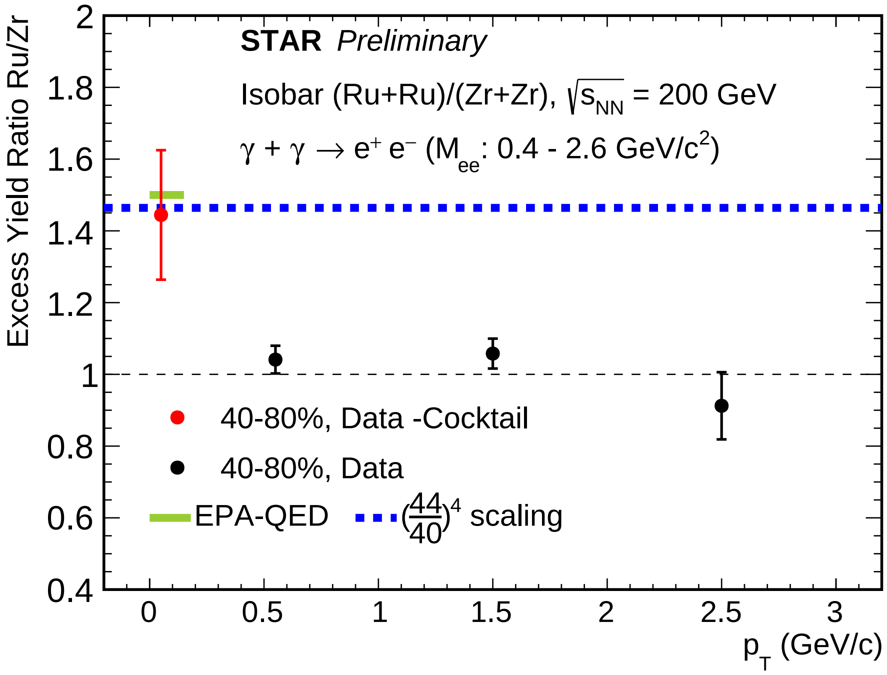

Figure 5.4 The p_T dependence of e^+e^- yield ratios between Ru+Ru and Zr+Zr collisions in 40-80% centrality. The statistical and systematical uncertainties are combined and shown as the vertical bars. The green solid line is the prediction at low-p_T based on EPA-QED[195] and the blue dash line is the $(\frac{44}{40})^4$ scaling.

For p_T > 0.1 GeV/c, the hadronic cocktail is not subtracted, and the yield ratio, shown as the black solid circles, is consistent with unity, indicating the hadronic contribution dominates in this p_T range and also is similar between Ru+Ru and Zr+Zr collisions. The two collision systems' distinct nuclear structures could be the cause of the small deviation from unity, for example the different nucleon numbers which has been discussed in the centrality definition Section (Sec. 3.3). At p_T < 0.1 GeV/c, the hadronic cocktail is subtracted in order to study the collision system dependence of the photon-induced production. The excess yield ratio, as the red solid circles shown, at low-p_T is significantly higher than unity. This ratio follows the $(\frac{44}{40})^4$ scaling displayed as the blue dash line and also can be described by the EPA-QED calculation[195] shown as the green line. This result also demonstrates that the e^+e^- excess yield at very low p_T range in the high energy heavy ion collisions is dependent on the initial electromagnetic field arising from the colliding nucleus ($\propto Z^4$). In order to further study the charge dependence, the measurements in Ru+Ru and Zr+Zr collisions are compared to these in Au+Au and U+U collisions at same energy, shown in Fig. 5.5. As one can see, the charge dependence of very low p_T e^+e^- excess yield is quite apparent, and can be described well by the EPA-QED calculation. According to the model calculation[195] and measured excess yield ratio (shown in the Figure5.4) between Ru+Ru and Zr+Zr collisions, the main difference of integrated e^+e^- excess yields from different collision system is due to the different charge number (Z) in the colliding nucleus. Since the cross section of coherent photon-photon interaction is proportional to the Z^4, the charge difference can be scaled and then the nuclear system dependence of coherent photon-photon interaction can be studied.

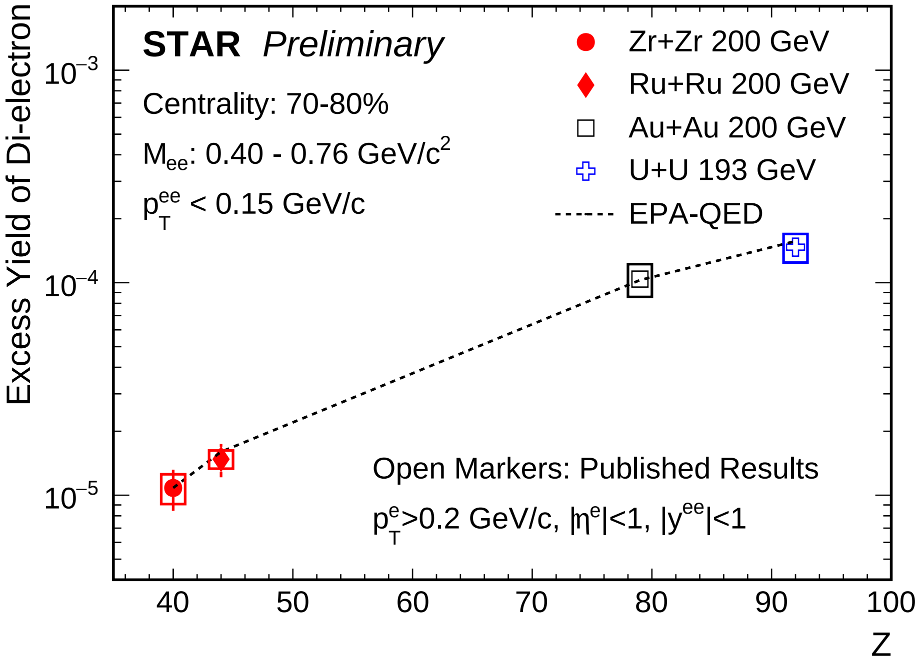

Figure 5.5 The collision system dependence of the integrated e^+e^- excess yield within the STAR acceptance, in 70-80% centrality. The dash line is the EPA-QED prediction[196].

Figure 5.6 shows the integrated excess yields in the mass region of 0.4-0.76 GeV/c^2 at p_T < 0.15 GeV/c in 70-80% centrality scaled by Z^4 as function of Z for different collisions. The red markers are the e^+e^- excess yield in Ru+Ru and Zr+Zr collisions respectively, while the open markers are the published results from Au+Au and U+U collisions within the same kinematic range and acceptance. After the Z^4 scaled, the yields among these collision systems are roughly similar. While the distribution still shows a clear collision system dependence, likely originating from the impact parameter dependence of photon-induced interactions, since the specific values of impact parameter b among these collision systems are different in the centrality class. The decreasing trend can be described by the EPA-QED calculations[196] taking such impact parameter dependence into account.

The angular modulation of e^+e^- pair production at very low p_T in isobaric collision are also studied in this analysis, and the collision system dependence of the angular modulation are researched by compared to the published results in Au+Au collisions.

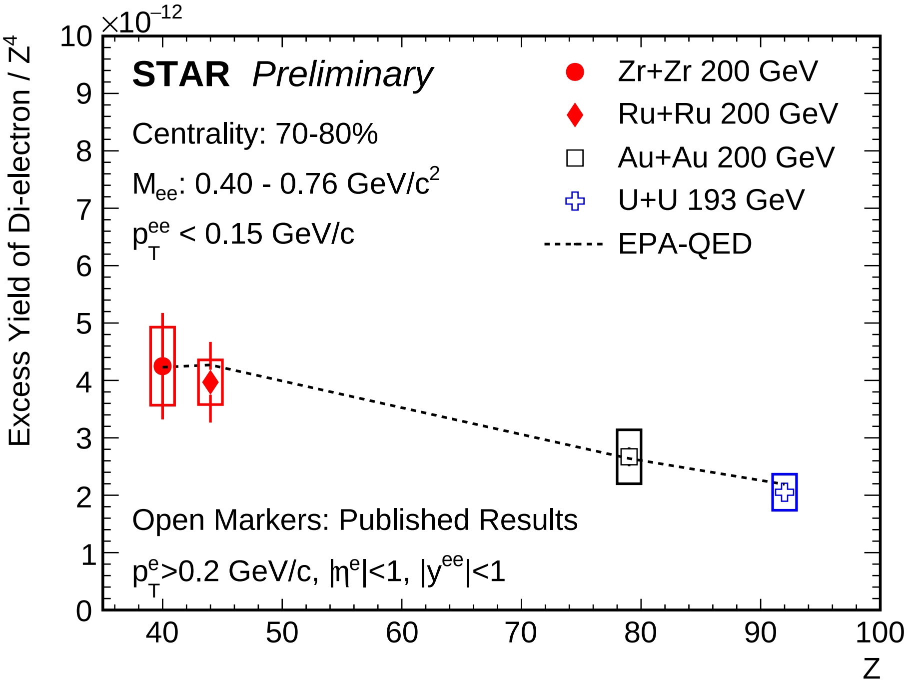

Figure 5.6 The collision system dependence of the integrated e^+e^- excess yield within the STAR acceptance, scaled with Z^4, in 70-80% centrality. The dash line is the EPA-QED prediction[196].

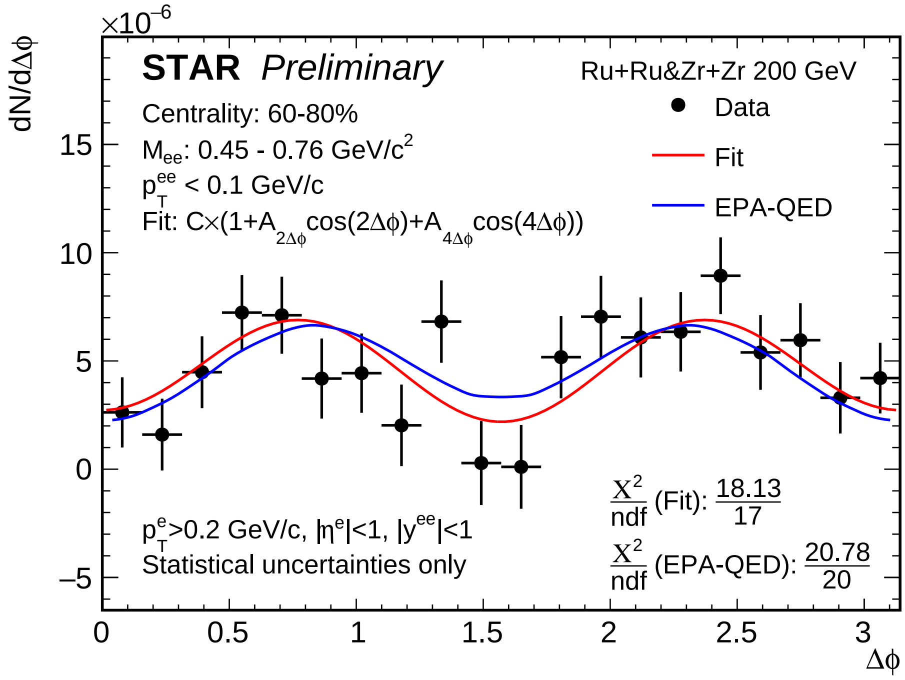

Figure 5.7 The $\Delta\phi$ distribution from 60-80% collisions in isobaric collisions for M_{ee} from 0.45 to 0.76 GeV/c^2. The red line is the fitted results and the blue line represents the calculations based on EPA-QED model[196].

As presented in the Fig. 5.7, the $\Delta\phi$ distribution of e^+e^- pair is measured and shown a clear cos($4\Delta\phi$) modulation. The black circles are measured results from data, and the red line is the fitting results based on the follow formula:

$$f(\Delta\phi) = C \times [1 + A_{2\Delta\phi}cos(2\Delta\phi) + A_{4\Delta\phi}cos(4\Delta\phi)], \tag{5.1}$$

where the C, $A_{4\Delta\phi}$, and $A_{4\Delta\phi}$ are free parameters. The blue line is the results based on EPA-QED calculation. The χ^2 over ndf from fitting using the equation 5.1 and EPA-QED calculation are listed in the Figure, which are $\frac{18.13}{17}$ and $\frac{20.78}{20}$ respectively. So the observed cos($4\Delta\phi$) modulation in isobaric collisions is consistent with EPA-QED calculations, and a comparison between isobaric collision and Au+Au collision are listed in the Table 5.1. A decreasing trend of magnitude of cos($4\Delta\phi$) modulation with impact parameter (b) increasing can be seen by comparing the results in isobaric collisions to these in peripheral and ultraperipheral Au+Au collisions.

	Collision System	Measurement	Calculation (QED)
$A_{4\Delta\phi}$	Isobar 60-80%	47±14	40
	Au+Au 60-80%	27±6	34.5
	Au+Au UPC	16.8±2.5	16.5
$A_{2\Delta\phi}$	Isobar 60-80%	6±13	0
	Au+Au 60-80%	6±6	0
	Au+Au UPC	2.0±2.4	0

Table 5.1 The magnitude of angular modulation in isobaric collision and Au+Au collisions. The EPA-QED calculations are also listed for isobaric and Au+Au collisions respectively.

From the Table 5.1, there is a hint that the magnitude of cos($4\Delta\phi$) modulation is different in isobaric and Au+Au collisions, due to the different impact parameters for same centrality bins in isobaric collision and Au+Au collisions, larger impact parameter means more obvious cos($4\Delta\phi$) modulation. This observation is also in line with the EPA-QED calculations.

5.2 J/ψ photoproduction in isobaric collisions at $\sqrt{s_{\rm NN}}$= 200 GeV

Figure 5.8 shows the invariant yield distribution of J/ψ meson as function of $p_{\rm T}$ in Ru+Ru and Zr+Zr collisions in 20-40%, 40-60% and 60-80% centrality bins. The solid markers are the results in Ru+Ru collisions while the open markers are same results in Zr+Zr collisions. The solid lines in the Fig. 5.8 are the fitting results to the data points at $p_{\rm T}$ larger than 0.2 GeV/c using the Tsallis function, which is defined as below formula:

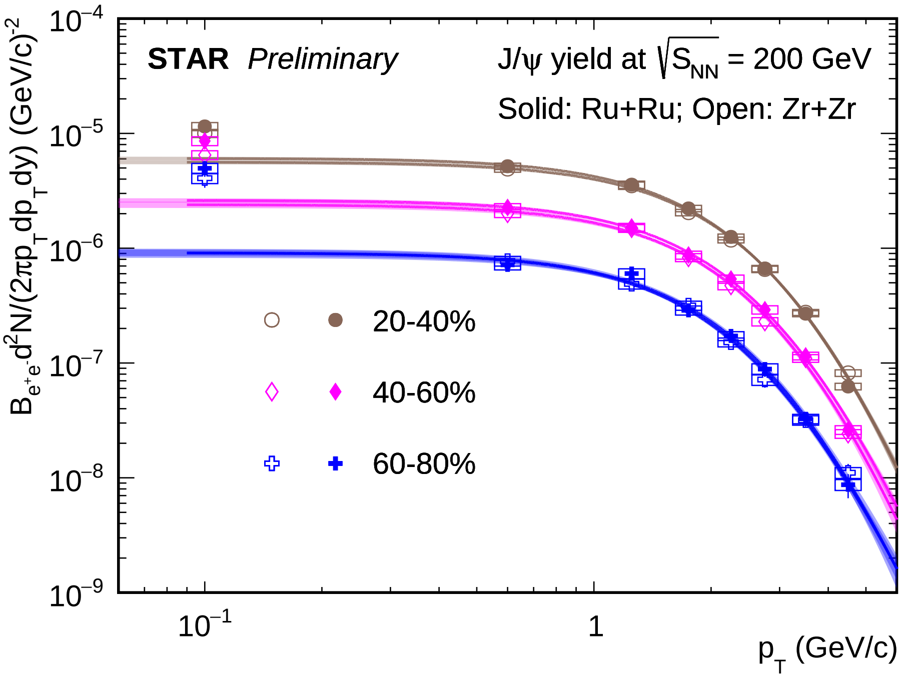

Figure 5.8 The J/ψ invariant yield spectra as function of p_{T} in Ru+Ru and Zr+Zr collisions respectively in three centrality bins.

$$\frac{d^2N}{dp_Tdy} = p_T\frac{dN}{dy}\frac{(n-1)(n-2)}{nC(nC+m_0(n-2))}(1+\frac{m_T-m_0}{nC})^{-n}, \tag{5.2}$$

As we can see, the extrapolations of the fitting results to the p_{T} range smaller than 0.2 GeV/c is significantly underestimate the yield for all three noncentral collision bins. To quantify the J/ψ production suppression in hadronic heavy ion collisions with respect to that in the p+p collisions, the nuclear modification factor (R_{AA}) as function of p_{T} are shown in the Fig. 5.9.

In Fig. 5.9, the suppression of J/ψ production is obvious at p_{T} > 0.2 GeV/c, however in the very low p_{T} bins, an enhancement of R_{AA} above unity is observed in peripheral collisions (40-80%) both for Ru+Ru and Zr+Zr collisions, which is the contribution of the coherent photon-nucleus interaction. The enhancement is smaller than that in Au+Au collision at same collisions, because the contributions of J/ψ from photon-induced production ($\propto Z^2$) decreases more than the contributions from hadronic interaction ($\propto N_{\mathrm{coll}}$) when transitioning from Au+Au collisions to Ru+Ru and Zr+Zr collisions. The ratio of $\langle N_{\mathrm{coll}}\rangle$ between Au+Au and Ru+Ru collision is about 1.8 in 60-80% centrality, while the $(\frac{Z_{Au}}{Z_{Ru}})^2$ is about 3.2.

The initial electromagnetic field dependence of photon-induce interaction can also be studied by measuring the very-low p_{T} J/ψ production in isobaric collisions. Figure 5.10 shows the p_{T} dependence of the J/ψ yield ratios in the pair mass range from 3.0

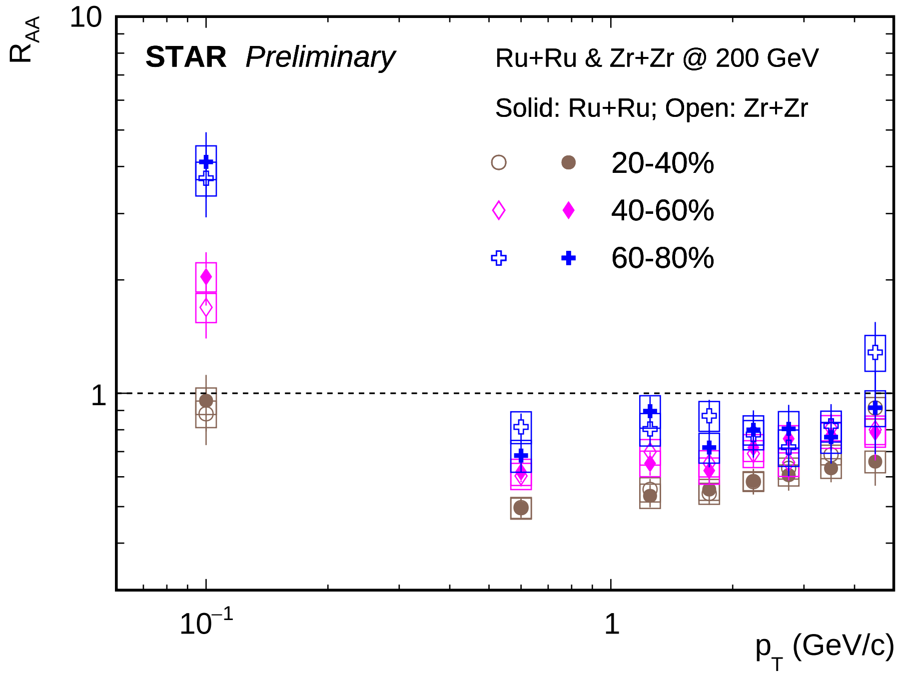

Figure 5.9 J/ψ R_{AA} as a function of p_T in three centrality bins in Ru+Ru and Zr+Zr collisions, respectively.

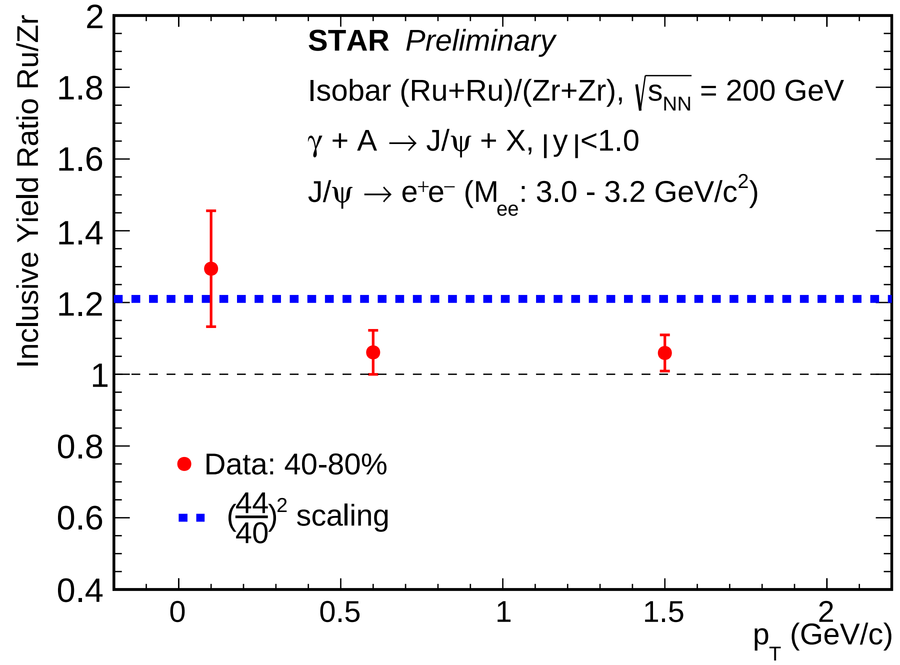

Figure 5.10 The p_T dependence of J/ψ yield ratios between Ru+Ru and Zr+Zr collisions in 40-80% centrality. The statistical and systematical uncertainties are combined and shown as the vertical bars. The blue dash line is the $(\frac{44}{40})^2$ scaling.

to 3.2 GeV/c^2 between Ru+Ru and Zr+Zr collisions in the 40-80% centrality. At $p_{\mathrm{T}} <$ 0.1 GeV/c, the yield ratio is higher than unity, which is consistent with the ratios of very low p_{T} e^+e^- pair. This ratio follows the $(\frac{44}{40})^2$ scaling displayed as the blue dash line.

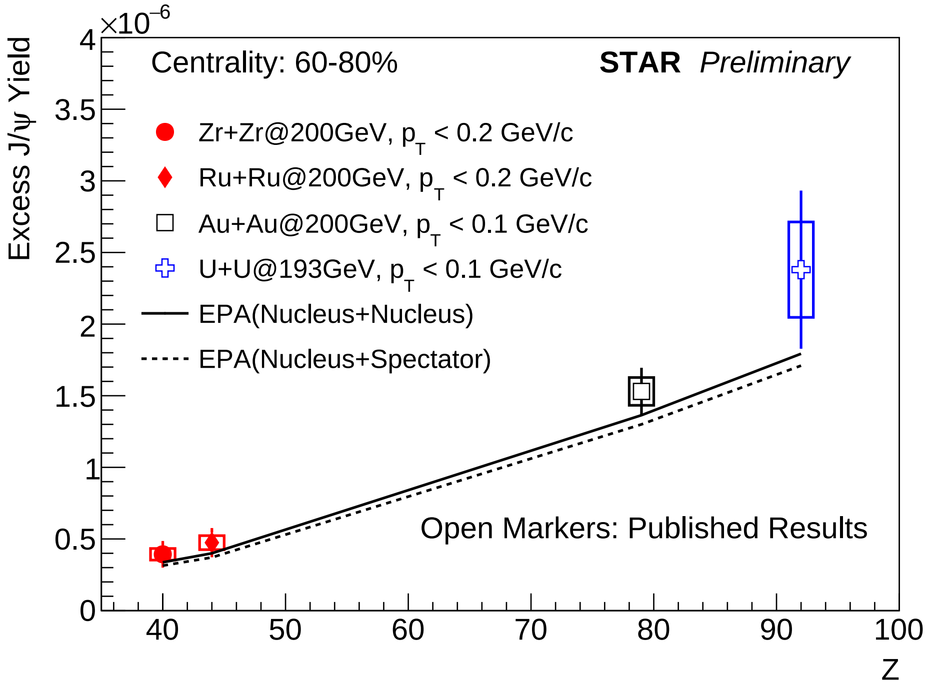

Figure 5.11 The collision system dependence of the J/ψexcess yield, in 60-80% centrality. The dash and solid lines are the EPA model prediction[197].

The extrapolations of the fitting results in the Fig. 5.8 to the very low p_{T} range has been treated as the expected hadronic contribution of J/ψ production at that p_{T} range, so, the excess J/ψ yield can be obtained after hadronic contribution subtraction. Figure. 5.11 shows the very low p_{T} J/ψ excess yields as a function of Z in same centrality class of Zr+Zr, Ru+Ru, Au+Au, and U+U collisions. As one can seen, there is also a quite apparent charge dependence of these excess yields. Two theatrical model calculation with different hypothesis, shown as the solid and dash lines, show the similar trend as experimental measurements.

Figure 5.12 shows the excess J/ψ yield after Z^2 scaled as function of different charge number (Z) at very low p_{T} range. The red markers are the results in isobaric collisions while the open markers are the similar published results from Au+Au and U+U collisions. As shown in the Fig. 5.12, there is no clear charge dependence of J/ψ excess yield after the charge difference scaled, which seems the impact parameter and form factor effect are balanced each other. This trend can be described by theatrical model calculations.

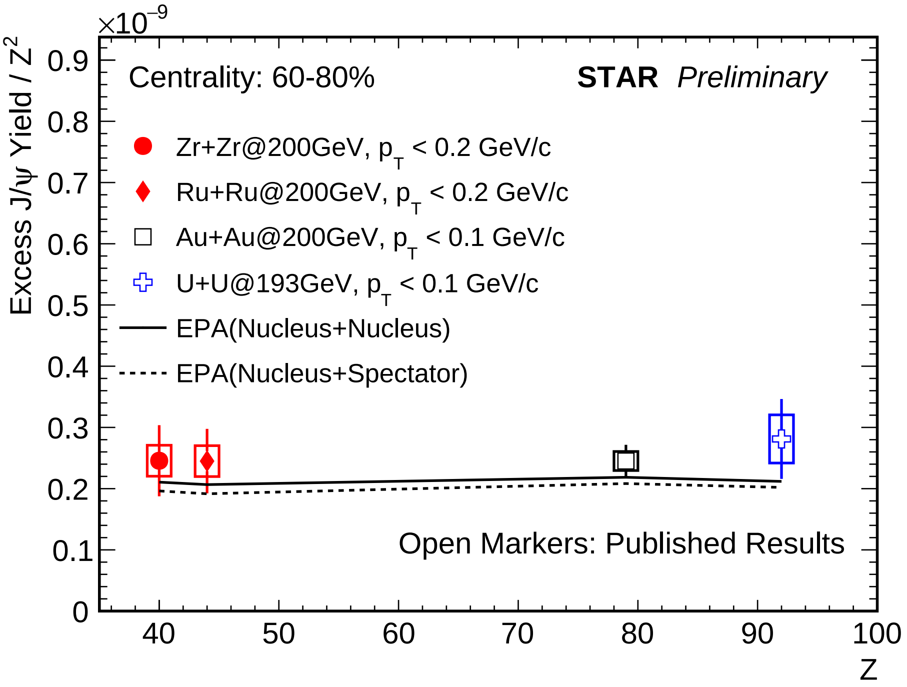

Figure 5.12 The collision system dependence of the J/ψexcess yield, scaled with Z^2, in 60-80% centrality. The dash and solid lines are the EPA model prediction[197].

5.3 J/ψ production in Au+Au collisions at $\sqrt{s_{\mathrm{NN}}}$= 54.4 GeV

5.3.1 The invariant yield

The J/ψ raw yield has been corrected by the efficiency and acceptance shown in the Fig. 4.10 in each p_{T} and centrality bins, and normalized to the number of events and phase space used in the Au+Au collisions at $\sqrt{s_{\mathrm{NN}}}$= 54.4 GeV. The invariant yield of inclusive J/ψ meson is calculated as:

$$B_{J/\psi\to e^+e^-}\frac{d^2N_{J/\psi}}{2\pi p_T dp_T dy} = \frac{\Delta N_{J/\psi}}{2\pi p_T \times \Delta p_T \times \Delta y \times N_{MB} \times \epsilon_{total}}, \tag{5.3}$$

where:

- $B_{J/\psi\to e^+e^-}$: branching ratio for the J/ψ decaying into two dlectrons.
- $\Delta N_{J/\psi}$: raw counts of J/ψ in each p_{T} bin for the interested centrality.
- Δ p_{T} the width of p_{T} bin.
- Δy: the rapidity coverage of this measurement, from -1 to 1.
- N_{MB}: the number of MB events in the interested centrality bins used in this analysis.
- ϵ_{total}: the total J/ψ pair efficiency.

The invariant yields of inclusive J/ψ within $|y| < 1$ as a function of p_{T} in Au+Au collisions at $\sqrt{s_{\mathrm{NN}}}$ = 54.4 GeV for different centrality classes are shown in Fig. 5.13. The horizontal bars on the data points indicate the bin width.

Data points are placed at p_{T} values whose yields are equal to the average yields of the bins[198]. The p_{T} positions are determined by fitting the differential yields iteratively with an empirical function:

$$f(p_{\mathrm{T}}) = A \times p_{\mathrm{T}} \times (1 + p_{\mathrm{T}}^2/B^2)^{-C}, \tag{5.4}$$

where A, B, and C are free parameters.

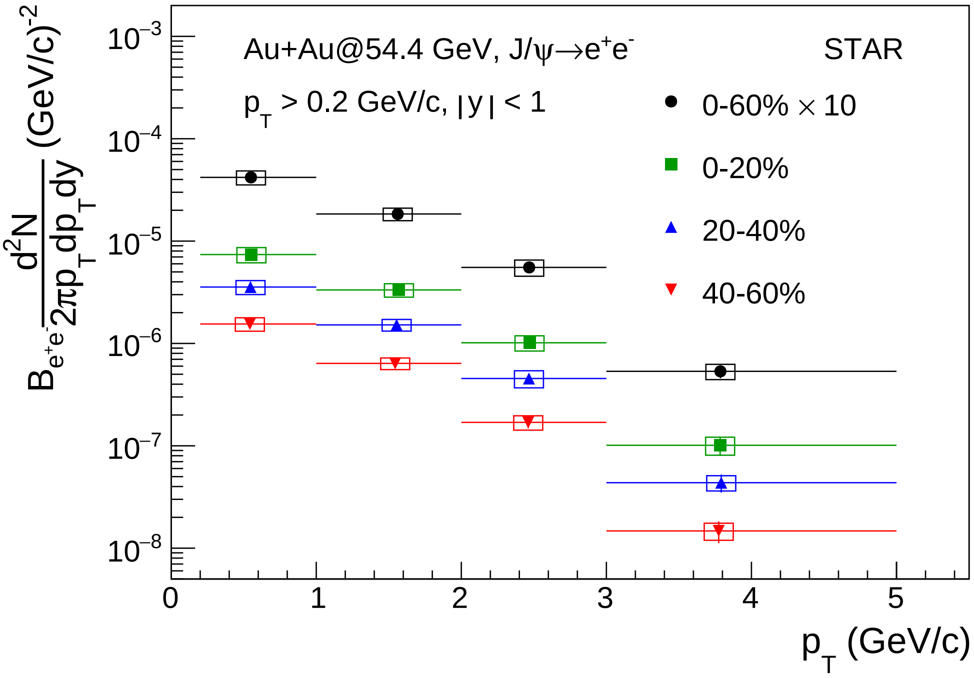

Figure 5.13 Inclusive J/ψ invariant yields as a function of p_{T} at mid-rapidity ($|y| < 1$) in Au+Au collisions at $\sqrt{s_{\mathrm{NN}}} = 54.4$ GeV in different centralities. The horizontal bars depict the p_{T} binning. Data points for 0-60% centrality are scaled up by a factor of ten for clarity.

5.3.2 The nuclear modification factor

The nuclear modification factor (R_{AA}) is used to quantify the modification to the J/ψ production and defined as:

$$R_{\mathrm{AA}} = \frac{1}{\langle N_{\mathrm{coll}} \rangle / \sigma_{\mathrm{pp}}^{\mathrm{inelastic}}} \frac{d^2 N_{\mathrm{AA}}/dp_{\mathrm{T}}dy}{d^2\sigma_{\mathrm{pp}}/dp_{\mathrm{T}}dy}, \tag{5.5}$$

where $d^2N_{\mathrm{AA}}/dp_{\mathrm{T}}dy$ is the J/ψ yield in A+A collisions and $d^2\sigma_{\mathrm{pp}}/dp_{\mathrm{T}}dy$ is the J/ψ cross section in p+p collisions. $\sigma_{\mathrm{pp}}^{\mathrm{inelastic}}$ is the inelastic p+p cross section. Since there are no experimental measurements for the inclusive J/ψ production cross section in p+p collisions at $\sqrt{s} = 54.4$ GeV, a data-driven method is used to derive it based on world-wide experimental data from p+p to p+A collisions ranging between $\sqrt{s_{\mathrm{NN}}} = 6.8 - 7000$ GeV[199]. Different formulas are used to fit the collision energy, rapidity and p_{T} dependence of inclusive J/ψ production cross section, and the difference in the interpolated values at 54.4 GeV between using these formulas is taken as the systematic uncertainty for the p+p baseline.

The p_{T}-integrated (> 0.2 GeV/c) R_{AA} of inclusive J/ψ as a function of $\langle N_{\mathrm{part}}\rangle$ is shown in Fig. 5.14 for Au+Au collisions at 54.4 GeV, and compared to previous results in Au+Au collisions at 39, 62.4 and 200 GeV[106-107]. The level of suppression increases from peripheral to central collisions, consistent with increasing hot medium effects. The newly measured J/ψ R_{AA} at 54.4 GeV is consistent with previous results at 39 and 62.4 GeV within uncertainties, while the precision is significantly improved in this measurement. Transport model calculations[200] from the Tsinghua group for 39, 54.4 and 62.4 GeV are shown as dashed curves in Fig. 5.14, which predicts very little difference among different energies as observed in data.

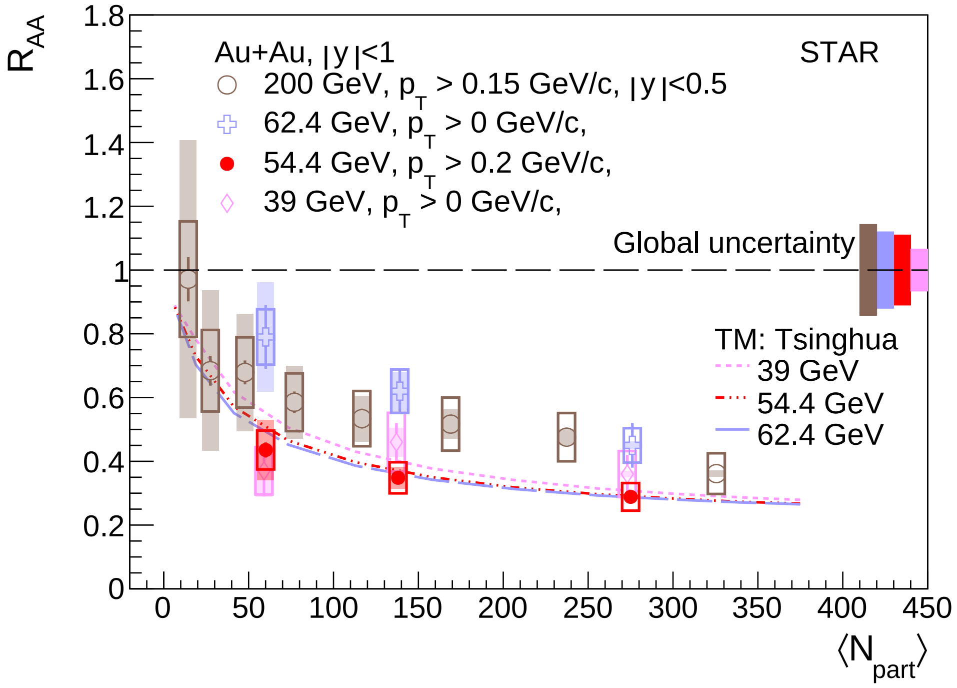

Figure 5.14 The R_{AA} of inclusive J/ψ at mid-rapidity as a function of $\langle N_{\mathrm{part}}\rangle$ in Au+Au collisions at different collision energies[106-107]. Theoretical calculations are shown as dashed lines for comparison[99]. The shaded bands on the data points indicate the uncertainties from the nuclear overlap function $\langle N_{\mathrm{coll}}\rangle$. The bands around unity indicate the uncertainties from the reference J/ψ cross sections in p+p collisions[199].

Figure 5.15 shows the collision energy dependence of J/ψ R_{AA} in central heavy-ion collisions of different species. No significant energy dependence is seen within uncertainties between 17.3 and 200 GeV. Two transport model calculations of the collision energy dependence of inclusive J/ψ R_{AA}, displayed by same line style, are shown on the left panel from the Tsinghua group[200] and the right panel from the TAMU group[99]. Blue dash-dot-tripled lines represent the suppressed primordial production due to CNM effects and dissociation in the QGP medium, while the red long dash lines denote the regeneration contribution. The final J/ψ R_{AA} calculations from two groups, considering both the suppressed effects and regeneration simultaneously, are shown as the black dash lines in the two planes of Fig. 5.15. The theoretical calculations, starting from 39 GeV, are consistent with the observed energy dependence of J/ψ R_{AA}, indicating that the J/ψ production in high-energy heavy-ion collisions is an interplay of dissociation in the QGP medium, regeneration, and CNM effects. At 17.3 GeV, the transport model calculation from the Tsinghua group clearly underestimates the experimental measurements.

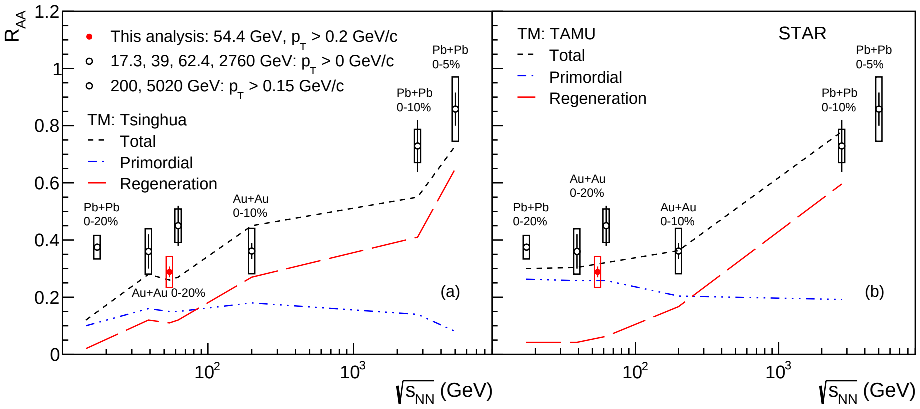

Figure 5.15 The R_{AA} of J/ψ as a function of collision energy in central collisions[103-107,190], in comparison with two transport model calculations from the Tsinghua group[200] (left) and the TAMU group[99] (right). The vertical bars and boxes around the data points signify the statistical uncertainties and systematic uncertainties, including those from p+p baseline and $\langle N_{\mathrm{coll}}\rangle$. The transport model calculations are shown as dashed line for the total J/ψ R_{AA}, dash-dot-tripled line for the suppressed primordial production and long dash line for the regeneration.

Figure 5.16 shows J/ψ R_{AA} as a function of p_{T} for the 0-60% centrality class at different collision energies (left)[106-107] and for different centrality classes at 54.4 GeV (right). As illustrated by the p_{T}-integrated case, the suppression of J/ψ production at 54.4 GeV is consistent with those observed at 39, 62.4 and 200 GeV within uncertainties. On the other hand, a flatter p_{T} dependence of inclusive J/ψ R_{AA} at low p_{T} is seen at $\sqrt{s_{\mathrm{NN}}}$ = 200 GeV compared to lower energies, which could be due to a larger regeneration contribution at 200 GeV and larger nuclear absorption at lower energies at low p_{T}. In Fig. 5.16 (b), a larger yield suppression is observed towards central collisions compared to that for peripheral collisions at $\sqrt{s_{\mathrm{NN}}}$ = 54.4 GeV, while the p_{T} dependence is similar across different centrality classes.

As mentioned above, J/ψ production in high-energy heavy-ion collisions is an interplay of different hot and cold medium effects, while the J/ψ p_{T} spectra shape are crucial to study these effects individually since different effects may dominate in dif-

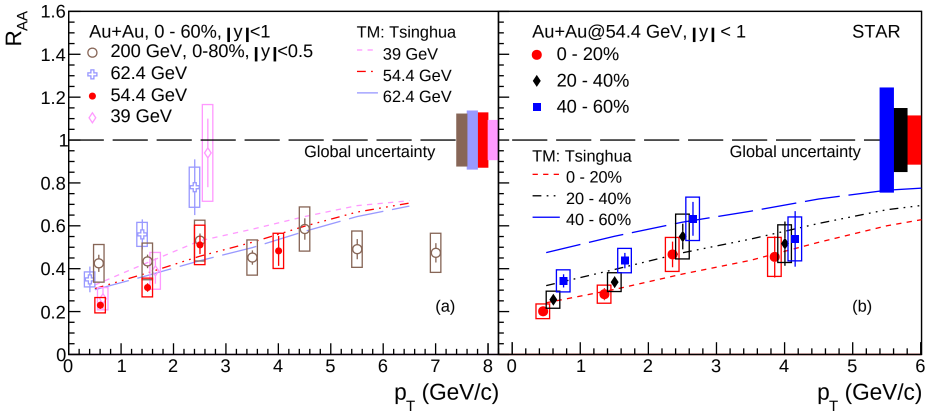

Figure 5.16 J/ψ R_{AA} **as a function of** p_{T} **in the 0-60% centrality class at different collision energies (left)[106-107] and for different centrality classes at 54.4 GeV (right). Theoretical calculations are shown as dashed lines for comparison[99].The vertical bars and boxes around the data points signify the statistical uncertainties and systematic uncertainties, respectively. The bands at unity show the relative uncertainties in the** p+p **baseline and** $\langle N_{\mathrm{coll}}\rangle$**.**

	Au+Au, $\sqrt{s_{\mathrm{NN}}}$ = 54.4 GeV		
	0-20%	20-40%	40-60%
$\langle p_{\mathrm{T}}^2\rangle$ (GeV/c)^2	$3.34 \pm 0.40 \pm 0.11$	$3.33 \pm 0.37 \pm 0.08$	$2.99 \pm 0.34 \pm 0.07$

Table 5.2 Inclusive J/ψ $\langle p_{\mathrm{T}}^2\rangle$ **at mid-rapidity in Au+Au collisions at** $\sqrt{s_{\mathrm{NN}}} = 54.4$ **GeV for different centrality classes.**

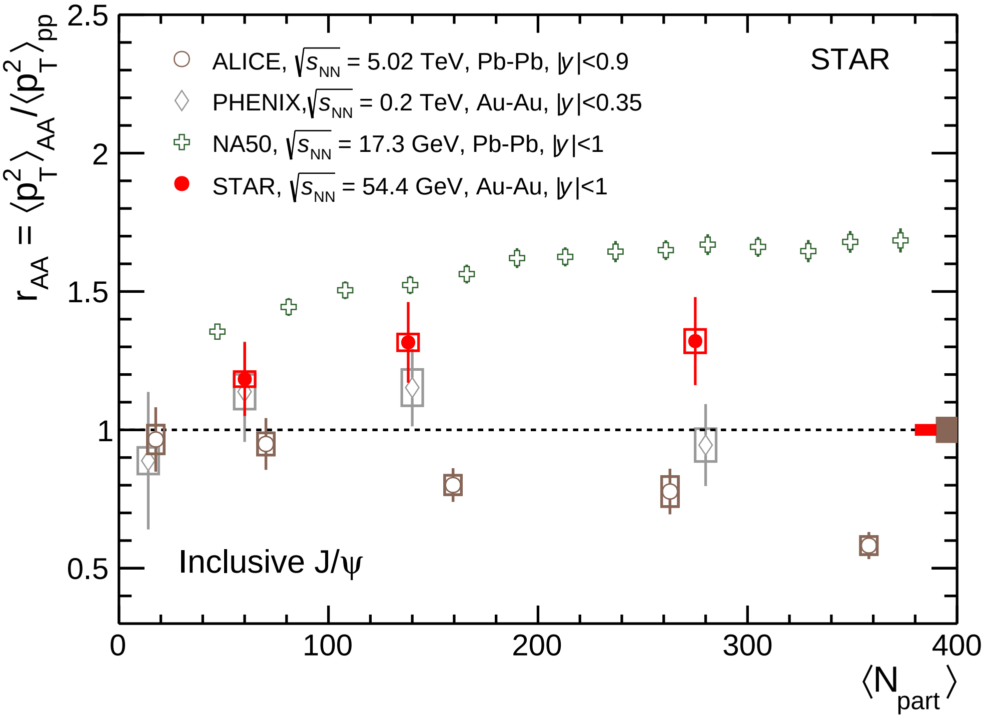

Figure 5.17 The inclusive J/ψ r_{AA} **as a function of** $\langle N_{\mathrm{part}}\rangle$ **in different collision systems[191,193,201-204] at mid-rapidity. The bands at unity show the global uncertainty.**

ferent p_{T} regions. The second moment ($\langle p_{\mathrm{T}}^2 \rangle$) is used to facilitate the comparison of the measured J/ψ p_{T} spectra shape in different centrality bins at $\sqrt{s_{\mathrm{NN}}} = 54.4$ GeV as well as at different collision energies. The $\langle p_{\mathrm{T}}^2 \rangle$ of inclusive J/ψ in different centrality classes of Au+Au collisions at $\sqrt{s_{\mathrm{NN}}} = 54.4$ GeV are displayed in Table 5.2, and no significant centrality dependence is seen. The corresponding $\langle p_{\mathrm{T}}^2 \rangle$ in p+p collisions at the same center-of-mass energy is derived to be 2.53 ± 0.05 (GeV/c)^2[199], which is systematically lower than those in Au+Au collisions. This is consistent with the observed p_{T} dependence of R_{AA}, which increases towards higher p_{T} as shown in Fig. 5.16. To quantify the change in $\langle p_{\mathrm{T}}^2 \rangle$, r_{AA} is used. It is defined as the ratio between $\langle p_{\mathrm{T}}^2 \rangle_{\mathrm{AA}}$ and $\langle p_{\mathrm{T}}^2 \rangle_{\mathrm{pp}}$, and shown as a function of $\langle N_{\mathrm{part}} \rangle$ in Fig. 5.17 for heavy-ion collisions with the collision energy ranging from 17.3 GeV to 5.02 TeV[191,193,201-204]. The r_{AA} at $\sqrt{s_{\mathrm{NN}}} = 54.4$ GeV shows a flat distribution against centrality and follows the trend of the collision energy dependence. On the other hand, r_{AA} decreases towards central collisions at 5.02 TeV, likely due to increased regeneration contribution at low p_{T}.

Chapter 6 Summary and Outlook

6.1 Summary

We present the inaugural measurements examining the dependence of initial electromagnetic fields on photon-induced interactions in $^{96}_{44}$Ru+$^{96}_{44}$Ru and $^{96}_{40}$Zr+$^{96}_{40}$Zr collisions at $\sqrt{s_{NN}}$ = 200 GeV, conducted by the STAR experiment at RHIC. Within the STAR acceptance cuts ($p_T^e > 0.2$ GeV/c, $|\eta^e| < 1$, and $|y^{ee}| < 1$), our measurements reveal a notable enhancement in the e^+e^- pair invariant mass spectrum at very low transverse momentum (p_{T}) in 70-80% Ru+Ru and Zr+Zr collisions in the mass range of 0.4-2.6 GeV/c^2. The corresponding enhancement factors display an increasing trend with increasing invariant mass, peaking around 10. The p_{T} distributions of e^+e^- pair production in Ru+Ru and Zr+Zr collisions indicate that excess yields are primarily concentrated in the very low p_{T} region. At intermediate p_{T} ranges, our data align well with expectations from hadronic cocktails. By statistically subtracting the hadronic contributions, we derive the excess e^+e^- yields, presented as a function of the N_{part} in Ru+Ru and Zr+Zr collisions, respectively. Remarkably, the integrated excess yields in Ru+Ru collisions systematically higher than those in Zr+Zr collisions, in accordance with theoretical predictions. The ratio of excess yield of e^+e^- pairs in Ru+Ru to Zr+Zr collisions exceeds unity by approximately 2.4σ, implying disparities in the initial electromagnetic fields between these collision systems. At very low p_{T} region ($p_{\mathrm{T}} < 0.1$ GeV/c^2), the excess yield ratio conforms to EPA-QED calculations based on photon-induced interactions, following the $(\frac{44}{40})^2$ scaling. This indeed means the initial electromagnetic field in Ru+Ru collisions is different when compared to that in Zr+Zr collisions. However, at intermediate p_{T} ranges, where hadronic contributions become significant, the yield ratios, inclusive of these contributions, converge to unity. Minor deviations above unity may be attributed to distinct nuclear structures between the two collision systems, such as the nucleon skin effect. Comparisons of excess e^+e^- yields between Ru+Ru and Zr+Zr collisions with published results from Au+Au and U+U collisions in the same centrality class and kinematic regions unveil differences are mainly due to variations in charge. After scaling by Z^4 to accommodate this charge difference, the excess yield distribution still exhibits clear dependence on the collision system, likely stemming from the impact parameter dependence of photon-induced processes. Last not the least, a clear $\cos(4\Delta\phi)$ modulation is observed in isobaric collisions, and the magnitude is consistent with the EPA-QED calculations. Compared to the published magnitudes of $\cos(4\Delta\phi)$

modulation in peripheral and ultraperipheral Au+Au collisions at $\sqrt{s_{\mathrm{NN}}}$= 200 GeV, a decreasing trend is seen as the specific values of impact parameter (b) increasing.

Additionally, we present measurements of very low p_{T} J/ψ meson production in Ru+Ru and Zr+Zr collisions at $\sqrt{s_{NN}} = 200$ GeV. Our analysis of the invariant yield distributions in non-central isobaric collisions reveals significant enhancements at very low p_{T} (< 0.2 GeV/c) in 20-40%, 40-60%, and 60-80% Ru+Ru and Zr+Zr collisions, respectively. Similarly, the nuclear modification factor (R_{AA}) distributions as a function of p_{T} yield analogous conclusions. To estimate the hadronic contribution of J/ψ mesons in the very low p_{T} region, we extrapolate the fitting results from higher p_{T} regions using the Levy function. Subsequently, we derive the excess J/ψ meson yields and compare them to published results in Au+Au and U+U collisions at the same centrality class. Similar conclusions are drawn that a significant charge dependence of excess J/ψ yields is seen mainly due to the charge difference. After scaling for the charges difference by Z^2, in contrast to the observations in e^+e^- measurements, we find that the excess yields exhibit no clear dependence on the collision system. The weak collision system dependence may be attributed to an interplay of the impact parameter and form factor effects.

This thesis also encompasses an analysis of inclusive J/ψ production in Au+Au collisions at $\sqrt{s_{NN}} = 54.4$ GeV. The invariant yields of inclusive J/ψ production are measured across four distinct centrality classes as a function of p_{T}. Additionally, the inclusive J/ψ R_{AA} is measured as a function of the N_{part} in Au+Au collisions at $\sqrt{s_{NN}} = 54.4$ GeV, and these results are compared with similar results from Au+Au collisions at $\sqrt{s_{NN}} = 39$, 62.4, and 200 GeV. Notably, the newly obtained result at $\sqrt{s_{NN}} = 54.4$ GeV exhibits significantly improved precision and remains consistent with previous measurements within uncertainties. When investigating to R_{AA} in central collisions as a function of different collision energies, ranging from SPS to LHC energies, it reveals no significant dependence on collision energy within uncertainties, spanning from 17.3 to 200 GeV. The distribution of J/ψ R_{AA} across collision energies is compared to two transport model calculations from Tsinghua and TAMU groups. Both models demonstrate consistency with data starting from 39 GeV, although the Tsinghua group's calculation appears to underestimate J/ψ R_{AA} at SPS energy (17.3 GeV). Further analysis involves measuring J/ψ R_{AA} as a function of p_{T} in four centrality classes in Au+Au collisions at $\sqrt{s_{NN}} = 54.4$ GeV. Increased suppression is observed towards more central and lower p_{T} regions, suggestive of reduced regeneration contributions at this energy. Based on the measured p_{T} spectra of J/ψ production in Au+Au collisions at $\sqrt{s_{NN}}$ = 54.4 GeV, $\langle p_{\mathrm{T}}^2 \rangle$as well as the r_{AA} are calculated. No significant centrality dependence of $\langle p_{\mathrm{T}}^2 \rangle$is observed at $\sqrt{s_{NN}}$ = 54.4 GeV. Moreover, the r_{AA} at this energy exhibits a flat distribution against centrality, aligning with the trend of collision energy dependence.

6.2 Outlook

The realization of RHIC's scientific objectives hinges on two central goals: i) delineating the phase diagram of Quantum Chromodynamics (QCD), and ii) probing the intricacies of the Quark-Gluon Plasma (QGP) by scrutinizing its properties at short length scales. The collaborative efforts between RHIC and LHC facilities in investigating the latter are scientifically imperative, resembling the necessity for multiple experiments to independently dissect the microstructure of the QGP. With anticipated increases in beam luminosity during Runs 23-25, RHIC will be uniquely positioned to embark on a thorough exploration of the microstructure of the QGP.

As an integral component of RHIC's detector suite, the STAR collaboration has not only installed the iTPC but has also operated it for several years. In addition to the iTPC upgrade, STAR's forward detectors, including the Forward Tracking System (FTS) and Forward Calorimeter System (FCS), have been successfully installed and initiated data acquisition. These advancements place the STAR collaboration in an advantageous position to capitalize on its substantially enhanced detection capabilities.

During Run 23, the STAR collaboration recorded approximately 6.8 billion events in Au+Au collisions at $\sqrt{s_{NN}}$ = 200 GeV, despite the actual data intake being lower than anticipated due to an unexpected helium leak in early August 2023. Nevertheless, this dataset surpasses the volume of all previous STAR data collected from Au+Au collisions at $\sqrt{s_{NN}}$ = 200 GeV. Additionally, another run for Au+Au collisions at $\sqrt{s_{NN}}$ = 200 GeV is scheduled for 2025.

6.2.1 The Dielectron Measurements in 23-25 runs

The inability of the STARLight model to accurately depict STAR data prompted the consideration that the broadening could be attributed to a residual magnetic field entrapped within an electrically conductive QGP. This insight is pivotal for investigating the chiral magnetic effect. In a similar vein, ATLAS discerned the effect through the acoplanarity of lepton pairs, contrasting measurements in UPC, and elucidated the additional broadening through multiple electromagnetic scatterings within the hot and dense medium. This phenomenon bears resemblance to the medium $P_\perp$-broadening observed in jet quenching. These explanations of broadening in hadronic collisions operate under the assumption of no impact parameter dependence in the transverse momentum distribution for electromagnetic production. Recent lowest-order QED calculations, which reintroduce impact parameter dependence, offer a reasonable description of the observed broadening by STAR and ATLAS, without invoking any in-medium effects.

Recent lowest-order QED calculations, incorporating impact parameter dependence, offer a promising explanation for the observed broadening by both STAR and ATLAS, without necessitating any in-medium effects. To unravel this puzzle, we propose a meticulous investigation into the initial $P_\perp$-broadening of dilepton pairs in ultra-peripheral collisions. Utilizing various neutron emission tags as centrality definitions will enable us to explore variations in the broadening baseline with impact parameter. Furthermore, dissecting the differential spectrum in terms of pair $P_\perp$, rapidity, and mass will facilitate a comprehensive study of the Wigner function of the initial electromagnetic field. This approach promises invaluable insights into extracting momentum and spatial correlations of the electromagnetic field.

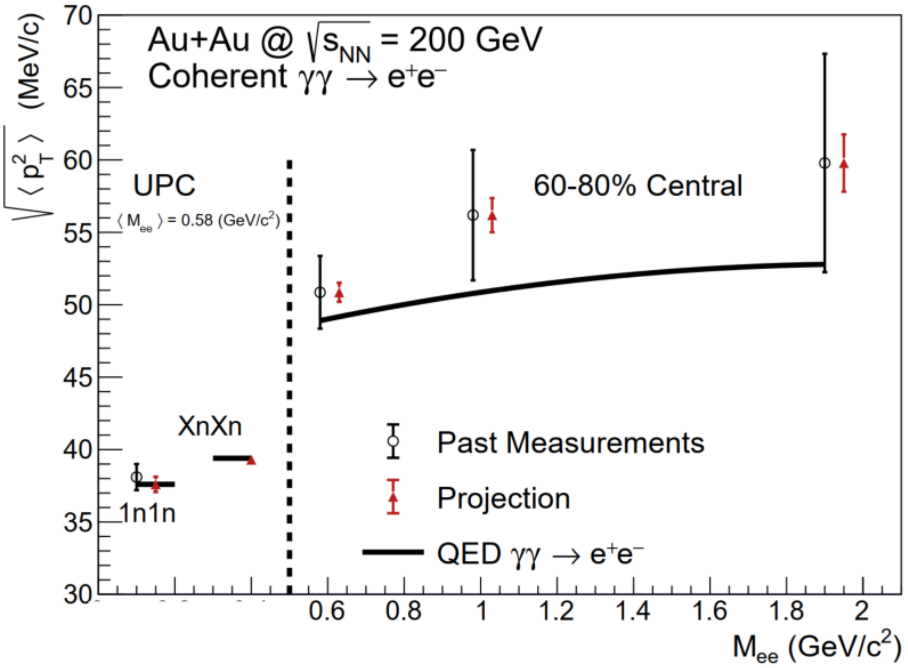

Figure 6.1 $\sqrt{\langle p_T^2 \rangle}$ **of** e^+e^- **pairs as a function of pair mass for 60-80% central and ultra-peripheral Au+Au collisions at** $\sqrt{s_{NN}}$ **= 200 GeV.**

As depicted in Fig. 6.1, a comparison with the latest QED calculation reveals the continued presence of additional broadening in peripheral collisions. Although its significance is only approximately 1σ, this leaves room for the potential influence of a medium effect. Looking ahead to Runs 25 together with the taken dataset in 2023, as projected in the figure, we anticipate the ability to discern the presence of additional broadening with significantly higher precision. This will allow us to further refine our understanding and constrain the strength of the final-state magnetic field within QGP.

6.2.2 The J/ψ Measurements in 23-25 runs

Measurements of charmonia in heavy-ion collisions provide crucial insights into the thermodynamic properties of the created medium. In Au+Au collisions at RHIC, the production of J/ψ mesons exhibits suppression compared to p+p collisions, attributed to the screening of the $c\bar{c}$ potential by the medium's color charges. Additionally, J/ψ production may be affected by the recombination of charm quarks in a later stage of collision evolution. The regeneration mechanism is expected to predominantly influence the low transverse momentum range of J/ψ.

The J/ψ elliptic flow (v_2) at low p_{T} is crucial to further understand the recombination mechanism. While, reported by STAR based on the 2010 Au+Au 200 GeV data sample, the v_2 of J/ψ was found to be consistent with zero. However, this observation is subject to significant statistical uncertainties and systematic uncertainties stemming from non-flow effects. The precision of the measurement was inadequate to differentiate between theoretical model calculations that exclusively consider primordial J/ψ production and those that include additional J/ψ production via recombination. This underscores the necessity for a larger sample of heavy-ion data at 200 GeV, which will be provided by RHIC in 2023 and 2025. Such expanded datasets would enable the observation of a potential non-zero J/ψ v_2 at RHIC energies and facilitate more stringent constraints on J/ψ production models, particularly regarding regeneration. Figure 6.2 shows the statistical projection for the J/ψ v_2 measurement in 0-80% central Au+Au collisions assuming 20 B minimum-bias events and HT triggered events corresponding to an integrated luminosity of $75nb^{-1}$.

ψ(2S) is the most loosely bound quarkonium state accessible in heavy-ion collision experiments. The relative suppression of ψ(2S) and J/ψ is highly sensitive to the temperature profile of the fireball generated in heavy-ion collisions and its space-time evolution. The measurement of ψ(2S) is considerably more challenging than that of J/ψ due to its much smaller production cross-section and dilepton decay branching ratio. This leads to a very low signal-to-background ratio. In a recent development, STAR has successfully detected the ψ(2S) signal in isobaric collisions, comprising approximately 4 billion minimum-bias events. This groundbreaking observation represents the

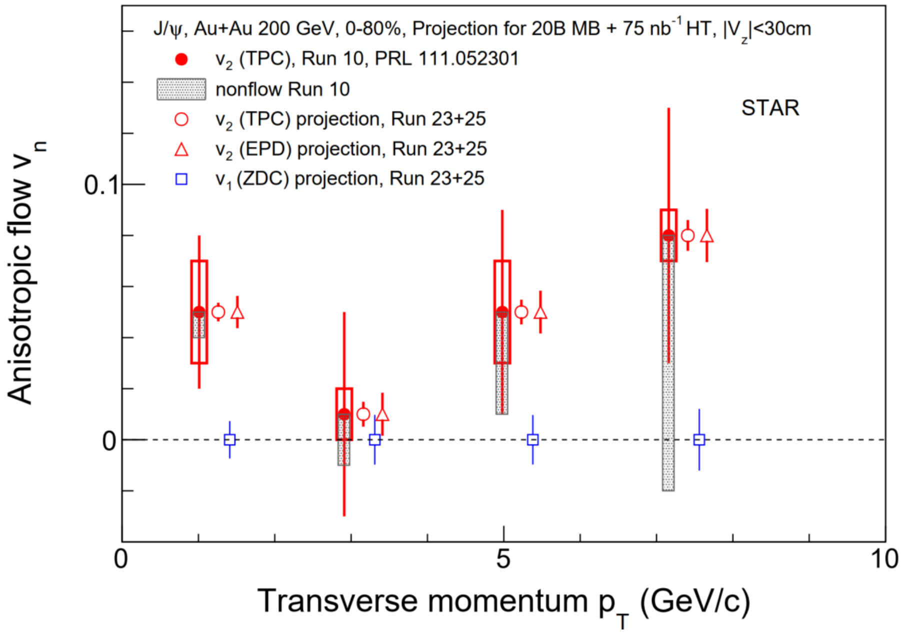

Figure 6.2 Projections for the J/ψ (decay to e^+e^-) directed (v_1) and elliptic (v_2) flow vs J/ψ p_T in 0-80% Au+Au collisions at $\sqrt{s_{NN}}$ = 200 GeV.

first measurement of ψ(2S) in heavy-ion collisions at RHIC, boasting an impressive significance level of about 6σ. This notable achievement signals a promising beginning, especially considering the forthcoming close to 20 billion minimum-bias events expected from Runs 23-25. These upcoming events will undoubtedly provide a significantly enhanced opportunity to delve into the transport properties of ψ(2S) in the Quark-Gluon Plasma (QGP) at mid-rapidity during heavy-ion collisions.

Bibliography

[1] WIKIPEDIA. https://commons.wikimedia.org/wiki/File:Standard_Model_of_Elementary_Particles.svg [Z].

[2] CHADWICK J. The Existence of a Neutron[J/OL]. Proc. Roy. Soc. Lond. A, 1932, 136(830): 692-708. DOI: 10.1098/rspa.1932.0112.

[3] YUKAWA H. On the Interaction of Elementary Particles I[J/OL]. Proc. Phys. Math. Soc. Jap., 1935, 17: 48-57. DOI: 10.1143/PTPS.1.1.

[4] GELL-MANN M. A Schematic Model of Baryons and Mesons[J/OL]. Phys. Lett., 1964, 8: 214-215. DOI: 10.1016/S0031-9163(64)92001-3.

[5] ZWEIG G. An SU(3) model for strong interaction symmetry and its breaking. Version 2[M]. 1964: 22-101.

[6] BJORKEN J D. Asymptotic Sum Rules at Infinite Momentum[J/OL]. Phys. Rev., 1969, 179: 1547-1553. DOI: 10.1103/PhysRev.179.1547.

[7] FRIEDMAN J I, KENDALL H W, TAYLOR R E. Nobel lectures in physics 1990[Z]. 1990.

[8] HAN M Y, NAMBU Y. Three Triplet Model with Double SU(3) Symmetry[J/OL]. Phys. Rev., 1965, 139: B1006-B1010. DOI: 10.1103/PhysRev.139.B1006.

[9] ON RESEARCHGATE S F. https://www.researchgate.net/figure/the-charge-screening-effect-in-QED$_f ig13_4 6076811[Z]$.

[10] GROSS D J, WILCZEK F. Ultraviolet behavior of non-abelian gauge theories[J/OL]. Phys. Rev. Lett., 1973, 30: 1343-1346. https://link.aps.org/doi/10.1103/PhysRevLett.30.1343.

[11] POLITZER H D. Reliable perturbative results for strong interactions?[J/OL]. Phys. Rev. Lett., 1973, 30: 1346-1349. https://link.aps.org/doi/10.1103/PhysRevLett.30.1346.

[12] DUKE D W, ROBERTS R G. Deep Inelastic Scattering and Asymptotic Freedom: A Detailed Analysis and Confrontation[J/OL]. Nucl. Phys. B, 1980, 166: 243-283. DOI: 10.1016/0550-3213(80)90227-8.

[13] GROUP P D, WORKMAN R L, BURKERT V D, et al. Review of Particle Physics[J/OL]. Progress of Theoretical and Experimental Physics, 2022, 2022(8): 083C01. https://doi.org/10.1093/ptep/ptac097.

[14] WEBPAGE. https://webific.ific.uv.es/web/en/content/lattice-qcd-numerical-approach-strong-force[Z].

[15] ADAMS J, et al. Experimental and theoretical challenges in the search for the quark gluon plasma: The STAR Collaboration's critical assessment of the evidence from RHIC collisions [J/OL]. Nucl. Phys. A, 2005, 757: 102-183. DOI: 10.1016/j.nuclphysa.2005.03.085.

[16] MOHANTY B, XU N. QCD Critical Point and High Baryon Density Matter[C]//Criticality in QCD and the Hadron Resonance Gas. 2021.

[17] FUKUSHIMA K, HATSUDA T. The phase diagram of dense QCD[J/OL]. Rept. Prog. Phys., 2011, 74: 014001. DOI: 10.1088/0034-4885/74/1/014001.

[18] BAZAVOV A, et al. Skewness and kurtosis of net baryon-number distributions at small values of the baryon chemical potential[J/OL]. Phys. Rev. D, 2017, 96(7): 074510. DOI: 10.1103/PhysRevD.96.074510.

[19] BAZAVOV A, et al. The QCD Equation of State to $\mathcal{O}(\mu_B^6)$ from Lattice QCD[J/OL]. Phys. Rev. D, 2017, 95(5): 054504. DOI: 10.1103/PhysRevD.95.054504.

[20] FUKUSHIMA K, MOHANTY B, XU N. Little-Bang and Femto-Nova in Nucleus-Nucleus Collisions[J/OL]. AAPPS Bull., 2021, 31: 1. DOI: 10.1007/s43673-021-00002-7.

[21] BHALERAO R S. Relativistic heavy-ion collisions[C/OL]//1st Asia-Europe-Pacific School of High-Energy Physics. 2014: 219-239. DOI: 10.5170/CERN-2014-001.219.

[22] VOGT R. J/ψ production and suppression[J/OL]. Phys. Rept., 1999, 310: 197-260. DOI: 10.1016/S0370-1573(98)00074-X.

[23] RAFELSKI J, MULLER B. Strangeness Production in the Quark - Gluon Plasma[J/OL]. Phys. Rev. Lett., 1982, 48: 1066. DOI: 10.1103/PhysRevLett.48.1066.

[24] ADCOX K, et al. Formation of dense partonic matter in relativistic nucleus-nucleus collisions at RHIC: Experimental evaluation by the PHENIX collaboration[J/OL]. Nucl. Phys. A, 2005, 757: 184-283. DOI: 10.1016/j.nuclphysa.2005.03.086.

[25] ARSENE I, et al. Quark gluon plasma and color glass condensate at RHIC? The Perspective from the BRAHMS experiment[J/OL]. Nucl. Phys. A, 2005, 757: 1-27. DOI: 10.1016/j.nuclphysa.2005.02.130.

[26] BACK B B, et al. The PHOBOS perspective on discoveries at RHIC[J/OL]. Nucl. Phys. A, 2005, 757: 28-101. DOI: 10.1016/j.nuclphysa.2005.03.084.

[27] BY CHUN SHEN M. https://u.osu.edu/vishnu/2014/08/06/sketch-of-relativistic-heavy-ion-collisions/[Z].

[28] GELIS F, IANCU E, JALILIAN-MARIAN J, et al. The Color Glass Condensate[J/OL]. Ann. Rev. Nucl. Part. Sci., 2010, 60: 463-489. DOI: 10.1146/annurev.nucl.010909.083629.

[29] MILLER M L, REYGERS K, SANDERS S J, et al. Glauber modeling in high energy nuclear collisions[J/OL]. Ann. Rev. Nucl. Part. Sci., 2007, 57: 205-243. DOI: 10.1146/annurev.nucl.57.090506.123020.

[30] KHARZEEV D, NARDI M. Hadron production in nuclear collisions at RHIC and high density QCD[J/OL]. Phys. Lett. B, 2001, 507: 121-128. DOI: 10.1016/S0370-2693(01)00457-9.

[31] ALBACETE J L, MARQUET C. Gluon saturation and initial conditions for relativistic heavy

ion collisions[J/OL]. Prog. Part. Nucl. Phys., 2014, 76: 1-42. DOI: 10.1016/j.ppnp.2014.01.004.

[32] MULLER I. Zum Paradoxon der Warmeleitungstheorie[J/OL]. Z. Phys., 1967, 198: 329-344. DOI: 10.1007/BF01326412.

[33] ISRAEL W, STEWART J M. Transient relativistic thermodynamics and kinetic theory[J/OL]. Annals Phys., 1979, 118: 341-372. DOI: 10.1016/0003-4916(79)90130-1.

[34] HUOVINEN P, PETRECZKY P. QCD Equation of State and Hadron Resonance Gas[J/OL]. Nucl. Phys. A, 2010, 837: 26-53. DOI: 10.1016/j.nuclphysa.2010.02.015.

[35] SONG H, BASS S A, HEINZ U, et al. Hadron spectra and elliptic flow for 200 A GeV Au+Au collisions from viscous hydrodynamics coupled to a Boltzmann cascade[J/OL]. Phys. Rev. C, 2011, 83: 054910. DOI: 10.1103/PhysRevC.83.054910.

[36] BJORKEN J D. Hadron Final States in Deep Inelastic Processes[J]. Lect. Notes Phys., 1976, 56: 93.

[37] ZHOU J. Measurements of dimuon production induced by ultra-strong electromagnetic fields [Z].

[38] SIRUNYAN A M, et al. Observation of Forward Neutron Multiplicity Dependence of Dimuon Acoplanarity in Ultraperipheral Pb-Pb Collisions at $\sqrt{s_{NN}}$=5.02 TeV[J/OL]. Phys. Rev. Lett., 2021, 127(12): 122001. DOI: 10.1103/PhysRevLett.127.122001.

[39] KHARZEEV D E, MCLERRAN L D, WARRINGA H J. The Effects of topological charge change in heavy ion collisions: 'Event by event P and CP violation'[J/OL]. Nucl. Phys. A, 2008, 803: 227-253. DOI: 10.1016/j.nuclphysa.2008.02.298.

[40] SKOKOV V, ILLARIONOV A Y, TONEEV V. Estimate of the magnetic field strength in heavy-ion collisions[J/OL]. Int. J. Mod. Phys. A, 2009, 24: 5925-5932. DOI: 10.1142/S0217751X09047570.

[41] VORONYUK V, TONEEV V D, CASSING W, et al. (Electro-)Magnetic field evolution in relativistic heavy-ion collisions[J/OL]. Phys. Rev. C, 2011, 83: 054911. DOI: 10.1103/PhysRevC.83.054911.

[42] BZDAK A, SKOKOV V. Event-by-event fluctuations of magnetic and electric fields in heavy ion collisions[J/OL]. Phys. Lett. B, 2012, 710: 171-174. DOI: 10.1016/j.physletb.2012.02.065.

[43] OU L, LI B A. Magnetic effects in heavy-ion collisions at intermediate energies[J/OL]. Phys. Rev. C, 2011, 84: 064605. DOI: 10.1103/PhysRevC.84.064605.

[44] DENG W T, HUANG X G. Event-by-event generation of electromagnetic fields in heavy-ion collisions[J/OL]. Phys. Rev. C, 2012, 85: 044907. DOI: 10.1103/PhysRevC.85.044907.

[45] BLOCZYNSKI J, HUANG X G, ZHANG X, et al. Azimuthally fluctuating magnetic field

and its impacts on observables in heavy-ion collisions[J/OL]. Phys. Lett. B, 2013, 718: 1529-1535. DOI: 10.1016/j.physletb.2012.12.030.

[46] BLOCZYNSKI J, HUANG X G, ZHANG X, et al. Charge-dependent azimuthal correlations from AuAu to UU collisions[J/OL]. Nucl. Phys. A, 2015, 939: 85-100. DOI: 10.1016/j.nuclphysa.2015.03.012.

[47] ZHONG Y, YANG C B, CAI X, et al. A systematic study of magnetic field in Relativistic Heavy-ion Collisions in the RHIC and LHC energy regions[J/OL]. Adv. High Energy Phys., 2014, 2014: 193039. DOI: 10.1155/2014/193039.

[48] HIRONO Y, HONGO M, HIRANO T. Estimation of electric conductivity of the quark gluon plasma via asymmetric heavy-ion collisions[J/OL]. Phys. Rev. C, 2014, 90(2): 021903. DOI: 10.1103/PhysRevC.90.021903.

[49] HUANG X G. Electromagnetic fields and anomalous transports in heavy-ion collisions — A pedagogical review[J/OL]. Rept. Prog. Phys., 2016, 79(7): 076302. DOI: 10.1088/0034-4885/79/7/076302.

[50] OLAUSEN S A, KASPI V M. The McGill Magnetar Catalog[J/OL]. Astrophys. J. Suppl., 2014, 212: 6. DOI: 10.1088/0067-0049/212/1/6.

[51] TUROLLA R, ZANE S, WATTS A. Magnetars: the physics behind observations. A review [J/OL]. Rept. Prog. Phys., 2015, 78(11): 116901. DOI: 10.1088/0034-4885/78/11/116901.

[52] GRASSO D, RUBINSTEIN H R. Magnetic fields in the early universe[J/OL]. Phys. Rept., 2001, 348: 163-266. DOI: 10.1016/S0370-1573(00)00110-1.

[53] APS. https://aps.org/newsroom/april/accelerators.cfm[Z].

[54] FUKUSHIMA K, KHARZEEV D E, WARRINGA H J. The Chiral Magnetic Effect[J/OL]. Phys. Rev. D, 2008, 78: 074033. DOI: 10.1103/PhysRevD.78.074033.

[55] SON D T, ZHITNITSKY A R. Quantum anomalies in dense matter[J/OL]. Phys. Rev. D, 2004, 70: 074018. DOI: 10.1103/PhysRevD.70.074018.

[56] METLITSKI M A, ZHITNITSKY A R. Anomalous axion interactions and topological currents in dense matter[J/OL]. Phys. Rev. D, 2005, 72: 045011. DOI: 10.1103/PhysRevD.72.045011.

[57] HUANG X G, LIAO J. Axial Current Generation from Electric Field: Chiral Electric Separation Effect[J/OL]. Phys. Rev. Lett., 2013, 110(23): 232302. DOI: 10.1103/PhysRevLett.110.232302.

[58] KHARZEEV D E, YEE H U. Chiral Magnetic Wave[J/OL]. Phys. Rev. D, 2011, 83: 085007. DOI: 10.1103/PhysRevD.83.085007.

[59] ERDMENGER J, HAACK M, KAMINSKI M, et al. Fluid dynamics of R-charged black holes[J/OL]. JHEP, 2009, 01: 055. DOI: 10.1088/1126-6708/2009/01/055.

[60] BANERJEE N, BHATTACHARYA J, BHATTACHARYYA S, et al. Hydrodynamics from charged black branes[J/OL]. JHEP, 2011, 01: 094. DOI: 10.1007/JHEP01(2011)094.

[61] SON D T, SUROWKA P. Hydrodynamics with Triangle Anomalies[J/OL]. Phys. Rev. Lett., 2009, 103: 191601. DOI: 10.1103/PhysRevLett.103.191601.

[62] JIANG Y, HUANG X G, LIAO J. Chiral vortical wave and induced flavor charge transport in a rotating quark-gluon plasma[J/OL]. Phys. Rev. D, 2015, 92(7): 071501. DOI: 10.1103/PhysRevD.92.071501.

[63] CHERNODUB M N. Chiral Heat Wave and mixing of Magnetic, Vortical and Heat waves in chiral media[J/OL]. JHEP, 2016, 01: 100. DOI: 10.1007/JHEP01(2016)100.

[64] YAMAMOTO N. Chiral Alfvén Wave in Anomalous Hydrodynamics[J/OL]. Phys. Rev. Lett., 2015, 115(14): 141601. DOI: 10.1103/PhysRevLett.115.141601.

[65] BERTULANI C A, KLEIN S R, NYSTRAND J. Physics of ultra-peripheral nuclear collisions [J/OL]. Ann. Rev. Nucl. Part. Sci., 2005, 55: 271-310. DOI: 10.1146/annurev.nucl.55.090704.151526.

[66] FERMI E. On the theory of collisions between atoms and electrically charged particles[J/OL]. Nuovo Cim., 1925, 2: 143-158. DOI: 10.1007/BF02961914.

[67] WILLIAMS E J. Nature of the high-energy particles of penetrating radiation and status of ionization and radiation formulae[J/OL]. Phys. Rev., 1934, 45: 729-730. DOI: 10.1103/PhysRev.45.729.

[68] AFANASIEV S, et al. Photoproduction of J/psi and of high mass e+e- in ultra-peripheral Au+Au collisions at s**(1/2) = 200-GeV[J/OL]. Phys. Lett. B, 2009, 679: 321-329. DOI: 10.1016/j.physletb.2009.07.061.

[69] AUBERT J J, et al. Experimental Observation of a Heavy Particle J[J/OL]. Phys. Rev. Lett., 1974, 33: 1404-1406. DOI: 10.1103/PhysRevLett.33.1404.

[70] AUGUSTIN J E, et al. Discovery of a Narrow Resonance in e^+e^- Annihilation[J/OL]. Phys. Rev. Lett., 1974, 33: 1406-1408. DOI: 10.1103/PhysRevLett.33.1406.

[71] FRITZSCH H. Producing Heavy Quark Flavors in Hadronic Collisions: A Test of Quantum Chromodynamics[J/OL]. Phys. Lett. B, 1977, 67: 217-221. DOI: 10.1016/0370-2693(77)90108-3.

[72] HALZEN F. Cvc for Gluons and Hadroproduction of Quark Flavors[J/OL]. Phys. Lett. B, 1977, 69: 105-108. DOI: 10.1016/0370-2693(77)90144-7.

[73] CHANG C H. Hadronic Production of J/ψ Associated With a Gluon[J/OL]. Nucl. Phys. B, 1980, 172: 425-434. DOI: 10.1016/0550-3213(80)90175-3.

[74] BAIER R, RUCKL R. Hadronic Production of J/psi and Upsilon: Transverse Momentum Distributions[J/OL]. Phys. Lett. B, 1981, 102: 364-370. DOI: 10.1016/0370-2693(81)90636

-5.

[75] BAIER R, RUCKL R. Hadronic Collisions: A Quarkonium Factory[J/OL]. Z. Phys. C, 1983, 19: 251. DOI: 10.1007/BF01572254.

[76] BODWIN G T, BRAATEN E, LEPAGE G P. Rigorous QCD analysis of inclusive annihilation and production of heavy quarkonium[J/OL]. Phys. Rev. D, 1995, 51: 1125-1171. DOI: 10.1103/PhysRevD.55.5853.

[77] ESKOLA K J, KOLHINEN V J, RUUSKANEN P V. Scale evolution of nuclear parton distributions[J/OL]. Nucl. Phys. B, 1998, 535: 351-371. DOI: 10.1016/S0550-3213(98)00589-6.

[78] ESKOLA K J, KOLHINEN V J, PAUKKUNEN H, et al. A Global reanalysis of nuclear parton distribution functions[J/OL]. JHEP, 2007, 05: 002. DOI: 10.1088/1126-6708/2007/05/002.

[79] DE FLORIAN D, SASSOT R. Nuclear parton distributions at next-to-leading order[J/OL]. Phys. Rev. D, 2004, 69: 074028. DOI: 10.1103/PhysRevD.69.074028.

[80] HIRAI M, KUMANO S, NAGAI T H. Determination of nuclear parton distribution functions and their uncertainties in next-to-leading order[J/OL]. Phys. Rev. C, 2007, 76: 065207. DOI: 10.1103/PhysRevC.76.065207.

[81] ESKOLA K J, PAUKKUNEN H, SALGADO C A. EPS09: A New Generation of NLO and LO Nuclear Parton Distribution Functions[J/OL]. JHEP, 2009, 04: 065. DOI: 10.1088/1126-6708/2009/04/065.

[82] LOURENCO C, VOGT R, WOEHRI H K. Energy dependence of J/psi absorption in proton-nucleus collisions[J/OL]. JHEP, 2009, 02: 014. DOI: 10.1088/1126-6708/2009/02/014.

[83] MCGLINCHEY D C, FRAWLEY A D, VOGT R. Impact parameter dependence of the nuclear modification of J/ψ production in d+Au collisions at $\sqrt{S_{NN}} = 200$ GeV[J/OL]. Phys. Rev. C, 2013, 87(5): 054910. DOI: 10.1103/PhysRevC.87.054910.

[84] MATSUI T, SATZ H. J/ψ Suppression by Quark-Gluon Plasma Formation[J/OL]. Phys. Lett. B, 1986, 178: 416-422. DOI: 10.1016/0370-2693(86)91404-8.

[85] SATZ H. Colour deconfinement and quarkonium binding[J/OL]. J. Phys. G, 2006, 32: R25. DOI: 10.1088/0954-3899/32/3/R01.

[86] XU X M, KHARZEEV D, SATZ H, et al. J/ψ suppression in an equilibrating parton plasma [J/OL]. Phys. Rev. C, 1996, 53: 3051-3056. https://link.aps.org/doi/10.1103/PhysRevC.53.3051.

[87] YAO X, MÜLLER B. Quarkonium inside the quark-gluon plasma: Diffusion, dissociation, recombination, and energy loss[J/OL]. Phys. Rev. D, 2019, 100: 014008. https://link.aps.org/doi/10.1103/PhysRevD.100.014008.

[88] SHARMA R, VITEV I. High transverse momentum quarkonium production and dissociation in heavy ion collisions[J/OL]. Phys. Rev. C, 2013, 87: 044905. https://link.aps.org/doi/10.11

03/PhysRevC.87.044905.

[89] BRAUN-MUNZINGER P, STACHEL J. (Non)thermal aspects of charmonium production and a new look at J/ψ suppression[J/OL]. Physics Letters B, 2000, 490(3): 196-202. DOI: https://doi.org/10.1016/S0370-2693(00)00991-6.

[90] GRANDCHAMP L, RAPP R, BROWN G E. In-Medium Effects on Charmonium Production in Heavy-Ion Collisions[J/OL]. Phys. Rev. Lett., 2004, 92: 212301. https://link.aps.org/doi/10.1103/PhysRevLett.92.212301.

[91] THEWS R L, SCHROEDTER M, RAFELSKI J. Enhanced J/ψ production in deconfined quark matter[J/OL]. Phys. Rev. C, 2001, 63: 054905. DOI: 10.1103/PhysRevC.63.054905.

[92] ABREU M C, et al. J / psi and psi-prime production in p, O and S induced reactions at SPS energies[J/OL]. Phys. Lett. B, 1999, 466: 408-414. DOI: 10.1016/S0370-2693(99)01108-9.

[93] ABREU M C, et al. Evidence for deconfinement of quarks and gluons from the J / psi suppression pattern measured in Pb + Pb collisions at the CERN SPS[J/OL]. Phys. Lett. B, 2000, 477: 28-36. DOI: 10.1016/S0370-2693(00)00237-9.

[94] ARNALDI R, et al. J/ψ production in Indium-Indium collisions at 158- GeV/nucleon[J/OL]. Conf. Proc. C, 2006, 060726: 430-434. DOI: 10.1103/PhysRevLett.99.132302.

[95] ADARE A, et al. J/ψ Production vs Centrality, Transverse Momentum, and Rapidity in Au+Au Collisions at $\sqrt{s_{NN}}$ = 200 GeV[J/OL]. Phys. Rev. Lett., 2007, 98: 232301. DOI: 10.1103/PhysRevLett.98.232301.

[96] ADAMCZYK L, et al. J/ψ production at low p_T in Au + Au and Cu + Cu collisions at $\sqrt{s_{NN}}$ = 200 GeV with the STAR detector[J/OL]. Phys. Rev. C, 2014, 90(2): 024906. DOI: 10.1103/PhysRevC.90.024906.

[97] BRAUN-MUNZINGER P, STACHEL J. (Non)thermal aspects of charmonium production and a new look at J / psi suppression[J/OL]. Phys. Lett. B, 2000, 490: 196-202. DOI: 10.1016/S0370-2693(00)00991-6.

[98] GRANDCHAMP L, RAPP R, BROWN G E. In medium effects on charmonium production in heavy ion collisions[J/OL]. Phys. Rev. Lett., 2004, 92: 212301. DOI: 10.1103/PhysRevLett.92.212301.

[99] ZHAO X, RAPP R. Charmonium in medium: From correlators to experiment[J/OL]. Phys. Rev. C, 2010, 82: 064905. https://link.aps.org/doi/10.1103/PhysRevC.82.064905.

[100] ZHAO X, RAPP R. Transverse Momentum Spectra of J/ψ in Heavy-Ion Collisions[J/OL]. Phys. Lett. B, 2008, 664: 253-257. DOI: 10.1016/j.physletb.2008.03.068.

[101] ZHAO X, RAPP R. Forward and midrapidity charmonium production at RHIC[J/OL]. Eur. Phys. J. C, 2009, 62: 109-117. DOI: 10.1140/epjc/s10052-009-0905-6.

[102] BRAMBILLA N, et al. Heavy Quarkonium: Progress, Puzzles, and Opportunities[J/OL].

Eur. Phys. J. C, 2011, 71: 1534. DOI: 10.1140/epjc/s10052-010-1534-9.

[103] KLUBERG L. 20 years of J/ψ suppression at the CERN SPS: Results from experiments NA38, NA51 and NA50[J/OL]. Eur. Phys. J. C, 2005, 43: 145-156. DOI: 10.1140/epjc/s2005-02245-6.

[104] ABREU M, ALESSANDRO B, ALEXA C, et al. Evidence for deconfinement of quarks and gluons from the J/ψ suppression pattern measured in Pb-Pb collisions at the CERN-SPS [J/OL]. Physics Letters B, 2000, 477(1): 28-36. DOI: https://doi.org/10.1016/S0370-2693(00)00237-9.

[105] ABELEV B, ADAM J, ADAMOVá D, et al. Centrality, rapidity and transverse momentum dependence of J/ψ suppression in Pb–Pb collisions at $\sqrt{s_{NN}}$=2.76 TeV[J/OL]. Physics Letters B, 2014, 734: 314-327. DOI: https://doi.org/10.1016/j.physletb.2014.05.064.

[106] ADAMCZYK L, ADKINS J, AGAKISHIEV G, et al. Energy dependence of J/ψ production in Au+Au collisions at $\sqrt{s_{\rm NN}}$=39,62.4 and 200 GeV[J/OL]. Physics Letters B, 2017, 771: 13-20. DOI: https://doi.org/10.1016/j.physletb.2017.04.078.

[107] ADAM J, ADAMCZYK L, ADAMS J, et al. Measurement of inclusive J/ψ suppression in Au+Au collisions at $\sqrt{s_{\rm NN}}$=200 GeV through the dimuon channel at STAR[J/OL]. Physics Letters B, 2019, 797: 134917. DOI: https://doi.org/10.1016/j.physletb.2019.134917.

[108] YAN L, ZHUANG P, XU N. J/ψ production in quark-gluon plasma[J/OL]. Phys. Rev. Lett., 2006, 97: 232301. https://link.aps.org/doi/10.1103/PhysRevLett.97.232301.

[109] ZHOU K, XU N, XU Z, et al. Medium effects on charmonium production at ultrarelativistic energies available at the cern large hadron collider[J/OL]. Phys. Rev. C, 2014, 89: 054911. https://link.aps.org/doi/10.1103/PhysRevC.89.054911.

[110] ZHAO X, RAPP R. Medium modifications and production of charmonia at lhc[J/OL]. Nuclear Physics A, 2011, 859(1): 114-125. DOI: https://doi.org/10.1016/j.nuclphysa.2011.05.001.

[111] ANDRONIC A, BRAUN-MUNZINGER P, REDLICH K, et al. Decoding the phase structure of QCD via particle production at high energy[J/OL]. Nature, 2018, 561(7723): 321-330. DOI: 10.1038/s41586-018-0491-6.

[112] REBYAKOVA V, STRIKMAN M, ZHALOV M. Coherent ρ and J/ψ photoproduction in ultraperipheral processes with electromagnetic dissociation of heavy ions at RHIC and LHC [J/OL]. Phys. Lett. B, 2012, 710: 647-653. DOI: 10.1016/j.physletb.2012.03.041.

[113] ADAM J, et al. Measurement of an excess in the yield of J/ψ at very low $p_{\rm T}$ in Pb-Pb collisions at $\sqrt{s_{\rm NN}}$ = 2.76 TeV[J/OL]. Phys. Rev. Lett., 2016, 116(22): 222301. DOI: 10.1103/PhysRevLett.116.222301.

[114] LIU Y P, QU Z, XU N, et al. J/psi Transverse Momentum Distribution in High Energy Nuclear Collisions at RHIC[J/OL]. Phys. Lett. B, 2009, 678: 72-76. DOI: 10.1016/j.physletb.2009.

06.006.

[115] ZHAO X, RAPP R. Medium Modifications and Production of Charmonia at LHC[J/OL]. Nucl. Phys. A, 2011, 859: 114-125. DOI: 10.1016/j.nuclphysa.2011.05.001.

[116] ZHA W, KLEIN S R, MA R, et al. Coherent J/ψ photoproduction in hadronic heavy-ion collisions[J/OL]. Phys. Rev. C, 2018, 97(4): 044910. DOI: 10.1103/PhysRevC.97.044910.

[117] BREIT G, WHEELER J A. Collision of two light quanta[J/OL]. Phys. Rev., 1934, 46(12): 1087-1091. DOI: 10.1103/PhysRev.46.1087.

[118] ADAMS J, et al. Production of e+ e- pairs accompanied by nuclear dissociation in ultra-peripheral heavy ion collision[J/OL]. Phys. Rev. C, 2004, 70: 031902. DOI: 10.1103/PhysRevC.70.031902.

[119] ABBAS E, et al. Charmonium and e^+e^- pair photoproduction at mid-rapidity in ultra-peripheral Pb-Pb collisions at $\sqrt{s_{\mathrm{NN}}}$=2.76 TeV[J/OL]. Eur. Phys. J. C, 2013, 73(11): 2617. DOI: 10.1140/epjc/s10052-013-2617-1.

[120] ZHA W, RUAN L, TANG Z, et al. Coherent lepton pair production in hadronic heavy ion collisions[J/OL]. Phys. Lett. B, 2018, 781: 182-186. DOI: 10.1016/j.physletb.2018.04.006.

[121] KLEIN S R. Two-photon production of dilepton pairs in peripheral heavy ion collisions [J/OL]. Phys. Rev. C, 2018, 97(5): 054903. DOI: 10.1103/PhysRevC.97.054903.

[122] HEISENBERG W, EULER H. Consequences of Dirac's theory of positrons[J/OL]. Z. Phys., 1936, 98(11-12): 714-732. DOI: 10.1007/BF01343663.

[123] WEISSKOPF V. The electrodynamics of the vacuum based on the quantum theory of the electron[J]. Kong. Dan. Vid. Sel. Mat. Fys. Med., 1936, 14N6(6): 1-39.

[124] SCHWINGER J S. On gauge invariance and vacuum polarization[J/OL]. Phys. Rev., 1951, 82: 664-679. DOI: 10.1103/PhysRev.82.664.

[125] TOLL J. The dispersion relation for light and its application to problems involving electron pairs., ph.d. thesis, princeton university, new jersey (1952)[Z].

[126] LI C, ZHOU J, ZHOU Y J. Impact parameter dependence of the azimuthal asymmetry in lepton pair production in heavy ion collisions[J/OL]. Phys. Rev. D, 2020, 101(3): 034015. DOI: 10.1103/PhysRevD.101.034015.

[127] HARRISON M, LUDLAM T, OZAKI S. RHIC project overview[J/OL]. Nucl. Instrum. Meth. A, 2003, 499: 235-244. DOI: 10.1016/S0168-9002(02)01937-X.

[128] ASCHENAUER E C, et al. eRHIC Design Study: An Electron-Ion Collider at BNL[A]. 2014. arXiv: 1409.1633.

[129] ANDERSON M, et al. The Star time projection chamber: A Unique tool for studying high multiplicity events at RHIC[J/OL]. Nucl. Instrum. Meth. A, 2003, 499: 659-678. DOI: 10.1016/S0168-9002(02)01964-2.

[130] BEDDO M, et al. The STAR barrel electromagnetic calorimeter[J/OL]. Nucl. Instrum. Meth. A, 2003, 499: 725-739. DOI: 10.1016/S0168-9002(02)01970-8.

[131] RUAN L, et al. Perspectives of a Midrapidity Dimuon Program at RHIC: A Novel and Compact Muon Telescope Detector[J/OL]. J. Phys. G, 2009, 36: 095001. DOI: 10.1088/0954-3899/36/9/095001.

[132] WHITTEN C A. The beam-beam counter: A local polarimeter at STAR[J/OL]. AIP Conf. Proc., 2008, 980(1): 390-396. DOI: 10.1063/1.2888113.

[133] LLOPE W J, et al. The STAR Vertex Position Detector[J/OL]. Nucl. Instrum. Meth. A, 2014, 759: 23-28. DOI: 10.1016/j.nima.2014.04.080.

[134] ADLER C, DENISOV A, GARCIA E, et al. The RHIC zero degree calorimeter[J/OL]. Nucl. Instrum. Meth. A, 2001, 470: 488-499. DOI: 10.1016/S0168-9002(01)00627-1.

[135] WANG S. MWPC Prototyping and Testing for STAR Inner TPC Upgrade[J/OL]. Int. J. Mod. Phys. Conf. Ser., 2018, 46: 1860079. DOI: 10.1142/S2010194518600790.

[136] ADAMS J, et al. The STAR Event Plane Detector[J/OL]. Nucl. Instrum. Meth. A, 2020, 968: 163970. DOI: 10.1016/j.nima.2020.163970.

[137] Physics Program for the STAR/CBM eTOF Upgrade[A]. 2016. arXiv: 1609.05102.

[138] SHAO M, RUAN L J, CHEN H F, et al. Beam test results of two kinds of multi-gap resistive plate chambers[J/OL]. Nucl. Instrum. Meth. A, 2002, 492: 344-350. DOI: 10.1016/S0168-9002(02)01355-4.

[139] AGAKICHIEV G, et al. Enhanced production of low mass electron pairs in 200-GeV/u S - Au collisions at the CERN SPS[J/OL]. Phys. Rev. Lett., 1995, 75: 1272-1275. DOI: 10.1103/PhysRevLett.75.1272.

[140] AGAKICHIEV G, et al. Low mass e+ e- pair production in 158/A-GeV Pb - Au collisions at the CERN SPS, its dependence on multiplicity and transverse momentum[J/OL]. Phys. Lett. B, 1998, 422: 405-412. DOI: 10.1016/S0370-2693(98)00083-5.

[141] AGAKICHIEV G, et al. e+ e- pair production in Pb - Au collisions at 158-GeV per nucleon [J/OL]. Eur. Phys. J. C, 2005, 41: 475-513. DOI: 10.1140/epjc/s2005-02272-3.

[142] ADAMOVA D, et al. Enhanced production of low mass electron pairs in 40-AGeV Pb - Au collisions at the CERN SPS[J/OL]. Phys. Rev. Lett., 2003, 91: 042301. DOI: 10.1103/PhysRevLett.91.042301.

[143] ARNALDI R, et al. First measurement of the rho spectral function in high-energy nuclear collisions[J/OL]. Phys. Rev. Lett., 2006, 96: 162302. DOI: 10.1103/PhysRevLett.96.162302.

[144] ARNALDI R, et al. Evidence for the production of thermal-like muon pairs with masses above 1-GeV/c**2 in 158-A-GeV Indium-Indium Collisions[J/OL]. Eur. Phys. J. C, 2009, 59: 607-623. DOI: 10.1140/epjc/s10052-008-0857-2.

[145] ADARE A, et al. Dielectron production in Au+Au collisions at $\sqrt{s_{NN}}$=200 GeV[J/OL]. Phys. Rev. C, 2016, 93(1): 014904. DOI: 10.1103/PhysRevC.93.014904.

[146] BONANNO A, PLATANIA A. Asymptotically safe inflation from quadratic gravity[J/OL]. Phys. Lett. B, 2015, 750: 638-642. DOI: 10.1016/j.physletb.2015.10.005.

[147] ADAMCZYK L, et al. Measurements of Dielectron Production in Au+Au Collisions at $\sqrt{s_{\mathrm{NN}}}$ = 200 GeV from the STAR Experiment[J/OL]. Phys. Rev. C, 2015, 92(2): 024912. DOI: 10.1103/PhysRevC.92.024912.

[148] ADAMCZYK L, et al. Dielectron Mass Spectra from Au+Au Collisions at $\sqrt{s_{\mathrm{NN}}}$ = 200 GeV [J/OL]. Phys. Rev. Lett., 2014, 113(2): 022301. DOI: 10.1103/PhysRevLett.113.022301.

[149] RAPP R, WAMBACH J. Low mass dileptons at the CERN SPS: Evidence for chiral restoration?[J/OL]. Eur. Phys. J. A, 1999, 6: 415-420. DOI: 10.1007/s100500050364.

[150] VAN HEES H, RAPP R. Comprehensive interpretation of thermal dileptons at the SPS[J/OL]. Phys. Rev. Lett., 2006, 97: 102301. DOI: 10.1103/PhysRevLett.97.102301.

[151] VAN HEES H, RAPP R. Dilepton Radiation at the CERN Super Proton Synchrotron[J/OL]. Nucl. Phys. A, 2008, 806: 339-387. DOI: 10.1016/j.nuclphysa.2008.03.009.

[152] YAN L, ZHUANG P, XU N. Competition between J / psi suppression and regeneration in quark-gluon plasma[J/OL]. Phys. Rev. Lett., 2006, 97: 232301. DOI: 10.1103/PhysRevLett. 97.232301.

[153] FERREIRO E G, FLEURET F, LANSBERG J P, et al. Cold nuclear matter effects on J/psi production: Intrinsic and extrinsic transverse momentum effects[J/OL]. Phys. Lett. B, 2009, 680: 50-55. DOI: 10.1016/j.physletb.2009.07.076.

[154] BAUR G, HENCKEN K, TRAUTMANN D, et al. Coherent gamma gamma and gamma-A interactions in very peripheral collisions at relativistic ion colliders[J/OL]. Phys. Rept., 2002, 364: 359-450. DOI: 10.1016/S0370-1573(01)00101-6.

[155] ADAM J, et al. Low-p_T e^+e^- pair production in Au+Au collisions at $\sqrt{s_{NN}}$ = 200 GeV and U+U collisions at $\sqrt{s_{NN}}$ = 193 GeV at STAR[J/OL]. Phys. Rev. Lett., 2018, 121(13): 132301. DOI: 10.1103/PhysRevLett.121.132301.

[156] ADAM J, et al. Observation of excess J/ψ yield at very low transverse momenta in Au+Au collisions at $\sqrt{s_{\mathrm{NN}}}$ = 200 GeV and U+U collisions at $\sqrt{s_{\mathrm{NN}}}$ = 193 GeV[J/OL]. Phys. Rev. Lett., 2019, 123(13): 132302. DOI: 10.1103/PhysRevLett.123.132302.

[157] KŁUSEK-GAWENDA M, SZCZUREK A. Photoproduction of j/ψ mesons in peripheral and semicentral heavy ion collisions[J/OL]. Phys. Rev. C, 2016, 93: 044912. https://link.aps.org /doi/10.1103/PhysRevC.93.044912.

[158] BRANDENBURG J D, XU Z, ZHA W, et al. Exploring gluon tomography with polarization dependent diffractive J/ψ production[J/OL]. Phys. Rev. D, 2022, 106(7): 074008. DOI:

10.1103/PhysRevD.106.074008.

[159] LUO J, LI X, TANG Z, et al. Effect of initial nuclear deformation on dielectron photoproduction in hadronic heavy-ion collisions[J/OL]. Phys. Rev. C, 2023, 108(5): 054906. DOI: 10.1103/PhysRevC.108.054906.

[160] BRANDENBURG J D, ZHA W, XU Z. Mapping the electromagnetic fields of heavy-ion collisions with the Breit-Wheeler process[J/OL]. Eur. Phys. J. A, 2021, 57(10): 299. DOI: 10.1140/epja/s10050-021-00595-5.

[161] ABDALLAH M, et al. Search for the chiral magnetic effect with isobar collisions at $\sqrt{s_{NN}}$=200 GeV by the STAR Collaboration at the BNL Relativistic Heavy Ion Collider [J/OL]. Phys. Rev. C, 2022, 105(1): 014901. DOI: 10.1103/PhysRevC.105.014901.

[162] SMIRNOV D, LAURET J, PEREVOZTCHIKOV V, et al. Vertex reconstruction at star: Overview and performance evaluation[J/OL]. Journal of Physics: Conference Series, 2017, 898: 042058. DOI: 10.1088/1742-6596/898/4/042058.

[163] REED R, BALEWSKI J, BARNBY L S, et al. Vertex finding in pile-up rich events for p+p and d+Au collisions at STAR[J/OL]. J. Phys. Conf. Ser., 2010, 219: 032020. DOI: 10.1088/1742-6596/219/3/032020.

[164] ABELEV B I, et al. Systematic Measurements of Identified Particle Spectra in pp, d^+ Au and Au+Au Collisions from STAR[J/OL]. Phys. Rev. C, 2009, 79: 034909. DOI: 10.1103/PhysRevC.79.034909.

[165] ZYLA P A, et al. Review of Particle Physics[J/OL]. PTEP, 2020, 2020(8): 083C01. DOI: 10.1093/ptep/ptaa104.

[166] DENG W T, HUANG X G, MA G L, et al. Test the chiral magnetic effect with isobaric collisions[J/OL]. Phys. Rev. C, 2016, 94: 041901. DOI: 10.1103/PhysRevC.94.041901.

[167] LI H, XU H J, ZHAO J, et al. Multiphase transport model predictions of isobaric collisions with nuclear structure from density functional theory[J/OL]. Phys. Rev. C, 2018, 98(5): 054907. DOI: 10.1103/PhysRevC.98.054907.

[168] HAMMELMANN J, SOTO-ONTOSO A, ALVIOLI M, et al. Influence of the neutron-skin effect on nuclear isobar collisions at energies available at the BNL Relativistic Heavy Ion Collider[J/OL]. Phys. Rev. C, 2020, 101(6): 061901. DOI: 10.1103/PhysRevC.101.061901.

[169] XU H J, LI H, WANG X, et al. Determine the neutron skin type by relativistic isobaric collisions[J/OL]. Phys. Lett. B, 2021, 819: 136453. DOI: 10.1016/j.physletb.2021.136453.

[170] XU H J, WANG X, LI H, et al. Importance of isobar density distributions on the chiral magnetic effect search[J/OL]. Phys. Rev. Lett., 2018, 121(2): 022301. DOI: 10.1103/PhysRevLett.121.022301.

[171] BICHSEL H. A method to improve tracking and particle identification in TPCs and silicon

detectors[J/OL]. Nucl. Instrum. Meth. A, 2006, 562: 154-197. DOI: 10.1016/j.nima.2006.03.009.

[172] ADARE A, et al. Detailed measurement of the e^+e^- pair continuum in $p + p$ and Au+Au collisions at $\sqrt{s_{NN}} = 200$ GeV and implications for direct photon production[J/OL]. Phys. Rev. C, 2010, 81: 034911. DOI: 10.1103/PhysRevC.81.034911.

[173] UP W5013 C P L L W. GEANT - Detector Simulation and Simulation Tool[Z].

[174] TANG Z, XU Y, RUAN L, et al. Spectra and radial flow at RHIC with Tsallis statistics in a Blast-Wave description[J/OL]. Phys. Rev. C, 2009, 79: 051901. DOI: 10.1103/PhysRevC.79.051901.

[175] TANG Z, YI L, RUAN L, et al. Statistical Origin of Constituent-Quark Scaling in the QGP hadronization[J/OL]. Chin. Phys. Lett., 2013, 30: 031201. DOI: 10.1088/0256-307X/30/3/031201.

[176] SJOSTRAND T, EDEN P, FRIBERG C, et al. High-energy physics event generation with PYTHIA 6.1[J/OL]. Comput. Phys. Commun., 2001, 135: 238-259. DOI: 10.1016/S0010-4655(00)00236-8.

[177] ADAMCZYK L, et al. Measurements of D^0 and D^* Production in $p + p$ Collisions at $\sqrt{s} =$ 200 GeV[J/OL]. Phys. Rev. D, 2012, 86: 072013. DOI: 10.1103/PhysRevD.86.072013.

[178] ADAMCZYK L, et al. Observation of D^0 Meson Nuclear Modifications in Au+Au Collisions at $\sqrt{s_{NN}} = 200$ GeV[J/OL]. Phys. Rev. Lett., 2014, 113(14): 142301. DOI: 10.1103/PhysRevLett.113.142301.

[179] MATSUI T, SATZ H. J/ψ suppression by quark-gluon plasma formation[J/OL]. Physics Letters B, 1986, 178(4): 416-422. DOI: https://doi.org/10.1016/0370-2693(86)91404-8.

[180] NAGLE J L, FRAWLEY A D, LEVY L A L, et al. Modeling of J/ψ modifications in deuteron-nucleus collisions at high energies[J/OL]. Phys. Rev. C, 2011, 84: 044911. https://link.aps.org/doi/10.1103/PhysRevC.84.044911.

[181] NAGLE J, BENNETT M. Initial state energy loss dependence of J/ψ and Drell–Yan in relativistic heavy ion collisions[J/OL]. Physics Letters B, 1999, 465(1): 21-26. DOI: https://doi.org/10.1016/S0370-2693(99)00988-0.

[182] CRONIN J W, FRISCH H J, SHOCHET M J, et al. Production of hadrons at large transverse momentum at 200, 300, and 400 GeV[J/OL]. Phys. Rev. D, 1975, 11: 3105-3123. https://link.aps.org/doi/10.1103/PhysRevD.11.3105.

[183] VOGT R. Are the J/ψ and $\chi(c)$ A dependencies the same?[J/OL]. Nuclear Physics A, 2002, 700(1): 539-554. DOI: https://doi.org/10.1016/S0375-9474(01)01313-6.

[184] FERREIRO E. Excited charmonium suppression in proton–nucleus collisions as a consequence of comovers[J/OL]. Physics Letters B, 2015, 749: 98-103. DOI: https://doi.org/10.1

016/j.physletb.2015.07.066.

[185] AUBERT J J, BECKER U, BIGGS P J, et al. Experimental observation of a heavy particle J [J/OL]. Phys. Rev. Lett., 1974, 33: 1404-1406. https://link.aps.org/doi/10.1103/PhysRevLett.33.1404.

[186] AUGUSTIN J E, BOYARSKI A M, BREIDENBACH M, et al. Discovery of a narrow resonance in e^+e^- annihilation[J/OL]. Phys. Rev. Lett., 1974, 33: 1406-1408. https://link.aps.org/doi/10.1103/PhysRevLett.33.1406.

[187] ADAM J, et al. J/ψ production cross section and its dependence on charged-particle multiplicity in $p+p$ collisions at $\sqrt{s}$ = 200 GeV[J/OL]. Phys. Lett. B, 2018, 786: 87-93. DOI: 10.1016/j.physletb.2018.09.029.

[188] ADARE A, et al. Transverse momentum dependence of J/ψ polarization at midrapidity in p+p collisions at $\sqrt{s}$ = 200 GeV[J/OL]. Phys. Rev. D, 2010, 82: 012001. DOI: 10.1103/PhysRevD.82.012001.

[189] SMITH K. J/ψ and $\psi(2S)$ Production in Small Systems with PHENIX[J/OL]. Acta Phys. Polon. Supp., 2023, 16(1): 1-A73. DOI: 10.5506/APhysPolBSupp.16.1-A73.

[190] ACHARYA S, et al. Measurements of inclusive J/ψ production at midrapidity and forward rapidity in Pb−Pb collisions at $\sqrt{s_{\rm NN}}$ = 5.02 TeV[A]. 2023. arXiv: 2303.13361.

[191] ADARE A, AFANASIEV S, AIDALA C, et al. j/ψ production versus centrality, transverse momentum, andrapidity in Au + Au collisions at $\sqrt{s_{NN}} = 200$ GeV[J/OL]. Phys. Rev. Lett., 2007, 98: 232301. https://link.aps.org/doi/10.1103/PhysRevLett.98.232301.

[192] ADAMCZYK L, et al. J/ψ production at high transverse momenta in $p+p$ and Au+Au collisions at $\sqrt{s_{NN}}$ = 200 GeV[J/OL]. Phys. Lett. B, 2013, 722: 55-62. DOI: 10.1016/j.physletb.2013.04.010.

[193] ADAM J, et al. Inclusive, prompt and non-prompt J/ψ production at mid-rapidity in Pb-Pb collisions at $\sqrt{s_{\rm NN}}$ = 2.76 TeV[J/OL]. JHEP, 2015, 07: 051. DOI: 10.1007/JHEP07(2015)051.

[194] BAI X. Quarkonium measurements in nucleus-nucleus collisions with ALICE[J/OL]. Nuclear Physics A, 2021, 1005: 121769. DOI: https://doi.org/10.1016/j.nuclphysa.2020.121769.

[195] ZHA W, RUAN L, TANG Z, et al. Coherent photo-produced J/ψ and dielectron yields in isobaric collisions[J/OL]. Phys. Lett. B, 2019, 789: 238-242. DOI: 10.1016/j.physletb.2018.12.041.

[196] ZHA W, BRANDENBURG J D, TANG Z, et al. Initial transverse-momentum broadening of breit-wheeler process in relativistic heavy-ion collisions[J/OL]. Physics Letters B, 2020, 800: 135089. https://www.sciencedirect.com/science/article/pii/S0370269319308111. DOI: https://doi.org/10.1016/j.physletb.2019.135089.

[197] WANG P, WU X, ZHA W, et al. Calculations of differential momentum transfer spectra for

J/ψ photoproduction in heavy-ion collisions[J/OL]. Chin. Phys. C, 2022, 46(7): 074103. DOI: 10.1088/1674-1137/ac5db8.

[198] LAFFERTY G, WYATT T. Where to stick your data points: The treatment of measurements within wide bins[J/OL]. Nuclear Instruments and Methods in Physics Research Section A: Accelerators, Spectrometers, Detectors and Associated Equipment, 1995, 355(2): 541-547. DOI: https://doi.org/10.1016/0168-9002(94)01112-5.

[199] ZHA W, HUANG B, MA R, et al. Systematic study of the experimental measurements on J/ψ cross sections and kinematic distributions in $p+p$ collisions at different energies[J/OL]. Phys. Rev. C, 2016, 93: 024919. https://link.aps.org/doi/10.1103/PhysRevC.93.024919.

[200] ZHAO J, ZHUANG P. Effects of cold and hot nuclear matter on J/ψ production at energies selected for the beam energy scan at the bnl relativistic heavy ion collider[J/OL]. Phys. Rev. C, 2022, 105: 064907. https://link.aps.org/doi/10.1103/PhysRevC.105.064907.

[201] ABREU M, ALESSANDRO B, ALEXA C, et al. Transverse momentum distributions of J/ψ, ψ', drell–yan and continuum dimuons produced in pb–pb interactions at the sps[J/OL]. Physics Letters B, 2001, 499(1): 85-96. DOI: https://doi.org/10.1016/S0370-2693(01)00019-3.

[202] ADARE A, AFANASIEV S, AIDALA C, et al. Ground and excited state charmonium production in $p+p$ collisions at $\sqrt{s} = 200$ GeV[J/OL]. Phys. Rev. D, 2012, 85: 092004. https://link.aps.org/doi/10.1103/PhysRevD.85.092004.

[203] ADARE A, AFANASIEV S, AIDALA C, et al. J/ψ production in $\sqrt{s_{NN}} = 200$ GeV Cu+Cu collisions[J/OL]. Phys. Rev. Lett., 2008, 101: 122301. https://link.aps.org/doi/10.1103/PhysRevLett.101.122301.

[204] ACHARYA S, ADAMOVá D, ADLER A, et al. Centrality and transverse momentum dependence of inclusive J/ψ production at midrapidity in Pb+Pb collisions at $\sqrt{s_{\mathrm{NN}}}$=5.02 tev[J/OL]. Physics Letters B, 2020, 805: 135434. DOI: https://doi.org/10.1016/j.physletb.2020.135434.

Acknowledgements

写到博士论文的最后一章，6 年读博阶段也走到了尾声，往昔的回忆开始涌上心头。一路走来，遇到了很多值得感谢的老师，朋友，同学以及平常生活中的可爱的人，能走到博士毕业，途中离不开你们的帮助和鼓励。

首先我要特别感谢的是我在科大的导师唐泽波老师，在读博期间，是他带领着我去探索高能物理的世界。唐老师对我的指导可以追溯到本科大三期间，科大的本科生在高年级阶段会有前往本校实验室参与科研的习惯，记得当时唐老师亲自带着我和我的同学梁政，一起做关于康普顿散射的实验，唐老师平易近人，讲解问题十分透彻。之后，在研究生期间，低年级时接触过探测器实验，虽然之后很快转向数据分析，但短暂的探测器工作经历也让我获益匪浅。从加入 STAR 合作组的第一个练手题目，到之后的第一个分析再到第二个分析，都离不开他的悉心指导和鼓励帮助。唐老师严谨的科研态度，发散的科研思路，以及耐心指导每一个学生的态度是我今后科研学习上的榜样。我还要特别感谢我在科大的另一个导师查王妹老师，查老师指导了我的本科毕业论文，在研究生期间指导我进一步探索本科毕业课题，帮助我解决了很多科研问题，和他讨论让我获益匪浅，我博士阶段取得的所有成果都离不开他的帮助和指导。我还要特别感谢 BNL 的马荣荣老师，从我开始参与 STAR 合作组，到如今临近博士毕业，马老师对我的帮助一直都没有中断过。由于我英语不好，马老师对我英语文章的修改细致入微，在每周的 MTD 组会上鼓励我们多用英语交流，对于我提出的任何问题都会耐心回答，在我去 BNL 值班的期间，无论是生活还是学习上，马老师都给予了我很多帮助，十分感谢。另外，我还要感谢科大的李澄老师，邵明老师，孙勇杰老师在我低年级时参与探测器实验时给予的帮助；感谢科大的张一飞老师和白晓智老师在分析和物理图像上的指导；感谢 BNL 的阮丽娟老师和许长补老师对我的帮助和指导，以及在 BNL 值班期间对我的照顾；感谢华南师范大学的杨帅老师和山东大学的杨钱老师，两位老师分别在和我博士期间息息相关的分析课题领域，给予了我很多帮助和指导。

同时，感谢我在科大实验室的同学，在生活和科研上的帮助。特别感谢已经毕业的刘圳师姐，刚开始做 STAR 的分析时，是刘圳师姐一直帮我解决 bug，寻找资料和讲解分析的步骤，在我分析的起步阶段帮助了我很多。感谢纪媛婧师姐在我分析遇到困难时给予的帮助和指导。感谢中午积极干饭小组的李子阳，吴鑫和王岩，让吃饭不只是吃饭。感谢曾经做过室友的卢鹏忠和梁政，感谢你们在生活上的帮助和包容。同时感谢实验室的所有同学, 罗加宣, 王恺扬, 刘哲进, 李欣柏, 熊圳君, 朱森杰等等，作为一个大集体，一起春游，一起轰趴，一起文献学习，

一起聚餐，充满了欢声笑语，让我的研究生生涯增贴了许多欢乐。

同时，感谢山东大学的王桢，王晓凤，沈丹丹，以及华南师范大学的张炜，感谢你们在博士科研道路上的陪同，让科研没那么孤单。

感谢在 BNL 值班期间认识的师兄师姐以及来各个单位的小伙伴的陪同和帮助，感谢 Kong 请我们吃饭，感谢早晨带我们去长岛捞螃蟹，晓璇带我们去纽约市区玩，以及很多小伙伴在我们没有车的时候带我们去购物，在 BNL 吃火锅和包饺子是伙食最好的时候。

感谢 STAR 合作组，让我能接触到那么多有趣的物理，以及开拓自己的眼见，在合作组内让我快速学习和成长，发挥自己的价值。

感谢科大，让我慢慢成长，在科大生活了快 10 年，已然是我的第二个故乡，来到科大是我荣幸，今后，祝愿自己不断前进。

最后，我要特别感谢我的父母和亲朋好友，没有你们的支持和鼓励，我无法顺利完成学业，感谢你们一直无条件的支持我。

Publications

Publications

1. **Kaifeng Shen** and (for the STAR Collaboration), Recent J/ψ results in p+p and Au+Au collisions from STAR, EPJ Web Conf. Volume 259, 2022.
2. **Kaifeng Shen** and (for the STAR Collaboration), J/ψ production in Au+Au collisions at 54.4 GeV, Proceeding of Science (CHARM2020) 037.
3. **Kaifeng Shen** and (for the STAR Collaboration), Initial electromagnetic field dependence of photon-induced production in isobaric collisions at STAR, EPJ Web Conf. Volume 276, 2023.

Prepare to publish

1. **Kaifeng Shen**, Xin Wu, Zebo Tang and Wangmei Zha, Exploring the photoproduction of ρ and ϕ in hadronic heavy-ion collisions, arXiv:2401.07480 (submitted to EPJC)
2. Measurement of J/ψ production in Au+Au collisions at $\sqrt{s_{\rm NN}}$ = 54.4 GeV with STAR experiment (Principal Author), Target Journal: Physics Letter B.
3. Initial electromagnetic field dependence of photon-induced production in isobaric collisions at STAR (Principal Author), Target Journal: Physical Review Letters.

Presentations

1. Initial electromagnetic field dependence of photon-induced production in isobaric collisions at STAR, **parallel talk** at international workshop on the physics of Ultra Peripheral collisions (**UPC 2023**), 10-15 Dec 2023, Playa del Carmen
2. Initial electromagnetic field dependence of photon-induced production in isobaric collisions at STAR, **parallel talk** at the 9^{th} Asian Triangle Heavy-Ion Conference (**ATHIC 2023**)
3. Initial electromagnetic field dependence of photon-induced production in isobaric collisions at STAR, **parallel talk** at the 9th edition of the Workshop for Young Scientists on the Physics of Ultra-relativistic Nucleus-Nucleus Collisions (**Hot Quarks 2022**), 11– 17 Oct 2022, Dao House, Estes Park, Colorado, USA
4. Initial electromagnetic field dependence of photon-induced production in isobaric collisions at STAR, **parallel talk** at the 20th International Conference on

Strangeness in Quark Matter (**SQM 2022**), 13-17 June 2022 Busan, Republic of Korea

5. Initial electromagnetic field dependence of photon-induced production in isobaric collisions at STAR, **poster** at 29th International Conference on Ultra-relativistic Nucleus-Nucleus Collisions (**QM2022**), April 4-10, 2022, KRAKÓW, POLAND
6. Recent J/ψ results in p+p and Au+Au collisions from STAR, **parallel talk** at the 19th International Conference on Strangeness in Quark Matter (**SQM 2021**), May 17-22, 2021, sponsored by Brookhaven National Laboratory, Upton, New York
7. HF highlight: J/ψ R_{AA} at $\sqrt{s_{\mathrm{NN}}}$= 54.4 GeV in Au+Au collisions, **invited plenary talk** at STAR Analysis Meeting – June 2021
8. J/ψ production in Au+Au collisions at $\sqrt{s_{\mathrm{NN}}}$ = 54.4 GeV, **parallel talk**, 10th International Workshop on Charm Physics (**CHARM 2020**)
9. J/ψ production in Au+Au collisions at $\sqrt{s_{\mathrm{NN}}}$ = 54.4 GeV, **parallel talk**, The 2020 Fall Meeting of the Division of Nuclear Physics of the American Physical Society (**DNP2020**), 29 October 2020 to 1 November 2020